IMAGE-BASED FORCE ESTIMATION AND HAPTIC RENDERING FOR ROBOT-ASSISTED CARDIOVASCULAR INTERVENTION

Amir Hooshiar

A Thesis

in

The Department

of

Mechanical, Industrial and Aerospace Engineering

Presented in Partial Fulfillment of the Requirements

for the Degree of

Doctor of Philosophy (Mechanical Engineering) at

Concordia University

Montréal, Québec, Canada

April 2021

CONCORDIA UNIVERSITY

School of Graduate Studies

This is to certify that the thesis prepared

By: **Mr. Amir Hooshiar**

Entitled: **IMAGE-BASED FORCE ESTIMATION AND HAPTIC RENDERING FOR ROBOT-ASSISTED CARDIOVASCULAR INTERVENTION**

and submitted in partial fulfillment of the requirements for the degree of

Doctor of Philosophy (Mechanical Engineering)

complies with the regulations of this University and meets the accepted standards with respect to originality and quality.

Signed by the Final Examining Committee:

_____ Chair
Dr. Arash Mohammadi

_____ External Examiner
Dr. Vincent Duchaine

_____ External Examiner
Dr. Amin Hammad

_____ Examiner
Dr. Muthukumaran Packirisamy

_____ Examiner
Dr. Sivakumar Narayanswamy

_____ Co-Supervisor
Dr. Javad Dargahi

Approved by: _____
Dr. Martin D. Pugh, Chair
Department of Mechanical, Industrial and Aerospace Engineering

March, – 2021 _____
Dr. Mourad Debbabi, Dean
Gina Cody School of Engineering

Abstract

IMAGE-BASED FORCE ESTIMATION AND HAPTIC RENDERING FOR ROBOT-ASSISTED CARDIOVASCULAR INTERVENTION

Amir Hooshiar, Ph.D.

Concordia University, 2021

Clinical studies have indicated that the loss of haptic perception is the prime limitation of robot-assisted cardiovascular intervention technology, hindering its global adoption. It causes compromised situational awareness for the surgeon during the intervention and may lead to health risks for the patients. This doctoral research was aimed at developing technology for addressing the limitation of the robot-assisted intervention technology in the provision of haptic feedback. The literature review showed that sensor-free force estimation (haptic cue) on endovascular devices, intuitive surgeon interface design, and haptic rendering within the surgeon interface were the major knowledge gaps. For sensor-free force estimation, first, an image-based force estimation methods based on inverse finite-element methods (iFEM) was developed and validated. Next, to address the limitation of the iFEM method in real-time performance, an inverse Cosserat rod model (iCORD) with a computationally-efficient solution for endovascular devices was developed and validated. Afterward, the iCORD was adopted for analytical tip force estimation on steerable catheters. The experimental studies confirmed the accuracy and real-time performance of the iCORD for sensor-free force estimation. Afterward, a wearable drift-free rotation measurement device (MiCarp) was developed to facilitate the design of an intuitive surgeon interface by decoupling the rotation measurement from the insertion measurement. The validation studies showed that MiCarp had a superior performance for spatial rotation measurement compared to other modalities. In the end, a novel haptic feedback system based on smart magnetoelastic elastomers was developed, analytically modeled, and experimentally validated. The proposed haptics-enabled surgeon module had an unbounded workspace for interventional tasks and provided an intuitive interface. Experimental validation, at component and system levels, confirmed the usability of the proposed methods for robot-assisted intervention systems.

Acknowledgments

I would like to acknowledge that this doctoral research was performed at Concordia University, located on unceded Indigenous lands. The Kanien'kehá:ka Nation is recognized as the custodians of Tiohtià:ke/Montreal, the lands and waters on which we gather today. This thesis is a result of a joyful and memorable period of my academic journey. During my doctoral study, there were more happy days than sad days and I am grateful for that. My happiest day was May, 1st, 2018, the day I received the NSERC Gilles-Brassard Doctoral Prize for Interdisciplinary Research during Canada Top Researchers Day at the Parliament of Canada. My saddest day was January, 8th, 2020 when flight PS752 was shot down and some of my friends from Concordia University and the University of Alberta were killed tragically.

First and foremost, I owe a huge debt of gratitude to my beloved wife, Dr. Naghmeh Bandari. Without her love, support, inspiration, companionship, and sacrifices none of my life's achievements would have been possible. Fulfilling the life's responsibilities and making up for me, when I was not at my best at home, while doing her Ph.D. demanded the very best humane qualities that are rare to find in a person. I am lucky, blessed, and grateful for having you by my side, Naghmeh. Thank you for being such a great partner.

I would also like to thank my supervisor, Prof. Javad Dargahi for giving me the opportunity of learning from him. His constant support, fatherly advice, and strategic vision in research were invaluable assets and strong driving force forward. I would like to express my gratitude to the members of my Examination Committee, Dr. Amin Hammad, Dr. Muthukumaran Packirisamy, and Dr. Sivakumar Narayanswamy for their time, diligent advice, and guidance throughout my doctoral study. My special thanks and gratitudes go to Dr. Mahdi Tavakoli, for giving me the chance of joining his team at

the University of Alberta for a research visit during 2019. His technical knowledge, professionalism, and modesty made him a role-model for my future academic career. I would also like to extend my thanks to Dr. Siamak Najarian from the University of British Columbia, Dr. Ahmedreza Arshi from Amirkabir University of Technology, and Dr. Hamidreza Katouzian who have constantly supported me since my undergraduate studies in Iran. I express my sincere gratitudes to Dr. Jake Barralet, Dr. Keving Lachapelle, and Dr. Rudolf Reindl from McGill University Health Center (MUHC), with whom I had the opportunity of collaboration during my term as a Surgical Innovation Fellow. Moreover, I would like to thank Dr. Christopher Kent, the CEO of ODS Medical Inc., Montreal, and his wonderful colleagues for their support during my industrial internship at ODS.

I was blessed with having great friends and colleagues. Not a single day passed on me without learning from them; for that I am in their debt. Specifically, I would like to thank Mr. Mohammad Kaviani, Mr. Amir Sayadi, Mr. Mohammad Jolaei, Mr. Alireza Payami, Mr. Alireza Beiglou, Dr. Sharham Shokouhfar, Dr. Siamak Arbatani, Dr. Mostapha Marzban, and Dr. Ehsan Zahedi.

I appreciate the financial support of Natural Sciences and Engineering Research Council of Canada for granting me an NSERC Vanier Scholarship, the NSERC Gilles-Brassard Doctoral Prize, and an NSERC CREATE Doctoral Fellowship for Surgical Innovation at McGill University. Also, I appreciate the FRQNT's support for offering me an FRQNT PBEEE Doctoral Scholarship. Concordia University, School of Graduate Studies, Gina Cody School of Engineering, and Mechanical, Industrial, and Aerospace Engineering Department supported my study through a Full-Tuition Recruitment Award, a Doctoral Fellowship, Concordia Public Scholars Award, and two Doctoral Seminar Awards, and I am grateful for that. Moreover, I would like to thank the staff of the Mechanical, Industrial, and Aerospace Engineering Department for their kind support, especially Ms. Leslie Hossein, Ms. Arlene Zimmerman, and Ms. Maureen Thuringer.

In the end, I would like to acknowledge my parents' efforts throughout my life. My father, Ghassem, a veteran nurse, was the first person who familiarized me with the surgical technology at the very early stages of my life. My childhood *Toys"R"Us* was my father's medical bag stacked with tweezers, graspers, and clamps. My mother, Batoul, had total devotion to the upbringing of me, my brother Ali, and my sister Maryam. She never stopped sacrificing for facilitating the best-in-town education for us. My parents' prayers and blessings have always been with me.

To:

the love of my life, Naghmeh,
my mother, and my father.

Contents

List of Figures

List of Tables

Nomenclature

Symbols

Operators

$\cdot$	Dot product
$\times$	Cross product
$\otimes$	Outer product
$\dot{(.)}$	Temporal derivative operator with respect to t
$(.)'$	Spatial derivative operator with respect to s
$(.)^{\wedge}$	Hat operator
$(.)^{\vee}$	Vee operator
$\|\|.\|\|$	Euclidean norm
$\nabla(.)$	Gradient operator
$\nabla \cdot (.)$	Divergence operator
$\nabla \times (.)$	Curl operator
det	Determinant operator

Greek Symbols

α	Magnitude of contact force, Spatial rotation angle
β	Location of unknown contact force
γ	Spread factor for Gaussian force interpolation
Γ	Bending plane
$\boldsymbol{\delta}$	Parameterized longitudinal extension of centerline

$\delta\tilde{\mathbf{f}}_{FEM}$	Increment of Nodal force vector
δt	Time increment
$\delta\tilde{\mathbf{u}}_{FEM}$	Increment of nodal displacement vector
ε	Residual deformation, residual internal force and moment
ζ	Traction coefficient
ϑ	Poisson's ratio
θ	Polar angle in spherical and cylindrical coordinates, pitch angle
κ	Total curvature
κ_g	Geodesic curvature
κ_n	Normal curvature
λ	Curvature control parameter for Bezier shape interpolation
$\lambda_{1,2,3}$	Principal stretches
$\mathbf{\Lambda}$	Left Cauchy-Green deformation tensor, Rotation matrix
Λ_{ij}	$ij-$th component of rotation matrix
μ	Statistical mean
μ_0	Magnetic permeability of vacuum
μ_r	Relative magnetic permeability
μ_f	Dynamic coefficient of friction
ξ_k	$k-$th Gauss node for Gauss quadrature
Π	Functional for tip force estimation
ρ	Density, radial distance in spherical coordinates
σ	Statistical standard deviation
σ_i	Normal true stress at inner radius
τ_g	Geodesic torsion
φ	Bending angle, roll angle
$\boldsymbol{\chi}$	Parameterized deformation vector of centerline
ψ	Yaw angle
Ψ	Camera calibration matrix, magnetic energy

$\boldsymbol{\omega}$	Angular velocity vector
Ω	Force indicator, stain energy
$\Omega^{\star}$	Total amended free energy function

English Symbols

$\mathbf{a}$	Acceleration
$\mathbf{b}$	Magnetic field intensity
b_{Θ}	Angular component of the magnetic field intensity
$\mathbf{b}_n$	Vector of Bernstein polynomials
b_R	Radial component of the magnetic field intensity
b_Z	Longitudinal component of the magnetic field intensity
$\mathbf{c}$	Centerline of deformed B-spline
$\mathbf{c}^{\star}$	Centerline of undeformed B-spline
$\mathbf{C}$	Right Cauchy-Green deformation tensor
$\mathbf{d}_{1,2,3}$	Orthonormal vectors of Darboux frame
d_{FSLP}	Location of force on FSLP sensor
D_r	Diameter of the active roller
$\hat{\mathbf{e}}_{(.)}$	Unit vector in $(.)-$direction
e_{ss}	Steady-state error
E	Elastic modulus
$\mathbf{f}$	External force vector
$\mathbf{f}_f$	Friction force vector
$\tilde{\mathbf{f}}_{FEM}$	Nodal force vector
f_{FSLP}	Magnitude of force on FSLP sensor
$\mathbf{f}^{\text{Tip}}$	Tip force vector
f_m	Magnetic body force per unit volume
$\mathbf{F}$	Deformation gradient tensor
$F^{\star}$	Desired force
$\vec{F}$	Force vector

F_{ATI}	Reference force measured by ATI Mini40 sensor
F_{avg}	Mean force
F_m	Total magnetic body force
F_{max}	Maximum force
F_{min}	Minimum detectable force
$\mathbf{g}$	Gravity vector
G_0	Initial shear modulus
$\mathbf{h}$	Magnetic field strength
H	Transfer function of DC-motor in $z-$space
I	Second moment of inertia
$\mathbf{I}$	3-by-3 identity matrix
$I_{1\cdots6}$	Scalar magnetoelastic deformation invariants
k	Flexural stiffness
$k_{P,I,D}$	Coefficients of PID controller
k_T	Torque constant of DC-motor
$\mathbf{K}$	Stiffness matrix
L	Inserted length of the endovascular device (analytical integration)
$\bar{L}$	Computed length of the endovascular device (discrete integration)
$\mathbf{m}$	Internal moment
$\mathbf{m}^{\text{Tip}}$	Tip moment vector
$\mathbf{n}$	Internal force
n_c	Number of contact points
N_p	Number of peak forces
$N(\mu, \sigma)$	Normal distribution with a mean on μ and a standard deviation of σ
p	Confidence interval, Lagrange multiplier
$\mathbf{P}$	Control points of B-spline
$\tilde{r}$	Residual internal force and moment vector
r	Radius of curvature

$\mathbf{R}$	Rotation matrix
R_i	Inner radius
R_o	Outer radius
R^2	Goodness-of-fit
s	Normalized curve parameter, magnet separation
t	Time, thickness
$\mathbf{t}$	Position vector of the tip of catheter
T	Torque
$\mathbf{T}$	Nominal stress tensor
$T_{5\%}$	Settling time (5%-variation)
T_r	Resistant torque, Rise time
T_f	Frictional torque
u	Horizontal position of pixels in image
$\mathbf{u}$	Parameterized bending and torsion of centerline
$\vec{u}$	Displacement vector
$\tilde{\mathbf{u}}_{FEM}$	Nodal displacement vector
v	Vertical position of pixels in image
$\vec{v}$	Velocity vector
$v_{1,2}$	Output voltages of FSLP sensor
w_k	$k-$th Gauss weight for Gauss quadrature
x	x-component of the tip position of catheter
$\mathbf{x}$	Spatial representation of the coordinates
$\mathbf{X}$	Material representation of the coordinates
y	y-component of the tip position of catheter
z	Longitudinal distance in cylindrical coordinate system

Abbreviations

3PB	Three-point bending
AA	Aortic artery
AFib	Atrial fibrillation
ANN	Artificial neural network
B-spline	Bezier spline
BCA	Brachiocephalic artery
CAS	Coronary artery stenosis
Cath-Lab	Catheterization laboratory
CF	Complementary filter
CM	Continuum mechanics
CRA	Cryo-ablation
CT	Computed tomography
CVR	Cardiac valve replacement
DAQ	Data-acquisition
DC	Direct current
DFR	Direct force reflection
DG	Differential geometry
DoF	Degree of freedom
ECF	Extended Kalman filter
ED	Endovascular device
EKF	Extended Kalman filter
EPI	Electrophysiologic intervention
EV	Endovascular
FBG	Fiber Bragg grating
FDA	Food and Drug Administration
FEM	Finite-element method
FFNN	Feed-forward neural network

FIT	Force impact over time
FPI	Fabry-Perot interferometry
Fr	French
FS	Frenet-Serret
FSLP	Force-sensing linear potentiometer
GMM	Gaussian mixture models
GPU	Graphics processing unit
GUI	Graphical user interface
iCORD	Inverse Cosserat rod model for endovascular devices
ID	Inner diameter
iFEM	Inverse finite-element method
IMU	Inertial measurement unit
LHS	Left-hand-side
LIM	Light intensity modulation
LSA	Left subclavian artery
MAE	Mean-absolute error
MAUDE	Manufacturer and User Facility Device Experience
MD	Multi-body dynamics
MDR	Medical Device Record
MIS	Minimally invasive surgery
ML	Machine learning
MRA	Magnetic resonance angiography
MRE	Magnetorheological elastomer
MRF	Magnetorheological fluid
MRI	Magnetic resonance imaging
NiTi	Nickel-Titanium
NL-FEM	Nonlinear finite-element method
NN	Neural network

NVI	Neurovascular intervention
OD	Outer diameter
OR	Operation room
PCI	Percutaneous cardiovascular intervention
PID	Proportional integral derivative
PPI	Percutaneous peripheral intervention
PTCA	Percutaneous transluminal coronary angioplasty
PSO	Particle swarm optimization
RCI	Robot-assisted cardiovascular intervention
RFA	Radio-frequency ablation
RHS	Right-hand-side
RMS	Root-mean-square
RNS	Remote navigation system
SD	Standard deviation
SMA	Shape memory alloy
SNR	Signal-to-noise ratio
SVR	Support vector regression
SVC	Support vector classification
SQP	Sequential quadratic programming
UDP	User datagram protocol
UI	User interface
UKF	Unscented Kalman filter
VR	Virtual reality

Chapter 1

Introduction

1.1 Background

Cardiovascular diseases (CVDs) are the prime cause of death globally[1]. Amongst different cardiovascular diseases, the most prevalent is the coronary artery stenoses (CAS) [1]. Both genetic and epigenetic factors might contribute to the development and extension of a CAS, e.g. sex [2], smoking [3], obesity[4], inadequate physical activity [5], hypertension [6], and diabetes [7].

Following the discovery of the blood-thinning effects of heparin in 1915, medications became the first medical intervention to treat CAS [8]. In 1950, Vineburg and Buller were the first surgeons who used an arterial bypass to re-establish the blood flow downstream to a stenosis [9]. This procedure soon became the gold standard in the treatment of CAS. However, it was associated with a relatively high mortality rate at that time [9]. Dotter *et al.* reported the first application of a minimally invasive surgery (MIS) approach for revascularization in 1964 [10]. Demonstration of success in the extremities, e.g., femoral, renal, and carotid arteries, led to the first *percutaneous transluminal coronary angioplasty* (PTCA) by Andreas Gruenzing, Zurich, Switzerland in 1977 [11]. This procedure is also referred to as *percutaneous coronary intervention* (PCI). A similar transluminal treatment of non-coronary arteries is recognized as the *percutaneous peripheral intervention* (PPI).

During a PCI, the femoral or radial artery of the patient is punched to make a port of access to the artery. Afterward, a short introducer sheath is placed into the port to secure it and reduce the friction.

Subsequently, a guiding catheter along with a metallic guide-wire is introduced into the artery passing through the introducer sheath. The guide-wire and catheter are manipulated and steered under live x-ray imaging, i.e., fluoroscopy, to access the site of a stenosis. Ultimately balloon angioplasty and/or stent implantation is performed at the discretion of surgeon [11, 12].

Improvement of the techniques and promising clinical outcomes led to the significant expansion of PCI and PPI. This expansion, inevitably, demanded more hours of operation for surgeons and surgical staff. Because of the significant dosage of ionizing radiation, surgeons and surgical staff are exposed to various health risks must wear very heavy lead aprons to protect their vital organs, e.g., thyroid, heart, lungs, breasts, genitals. A typical set of aprons, i.e., a chest vest and a skirt, weighs more than 7 kg. Many studies have reported a significant correlation of orthopedic diseases with the time of wearing lead aprons [13, 14]. Physical demand, along with risks exposed to pregnancy because of X-ray radiation, has significantly reduced the number of female cardiac interventionists [15, 16]. Furthermore, etiological studies emphasize that due to the risks of infection, cataract, and skin anomalies, the catheterization laboratory (cathlab) is recognized as a high-risk environment for surgeons and staff [13, 14]. The available literature is rich in evidence to this stipulation, e.g., 50% chance of orthopedic diseases, 5% of radiation-related skin diseases, and 5.5% of cataract, needle sticking, and glove perforation [17, 18]. In addition to that, needle stick injury and glove perforation are among the infection hazards with rates of 0.6% and 1%, respectively. Additionally, complications due to the imprecise localization of stenosis, inaccurate length estimation, and stent misplacement are among the most reported risks for patients undergoing PCI [19]. Furthermore, patients are exposed to continuous X-ray during PCI. Also, in complex or multi-stage operations, excessive injection of contrast agents is a risk factor. These agents are radiopaque and are used to visualize the blood flow in X-ray [20]. Nephropathies, secondary to the clearance of contrast agent from kidneys, have been reported in PCI patients[20].

To alleviate these problems, the first robot-assisted cardiovascular intervention system was introduced to reduce health risks for patients, occupational hazards for surgeons, and improve the surgeon's dexterity and precision. Such systems have utilized a surgeon—patient architecture for performing a telerobotic cardiovascular intervention. As depicted in Fig. 1.1, this configuration reduced X-ray exposure to the surgeon and staff; however, introduced new health risks to the patient, mainly

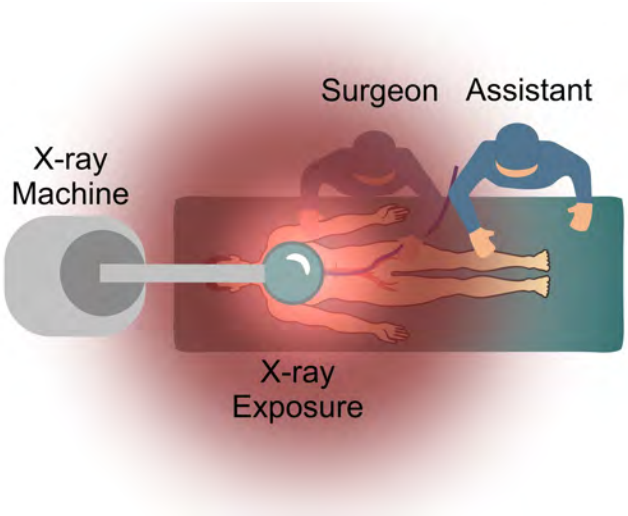

(a)

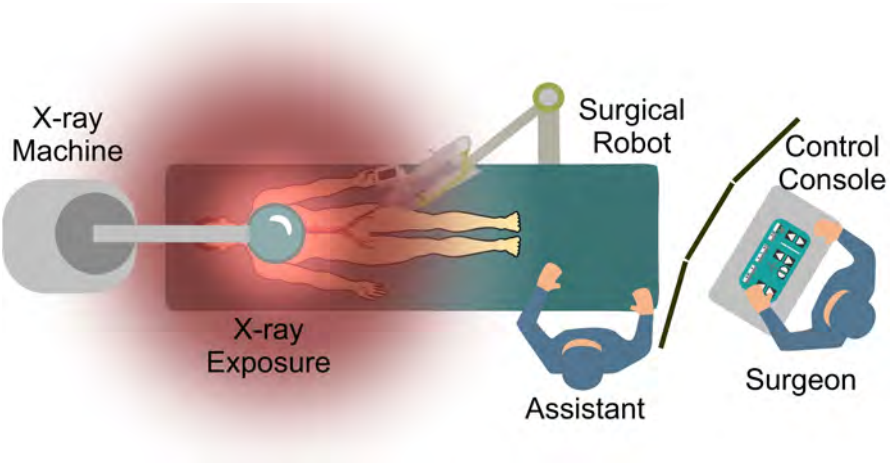

(b)

Figure 1.1: Schematic view of X-ray exposure to a surgeon and assistant in (a) conventional cardiovascular intervention, and (b) robot-assisted cardiovascular intervention.

due to the loss of haptic feedback during the procedure.

Based on the results, the reviewed literature were categorized under *surgical instrumentation*, *surgical planning and assistance*, *mechanisms and robotics*, *vascular contact mechanics*, *clinical and post-market surveillance*, or *ergonomics and occupational safety* areas. Furthermore, the most investigated topics in each research area are categorized in Fig. 1.2. Researchers may find this layout utile for expediting a literature exploration.

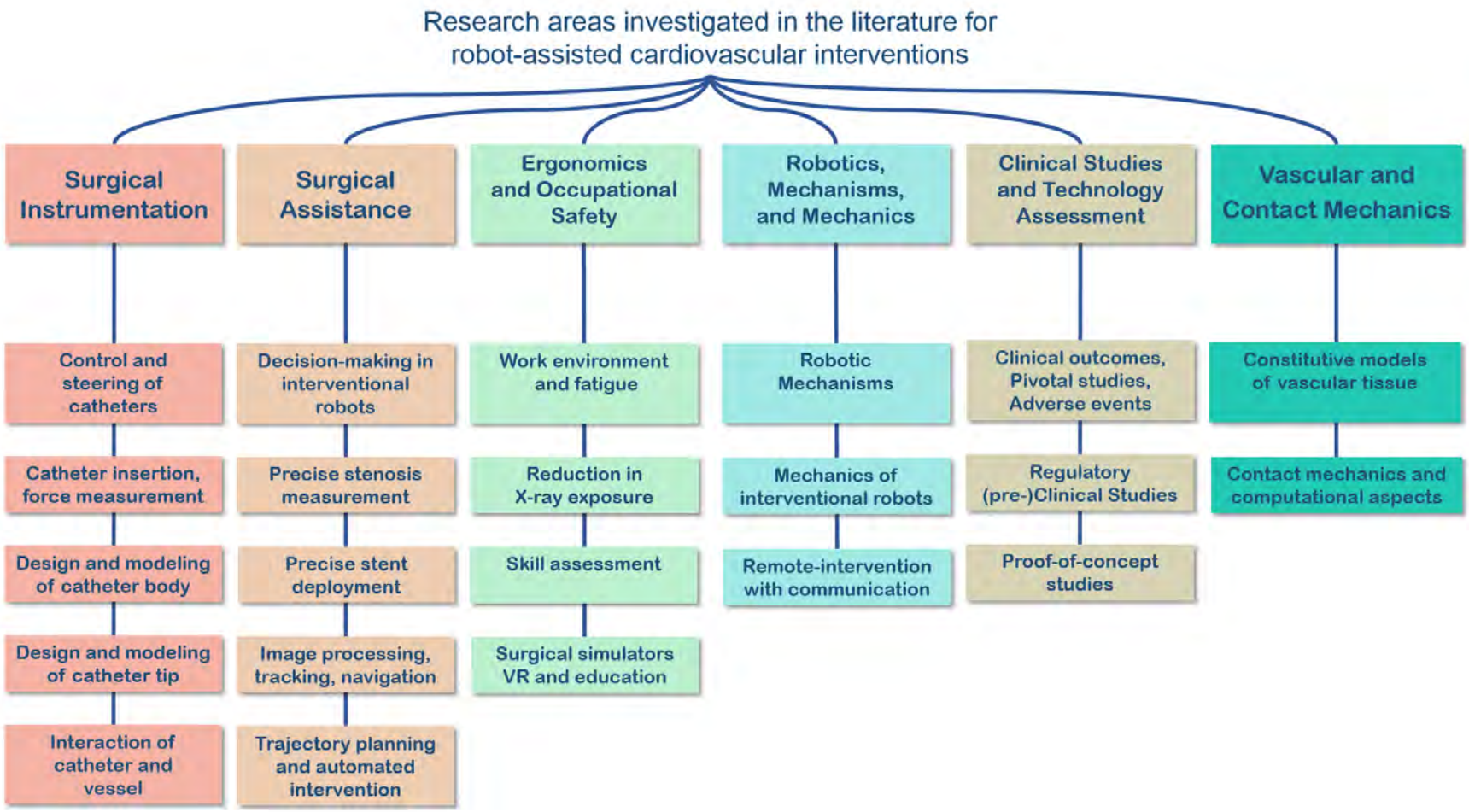

Figure 1.2: Research areas in the literature pertinent to robot-assisted cardiovascular intervention.

1.1.1 Robot-assisted Cardiovascular Interventions: System Overview

Robot-assisted cardiovascular intervention systems are mainly utilized for three major procedures: *percutaneous coronary intervention* (PCI), *percutaneous peripheral intervention* (PPI), *electrophysiologic intervention* (EPI). For the sake of brevity, these procedures are referred to as robotic PCI, robotic PPI, robotic EPI, hereinafter.

From 2000 to 2019, various remote-control robotic catheterization systems were developed to alleviate some of the risks associated with conventional cardiovascular interventions. Ernst *et al.* [21] investigate the applicability of such systems for electrophysiological mapping and radio-frequency ablation in 2003. This study was the first robotic EPI procedure and served as a cornerstone for further development of the first non-navigated endovascular robotic catheter system by Hansen Medical in 2004, i.e., *SenseiRobotics*^{TM} Catheter System, Hansen Medical, Mountain View, CA, USA.

The development of the first robotic PCI system was accelerated since 2004, aspired by the promising results of robotic EPI. Beyar *et al.* [22] performed the first robotic PCI on human subjects in 2006. The first generation of remote-control robot used by Beyar *et al.* consisted of an operator module and a patient module. The operator module was equipped with a touch screen monitor and a joystick, and the patient module was a three degree-of-freedom (DOF) robot. It was capable of insertion, withdrawal, and rotation of a guidewire and endoluminal device, e.g., balloon catheter[22]. It was initially introduced as a remote navigation system (RNS), but after modifications and further development, it was launched as the first commercial robotic PCI system in 2012, *CorPath*^{TM}*200*, Corindus Inc., Waltham, MA, USA. At the time of its launch, *CorPath*^{TM}*200* was cleared by FDA solely intended for robotic PCI procedures; however, its last generation, *CorPath*^{TM}*GRX*, was granted FDA approval for robotic PPI procedures in 2016.

Later in 2013, Hansen Medical, Mountain View, CA, USA, launched *Magellan*^{TM} vascular robotic system, was approved for robotic PPI. Both *CorPath*^{TM}*200* and *Magellan*^{TM} employ a surgeon-patient teleoperation system design. However, their compatible catheters and driving mechanisms differ. More specifically, *Magellan*^{TM}, can only accommodate its compatible catheters while *CorPath*^{TM}*200* and *CorPath*^{TM}*GRX* are capable handling commercially available cardiac catheters.

In contrast to the generic cardiac catheters, the distal tip of *Magellan*^{TM} catheters can actively be

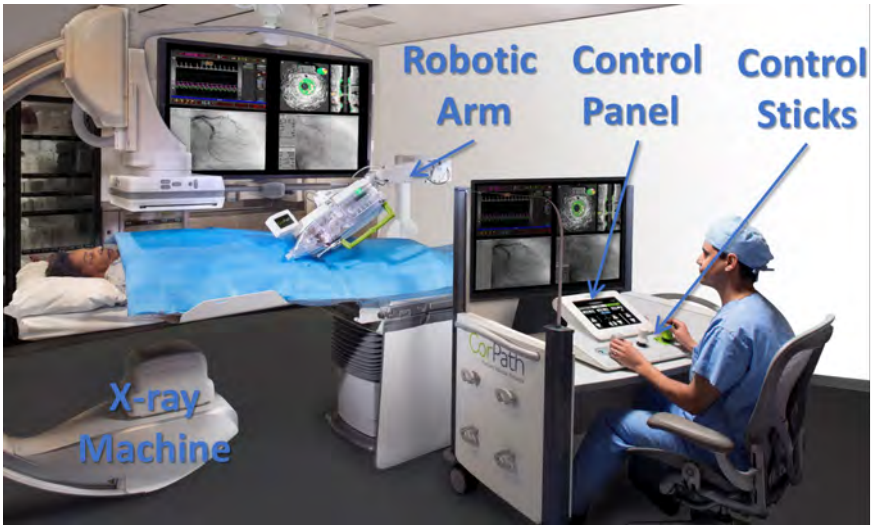

Figure 1.3: System components of a *CorPath*^{TM}*GRX* robotic PCI system. (Courtesy of Corindus Inc., Waltham, MA, USA).

steered to bend about two perpendicular axes using a cable-driven mechanism [23]. This feature enables the surgeon to introduce the catheter while it is steered towards the target distally. This functionality could not be achieved using the conventional catheters which were guided proximally (from the portion outside the patient's body). Fig. 1.3 represents the system components of a robotic PCI procedure at cathlab.

1.1.2 Robot-assisted Cardiovascular Interventions: Clinical Outcomes and Limitations

Early clinical outcomes of the robotic PCI in human subjects were assuring and encouraging [22, 24, 25]. Weisz *et al.* [25] reported a success rate of 98.8% for robotic PCI in an early pivotal study on 164 patients in 2013. Their results showed that robotic intervention with *CorPath*^{TM}*200* was effective and successful in the reduction of X-ray exposure to the surgeon by 95% [25]. Others have also investigated the effectiveness of robotic PCI in increasing the precision of stent placement [26, 27], decreasing occupational hazards [28], and X-ray exposure to surgeon [29].

Based on this survey, it is evident that the majority of clinical researchers advocate this technology based on its efficacy in risk reduction and enhancing precision. Some even have referred to the robotic PCI as *"the dawn of a new era"* [30]. On the other hand, some studies escalate serious

doubt about its long-term efficiency. The latter studies mainly express concern about the cost burden [31, 32] and loss of haptic feedback [28, 32].

Despite this conflict of opinion, a recent study revealed that the use of robotic PCI, both in number and variety of procedures, is increasing [33]. Also, recent advancements in teleoperation for robotic PCI has raised hopes for telestenting [34, 35]. However, the gap between critical and in-favor opinions amongst clinicians is still large [32, 35]. One of the common grounds between the advocates and critiques is the recognition of the loss of haptic feedback as the prime limitation of current technology and a significant barrier for global expansion robot-assisted cardiovascular interventions [32, 33, 35].

1.1.3 Necessity for Haptic Feedback and Challenges

Serious concerns about the loss of haptic feedback during robotic interventions are expressed in clinical investigations [36–39]. Seto *et al.* [32], and Smilowitz *et al.* [28] have likened the robotic intervention without haptic feedback to a blind control of catheter and guidewire. The first difficulty inherited by the loss of haptic feedback in robotic intervention is the poor hand-eye coordination [40]. Consequently, a surgeon's geometric perception of the catheter and vessels gets limited [39, 41–44]. It is also postulated to contribute to the oversteering of the endovascular devices and vascular rupture [45]. Furthermore, studies have shown that significant risk of embolization, perforation, thrombosis, and dissection is associated with excessive contact force between the catheter and vascular wall [41–43, 45, 46]. Uncertainty about the catheter insertion force and depth is reported as causes of withdrawal of the robotic procedures[17, 32, 35, 39]. Rafii-Tari *et al.* [42] have recently identified significantly different force-time signatures between novice and expert interventionists in five common robotic interventional procedures. They also have observed that the pulling force for novices group was up to six times larger than experts. On the other hand, other studies have reported up to 76% reduction in the contact force between catheter and vessel by providing force feedback to a surgeon in a simulated aortic cannulation [43, 47]. Also, studies have revealed that the effectiveness of robotic EPI procedures is significantly dependent on the ability of the surgeon to maintain the contact force in the range of 20 ± 10 grf[48, 49]. Furthermore, a recent study has shown that surgeons' motor reaction to the catheter force is almost three times faster than visual

reaction time. This postulates the possibility of early risk prevention with haptic feedback [50]. Therefore, the role of haptic feedback in the safety and effectiveness of robotic interventions is evident.

Researchers have investigated various approaches and methods to tackle this problem; however, haptic feedback, and consequently haptic teleoperation, is yet to be embedded in the commercially available systems. Currently available robotic PCI systems, i.e. *CorPath™ 200* and *CorPath™ GRX*, are not equipped with haptic feedback. However, intended for robotic EPI, *IntelliSensce®* system, integrated on *Sensei X®* robotic system (Hansen Medical, Mountain View, CA, USA), provides force feedback to surgeon's hand. Nevertheless, the main limitation of force feedback in *Sensei X®* is that it only provides distal force, i.e., feedback taken from the tip of the catheter. This provides the surgeon with a feeling of the contact status at the tip of the catheter, not the insertion force. Therefore, the author would consider that as tactile feedback rather than haptic.

In *Sensei X®* robotic system, the force feedback is estimated based on a mechanical model of the catheter tip. *Sensei X®* robotic system utilizes a custom designed family of steerable catheters, i.e. *Artisan®*. This catheter has a tendon-driven tip which has a large work-space inside the atria. A mechanical model based on multi-body dynamics is used to estimate the force at the tip of the catheter based on the tendon tension. Camarillo *et al.* [23] and Ganji and Janabi-Sharifi [51] have postulated two methods for this purpose. Although some EPI catheters, e.g. *TactiCath®* with *TactiSys™* system (St. Jude Medical Inc., MI, USA), are capable of providing real-time force measurement, these catheters are yet to be integrated in robotic EPI systems. A comprehensive review on steerable and force measuring catheters, modeling approaches and methods was published by Awaz *et al.* [52].

Despite the advancements, Guo *et al.* has reported that the force feedback in the current robotic intervention systems is often assessed as inaccurate [46]. The reason might be related to either the location for which the force feedback is estimated, i.e., the tip of the catheter, or the type of haptic cue, i.e., vibration, delivered to the surgeon. As stated earlier, the force feedback in *Sensei X®* is estimated for the tip of Artisan® catheter; nevertheless, surgeons are used to feel the insertion force at the vascular access port along with vibrational tactile cues [41]. This haptic perception might be perceived as different from the surgeons' experiences. This exemplifies the importance of proper

definition and assessment of haptic feedback in robot-assisted cardiovascular interventions. Besides, the lack of systematic investigation on the choice of reference point for haptic feedback is evident in the literature. Interested researchers would find a comprehensive review of the taxonomy and clinical outcomes of different commercially available robotic systems in [41] and [17], respectively.

1.2 Motivation

Based on the literature review, sensor-free force estimation (haptic cue) on endovascular devices, intuitive surgeon interface design, and compatible haptic rendering modality with the surgeon interface were the major knowledge gaps. Thus, the motivation of this doctoral research was to address these limitations. In the following, the rationale and motivation of this research are summarized:

(1) Robot-assisted cardiovascular intervention (RCI) provides superior surgical accuracy and radiation safety for patients and surgeons. Clinical studies have indicated that the main technical limitation hindering the global adoption of this technology is the loss of intraoperative haptic perception for surgeons. The main haptic perception mechanism involved in perceiving the insertion force of endovascular devices is through exteroception [53]. Studies, e.g., [42], have shown that the most significant haptic cue during the cardiovascular interventional procedures is the insertion force felt by the surgeon intraoperatively. Thus, a method to measure or estimate the insertion force and render it as haptic feedback to the surgeons is a clinical need. Currently, the commercial sensor-embedded catheters are capable of measuring forces on the catheters. However, their usability for haptic provision is limited due to:

   (a) they measure internal forces of the catheter at a limited number of points along the catheter, e.g., tip forces, while the contact forces may occur and change at multiple points along the catheter intraoperatively,

   (b) their indication for use is limited only to radio-frequency ablation procedures, while RCI systems are general-purpose and may be used for other procedures, e.g., percutaneous cardiovascular interventions,

   (c) their structure, thus their exhibited deformation with insertion force, is different than

conventional catheters as they are actively steerable, e.g., through tendon-driving, while the conventional catheters deform passively in response to insertion force and lateral contact forces.

(2) Moreover, measuring the insertion force at the insertion point of the catheter to the patient's body is not a viable solution. User studies, e.g., [41], have shown that surgeons have not perceived this mode of force feedback intuitive mainly due to the pollution of the force measurement with high frictional forces within the RCI system. Thus, a sensor-free force estimation method capable of real-time performance is of high clinical relevance for haptic rendering.

(3) Another motivation of this study was to avoid introducing a new technological requirement, e.g., custom-designed catheters, to the surgical workflow. RCI systems have already disrupted the conventional intervention workflow by requiring multiple preoperative setting up steps. Thus, it was motivated that the proposed force estimation should work with the available hard and soft resources within the interventional workflow. Given that the use of X-ray imaging (fluoroscopy) is a standard-of-care, the proposed force estimation methods in this research were merely image-based and could function with the intraoperative images. Also, the compatibility of the proposed methods with the typical conventional endovascular devices was at the core of this research.

(4) Also on this note, it was considered that the proposed force estimation methods should not rely on any *a-priori* knowledge of the patient's anatomy. A critical limitation of the previous studies on force estimation on endovascular devices is their dependency on preoperative computed tomography (CT-) or magnetic resonance imaging (MRI-) scan to obtain the patient's vasculature shape. In practice, generally neither CT- or MRI-scan is required for cardiovascular intervention procedures. Given the fact that the majority of the patients undergoing interventional procedures are in critical conditions, there is practically no time for an unnecessary preoperative imaging.

(5) Furthermore, the state-of-the-art designs of the surgeon interface for RCI systems are either non-intuitive, e.g., knobs, or have usability limitations, e.g., limited insertion stroke. In fact,

the provision of favorable haptic feedback through the currently-available surgeon interfaces is not feasible. Surgeons are used to holding long flexible endovascular devices in hand and insert and rotate those into the patient's body as much as required and without spatial limitation. However, the current interface designs do not allow the surgeon to maneuver the endovascular devices as they would normally do during manual surgery. On top of that, because of the fundamental differences between the kinematics of conventional catheterization and the developed surgeon interfaces, the currently available surgeon interfaces do not provide a favorable platform for haptic augmentation.

(6) To design a more intuitive surgeon interface, some studies have proposed to use a rotary encoder stacked on a linear stage to measure the insertion stroke and rotation, e.g., [54]. Apart from the limitation of the stroke course in such designs, a haptic feedback system on this design requires to overcome the inertia of the rotary measurement system. Thus, the haptic force feedback is affected by the inertial of the rotation measurement. In this research, it was motivated to decouple the rotation measurement from insertion measurement to avoid the coupling effect.

(7) The most adopted technique for haptic rendering in medical robotics is through direct force reflection (DFR) by controlling the torque of one or multiple DC-motor assembled in a kinematic chain with its end-effector at the hand of the user, e.g., surgeon. Torque control of DC-motors is an active process that requires constant current feeding to the motors. Also, the robustness and stability of the current control loop for force rendering require accurate system modeling and noise filtering, especially when subjected to large desired force gradients. As an alternative, to improve robustness and to simplify the force control framework, another motivation of this research was to develop a novel semi-active haptic rendering modality to couple with the proposed surgeon interface.

1.3 Research Objectives

To address the identified knowledge gaps, stated in Sec. 1.2 the specific objectives of this research were:

(1) To identify the design requirements pertinent to the provision of haptic feedback for robot-assisted cardiovascular intervention procedures, e.g., haptic cue, operational range, required accuracy, haptic rendering modality, surgeon module workspace, and refresh rate.

(2) To conceptualize, design, and validate an alternative system configuration for the robot-assisted cardiovascular intervention systems that can accommodate the design requirements of image-based haptic feedback.

(3) To develop, implement, and validate force estimation methods to estimate contact and insertion force along with the endovascular devices that:

   (a) are purely image-based and compatible with 2D fluoroscopy images available at catheterization labs,

   (b) are independent of *a-priori* knowledge of the patient's anatomy,

   (c) can be used for both conventional and steerable endovascular devices,

   (d) can be solved fast to perform in real-time, i.e., minimum refresh rate of 25 Hz, and

   (e) are accurate with less than 10% error of full-scale within the operational range of insertion forces, i.e., 0–2 N.

(4) To develop, implement, and validate a technology to decouple the rotation measurement from insertion measurement at the surgeon module that:

   (a) is drift-free to avoid the temporal error accumulation,

   (b) can be used for multiple consecutive and continuous rotations of the endovascular devices in space without workspace limitation,

   (c) is accurate with less than 10% error, and

   (d) can exhibit a refresh rate of at least 25 Hz.

(5) To develop, implement, and validate an intuitive surgeon module that:

   (a) is haptics-enabled,

   (b) its haptic rendering is accurate with less than 10% error of the desired force,

(c) can exhibit a haptic rendering refresh rate of at least 25 Hz,

(d) its force rendering range is compatible with the operational insertion forces, i.e., 0–2 N,

(e) can work with the commercially available endovascular devices, e.g., catheters and guidewires, and

(f) provides an unbounded continuous workspace for rotation and insertion degrees of freedom.

1.4 Research Scope

To attain the research objectives, the scope of this research was:

(1) Developing a force estimation method for endovascular devices based on inverse finite-element method (iFEM) that included:

(a) image-based shape estimation based on stereo-vision and 3D Bezier shape interpolation,

(b) derivation of the continuum mechanics-based balance equations for the endovascular devices considering large deformations,

(c) development of a computationally-efficient inverse solution to determine the location and magnitude of contact forces,

(d) verification of the developed solution scheme through comparison with commercial finite-element softwares, and

(e) simulation-based and experimental validation of the proposed force estimation method for interventional tasks.

(2) Developing a force estimation method for endovascular devices based on inverse Cosserat rod model (iCORD) for non-steerable devices that included:

(a) image-based shape estimation based on stereo-vision and 3D Bezier shape interpolation,

(b) derivation of the continuum mechanics-based balance equations for the endovascular devices considering large deformations,

(c) development of a computationally-efficient inverse solution to determine the location and magnitude of contact forces, and

(d) experimental validation of the proposed force estimation method for interventional tasks.

(3) Adapting the developed force estimation method for endovascular devices based on inverse Cosserat rod model (iCORD) for steerable catheters that included:

(a) image-based shape estimation based on stereo-vision and 3D Bezier shape interpolation with constant bending curvature assumption,

(b) derivation of the continuum mechanics-based balance equations for the steerable catheters considering the constant bending curvature,

(c) analytical solution of the inverse model to determine the magnitude of the tip contact force, and

(d) simulation-based and experimental validation of the proposed force estimation method for interventional tasks.

(4) Developing an integral-free spatial rotation measurement through stereo-accelerometry for decoupling the rotation measurement from insertion measurement that included:

(a) developing a wearable device to decouple the inertia of the rotation measurement from surgeon interface,

(b) proposing an integral-free method to measure the spatial orientation of wrist through stereo-accelerometry and sensor fusion,

(c) proposing a fast, easy, and one-time calibration for the proposed device,

(d) artificial neural network (ANN-) based implementation of the proposed sensor fusion for fast real-time performance, and

(e) demonstration of the feasibility of integrating the proposed wearable device for interventional tasks.

(5) Developing a haptics-enabled surgeon module based on magnetostriction of magnetoelastic elastomers that included:

(a) multi-physics continuum mechanics-based modeling of the magnetoelastic behavior of the magnetorheological elastomers,

(b) analytical solution of the developed magnetoelastic model for the magnetostriction phenomenon in the magnetorheological elastomer,

(c) generation of a radial magnetic field using permanent magnets without a need for induction coils,

(d) proposing and prototyping a mechatronics system for force rendering,

(e) integration of the proposed surgeon interface with a representative RCI system and its experimental validation interventional tasks, and

(f) assessment of the feasibility of integrating the proposed surgeon interface with the iCORD force estimation for interventional tasks.

1.5 Thesis Contributions

To the best of the author's knowledge, this study was the first to address the limitation of haptic feedback provision for RCI systems with a top-to-bottom systemic approach. In this study, first, the main technological gaps that had hindered the haptic provision were identified. Afterward, a new system design for incorporating the image-based haptic provision in the RCI systems was proposed. Next and based on the proposed system design, the required system components, i.e., image-based force estimation, decoupled drift-free rotation measurement, haptics-enabled intuitive surgeon interface, were developed and validated. In addition, each of the developed components was integrated with the proposed system design and their performances were studied at the system level.

With respect to addressing the knowledge gaps in the available literature, the main contributions and novelties of this research were in:

(1) Derivation of differential geometry-based kinematics (Bezier spline) of endovascular devices with large deformation, which allowed for unifying the rigorous definition of small and large deformations.

(2) Development and validation of sensor-free, robust, and accurate force estimation methods for steerable and non-steerable endovascular devices based on Cosserat rod model. Cosserat rod provided a single set of governing equations for small and large deformations of the endovascular devices. Also, it allowed for the incorporation of the Bezier spline kinematics to achieve real-time performance for force localization and estimation.

(3) Incorporation of Bezier spline-based kinematics with continuum mechanics-based balance equations which allowed for fast parallelized global optimization of the contact forces.

(4) Development and validation of an integral-free spatial rotation measurement based on stereo-accelerometry. To the best of the author's knowledge, the concept of stereo-accelerometry and integral-free rotation measurement is unprecedented in the literature.

(5) Adoption of a learning-based (ANN-based) sensor-fusion technique for rotation measurement in real-time without a need for attitude resetting.

(6) Development and validation of a wearable device for robust and unbounded rotation measurement of endovascular devices. Thanks to the wearable design of the developed device, its inertial was decoupled from the insertion measurement system, thus the proposed force rendering system did not require to compensate for the inertia of the rotation measurement system.

(7) Development and analytical solution of a multi-physics-based model for the mechanical behavior of magnetorheological elastomers. The obtained multi-physics-based analytical model of the magnetorheological elastomers allowed for adopting an accurate physics-based calibration model for the developed haptic device.

(8) Development and validation of a magnetostriction-based haptic rendering system with simple structure and control method. To the best of the author's knowledge, the proposed design concept, the proposed method for radial magnetic field generation, and the validated analytical model are unprecedented in the literature.

1.6 Publications

The following list summarizes the author's contributions during this doctoral research:

Patents

(1) Amir Hooshiar, Mohammad Jolaei, and Javad Dargahi. Sensor-free force and position control of tendon-driven catheters through interaction modeling, January 11 2021. US Patent application no. 63/136100 [55],

(2) Amir Hooshiar, Mohammad Jolaei, and Javad Dargahi. Sensor-free force control of tendon-driven ablation catheters through position control and contact modeling, January 17 2020. US Patent application no. 62/962522 [56],

(3) Amir Hooshiar, Ali Alkhalaf, and Javad Dargahi. Tactile interface system with magnetorheological elastomer and method for stiffness adaptation, October 4 2019. US Patent application no. 62/910916[57].

Journal Papers

(1) Amir Hooshiar, Javad Dargahi, and Siamak Najarian. Real-time image-based force estimation along endovascular devices using inverse cosserat rod model (icord) for robot-assisted cardiovascular interventional surgery. *IEEE Transactions on Robotics*, Revision requested, 2021 [58],

(2) Amir Hooshiar, Amir Sayadi, Javad Dargahi, and Siamak Najarian. An integral-free rotation measurement method via stereo-accelerometery with application in robot-assisted catheter intervention. *IEEE/ASME Transactions on Mechatronics*, In-press, 2021 [59],

(3) Amir Hooshiar, Alireza Payami, Javad Dargahi, and Siamak Najarian. Magnetostriction-based force feedback for robot-assisted cardiovascular surgery using smart magnetorheological elastomers. *Mechanical Systems and Signal Processing*, In-press, 2021 [60],

(4) Ali Alkhalaf, Amir Hooshiar, and Javad Dargahi. Composite magnetorheological elastomers for tactile displays: Enhanced mreffect through bi-layer composition. *Composites Part B: Engineering*, page 107888, 2020 [61],

(5) A. Hooshiar, S. Najarian, and J. Dargahi. Haptic telerobotic cardiovascular intervention: A review of approaches, methods, and future perspectives. *IEEE Reviews in Biomedical Engineering*, 13:32–50, 2020 [62],

(6) Amir Hooshiar, Ali Alkhalaf, and Javad Dargahi. Development and assessment of a stiffness display system for minimally invasive surgery based on smart magneto-rheological elastomers. *Materials Science and Engineering: C*, 108:110409, 2020 [63],

(7) Mohammad Jolaei, Amir Hooshiar, Javad Dargahi, and Muthukumaran Packirisamy. Toward task autonomy in robotic cardiac ablation: Learning-based kinematic control of soft tendon-driven catheters. *Soft Robotics*, Accepted(2020.0006), 2020 [64],

Conference Papers

(1) Amir Hooshiar, Amir Sayadi, Javad Dargahi, and Siamak Najarian. Analytical tip force estimation on tendon-driven catheters through inverse solution of cosserat rod model. In *International Conference on Intelligent Robots and Systems (IROS) 2021 (Under review)*. IEEE, 2021 [65],

(2) Amir Hooshiar, Amir Sayadi, Mohammad Jolaei, and Javad Dargahi. Accurate estimation of tip force on tendon-driven catheters using inverse cosserat rod model. In *2020 International Conference on Biomedical Innovations and Applications (BIA)*, pages 37–40. IEEE, 2020 [66],

(3) Amir Sayadi, Amir Hooshiar, and Javad Dargahi. Impedance matching approach for robust force feedback rendering with application in robot-assisted interventions. In *2008 IEEE International Conference on Control, Mechatronics, and Automation*, pages 18–22. IEEE, 2020 [67],

(4) Alireza Payami, Amir Hooshiar, Ali Alkhalaf, and Javad Dargahi. Modeling of rate-dependent force-displacement behavior of mres using neural networks for torque feedback applications. In *2008 IEEE International Conference on Control, Mechatronics, and Automation*, pages 58–62. IEEE, 2020 [68],

(5) Pegah Yaftian, Naghmeh Bandari, Amir Hooshiar, and Javad Dargahi. Image-based contact detection and static force estimation on steerable rfa catheters. In *2020 International Conference on Biomedical Innovations and Applications (BIA)*, pages 57–60. IEEE, 2020 [69],

(6) Mohammad Jolaei, Amir Hooshiar, Amir Sayadi, Javad Dargahi, and Muthukumaran Packirisamy. Sensor-free force control of tendon-driven ablation catheters through position control and contact modeling. In *2020 42nd Annual International Conference of the IEEE Engineering in Medicine & Biology Society (EMBC)*, pages 5248–5251. IEEE, 2020 [70],

(7) Mohammad Jolaei, Amir Hooshiar, and Javad Dargahi. Displacement-based model for estimation of contact force between rfa catheter and atrial tissue with ex-vivo validation. In *2019 IEEE International Symposium on Robotic and Sensors Environments (ROSE)*, pages 1–7. IEEE, 2019 [71],

(8) Ali Alkhalaf, Amir Hooshiar, and Javad Dargahi. Enhancement of mr-effect in magnetorheological elastomers through bi-layer composition: Theory and validation. In *Proceeding of 30th International Conference on Adaptive Structures and Technologies*, volume 1, pages 1–2. Concordia University, 2019 [72],

(9) Mohammad Jolaei, Amir Hooshiar, and Dargahi. Kinematic analysis and position control of flexible tendon-driven catheter for minimally invasive cardiac surgery. In *30th International Conference on Adaptive Structures and Technologies*, pages 1–2. Concordia University, 2019 [73],

(10) Amir Hooshiar, Naghmeh M Bandari, and Javad Dargahi. Image-based estimation of contact forces on catheters for robot-assisted cardiovascular intervention. In *Proc. Hamlyn Symp. Med. Robot.*, pages 119–120, 2018 [74],

(11) A. Molaei, A. H. Ahmadi, V. Karamzadeh, E. Abedloo, and J. Dargahi. Pretensioned structures as multi axis force sensors. In *2017 5th RSI International Conference on Robotics and Mechatronics (ICRoM)*, pages 416–420, 2017 [75],

(12) Amir Hooshiar, Masoud Razban, Naghmeh M Bandari, and Javad Dargahi. Sensing principle for real-time characterization of viscoelasticity in the beating myocardial tissue. In *Computational Intelligence and Virtual Environments for Measurement Systems and Applications (CIVEMSA), 2017 IEEE International Conference on*, pages 72–77. IEEE, 2017 [76],

(13) Naghmeh M Bandari, Amir Hooshair, Muthukumaran Packirisamy, and Javad Dargahi. Optical fiber array sensor for lateral and circumferential force measurement suitable for minimally invasive surgery: Design, modeling and analysis. In *Specialty Optical Fibers*, pages JTu4A–44. Optical Society of America, 2016 [77],

1.7 Thesis Layout

This thesis is prepared in manuscript-based style according to the *"Thesis Preparation and Thesis Examination Regulations (version-2020) for Manuscript-based Thesis"* of the School of Graduate Studies of Concordia University. It includes eight chapters and one appendix. In the continuation of this thesis:

Chapter 2 presents the results of a critical literature review of haptic telerobotic cardiovascular intervention technology with regards to the state-of-the-art, modeling approaches, methods, and knowledge gaps, published in *IEEE Reviews in Biomedical Engineering* journal:

(1) A. Hooshiar, S. Najarian, and J. Dargahi. Haptic telerobotic cardiovascular intervention: A review of approaches, methods, and future perspectives. *IEEE Reviews in Biomedical Engineering*, 13:32–50, 2020 [62].

The second author of [62] contributed as a scientific advisor.

Chapter 3 presents the development and validation of an image-based force estimation method based on inverse finite-element method (iFEM) partly presented during the *2018 Hamlyn Symposium on Medical Robotics*, London, UK:

(1) Amir Hooshiar, Naghmeh M Bandari, and Javad Dargahi. Image-based estimation of contact forces on catheters for robot-assisted cardiovascular intervention. In *Proc. Hamlyn Symp. Med. Robot.*, pages 119–120, 2018 [74].

The second author of [74] assisted in the selection of hardware components for the development of the setup for 2D validation using force-sensing linear potentiometers.

Chapter 4 presents the development and validation of an image-based force estimation method based on inverse Cosserat rod model (iCORD) for non-steerable endovascular devices, under review (revision requested) as an original research article in *IEEE Transactions on Robotics* journal:

(1) Amir Hooshiar, Javad Dargahi, and Siamak Najarian. Real-time image-based force estimation along endovascular devices using inverse cosserat rod model (icord) for robot-assisted cardiovascular interventional surgery. *IEEE Transactions on Robotics*, Revision requested, 2021 [58].

The second author of [58] contributed as a scientific advisor.

Chapter 5 presents the development and validation of an image-based force estimation method based on inverse Cosserat rod model (iCORD) for steerable catheters, partly published in *Soft Robotics* journal, partly presented during *2020 IEEE Conference on Biomedical Innovation and Applications*, Varna, Bulgaria, and partly filed in two provisional patents with the *United States Patent and Trademark Office (USPTO)*:

(1) Amir Hooshiar, Amir Sayadi, Mohammad Jolaei, and Javad Dargahi. Accurate estimation of tip force on tendon-driven catheters using inverse cosserat rod model. In *2020 International Conference on Biomedical Innovations and Applications (BIA)*, pages 37–40. IEEE, 2020 [66],

(2) Amir Hooshiar, Mohammad Jolaei, and Javad Dargahi. Sensor-free force control of tendon-driven ablation catheters through position control and contact modeling, January 17 2020. US Patent application no. 62/962522 [56],

(3) Amir Hooshiar, Mohammad Jolaei, and Javad Dargahi. Sensor-free force and position control of tendon-driven catheters through interaction modeling, January 11 2021. US Patent

application no. 63/136100 [55].

(4) Mohammad Jolaei, Amir Hooshiar, Javad Dargahi, and Muthukumaran Packirisamy. Toward task autonomy in robotic cardiac ablation: Learning-based kinematic control of soft tendon-driven catheters. *Soft Robotics*, Accepted(2020.0006), 2020 [64],

The author's contributions in [64] were in the rigorous derivation of the kinematics of the catheter and workspace analysis (included in **Chapter 5**). The second and third authors of [66] assisted in the deployment of the developed software for image-processing and in the preparation of the validation test setup, respectively.

Chapter 6 presents the development and validation of an integral-free wearable device, as a part of the surgeon interface, published as an original research article in *IEEE/ASME Transactions on Mechatronics*:

(1) Amir Hooshiar, Amir Sayadi, Javad Dargahi, and Siamak Najarian. An integral-free rotation measurement method via stereo-accelerometery with application in robot-assisted catheter intervention. *IEEE/ASME Transactions on Mechatronics*, In-press, 2021 [59].

The second author of [59] assisted in the deployment of the developed artificial neural network on the wearable device and during the remote data-acquisition for the validation study.

Chapter 7 presents the development and validation of an intuitive surgeon interface, partly published in *Material Science and Engineering: C*, partly published as an original research article in *Mechanical Systems and Signal Processing* journal, partly filed in a provisional patent with the *United States Patent and Trademark Office (USPTO)*:

(1) Amir Hooshiar, Ali Alkhalaf, and Javad Dargahi. Tactile interface system with magnetorheological elastomer and method for stiffness adaptation, October 4 2019. US Patent application no. 62/910916 [57],

(2) Amir Hooshiar, Ali Alkhalaf, and Javad Dargahi. Development and assessment of a stiffness display system for minimally invasive surgery based on smart magneto-rheological elastomers. *Materials Science and Engineering: C*, 108:110409, 2020 [63],

(3) Amir Hooshiar, Alireza Payami, Javad Dargahi, and Siamak Najarian. Magnetostriction-based force feedback for robot-assisted cardiovascular surgery using smart magnetorheological elastomers. *Mechanical Systems and Signal Processing*, In-press, 2021 [60].

The author's specific contributions in [63] that were included in **Chapter 7** were in the design of the hardware and software of the magnets controller, controller design and validation. The second author of [60] assisted in material preparation and co-development of the PLK image-processing algorithm. The third author of [60] contributed as a scientific advisor.

The continuity of the contents of this thesis is as follows:

Chapter 2 summarizes the knowledge gaps hindering the provision of haptic feedback for RCI systems. To address the first knowledge gap, i.e., sensor-free force estimation on endovascular catheters, **Chapter 3** proposes a force estimation method based on iFEM that was indicated as the most accurate method in the literature. To address the suboptimal real-time performance of the proposed iFEM method, **Chapter 4** proposes an alternative force estimation method based on iCORD method which resulted in acceptable real-time performance. In continuation, **Chapter 5** expands the scope of the proposed iCORD method to steerable catheters, which resulted in an analytical framework for force estimation on steerable catheters. Next, the second knowledge gap, i.e., coupling effects of rotation and insertion measurement at surgeon interface, was addressed in **Chapter 6**. Afterward a feasible solution for the third knowledge gap, i.e., intuitive surgeon interface, is provided in **Chapter 7**. In the end, **Chapter 8** summarizes the main findings of this research, verifies the fulfillment of the research objectives provided in Sec. 1.3, and provides potential future directions.

Chapter 2

Haptic Telerobotic Cardiovascular Intervention: A Review of Approaches, Methods, and Future Perspectives

Cardiac diseases are recognized as the leading cause of mortality, hospitalization, and medical prescription globally. The gold standard for the treatment of coronary artery stenosis is the percutaneous cardiac intervention which is performed under live X-ray imaging. Substantial clinical evidence shows that the surgeon and staff are prone to serious health problems due to X-ray exposure and occupational hazards. Telerobotic vascular intervention systems with a surgeon-patient architecture reduced the X-ray exposure and enhanced the clinical outcomes; however, the loss of haptic feedback during surgery has been the main limitation of such systems. This chapter provides a critical review of the state-of-the-art for haptic telerobotic cardiovascular interventions. A survey on the literature published between 2000 to 2019 was performed. Results of the survey were screened based on their relevance to this work. Also, the leading research disciplines were identified based on the results of the survey. Furthermore, different approaches for sensor-based and model-based haptic telerobotic cardiovascular intervention, haptic rendering and actuation, and the pertinent methods were critically reviewed and compared. In the end, the current limitations of the state-of-the-art, unexplored research areas as well as the future perspective of the research on this

technology were laid out.

2.1 Method of Survey

Researchers have investigated the robot-assisted cardiac intervention systems from various points of view, e.g., engineering, biomedical, medicine, regulatory, reimbursement, women studies. This has constituted the broad-range and multi-disciplinary available literature. This review is based on a literature survey done on Compendex, Google Scholar, Scopus, and PubMed online databases using a combination of multiple keywords summarized in Table 2.1. The survey was limited to the years of 2000 to Feb. 2019; however, should the background research demand, articles before 2000 were included individually. The results of the literature survey were compiled in a single BibTeX database and filtered for duplicates. Afterward, each article underwent two rounds of screening; first to examine if the article were in the context of this study, and second to determine if it had a focus on haptic teleoperation. Table 2.1 summarizes the results of the comprehensive screening.

Table 2.1: Summary of the literature survey and screening.

Query string	"*Vascular*" **OR** "*Cardiac*" **OR** "*Peripheral*" **OR** *Cerebral*" **AND** "*Catheterization*" **OR** "*Intervention*" **OR** "*Angiography*" **AND** "*Robotic*" **OR** "*Robot-assisted*" **OR** "*Robot*" **AND** "*Haptic*" **OR** "*Force*"	
Total no. of articles (duplicates removed)	**Robotic intervention articles (after screening round I)**	**Haptic feedback articles (after screening round II)**
736	402	211

2.2 Haptic Teleopeation for Robotic Interventional Surgery

During manual catheterization, the surgeon controls the position and orientation of the catheter tip (or guidewire) by maneuvering its proximal portion, a few centimeters outside the patient's body.

The catheterization procedure is performed under live X-ray imaging, a.k.a. Fluoroscopy or angiography. Therefore, the natural haptic feedback perceived by the surgeon is based on forces at the proximal portion of the catheter. However, a recent study postulated that surgeons might assimilate the contact force information, by perceiving vibrations transmitted through the catheter [42].

Early studies emphasized on the provision of haptic feedback for robotic EPI, where maintaining catheter-tissue contact was necessary. Nevertheless, the expansion of robotic PCI and telestenting in recent years has opened a new front for the haptic teleoperation for vascular intervention [34, 35]. Also, the emergence of virtual reality training systems has substantiated the need for computational tools to obtain high fidelity haptic feedback during simulated procedures[46, 78].

Haptic teleoperation for robotic interventions has been realized using two distinct approaches, i.e. *sensor-based*, a.k.a. direct, and *model-based*, a.k.a sensorless. In the sensor-based approach, the haptic forces and torques, a.k.a. Haptic cues or haptic stimuli, are measured using sensors at the patient module (slave) and replicated (rendered) by a haptic device at the surgeon module (master). On the other side, in the model-based approach, the haptic stimulus is estimated using a computational model [53] (see Fig. 2.1). Such computational models usually incorporate a mechanical model of the catheter (and guidewire), an image processing engine for shape sensing, and a force/torque estimation module.

In the model-based approach, however, proximal force/torque and position/orientation feedbacks are necessary to constrain the model with proper boundary conditions. Such feedbacks are obtained utilizing force/torque sensors and position/orientation encoders. The choice of boundary condition is determined by the model formulation and solution schema[46, 74, 76]. Table 2.2 compares some of the studies for the provision of haptic feedback in interventional surgery and Fig. 2.1, illustrates the system architecture for haptic telerobotic cardiovascular intervention for both direct and model-based approaches.

2.3 Sensor-based Haptic Feedback

As depicted in Fig. 2.1(a), in sensor-based systems, haptic force and torque is measured using one or multiple sensors. Depending on the surgical procedure, various ranges and resolutions for

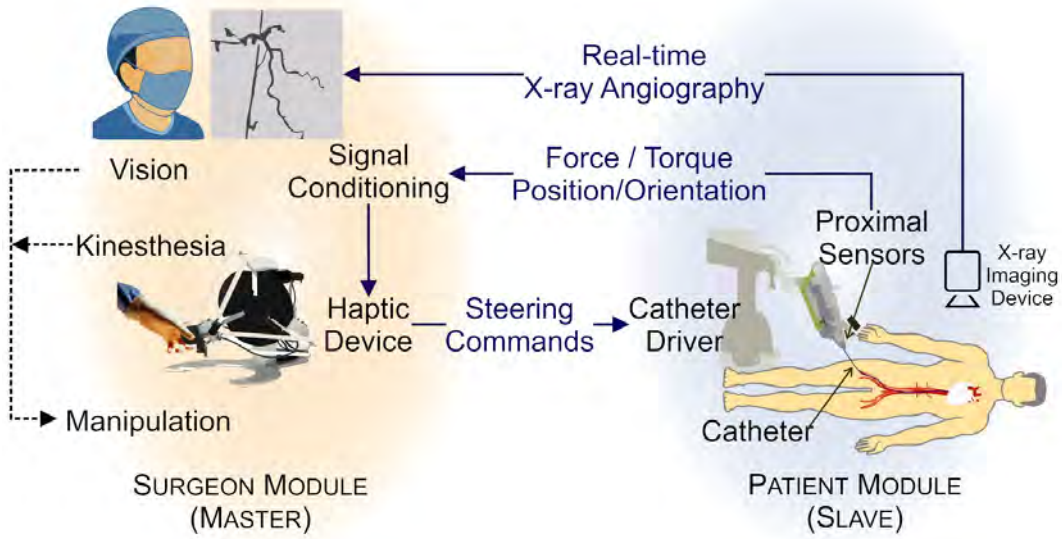

(a)

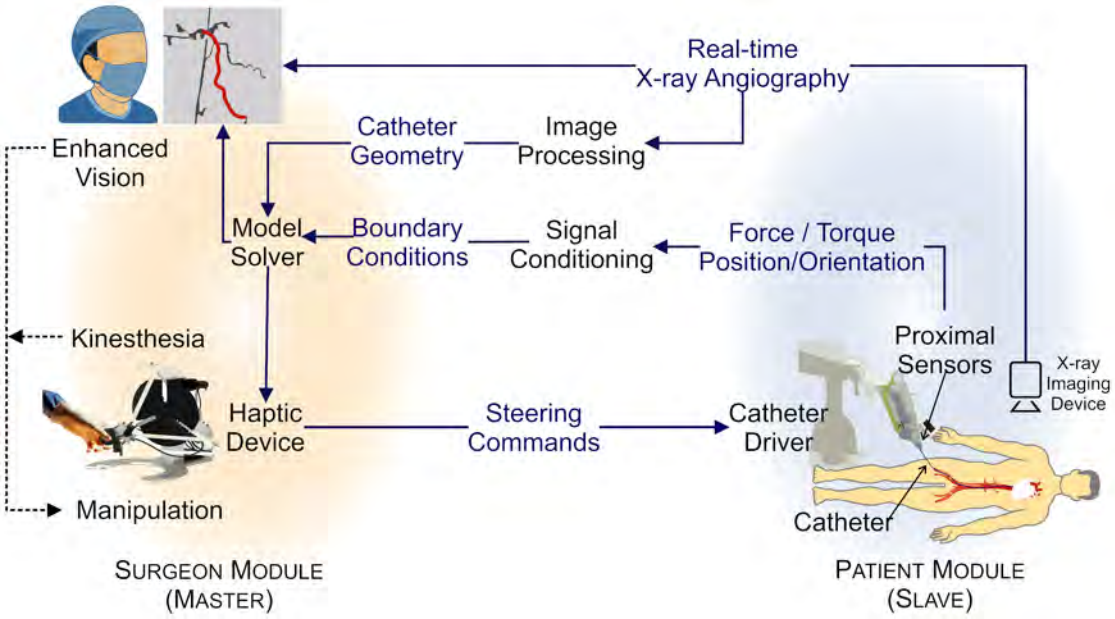

(b)

Figure 2.1: Haptic feedback provision in: (a) sensor-based and (b) model-based haptic feedback approaches [74].

Table 2.2: Representative studies for haptic teleoperation for robot-assisted PCI systems

Authors	Application	Haptic Estimation	Distal Feedback	Proximal Feedback	Customized Catheter
Meiβ *et al.* (2009) [79]	EV*	Sensor-based	✓	×	✓
Payne *et al.* (2012) [47]	EV	Sensor-based	✓	×	✓
Guo *et al.* (2013) [80]	EV	Sensor-based	✓	×	✓
Moon *et al.* (2014) [81]	VR**	Model-based	×	✓	×
Wang *et al.* (2015) [82]	EV	Model-based	×	✓	×
Hasanzadeh *et al.* (2016) [83]	EV	Model-based	✓	×	×
Guo *et al.* (2016) [46]	VR	Model-based	✓	×	×
Bao *et al.* (2016) [84]	EV	Sensor-based	✓	✓	✓
Chen *et al.* (2016) [85]	VR	Model-based	×	×	×
Yin *et al.* (2016) [86]	EV	Sensor-based	×	✓	×
Tavallei *et al.* (2017) [87]	EV	Sensor-based	×	✓	×
Zhang *et al.* (2017) [88]	EV	Sensor-based	×	✓	×
Guo *et al.* (2018) [89]	EV	Sensor-based	×	✓	×
Wang *et al.* (2018) [90]	EV	Sensor-based	×	✓	×
Hooshiar *et al.* (2018) [74]	EV	Model-based	×	×	×

*EV: Endo-vascular intervention **VR: Virtual reality simulators

sensors are suggested in the literature. Measuring the force at the tip of the catheter using a catheter-integrated sensor was the first design principles investigated by researchers.

In an early effort, Tanimoto *et al.* [91] was successful in measuring and replicating the contact forces between the catheter tip and the vessel phantom by integrating a miniature strain-gauge force sensor at the tip of a catheter. Meiβ *et al.* [79, 92, 93] used a highly miniaturized piezoelectric force sensor integrated on a cardiac catheter (HapCath) to measure the tip contact force with the vascular wall. However, because of the piezoelectric characteristics, HapCath could only measure the dynamic contact forces, not the static forces. To enhance usability under dynamic conditions, researchers investigated the utilization of piezoresistive and strain-gauge sensors which were capable of measuring both the dynamic and static forces [47, 80, 84, 86–88, 94–97]. Despite the good linearity, piezoresistive and strain-gauge sensors are doubted from the reliability point of view for use in robot-assisted cardiovascular intervention systems [98]. Because of the metallic backing and embedded circuitry, piezoresistive and strain-gauge sensors are intrinsically susceptible to electromagnetic interference with other devices in the operating room. Another limitation of using electrically active sensors, e.g., strain gauge and piezoresistive, is the electrolytic nature of blood. Both electromagnetic interference and electrolytic environment, might adversely affect the readings and eradicate the accuracy of measurements [46]. To alleviate the interference problems, researchers have investigated optical fiber-based sensors for intravascular force measurement [77, 95, 98–107]. Optical-fiber-based sensors have been mainly proposed based on three sensing principles, i.e. fiber-brag-grating (FBG), Fabry-Perot interferometry (FPI), and light-intensity-modulation (LIM) [108, 109]. Among the three principles, the LIM principle has been investigated in more studies. The reason might be more simplicity of setup and easier interrogation of the sensor [98, 110]. LIM-based sensors have been mainly intended for measuring contact forces at the tip of cardiac catheters [77, 100–103, 106, 111], as well as along the body of the catheter [112, 113].

Various factors have been introduced in the literature playing a role in making the sensor-based haptic feedback more realistic, a.k.a. high-fidelity haptic feedback. Among such factors, the location of the sensor(s) [42], type and characteristics of the sensor(s) [46, 80, 89, 106], signal conditionings applied on the sensor measurements [86, 106, 112], and the type and design of the haptic device [46, 89] are of high practical importance. The author would also like to add the *refresh rate* to the

above-mentioned factors [74].

2.3.1 Distal vs. Proximal Sensing

Researchers have investigated sensor-based haptic feedback by measuring the haptic stimulus at both the distal and proximal part of the catheter. Based on this, studies would be categorized if incorporated *distal* or *proximal* feedback. In an early effort, Thakur *et al.* [114] proposed a surgeon-patient mechanism to replicate the motion acquired by a catheter-like user interface. Their system, however, was not designed for haptic feedback provision but the concept of proximal sensing was implemented to assure reliable motion replication. Their study revealed valuable force, torque, and motion data for a typical cannulation intervention [114]. Besides, one could also find valuable force, torque, and motion information in [42] for aortic, carotid, and subclavian interventions.

The majority of researchers have postulated a surgeon-patient configuration capable of controlling the catheter insertion and rotation and provision of haptic feedback as the basis of their design for robotic intervention [80, 84, 87, 88, 94, 96, 97]. In a surgeon-patient configuration, the main contributors to the catheter insertion force (and consequently the haptic force) are the *weight* of unsupported portion of catheter (between the robot and patient), *contact forces* between catheter and vasculature, *friction* between the catheter and vascular access port, and the *bearing friction* between robot parts. The last two factors are identified to as disturbance and are known accountable for *'polluting'* the haptic perception[41].

In the current literature, a clear preference in the utilization of the proximal feedback was observed in studies focusing on PCI or PPI[87–90]. On the other hand, the studies aiming at robotic EPI have exploited distal sensing[46, 50, 77, 100, 101, 106]. By further employing miniaturization techniques [115] and the use of novel materials, e.g. conductive nanocomposites [115, 116] for soft-sensors, a research front is emerging on the embedded-soft sensors[112]. Such distributed sensors show a high potential of being used for shape-sensing and multiple contact force measurements[112].

2.3.2 Sensor Types and Characteristics

Different sensing principles, a.k.a. transduction mechanisms have been suggested in the literature for the use in cardiovascular catheter-based interventions. Piezoelectric, piezoresistive, and optical-fiber-based sensors are the most-employed sensor types. Piezoelectric and piezoresistive sensors have shown reliable and linear characteristics [95, 98, 117]. These sensors, however, differ in their dynamic response. Piezoresistive sensors are capable of both static and dynamic force measurements, while piezoelectric sensors can merely measure dynamic forces [53]. On the other hand, due to the induced micro-currents and larger circuitry, piezoresistive sensors are more prone to electromagnetic interference. Optical-based sensors, on the other hand, outperform both in terms of dynamicity and interference inertia[107].

Because of their transduction medium, light, and the carrier medium, 125μm-optical-fiber, optical sensors are both inert to electromagnetic interference and small in size[53, 107]. However, the physics behind optical transduction is far more complex and nonlinear than piezoelectricity and piezoresistivity[53, 98, 107]. Also, calibration of optical-fiber-based sensors is rather a more cumbersome procedure[106, 107, 111]. Therefore, the choice of a sensor type is highly dependent on the requirements of the specific surgical procedure. The most studied requirements emphasized in the literature are size, range of force, accuracy, resolution, dynamicity, bio-compatibility, electrical-passivity, and magnetic resonance (MR)-compatibility. Fig. 2.2 compares some of the functional requirements of embedded sensors for the common cardiac intervention applications.

To be embedded on a catheter, sensors must be cylindrical. Also, must be of a diameter no larger than the nominal gauge of the catheter, e.g., $4 - 18$Fr. Therefore, the scalability of the sensing principle for it being miniaturized is of prominent importance. Furthermore, bio-compatibility is a must-to-have feature across all the principles for in-vivo usability. On this front, optical-fiber-based sensors outweigh the other principles [53, 110]. MR-compatibility becomes necessary merely if the procedure is performed under MR-imaging guidance, e.g., neurovascular interventions (NVI). Examples of catheter-integrated force sensors are depicted in Fig. 2.3. Comprehensive reviews of piezoelectric biomaterials for sensors and optical fiber-based sensors for MR-based interventions are provided in [121] and [107], respectively.

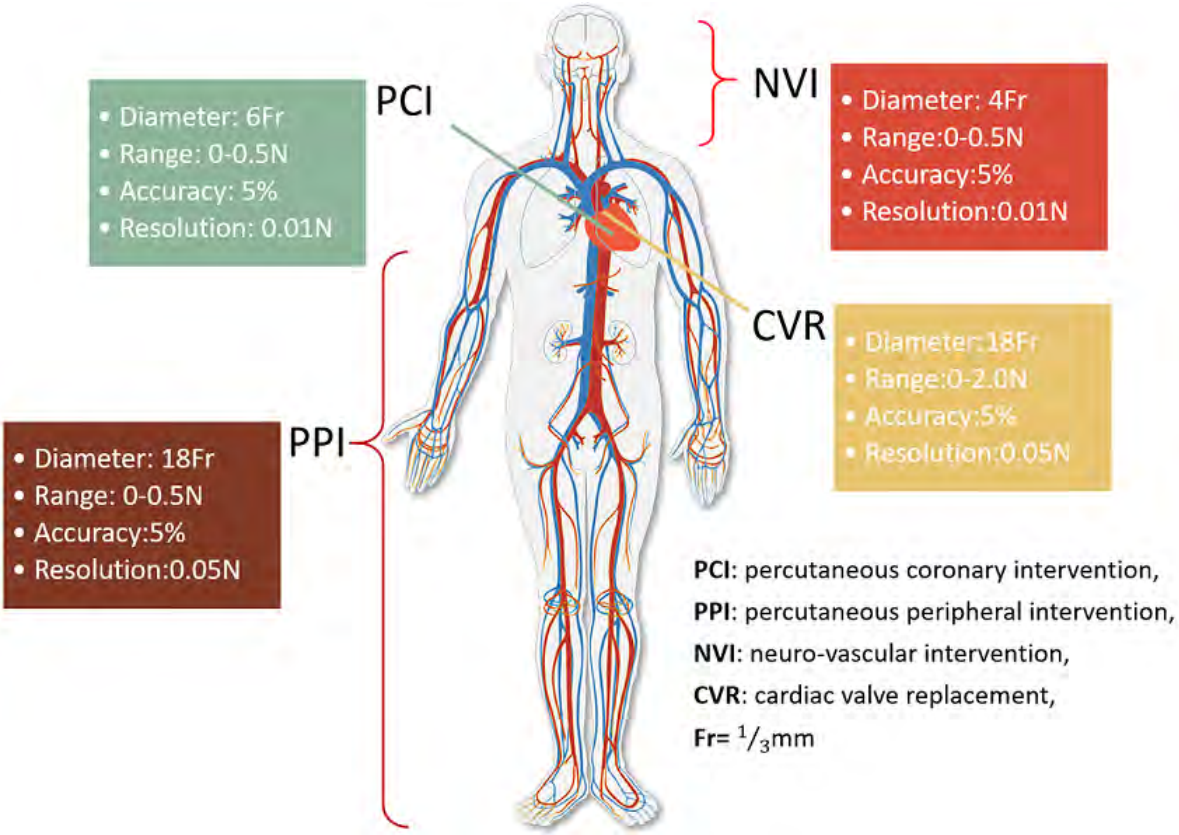

Figure 2.2: Functional requirements for embedded sensors for application in different interventional surgeries [106, 111, 118–120].

2.3.3 Signal Conditioning

Various signal conditioning techniques have been proposed for using sensor readings in real-time and off-line applications. Signal filtering, synchronization, and feature-extraction are among the most important techniques for signal conditioning. Noise appears on sensor readings due to sampling, analog-to-digital conversion, and electromagnetic interference. Also, due to heart-beat, blood pressure wave, and breathing are known among the sources producing noise on sensor readings [53]. Usually, the signature of reading noises are high-frequency, e.g., $10 - 50$Hz. Therefore, utilization of a hardware low-pass filter or a digital filter [122] is necessary for the improvement of signal-to-noise ratio (SNR).

Additionally, since in a haptic robotic system multiple force sensors and haptic devices with different data sampling-rates are used, synchronization is vital [46, 80, 89]. Usually, the synchronization is carried out by down-sampling or averaging readings from the fastest devices to match up with the slowest readings. However, when the frequency of the slowest readings is less than the minimum requirement of the haptic device ($25 - 30$Hz), utilizing a predictive filter, e.g., Kalman-filter, is necessary [106]. For the predictive filters to work accurately, a fairly accurate statistical model of noise and input is needed. Such a model might not be straightforward to obtain and thus insufficient model fitting compromises the system accuracy. Besides, some studies have employed machine-learning algorithms for mining extra information from the sensor signals, e.g., contact forces [112], catheter curvature[123]. Such algorithms require features in real-time, i.e., statistical parameters like median, mean, median frequency, etc. Nevertheless, using digital filters with feature-extraction imposes a computational surplus to the system and further complicates the sensor-based systems. Thus, there is a trade-off between the system refresh rate and accuracy [74].

2.3.4 Refresh rate

Refresh rate is the frequency at which the input to the control loop of haptic rendering is updated[53]. The normal range of frequency human's mechanosensory system perceives haptic cues is between $30 - 60$Hz [53, 124]. Therefore, the sensor-based haptic systems must update at a minimum of

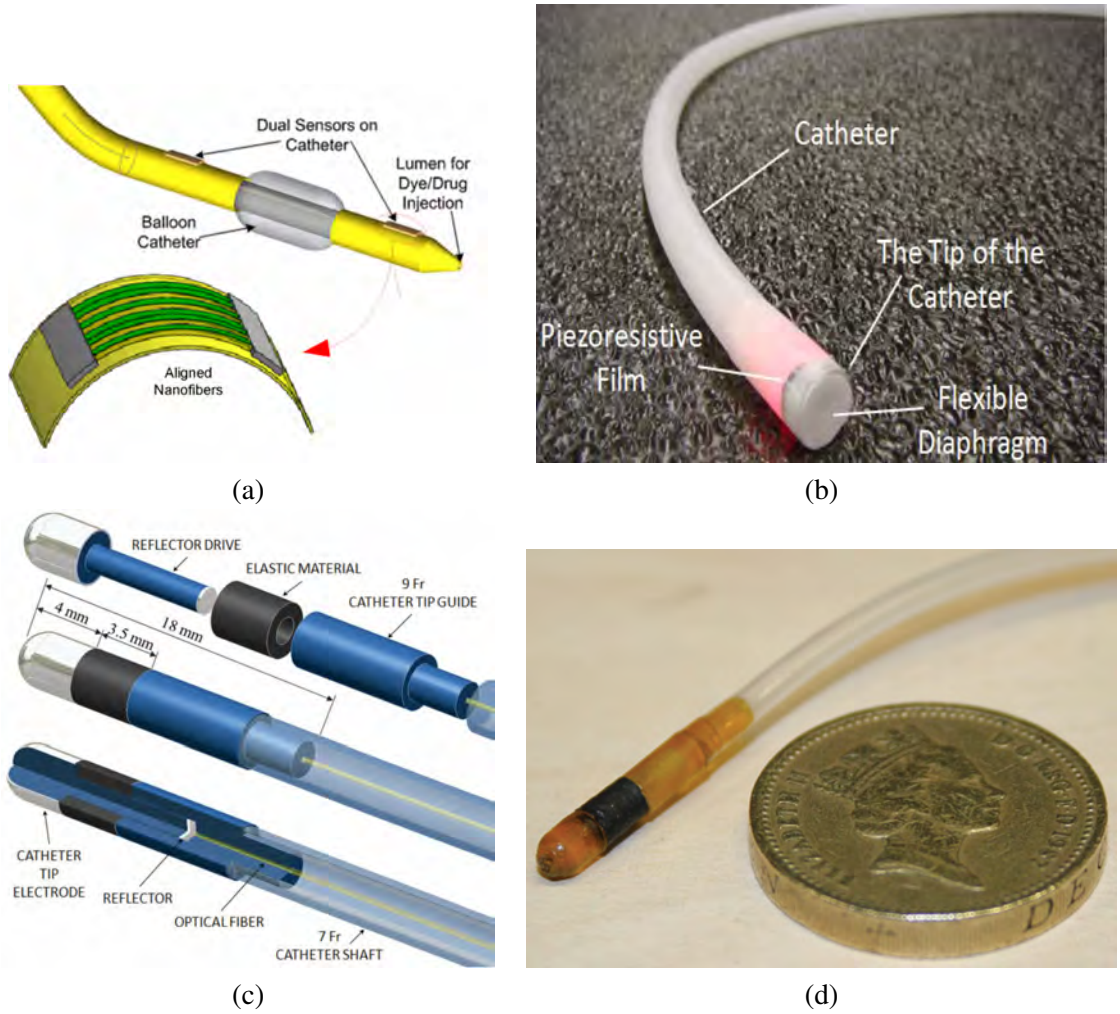

Figure 2.3: Sensor-integrated catheter with (a) piezoelectric sensors [122], (b) piezoresistive sensor [95], and (c)-(d) optical fiber sensors [101].

60Hz. Factors compromising the refresh rate include but are not limited to the sampling-frequency of data acquisition, communication delay, and the computational surplus of the signal conditioning, filtering, feature extraction, and synchronization. Although the commercially available catheter-embedded sensors, e.g., HapCath, have high sampling-rates (nominally at 1kHz), they are offered in closed-packages. Given the fact that medical device regulations mandate a design-freeze for such products before being cleared for the off-the-shelf market, researchers are at no liberty of changing the hardware and software configuration of the sensors to suit their needs better. Therefore, inevitably most of the studies have devised their specific sensors, which were not necessarily superior to those commercially available.

2.3.5 Advantages and Limitations

Utilization of sensors for direct measurement of forces or torques entails embedding a miniaturized sensor on a cardiovascular catheter. This might be a cumbersome process due to the limitations in size, material, electromagnetic compatibility, and structural flexibility of the catheter. However, sensors are capable of providing direct valuable information from the anatomical site, e.g., contact points. In comparison with model-based feedback, sensor-based systems have less dependency on uncertain parameters such as catheter stiffness or design. Also, sensor-based systems have a relatively lower computational surplus and run at much higher refresh rates, e.g., 1kHz.

Although sensors can provide instant feedback, they have intrinsic limitations. For example for robotic EPI, since the atrial space is relatively larger than coronary arteries, and the fact that catheter is in contact with the cardiac wall only at its tip, utilization of sensor-embedded catheters is a fit [36, 106]. However, the inner diameter of the coronary arteries hardly exceeds 2.5 millimeters [125]. Also, the force or motion data taken from a sensor on a catheter is limited to its installation spot, where the contact with the tissue may or may not occur. In other words, the sensor data is related to the point of its attachment; therefore, in order to have a wider knowledge of force distribution or shape sensing, one needs multiple or array sensors distributed on the catheter body [126]. As of present, the state-of-the-art is yet to reach that form-factor. Also, some highlight the applicability limitations and state that the sensor-embedded catheters are counter-intuitive for surgeons due to the significant change in their flexibility and weight [17]. Higher cost-per-patient and inapplicability to the virtual-reality systems are also among the reported limitations of sensor-based systems [17, 32]. Considering the limitations above and despite the introduction of sensor-integrated catheters for EPI applications, e.g. *Tacticath*® (St. Jude Medical Inc., MI, USA) and *Thermocool*® (Biosense Webster Inc., CA, USA), the use of sensor-integrated catheters in PCI and robotic PCI is not feasible.

2.4 Model-based Haptic Feedback

As depicted in Fig. 2.1(b), haptic feedback in model-based systems is estimated computationally via incorporation of boundary conditions from sensors, live imaging, and a mechanical model of the catheter (or guidewire). As elaborated in Chapter 1, the risks associated with the loss or inaccurate

haptic feedback during the telerobotic cardiac surgery are severe; therefore, not only the mechanical model must be precise but also the solution process has to be real-time, accurate, and stable [46, 83]. Guidewires and catheters are long and highly slender structures made of a metallic mandrel and a spring coil. The core and coil are made of a biocompatible metal such as stainless steel, Chromium-Cobalt-Molybdenum alloys, Nickel-Titanium alloys, Gold, Platinum, or Tungsten. The coil usually has a hydrophilic or hydrophobic coating, an anti-thrombogenic agent, or a drag-reducing material like Silicon or tetrafluoroethylene (TFE) [127].

Due to high slenderness, the catheters and guidewires are usually modeled as one-dimensional flexible structures (lines), kinematically. Various approaches have been postulated to model the catheters: *continuum mechanics*-, *multibody dynamics*-, *differential geometry*-, and *particle-based models*.

2.4.1 Continuum Mechanics Models

In an early effort, Baily and Amirat [128] presented a continuous description of static deflection in a catheter for cardiac intervention (*MALICA*) in 2005. Camarillo *et al.* [23] developed a similar continuum model of a tendon-driven catheter, which showed promising performance in predicting the shape of the catheter under quasi-static manipulation. Nonetheless, both above models were not real-time and assumed quasi-static condition; moreover, the models required detailed structural information, e.g., non-linear material compliance and measurement of the force at the catheter tip [129]. Besides all, the quasi-static condition is far from the physiologic conditions of the cardiac vessels and makes the above models inadequate for robotic PCI applications.

The continuum deflection model, introduced by Khoshnam *et al.* [130] in 2012, modeled the large deflection of a steerable catheter using the Bernoulli-Euler beam theory (e.g., see [131] for details). The shear effects and out-of-plane warping of the cross-section were excluded. This assumption seems reasonable due to the high slenderness of the catheters; however, the model was based on a quasi-static assumption. In continuation, Khoshnam *et al.* in [123] and [120] have reported successful implementation of the large deflection analysis method, postulated in [130], to predict contact forces at the tip of a catheter with a steady-state error of less than 5%. Although their results were

promising with regards to the accuracy, their model was not adequate to consider the multiple point loads and wall contact conditions that occur during robotic PCI. In addition to that, their model was two-dimensional with a planar cantilever beam. In three-dimensional problems, finding a closed-form solution to a large deformation problem needs a rigorous analysis and necessitates simplifying assumptions.

Gao *et al.* [132] used a linear finite element model with Bernoulli-Euler elements to estimate the contact forces between a cardiac catheter and the vessels in a vascular phantom. The results revealed that the model had underestimated the contact forces compared to the other clinical studies. The reason might be because of excluding the geometric non-linearity evolved by large-deformation of the beam [133]. Although FEA can be of high precision in modeling catheters and guidewires, it is computationally expensive and is prone to erroneous results if implemented with inadequate constraints. The exact constraint definition and treatment is of high importance, especially in case of large deformation or contact analysis [130].

To shorten the solution times of the finite element models, various theoretical and software advancements have been made, e.g. co-rotational updated Lagrangian formulation [134], explicit dynamics formulation [135], GPU computation [136], and sub-structural analysis and condensed stiffness matrix storage [137]. However, the FEA is still the most computationally-expensive amongst the modeling modalities for robotic cardiovascular intervention applications. In the absence of an analytic solution, the numerical method used by researchers for large deformation analysis is the structural finite element analysis (FEA). In the FEA theory, the geometry is discretized into finite elements, while the deflection is considered to vary continuously (linearly or quadratically) within each element [138]. Therefore, the deflection and internal forces vary continuously. Some researchers have investigated the deflections of catheters and guidewires as a finite element beam structure. In an early effort, Wang *et al.* [139] used static structural finite element analysis to find the distributed forces acting on the cardiac guidewire during the conventional PCI; however, the vascular wall was modeled as rigid. In addition to that, the width span and variation rule of the distributed forces were pre-set as constraints. Duriez *et al.* [140, 141] performed an incremental finite element analysis on a guidewire which was modeled by three-dimensional Bernoulli-Euler beam elements. In order to capture the geometric non-linearities, the elemental stiffness matrix was updated at each increment

based on the augmented Lagrangian method proposed in [133].

2.4.2 Multibody Dynamics Models

Because of the simplicity and computational efficiency, this framework is also widely used in modeling the motion and deformation of flexible and slender structures, e.g., catheters and guidewires [142]. To derive the kinematics, the structure is approximated by a set of rigid serial links connected by a set of spherical joints. One or two torsional springs are assumed to connect two adjacent links, depending on the dimensionality of the model, i.e., two or three-dimensional. The torsional degree of freedom might be included at any joint by an additional torsional spring. The tructural damping phenomenon of the material could be modeled by adding torsional dampers at the joints. This method was initially introduced by Shabana in 1997 as a *finite segments method*[143].

To have physically plausible results from multi-body dynamics models, a proper determination the spring and damper constants is essential. Amongst different methods to estimate the spring stiffness and damper constants, optimal parameter identification [51] and sub-structural finite element stiffness estimation are the most adopted in the literature [140, 143, 144].

In an early effort, Alderliesten *et al.* [145] provided a two-dimensional model of a typical catheter as a multibody system. The kinematics was defined following the D-H convention, and the total kinetic energy of the system was defined as the summation of both rotational and translational kinetic energies. The total potential energy was obtained by adding the gravitational potential and the stored energy in the springs considering the stiffness of the rotational springs as the flexural rigidity of the structure. It was assumed that maneuvers of the catheter are performed with a constant and relatively slow speed (quasi-static assumption); therefore, the minimum total potential principle was applied to obtain the optimal configuration of the structure. This hypothesis seems invalid, considering the dynamic motion of the heart.

In another study, Guo *et al.* [146], proposed a computationally efficient algorithm for collision detection and force-estimation for virtual reality training purposes. In their model, the equations of motion were derived by the Lagrangian method and were integrated from a time-history of insertions and rotations to estimate the current configuration. Chembrammel *et al.* [147] enhanced Guo *et*

al. 's [146] model by considering a linear elastic deformable vascular wall. The vessel was modeled as an elastic membrane and was parameterized piecewise-continuously. The contact was assumed to be frictionless. Each constraint was set active and solved by the Lagrange multipliers method, upon the collision detected. This study estimated a more realistic contact force by considering the vessel as deformable; however, the material model of the vessel was linear elastic. Linear elastic material model caused post-collision vibration (instability) in the catheter and vascular wall [147]. In reality, the viscoelastic energy loss in the vascular wall, the viscous friction of the blood flow, and frictional contact between the catheter and the vascular wall would lead to rapid attenuation of the vibration wave through the catheter [148, 149].

The models using multibody dynamics are computationally efficient through the significant reduction in total degrees of freedoms of the system; however, the accuracy of the results is influenced by the resolution of the geometric discretization. There is a continuous effort to modify multibody models of flexible structures to increase computational efficiency while maintaining acceptable accuracy [150, 151].

2.4.3 Differential Geometric Models

In this method, the shape of the whole structure is assumed to be controlled by the position of a certain number of key-points. Each key-point might not necessarily belong to the structure and is merely a mathematical entity. The polynomial interpolation is the primary example of the differential geometric representation. Other piecewise differentiable continuous curves like splines and B-splines could be used to represent the shape of the structure. The equations of motion in this method could be derived by defining the kinetic, potential (gravitational and strain energy) and dissipative (friction or viscoelastic) energies of the structure in terms of the spine curve parameter and using the Lagrangian equation of motion. Since the spine curve is a function of the position of key-points, the acceleration of any point on the curve is a function of the position, velocity, and acceleration of all the key-points (see [143, 152] for details). However, considering the dependency of the formulation on the *translational* kinematics and kinetics of the key-points (not the *rotational*), this method can not capture the torsional deformation of the structure [143].

In order to enable the torsional degrees of freedom using differential geometric methods, Spillmann

and Teschner [153] proposed a rod element (CoRdE) for the dynamic simulation of one-dimensional elastic objects based on the Cosserat's rod theory (see Dixon [154] for theoretical background). In this theory, the structure was discretized into line segments by a finite number of vertices. The line segments had no physical interpretation and were mathematical entities [153]. In this method, an orthogonal Frenet-Serret (FS) frame is defined for each segment (or vertex) by *tangent*, $\vec{t}(s)$, *normal*, $\vec{n}(s)$, and *bi-normal*, $\vec{b}(s)$ unit vectors. The FS frame was used as a local coordinate system to define the kinematics of the motion and deformation of the segments. Since the FS frame was parametrically defined by the interpolating functions of the spine curve, $s(x, y, z)$, the rotational degrees of freedom (two bending and one torsional) were involved through projecting two neighboring FS frames [153]. To avoid the *gimbal lock* singularity raised from rotation matrices, Spillmann and Teschner used a singularity-free quaternion description of the rotation (see [155] for details). This methodology was used by Tang *et al.* [156] in a hybrid model, which modeled the body of the catheter as a Cosserat rod and the tip of the catheter as a Bernoulli-Euler beam. This study could predict the 3D configuration of the catheter under forced insertion with a maximum position error of 2 millimeters. Luo *et al.* [157] proposed a haptic feedback setup that used a similar method to be used in PCI training. Recently Cardoso *et al.* [158] reported a maximum position error of less than 1 millimeter by implementing a differential geometric model based on active contours.

2.4.4 Particle-based Dynamics Models

Particle-based models (or mass-spring models) have been mainly used in obtaining the deformation of vascular tissue [46, 159]. The number of studies investigating methods of parameter identification for the particle-based models in modeling catheters and guidewires is increasing [151, 160, 161]. The main reason is for theoretical simplicity and computational stability [160]. In addition to that, in the case of contact between the catheter and the vessel, it could be treated by the penalty method to save the computational resources. The advocates of this approach accept the cost of a slight inaccuracy to gain real-time performance. Lenoir *et al.* [162] modeled the catheter using the mass-spring modeling technique. The vessel was considered rigid and the collision detection between catheter and guidewire was performed using the gap volume technique [163]. The equations of motion for the models were derived from Newton's laws. The solution started from the velocity boundary

conditions after re-arranging the equations into an explicit form. The solution then estimated the displacement of the entire structure iteratively [159].

Despite the computational efficiency, mass-spring models usually do not produce physically plausible results [120]. The main reason for this inaccuracy is the accumulation of constraint residues that maintain the integrity of the structure [159]. As postulated by Koning *et al.* [142], this accumulation of error might further lead to the violation of the constant length assumption for the structure. Extensive studies have been done to minimize the residue of the constraints and increase the reliability of the mass-spring models (e.g., see [159, 164–166]).

2.4.5 Advantages and Limitations

Current research focuses more on model-based haptic feedback, although sensor-based haptic feedback has a less computational cost and shorter response time. Some factors leading to this preference are less susceptibility to noise, lower cost, and simplicity of implementation, easy plugging to the currently available robotic PCI systems, and the feasibility to be used in surgical simulators [46].

In adopting a modeling approach, there is always a compromise between accuracy, and computational efficiency [167, 168]; hence a coherent comparative study to compare the performance of four approaches is yet to be done. Considering the characteristics indicated in this section, a comparison table for some of the studies addressing the model-based haptic feedback in robotic PCI is presented in Table 2.3.

Due to assuming deformation as a continuous field, continuum mechanics models of the catheters and guidewires are the most accurate amongst the four approaches above [130]; however, adopting a physically meaningful set of equations addressing continuity, conservation of momentum, and conservation of energy is crucial for the accuracy [133]. The catheters or guidewires are classified as *hyper-redundant* structures regarding deformations [169, 170]; therefore, to enforce the solution to converge to an acceptable deformation, a redundancy treatment method is needed [170].

A widely-adopted technique to treat the hyper-redundancy of continuum structure is to impose proper geometric constraints on the deflection of the structure [129], e.g. planar deflection [171], single radius curvature [172], piece-wise constant curvature [173, 174]. Webster and Jones [129] have indicated the calculation of the velocity and the acceleration Jacobian as a bottleneck in using

continuum robot models. Researchers have postulated to to determine the Jacobian via fitting a closed-form solution to the deflection of the structure [129]. Nevertheless, the most critical limitation of the model-based haptic feedback in the literature has been the sensitivity of results to the uncertain parameters, e.g., mechanical properties of the catheter and vessels, discretization length, solution schema, the beating motion of the vasculature. As Hasanzadeh *et al.* has shown in [83], results of the inverse solution are strongly sensitive to the model parameters and perturbations.

2.5 Model Components for Haptic Feedback

Based on the literature survey, any model intended to be used for haptic feedback in the cardiovascular system shall at least contain the following components:

2.5.1 Imaging, Segmentation, and Shape sensing

Essentially, identifying the pixels of an image that show the shape of the catheter is called catheter segmentation. The goal of segmentation is to find the current shape of a catheter and estimate its deformation by caparison to its undeformed (initial) shape. This process is also often referred as *shape sensing* in the literature. Fig. 2.4 schematically depicts a generic deformation estimation algorithm as well as an example of a segmented catheter in three consecutive X-ray angiographic frames. Different methods have been postulated for catheter segmentation and tracking in X-ray images, [175–180] and cinematographic (video) imaging [23, 43, 83, 119, 178, 181–185]. To evaluate and compare the performance of different segmentation techniques, Dalvand *et al.* proposed a set of characteristics, i.e. refresh rate (fps), accuracy ($\pm 1mm$), no dependency to more than two cameras, no dependency to fiducial markers, auto calibration, no dependency to initial guess, no approximation by circular arcs, automatic detection of the tip of catheter, and 3D reconstruction capability. The author would like to suggest adding *no dependency to prior knowledge of the anatomy*, and *curve parameterization* to the characteristics above.

Table 2.3: Summary of the studies using a model-based approach for contact force estimation between catheter and vasculature.

Authors	Application	Modeling Approach	Theory	DoF(s) per Node			Energy Formulation	Contact Treatment	Arc-length parametrization	Workspace Accessibility	Real-time Imaging	Haptic Device
				Translation	Bending	Torsion						
Bailly and Amirat (2005)[128]	PPI	Continuum Model	Constant Radius Actuator	2	1	×	Weak	×	✓	Low	×	×
Cotin *et al.* (2005)[141]	VR PCI	Continuum Model	Beam Finite Elements	2	1	0	Weak	Augmented Lagrange	×	High	Simulated	×
Duriez *et al.* (2006)[140]	VR PCI	Continuum Model	Beam Finite Elements	2	1	0	Weak	Augmented Lagrange	×	High	Simulated	×
Lenoir *et al.* (2006)[162]	VR PCI	Particle-based	×	2	0	0	Weak	Lagrange Multipliers	×	Low	Simulated	×
Tang *et al.* (2012)[156]	VR PCI	Differential Geometry	Cosserat Rod	3	2	1	Exact	Penalty	✓	High	Simulated	×
Khoshnam *et al.* (2012)[130]	PCI	Continuum Model	Beam Pseudo-Rigid Body	2	1	×	Weak	×	✓	Low	✓	×
Chembrammel *et al.* (2013)[147]	VR PCI	Multi-body Dynamics	Contrained Multi-body	3	1	0	Weak	Penalty	×	High	Simulated	×
Luo *et al.* (2014)[157]	VR PCI	Differential Geometry	Kirschhoff Rod	2	0	0	Weak	Augmented Lagrange	✓	○	Simulated	✓
Khoshnam *et al.* (2014)[120]	PCI	Continuum Model	Curvature Analysis	2	1	×	×	×	✓	×	✓	×
Wang *et al.* (2015)[82]	VR PCI	Multi-body Dynamics	Finite Segments	3	2	1	Exact	Augmented Lagrange	×	High	Simulated	✓
Wu *et al.* (2015)[151]	VR PCI	Multi-body Dynamics	Finite Segments	3	2	1	Exact	Penalty	×	High	Simulated	✓
Venkiteswaran & Su (2015)[144]	VR PCI	Multi-body Dynamics	Pseudo-Rigid Body	2	1	0	Weak	Penalty	✓	Low	×	×
Guo *et al.* (2016)[46]	VR PCI	Multi-body Dynamics	○	3	2	1	Exact	Penalty	×	High	Simulated	✓
Li *et al.* (2016)[160]	VR PCI	Particle-based	×	3	0	0	Weak	Lagrange Multipliers	×	Low	Simulated	✓
Cardoso *et al.* (2016)[158]	VR PCI	Differential Geometry	×	3	1	0	Weak	Penalty	×	Low	Simulated	×
Guo *et al.* (2017)[186]	VR PCI	Multi-body Dynamics	×	3	1	0	○	Penalty	×	Low	Simulated	×
Cai *et al.* (2017)[187]	VR PCI	Differential Geometry	Kirschhoff Rod	2	0	0	Weak	Augmented Lagrange	✓	×	Simulated	×
Back *et al.* (2018)[188]	PCI	Differential Geometry	Cosserat Rod	3	2	1	Exact	×	✓	×	✓	×

○: Not applicable ×: Not indicated

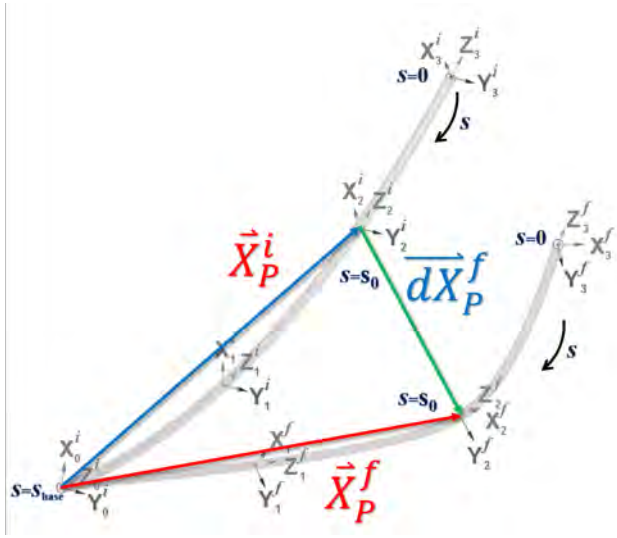

(a)

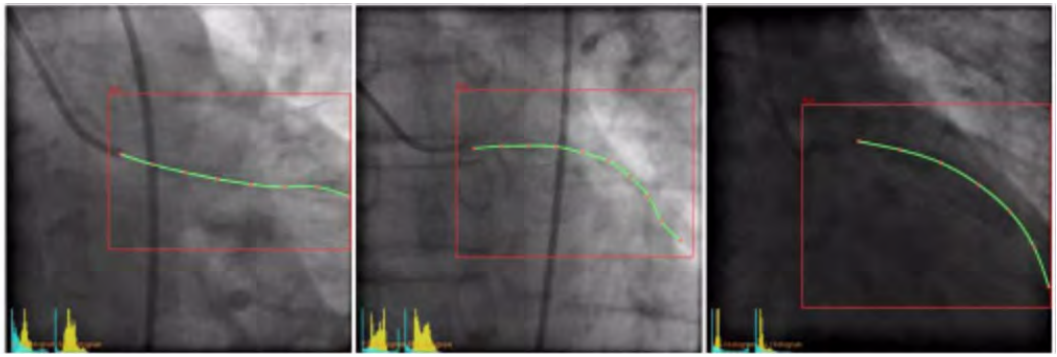

(b)

Figure 2.4: (a) Estimation of deformation on an schematic 3D shape of the catheter in its final shape (denoted by f superscript) with respect to its initial shape (denoted by i superscript) , and (b) segmentation and tracking of a guidewire in three consecutive X-ray images using a B-spline tube model approximation method [189].

2.5.2 Curve Parameterization and Deformation Parameterization

In the curve parameterization, the extracted catheter shape is described analytically as a parameterized formulation [190]. In other words, curve parameterization is the interpolation of (x, y, z) coordinates of a set of points, P_i belonging a the image-extracted spine of the catheter, i.e., curve $\mathbb{C}$, in terms of a parameter s. Conventionally s is a normalized real positive number which $s = 0$ entails the tail and $s = 1$ refers to the tip of curve [74]. As depicted in Fig. 2.4, curve parameterization facilitates definition of local Fernet-Serret (FS) curvilinear coordinate systems which are further used for deformation estimation (e.g. see [190] for details).

2.5.3 Force Estimation based on X-ray Image-feed and Shape Sensing (inverse formulation)

These methods are to estimate the unknown acting forces on the catheter based on its deformation state (inverse problem). To be able to solve this problem, it is necessary to define, assemble, and solve a constrained-enough set of dynamic equations governing the motion and deformation of the catheter. In the literature, this topic has been referred as the *structural modeling* of catheter and guidewire. Researchers have adopted various approaches to formulating the mechanics of the catheter deformation. Generally, all approaches require addressing the conservation principles of:

(1) conservation of mass (kinematics)

(2) conservation of linear and angular momentum (dynamic/static force balance including the unknown forces for the whole structure), and

(3) conservation of energy (constitutive equations),

as functions of the deformations, external loading, and material properties.

Three main sets of equations described above are necessary for the assembly of the inverse problem. However, this system of equations might constitute ill-conditioned or redundant problems, without imposing proper constraints [74, 169, 186]. Arc-approximation [83, 120, 173, 174] and length-preservation [135, 162, 172] assumptions have been proposed to treat the redundancy issues. Also

recently, the contact-zone detection with [186] and without [74] *a priori* knowledge of the vascular anatomy have been employed to properly constraint the models, respectively.

2.5.4 Force Estimation based on Virtual Interactions (forward formulation)

In surgical simulators, in contrast to real surgical conditions, the X-ray image feed is not available. Alternatively, a computational model detects the contact points and calculates the deformation of the catheter (and guidewire) at a given time (forward formulation). To obtain a real-time performance in surgical simulators, the incremental solution approach is preferable. Algorithm 1 describes a generic incremental process to estimate the acting forces based on the input from the catheter steering device, 3D model of vasculature, and mechanical model of the catheter [46, 82].

2.6 Haptic Rendering and Haptic Devices

Human body perceives external haptic (kinesthetic) stimuli, e.g., force and torque, through exteroception mechanism in skeletal joints [53]. Haptic rendering is defined as the process of replicating estimated or measured forces and torques for a user computationally to perceive the same haptic stimuli as they would through real interaction [53]. The device with which a user interacts and through which the haptic stimuli are generated and transferred to the user's hand is the haptic device. Haptic rendering is realized in a closed-loop force control system as depicted in Fig. 2.1. For the robotic intervention application, different haptic devices have been proposed, e.g., general-purpose multiple-DOF devices, custom-designed devices.

Six-DoF Phantom devices (3DSystems Inc., SC, US) have been among the first systems used as the control and haptic interface for the active catheter insertion application [119, 191–195]. Similarly, Omega haptic device (Force Dimension, Nyon, Switzerland) has been used for relaying catheter insertion forces to the surgeon's hand [196, 197]. Phantom devices are constructed as serial robotic mechanisms and generate torque and force feedbacks through multiple capstan mechanisms and current control on independent DC motors (one-motor per DoF). Such an architecture has allowed this family of devices to provide a wide kinematic range in working space, e.g., $838 \times 584 \times 406$mm,

Algorithm 1 An explicit algorithm for the estimation of the model-based haptic feedback

Input: *Initial Conditions:* Initial steering force $\Sigma\vec{F}_s$, position, orientation, and velocity of the proximal part at the catheter

Input: *Constants:* Mechanical properties of the catheter, δt

Input: *Models:* Wall-catheter contact model, wall material model, catheter material model, catheter deformation model, discretized geometric model of catheter

Output: Contact forces $\vec{F}_c$, deformation of catheter $\vec{u}_c$ and deformation of vascular wall $\vec{u}_v$

1: *Initialization* :
2: $i = 0$
3: *LOOP Process*
4: **while** $t \leqslant t_{final}$ **do**
5: update boundary conditions from the input device
6: calculate the elemental acceleration $\vec{a}^i$ over the catheter by enforcing initial and boundary conditions in mechanical model of catheter
7: integrate acceleration to obtain the velocity of catheter: $\vec{v}^{i+1} = \vec{v}^i + \vec{a}^i \cdot \delta t$
8: integrate velocity to obtain the shape of catheter: $\vec{u}_c^{i+1} = \vec{u}_c^i + \vec{v}^i \cdot \delta t$
9: check for penetration of the catheter into vascular wall
10: **if** $penetration$ is occurded **then**
11: use contact model to estimate the contact forces $\vec{F}_c$
12: check the force balance between contact forces and boundary conditions
13: **if** $\Sigma\vec{F}_c \neq \Sigma\vec{F}_s$ **then**
14: perform bi-section: divide δt by 2
15: go to 6
16: **end if**
17: re-solve the mechanical model of catheter with the updated contact forces $\vec{F}_c$
18: go to 7
19: **end if**
20: send $\Sigma\vec{F}_c$ to the haptic device
21: $t = t + \delta t$
22: $i = i + 1$
23: **end whilereturn**

and a fine spatial resolution, e.g., 0.007mm. However, the serial architecture has compromised the overall system stiffness, i.e., 3.5N.mm^{-1}.

On the other hand, the Omega device uses a delta-based parallel mechanism and controls forces and torques through simultaneous current control on multiple motors. Such a parallel mechanism has both increased the stiffness of the device, e.g., 14.5N.mm^{-1} and has made it intrinsically symmetric along the X, Y, and Z axes. However, Omega devices have a relatively more restricted workspace, e.g., 160×110mm. Both the devices provide reliable industrial-standard solutions for the provision of haptic feedback within the catheter insertion force range $(0 - 2\text{N})$ [42, 43] and spatial resolution (0.1mm) [42]. Also, both systems are well-maintained, and manufacturers offer comprehensive software development kits (SDK). The SDKs allow a designer to control the device at both high-level (needs the least programming skills) and low-level (requires more programming skills) to best accommodate application requirements.

Clinicians believe that the utilization of a pen-like (stylus) interface, used in Phantom and Omega systems, for robotic intervention is non-intuitive and would lead to a steep learning curve [17, 32]. Therefore, researchers have developed intuitive haptic interfaces to better accommodate with the clinical need [54, 84, 198–204].

Studies have explored active, semi-active, and passive actuation for the force control and haptic rendering [54, 84, 86, 198–205]. The choice of actuation highly depends on its application and the range of desired forces. With active actuation, e.g., use of DC motors, haptic device can comply freely with the user (at zero current) or actively oppose the user's motion (at the maximum current). However, active actuation is known to be prone to instability, backlash, force insufficiency and jitter, and energy dissipation [205]. Semi-active actuation has been suggested to increase the stability of the motor-driven devices. It is performed through simultaneous use of a DC motor and a mechanical brake. The integrated break introduces a level of friction damping to the system and increases the stability[206]. However, this also comes at the price of compromised peak force and lower agility[205, 206]. In passive actuation, haptic rendering is realized through controlling the resistance against the motion, e.g., viscous friction on the catheter. Recently, Yin *et al.* [86, 205, 207] have utilized a medium filled with a magneto-rheologic-fluid (MRF) as the haptic interface. A catheter was passed through the medium and the viscosity of the MRF was controlled by the current

in a coil surrounding the medium. Therefore, viscous friction on the catheter (resistance against the motion) was controlled, so that the total insertion force of the user matches up with that measured at the slave side[207]. The development of haptic interfaces for robot-assisted cardiovascular intervention is still in its infancy, and new technologies such as wearables must be investigated for the proposing intuitive haptics-enabled surgeon interfaces.

2.7 Summary

The provision of haptic feedback for robot-assisted cardiovascular interventions is the most prominent technological challenge for this technology. Although many studies have focused on the force feedback for robotic EPI, the current literature for the robotic PCI and PPI is not promising. This review was an attempt to gather the state-of-the-art for haptic telerobotic cardiovascular interventions. The article was tailored to deliver the results of the literature survey in a system-to-component hierarchy.

In this chapter, initially, an overview of the research topics pertinent to the robot-assisted haptic feedback in cardiovascular interventions was presented. The literature-tree provided in this chapter would be utile for the researchers who are willing to expedite their literature review, as well as those keen to gather the state-of-the-art. Furthermore, a review of the clinical significance for the provision of haptic feedback in robotic interventional procedures was performed. Finally, two system architectures for sensor-based and model-based haptic feedback systems were explored, and related methods, notes on implementation, advantages, and limitations of each were critically discussed. On this front, it was tried to cross-validate the basic assumptions in the reviewed methods; however, the available literature was not sufficient in some parts, e.g., particle-based mechanical models of the catheter.

A prominent finding of this review was that the use of model-based haptic feedback had been mainly investigated for virtual reality applications. The reason might be due to the computational advancements, high detailed visualization, or relatively compact setup for performing experiments. While this is welcome, more efforts are needed for concept validation and feasibility study of integrating

the model-based haptic provision in clinical setups. To adopt a proper method of modeling and solution, one should notice the essential difference between VR and real applications; whereas, the vascular anatomy (3D image) is a *priori* knowledge in VR but not in a real cardiac intervention. Gathering such information pre-operatively necessitates additional computed tomography (CT) or magnetic resonance (MR) imaging, which is both ethically and economically not welcome.

Despite the researchers' efforts for the generalization of their results, an apparent limitation of the majority of investigations for robotic PCI and PPI is the limitation of the scope of studies to one specific component of the system, e.g., image-processing, haptic device, or mechanical modeling. The need for more thorough studies to investigate the mutual effects of the specification of major system components on the quality of haptic feedback is evident. To exhibit an acceptable level of clinical applicability, studies should be accompanied by enough experimental evidence and statistical analysis.

Both sensor data and model data are needed for robotic PCI and PPI. As explored in Section 2.2, sensor data is irreplaceable with mere model predictions; however, mining extra information is possible through the combination of model and sensor readings. Therefore, more extensive research on the requirements for a model-based haptic feedback and procedure-specific parameters, e.g., range of forces, kinematics of catheter, specifically for robotic PCI and PPI is needed.

Moreover, as another front of possible enhancement, specifically for the model-based haptic provision, is the model verification and validation (V&V). As certification bodies, e.g., US FDA, Canada Health, European Notified Bodies, etc., are advancing their measures in recognizing the use of model and simulation results in the medical technology, more efforts should be directed towards the means and methods of the verification and validation of models. To this end, ample studies would be needed to build an acceptable level of confidence on certain aspects of model-based haptic provision such as justification of primary assumptions, definition, and test of accuracy, repeatability, and reliability. Such direction in future research would result in shorter prototype-to-product time and better global acceptability of the telerobotic cardiac intervention technology.

In the following chapters, the three major identified knowledge gaps, i.e., sensor-free force estimation, independent rotation and insertion measurement, and intuitive surgeon unit design, that have hindered the provision of haptic feedback for RCI systems are addressed.

Chapter 3

Image-based Estimation of Contact Forces on Catheters for Robot-assisted Cardiovascular Intervention

Clinicians have reported the loss of haptic feedback during the robot-assisted cardiovascular intervention (RCI) as the most challenging limitation of the state-of-the-art. This limitation is a risk factor that causes poor hand-eye coordination for surgeons, compromised situational awareness, and may lead to adverse events such as vascular perforation. To alleviate this problem, researchers have postulated using embedded force/torque sensors at the distal or proximal end of catheters. However, this integration is cumbersome and not feasible for the majority of the commercially available intraluminal devices, e.g., catheters and guidewires. In this chapter, a new image-based force estimation for haptic rendering, as an alternative to sensor-based force measurement, is described. The proposed method is based on image-based shape-sensing and inverse finite-element method for force estimation. The proposed method was validated for robot-assisted cardiovascular intervention through a series of simulation-based and experimental studies. The results showed that the proposed method was accurate within the requirements for estimating the catheter insertion force. However,

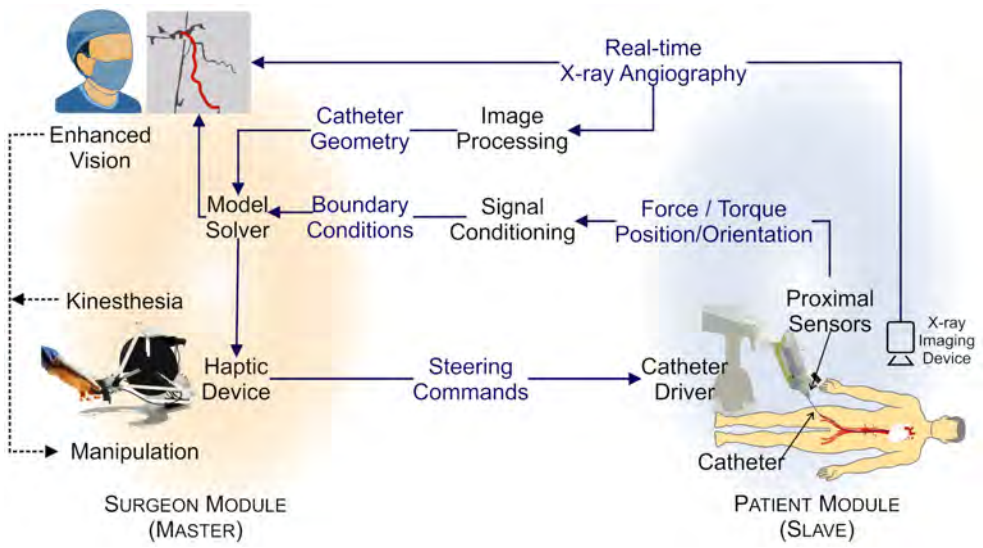

Figure 3.1: System architecture of the model-based haptic feedback for RCI applications.

its real-time performance did not meet the required refresh rate.

3.1 Introduction

The clinical evidence discussed in Section 1.1.3 showed the clinical significance of the need for haptic feedback in RCI applications. Provision of haptic feedback entails two major components: force measurement (or estimation) and haptic rendering. Fig. 3.1 depicts the system architecture for the model-based haptic feedback provision. An integral part of the model-based haptic provision for RCI applications is the force estimation framework. Model-based force estimation is an alternative to the direct force measurement method which resolved its main technical limitations discussed in Section 2.3.5, i.e., in the integration of force sensors.

In this chapter a new image-based force estimation framework for catheters is presented. This framework is intended for finding the location and magnitude of the structural shear forces on a deformed catheter in real-time using its shape and inverse finite-element method (iFEM). In the following a brief review of the related work, proposed methodology, results of validation studies, and concluding remarks are provided.

3.1.1 Related Work

The finite element method has been regarded as the most accurate method for the simulation of catheter deformations in the vasculature [62]. In this regard, Gao *et al.* [132] used a linear finite element model with Euler-Bernoulli elements to estimate the contact forces between a cardiac catheter and the vessels in a vascular phantom. The results revealed that the model had underestimated the contact forces compared to the other clinical studies. The reason might be because of excluding the geometric non-linearity evolved by large-deformation of the beam [133]. Although FEM is of high precision in modeling catheters and guidewires, it is computationally expensive and is prone to erroneous results if implemented with inadequate constraints. The exact constraint definition and treatment are of high importance, especially in the case of large deformation or contact analysis [130].

To accelerate the solution of the finite element models, various theoretical and software advancements have been made, e.g. co-rotational updated Lagrangian formulation [134], explicit dynamics formulation [135], GPU computation [136], and sub-structural analysis and condensed stiffness matrix storage [137]. However, the FEM is still the most computationally-expensive amongst the modeling modalities for robotic cardiovascular intervention applications. In the absence of an analytic solution, the numerical method used by researchers for large deformation analysis is the structural FEM. In the FEM theory, the geometry is discretized into finite elements, while the deflection is considered to vary continuously (linearly or quadratically) within each element [138]. Therefore, the deflection and internal forces vary continuously. Some researchers have investigated the deflections of catheters and guidewires as a finite element beam structure. In an early effort, Wang *et al.* [139] used static structural finite element analysis to find the distributed forces acting on the cardiac guidewire during the conventional PCI; however, the vascular wall was modeled as rigid. In addition to that, the width span and variation rule of the distributed forces were pre-set as constraints. Duriez *et al.* [140, 141] performed an incremental finite element analysis on a guidewire which was modeled by three-dimensional Euler-Bernoulli beam elements. In order to capture the geometric non-linearities, the elemental stiffness matrix was updated at each increment based on the augmented Lagrangian method proposed in [133].

Despite the efforts, the FEM-based force estimations frameworks still suffer from two shortcomings. Firstly, the proposed methods in the literature depend on *a-priori* knowledge of the vascular anatomy. This information required preoperative volumetric imaging, 3D reconstruction, and segmentation of the heart and vessels. Secondly, as the shape of the vessels and heart change intraoperatively, the preoperative 3D shapes must be deformed computationally to conform to the intraoperative shape (non-rigid registration). Intraoperative non-rigid registration is a computationally expensive procedure. Moreover, even with proper knowledge of the vessels and heart during the surgery, force estimation requires real-time contact detection between the catheter and vessels which exacerbates the computational cost.

3.1.2 Motivation and Contributions

The FEM-based force estimation was selected in this study to investigate its capability in estimating accurate insertion forces on catheters. Addressing the technical limitation of the available FEM-based force estimation frameworks, i.e., high computational cost and dependency on the vascular anatomy, was the motivation of this study. It was hypothesized that a desirable force estimation framework for haptic provision in RCI applications shall be independent of the vascular anatomy and be performed merely based on the deformation of the catheter. The reason is that the deformed shape of the catheter is obtained in real-time with negligible computational cost through preliminary image-processing techniques, e.g., background removal [185]. The main contributions of this study are:

(1) proposing a novel force estimation framework based on inverse finite element method (iFEM),

(2) utilization of a fast shape-sensing method for curve parameterization of the catheters,

(3) independency of the proposed force estimation method from vascular anatomy and elimination of the need for computational contact treatment,

(4) proposing a new force indicator parameter for determining the positions of external forces along the catheters,

(5) proposing a fast inverse finite element solution for force estimation,

(6) integration of the proposed method with a representative RCI system for haptic provision.

3.2 Force Estimation Framework

The proposed force estimation in this study was based on real-time shape-sensing, shape-based identification of the contact points (location of the contact forces), and optimization-based force estimation at the contact points using an iFEM framework. The proposed method included the required model-based components introduced in Sec. 2.5, i.e., imaging, segmentation, shape-sensing, curve parameterization and deformation estimation, inverse formulation, and fast solution. The proposed method was based on identifying the location of external forces from a geometric parameterized force indicator, $\zeta(s)$. The proposed force indicator is based on a physical interpretation from the force-deformation relationship in slender (Euler-Bernoulli) beams (discussed in Sec. 3.2.6). Algorithm 2 describes the proposed framework in a pseudo-code format.

Algorithm 2 Pseudo-code for the proposed iFEM-based force estimation.

Input: *Camera Calibration:* The camera calibration matrix, $\mathbf{\Psi}$ to map the segmented pixels $\begin{pmatrix} {}^{j}u_1 & {}^{j}v_1 & {}^{j}u_2 & {}^{j}v_j & 1 \end{pmatrix}^{\mathsf{T}}$ to global coordinates $\begin{pmatrix} x_j & y_j & z_j \end{pmatrix}^{\mathsf{T}}$ ▷ $\mathbf{\Psi} \in \mathfrak{R}^{3\times 5}$
Input: *Initial Shape:* Original shape of the catheter $\mathbf{c}^{\star}(s)$ ▷ $s \in [0, 1]$
Input: *Constants:* Geometric and mechanical properties of the catheter ▷ E, ϑ, I, L
Output: *Contact points:* s_i^c ▷ $i = 1 \cdots n_c$
Output: *Magnitude of perpendicular contact forces:* f_i^c ▷ $i = 1 \cdots n_c$

```
Initialize:
    Calculate initial curvature of the catheter: κ*(s)                    ▷ Appendix A
while the catheter is being inserted do
    procedure CONTACTPOINTSDETECTION(κ*(s), c(s))
        Calculate the change in the curvature of the catheter             ▷ δκ(s) = κ(s) − κ*(s)
        Calculate the force indicator                                     ▷ Ω = (d²/ds²) δκ(s)
        Identify the singularities of Ω as the location of the contact forces ▷ s_i^c
    end procedure
    procedure FORCEESTIMATION(s_i^c, c*(s))
        find f_i: argmin(||c(s) − c*(s) − u_FEM||) s.t. f(s) = 0 if s ∉ s_i^c ▷ iFEM+PSO
    end procedure
end while
    return
```

3.2.1 Image Processing and Segmentation

Since the live X-ray images are available intraoperatively, an image-based catheter shape extraction was proposed. In this study, camera imaging was used to obtain the shape of the flexible catheter through stereo vision. Using the stereo vision, in laboratory experiments, has been validated for catheter shape extraction in the literature, e.g., [185].

Two USB cameras (C920, Logitec Inc., Switzerland), were installed on a frame for providing stereo vision. The cameras were calibrated using MATLAB Stereo Camera Calibration Toolbox (MATLAB R2017b, MathWorks Inc., MA, USA) with a pinhole camera model [208]. Fig. 3.2(a) shows the pose of cameras with respect to the vascular model. The checkerboard calibration and re-projection test confirmed a root-mean-square (RMS) re-projection error of 0.27, 0.11, and 0.31 mm for x, y, and z estimation (Fig. 3.2(b)). The calibration template was a standard 19×12 checkerboard with 20mm edge size. Also, the goodness-of-fit for the pinhole model as a mapping from camera coordinates to world coordinates was $\mathrm{R}^2 = 0.98$. Equation 1 shows a representative calibration matrix obtained from stereo-calibration.

$$\mathbf{\Psi} = \begin{pmatrix} -0.3078 & -0.0121 & -0.2941 & 0.0021 & 401.2635 \\ -0.2212 & -0.3317 & 0.3196 & 0.2218 & 242.7941 \\ 0.0470 & -0.0422 & 0.0009 & 0.0726 & 584.1171 \end{pmatrix} (\frac{\text{mm}}{\text{px}}) \tag{1}$$

For the experiments, a vascular phantom (SAM plus, Lake Forest Anatomical Inc., IL, USA) with femoral, abdominal, and thoracic aorta was used. Also, a master–slave robotic mechanism was developed in-house and was used for remote robotic steering of the catheter.

To segment the catheter, each frame of each camera was converted to gray-scale and was subtracted from the background image obtained with the same camera (image of the setup before inserting the catheter). Afterward, by performing thresholding, adopted from [185, 209], a binary map representing the catheter in each frame was obtained and was used for 3D reconstruction. The 3D reconstruction of the pixels from binary maps were performed using the calibration mapping matrix of stereo-cameras, i.e. $\mathbf{\Psi}_{3\times5}$ obtained from camera calibration; whereas, m segmented pixels in the left $({}^{j}u_1, {}^{j}v_1)^{\mathsf{T}}$, and the right $({}^{j}u_2, {}^{j}v_2)^{\mathsf{T}}$ camera were mapped to the 3D point $\bar{\mathbf{p}}_j$ by triangulation

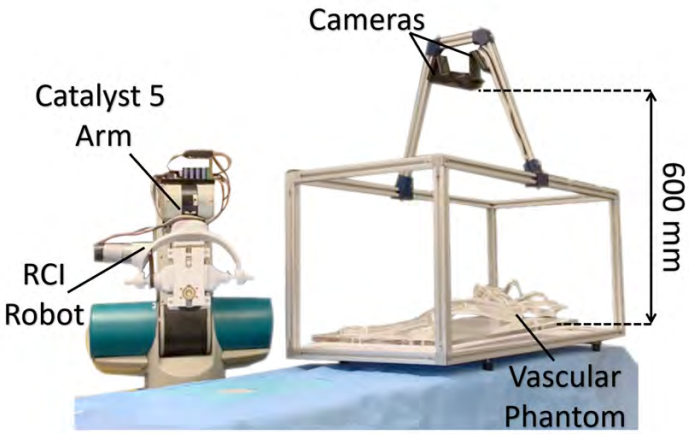

(a)

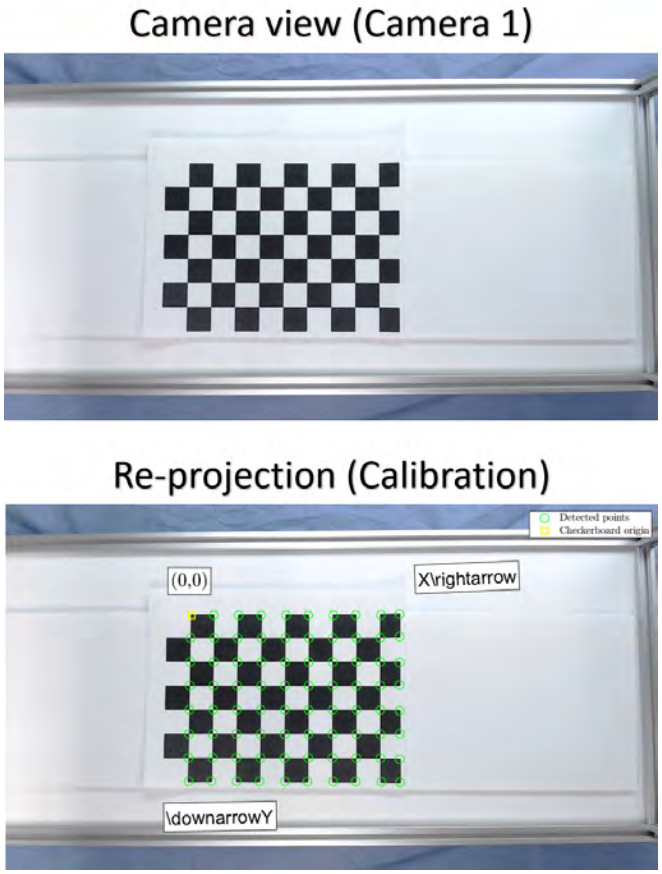

(b)

Figure 3.2: (a) Experimental setup with the cameras, RCI system, and vascular phantom, (b) back-propagation result from camera calibration.

method using Eq. 2.

$$\bar{\mathbf{p}}_j = \mathbf{\Psi} \begin{pmatrix} {}^j u_1 & {}^j v_1 & {}^j u_2 & {}^j v_2 & 1 \end{pmatrix}^{\mathsf{T}} \qquad j = 1 \cdots m \tag{2}$$

3.2.2 Shape Parameterization

The goal of the shape parameterization was to find a continuously differentiable representation for the shape of the catheter in each frame. In contrast to graph representation (a collection of points with numerical values), parameterized shape allowed for finding a differentiable representation of the shape and deformation. Each of the points acquired from stereo-vision, $\bar{\mathbf{p}}_j$, was associated with a normalized curve parameter $\bar{s_j}$ defined as:

$$\bar{s}_j = \frac{1}{\bar{\mathrm{L}}} \sum_{k=2}^{j} ||\bar{\mathbf{p}}_k - \bar{\mathbf{p}}_{k-1}||, \tag{3}$$

$$\bar{\mathrm{L}} = \sum_{k=2}^{m} ||\bar{\mathbf{p}}_k - \bar{\mathbf{p}}_{k-1}||, \tag{4}$$

where $\bar{\mathrm{L}}$ is the total length of the segmented catheter. Therefore, the discretized centerline $\bar{\mathbf{c}}(\bar{s}_j)$ was defined as a collection of $\bar{\mathbf{p}}_j$-s such that:

$$\bar{\mathbf{c}}(\bar{s}_j) = \bar{\mathbf{p}}_j = \begin{pmatrix} \bar{x}_j \\ \bar{y}_j \\ \bar{z}_j \end{pmatrix}, \qquad j = 1 \cdots m \tag{5}$$

with $\bar{x}_j$, $\bar{y}_j$, and $\bar{z}_j$ in the global coordinates.

The centerline of the catheter, $\mathbf{c}(s)$, was interpolated using a Bezier curve. Bezier curves are Pythagorean–hodograph curves with Bernstein polynomial tuple basis [210], which are widely used for 3D shape reconstruction of curves. A Bezier curve of n–order is a function of normalized length parameter $s \in [0, 1]$ and provides a continuous and differentiable interpolation using $n + 1$ control points $\mathbf{p}_{0-n}$. Therefore, the centerline $\mathbf{c}(s)$ was parameterized as a Bezier curve of degree n with

the form:

$$\mathbf{c}(s) = \begin{pmatrix} x(s) \\ y(s) \\ z(s) \end{pmatrix} = \sum_{i=0}^{n} b_{i,n}(s)\mathbf{p}_i, \tag{6}$$

where $\mathbf{p}_i = (x_i, y_i, z_i)^\mathsf{T}$ represent the i-th control point in global coordinates and $b_{i,n}$ is the $(i-1)$-th Bernstein basis polynomial of degree n with the form:

$$b_{i,n}(s) = \begin{pmatrix} n \\ i \end{pmatrix} (1-s)^{n-i}\, s^i. \tag{7}$$

In general, the control points do not coincide with the curve, however, $\mathbf{p}_0$ and $\mathbf{p}_n$, associated with $s = 0$ and $s = 1$, necessarily reside on the tail and the tip of the curve, respectively. This would further facilitate the localization of the beginning (tail) and the ending (tip) of the catheter in the reconstructed shape. The matricial form of Eq. 6 was:

$$\mathbf{c}(s) = \mathbf{P}\mathbf{b}_n(s) = \begin{pmatrix} \mathbf{p}_0 & \cdots & \mathbf{p}_n \end{pmatrix} \begin{pmatrix} b_{0,n}(s) \\ . \\ . \\ . \\ b_{n,n}(s) \end{pmatrix}. \tag{8}$$

Fitting the discrete shape of the centerline $\bar{\mathbf{c}}(s_j)$ with the Bezier curve $\mathbf{c}(s)$ constituted an unconstrained least-square optimization (LSO) problem defined by Eq. 9 with $\mathbf{P}$ unknown.

$$mininmize \sum_{j=1}^{m} \left(\mathbf{P}\mathbf{b}_n(\bar{s}_j) - \bar{\mathbf{c}}(\bar{s}_j)\right)^\mathsf{T} \left(\mathbf{P}\mathbf{b}_n(\bar{s}_j) - \bar{\mathbf{c}}(\bar{s}_j)\right), \tag{9}$$

Moore-Penrose pseudo-inverse theorem guarantees the existence and uniqueness of a $\mathbf{P}$ minimizing Eq. 9, if and only if:

$$\mathbf{P} = \begin{pmatrix} \mathbf{p}_0 & \cdots & \mathbf{p}_n \end{pmatrix} = \bar{\mathbf{C}}\bar{\mathbf{B}}^T(\bar{\mathbf{B}}\bar{\mathbf{B}}^T)^{-1}, \tag{10}$$

with,

$$\bar{\mathbf{C}} = \begin{pmatrix} \bar{\mathbf{p}}_1 & \cdots & \bar{\mathbf{p}}_m \end{pmatrix} \tag{11}$$

and,

$$\bar{\mathbf{B}} = \begin{pmatrix} \mathbf{b}_n(\bar{s}_1) & \cdots & \mathbf{b}_n(\bar{s}_m) \end{pmatrix}. \tag{12}$$

Fig. 3.3 depicts the reconstructed shape of the catheter for two representative deformations. By obtaining $\mathbf{P}$, the accurate total length of the catheter L was obtained using the arc-length integration over $s \in [0, 1]$ domain:

$$L = \int_0^1 ||\mathbf{c}'(s)||\mathrm{d}s, \tag{13}$$

where $(.)' = \frac{\mathrm{d}}{\mathrm{d}s}$ is the derivative operator. For fast numerical integration, the five-node Gauss quadrature method was adopted. To avoid noise injection by numerical derivation, the recursive De Casteljau's algorithm was used to obtain the derivative terms in Eq. 13 [210]. The analytical expressions of the derivatives of $\mathbf{c}(s)$ are provided in Appendix A. For demonstration, the proposed catheter segmentation was applied on a representative X-ray image of a PCI procedure (Fig. 3.4).

3.2.3 Kinematics

In this study, the catheter was modeled as a slender Euler-Bernoulli beam with large deformations. Any given point along the centerline of the catheter, $\mathbf{c}(s)$, has three degrees-of-freedom (DoFs) in spatial translation, two bending DoFs in geodesic and normal bending within the normal plane of the centerline, and one torsional DoF in twisting about the tangent unit vector of the centerline.

For the sake of simplicity and without loss of generality, the original shape of the centerline of the catheter, $\mathbf{c}^\star(s)$ was assumed to be a straight line and tangent to the deformed shape at $s = 0$.

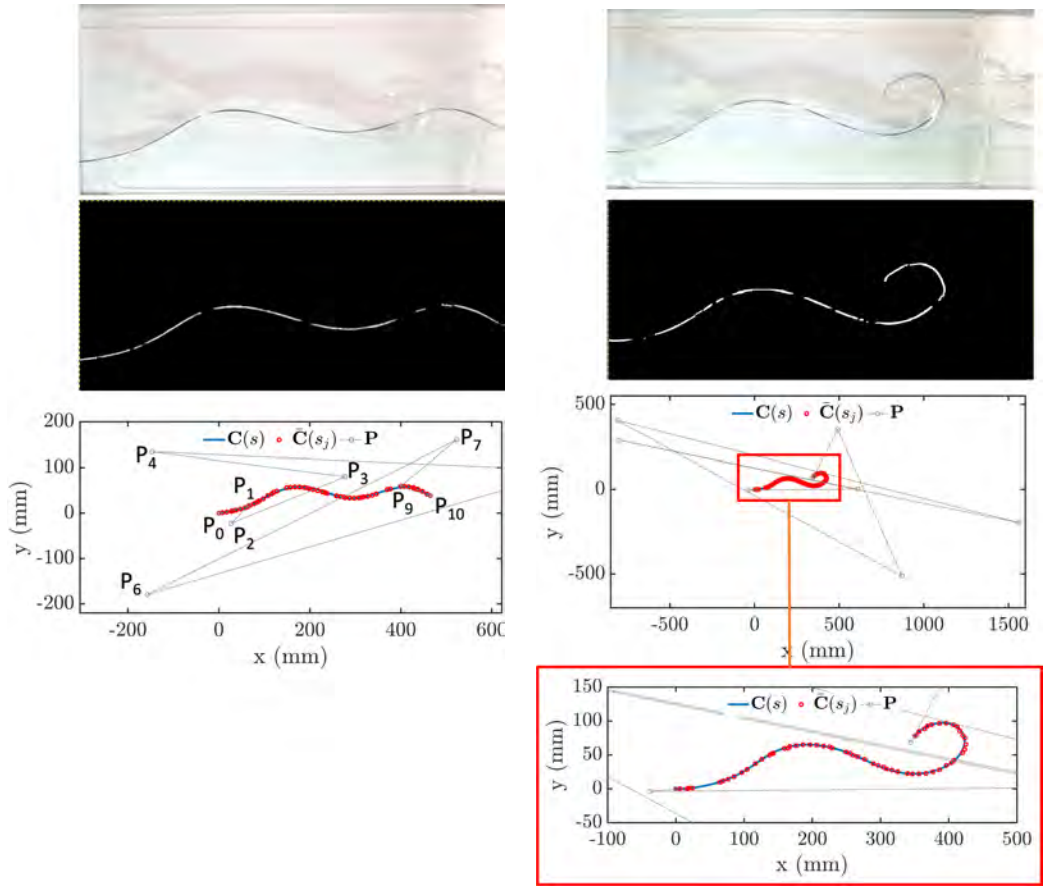

Figure 3.3: Top view of reconstructed shapes of the catheter with two deformations using Bezier shape fitting and reconstruction.

(a) (b) (c)

Figure 3.4: (a) Intraoperative X-ray image with a PCI catheter, (b) segmented catheter, (c) interpolated shape of the catheter using Bezier spline.

Therefore:

$$\mathbf{c}^{\star}(s) = \begin{pmatrix} \mathbf{p}_0 & L\mathbf{p}_1 \end{pmatrix} \mathbf{b}_1(s). \tag{14}$$

Using Eq. 14 and parameterized shape of the catheter, the parameterized positional displacement of the catheter was obtained as:

$$\mathbf{u}(s) = \mathbf{c}(s) - \mathbf{c}^{\star}(s) = \mathbf{P}\mathbf{b}_n(s) - \begin{pmatrix} \mathbf{p}_0 & \mathrm{L}\mathbf{p}_1 \end{pmatrix} \mathbf{b}_1(s) \tag{15}$$

Vector $\mathbf{u}_{3\times1}(s)$ expresses the positional deflection of the catheter in each frame.

The Frenet-Serret (FS-) frame is the most adopted moving frame choice for representing the spatial orientation of parameterized curves. However, the FS-based curvature $\kappa(s)$ is singular at the inflection points of the curve [210]. To alleviate this problem, orthonormal Darboux frame [211, 212] was used in this study to parameterize the spatial orientation of $\mathbf{c}(s)$. Using the definitions of the orthonormal unit vectors $\mathbf{d}_{1-3}(s)$, the local Darboux frame $\mathbf{R}$ was defined as:

$$\mathbf{R} = \begin{pmatrix} \mathbf{d}_1(s) & \mathbf{d}_2(s) & \mathbf{d}_3(s) \end{pmatrix} \tag{16}$$

The choice of Darboux frame allowed for finding analytical expressions of the geodesic curvature $\kappa_g(s)$ and normal curvature $\kappa_n(s)$ as . Furthermore, the total curvature of the centerline was obtained as [210]:

$$\kappa^2(s) = \kappa_g^2(s) + \kappa_n^2(s). \tag{17}$$

Fig. 3.5 depicts the schematic deformed shape of the catheter with representative Darboux frames.

3.2.4 Force Balance

The external forces acting on the intraluminal devices are the insertion force (along $\mathbf{d}_1(0)$) and torsional torque (about $\mathbf{d}_1(0)$), distributed weight (along global z-axis), hemodynamic drag (along $\mathbf{d}_1(s)$), contact forces with the vessels (in $\mathbf{d}_2(s)$-$\mathbf{d}_3(s)$-plane), and contact friction (along $\mathbf{d}_1(s)$ at contact points).

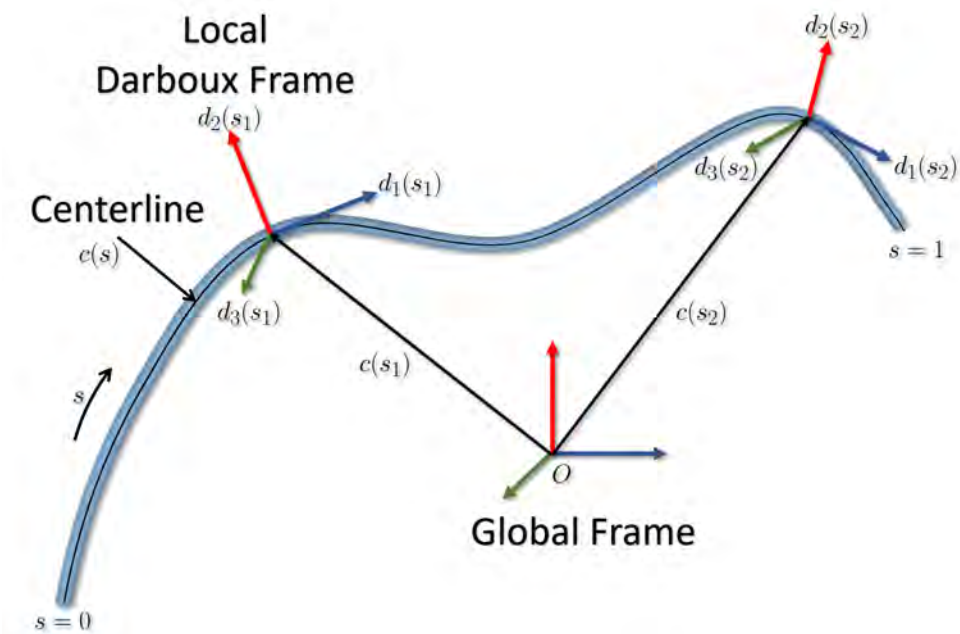

Figure 3.5: Schematic deformed shape of the catheter, $\mathbf{c}(s)$ with representative local Darboux frames.

In this study, the catheter was assumed in quasi-static equilibrium and with a negligible torsional twist as a simplifying assumptions. Also, given the fact that catheters are coated with superhydrophobic agents, the hemodynamic drag was not considered in the model. Fig. 3.6 depicts the free-body-diagram of a portion of a catheter cut at s.

The internal force and moments of the beam in global coordinates are related to the external forces through [213]:

$$\mathbf{n}(s) = \mathbf{n}_0 - \int_0^s (\mathbf{f}(\eta) + \mathbf{f}_f(\eta) + \rho \mathrm{A}\mathbf{g})\mathrm{d}\eta \tag{18}$$

$$\mathbf{m}(s) = \mathbf{m}_0 - \int_0^s \mathbf{c}'(\eta) \times \mathbf{n}(\eta)\mathrm{d}\eta, \tag{19}$$

with ρ the density of the catheter, A the cross-sectional area of the catheter, and $\mathbf{g} = \begin{pmatrix} 0 & 0 & -9.81 \end{pmatrix}^{\mathsf{T}}$. Alternatively, $\mathbf{m}(s)$ was calculated using the hat operator $(.)^\wedge$ (defined in Appendix A) [213]:

$$\mathbf{m}(s) = \mathbf{m}_0 - \int_0^s \mathbf{c}'(\eta)^\wedge \mathbf{n}(\eta)\mathrm{d}\eta. \tag{20}$$

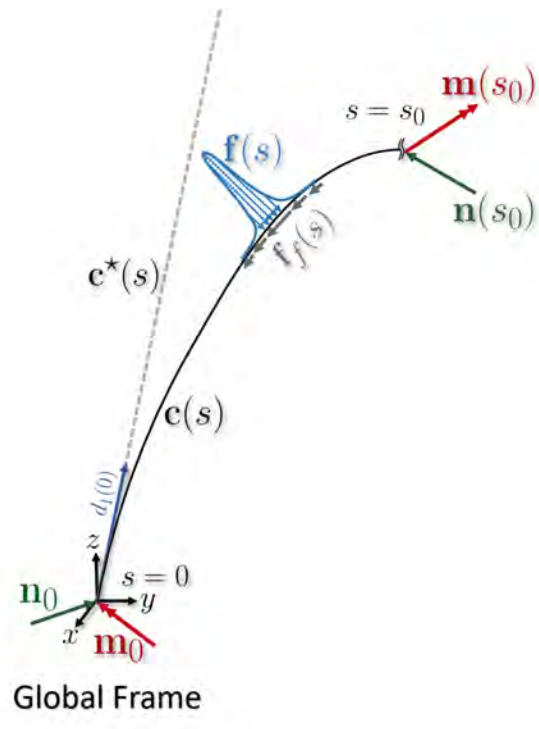

Figure 3.6: The free-body-diagram (FBD) of a portion of the catheter with representative external force and insertion force and torque.

3.2.5 Constitutive Equation

Medical catheters are usually constituted of a medical-grade Nickel-Titanium (NiTi) alloys coil [214] covered with a thin polymeric drag-reducing sheet. Despite the large geometrical deformation of the catheter, it remains within the limits of the linear elastic region, thanks to the super-elastic properties of NiTi alloys [188, 215]. Using the Euler-Bernoulli theory, the bending constitutive equation of the catheter in global coordinates at any s is:

$$\mathbf{m}(s) = \mathbf{R}\mathbf{K}_b \begin{pmatrix} \tau_g \\ \kappa_n \\ \kappa_g \end{pmatrix} - \mathbf{R}^\star \mathbf{K}_b \begin{pmatrix} \tau_g^\star \\ \kappa_n^\star \\ \kappa_g^\star \end{pmatrix}, \tag{21}$$

with $\mathbf{K}_b$ as the bending and torsional stiffness matrix defined as:

$$\mathbf{K}_b = \begin{pmatrix} \frac{\mathrm{EI}}{1+\vartheta} & 0 & 0 \\ 0 & \mathrm{EI} & 0 \\ 0 & 0 & \mathrm{EI} \end{pmatrix}. \tag{22}$$

Given that the initial shape of the catheter was assumed to be a straight line, $\kappa_g^\star$, $\kappa_n^\star$, and $\tau_g^\star$ were zero. Thus, the second term in the right-hand-side (RHS) of Eq. 21 became zero. Should not the catheter be of a linear shape, the second term in RHS would become a non-zero constant vector. Using the moment balance Eq. 20, the constitutive equation was re-arranged as:

$$\mathbf{m}_0 - \int_0^s \mathbf{c}'(\eta)^\wedge \mathbf{n}(\eta)\mathrm{d}\eta = \mathbf{R}\mathbf{K}_b \begin{pmatrix} \tau_g \\ \kappa_n \\ \kappa_g \end{pmatrix}. \tag{23}$$

In each frame, $\mathbf{m}_0$ was obtained by evaluating Eq. 23 for $s = 0$:

$$\mathbf{m}_0 = \mathbf{K}_b \begin{pmatrix} 0 \\ \kappa_n(0) \\ \kappa_g(0) \end{pmatrix}. \tag{24}$$

Eq. 23 provides an analytical description of the relationship between the curvature and twist of the catheter with the external force distribution. The RHS of this equation is parameterized with s, thus with proper rigorous derivation the left-hand-side (LHS) (including the unknown $\mathbf{f}(s)$ and $\mathbf{f}_f(s)$) could be obtained as a function of s. The remaining unknowns were $\mathbf{f}(s)$ and $\mathbf{f}_f(s)$. In an empirical study, Takashima *et al.* [216] found that Coulomb friction with $\mu_f = 0.04$ could adequately model the friction of catheters and vessels. Accordingly, the adopted friction model for this study was:

$$\mathbf{f}_f(s) = -\mathrm{sgn}\big(\dot{\mathbf{c}}(s) \cdot \mathbf{d}_1\big)\mu_f||\mathbf{f}(s)||\mathbf{d}_1(s) = -\mathrm{sgn}\big(\dot{\mathbf{P}}\mathbf{b}_n(s) \cdot \mathbf{d}_1\big)\mu_f||\mathbf{f}(s)||\mathbf{d}_1(s) \tag{25}$$

with sgn as the sign function, $\dot{(.)} = \frac{\mathrm{d}}{\mathrm{d}t}$, the temporal derivation operator, and $\dot{\mathbf{P}}$ as the velocity of the control points. The temporal derivative terms were calculated using the third-order backward differentiation formula:

$$\dot{\mathbf{P}} = \frac{\frac{11}{6}\mathbf{P}_t - 3\mathbf{P}_{t-h_t} + \frac{3}{2}\mathbf{P}_{t-2h_t} - \frac{1}{3}\mathbf{P}_{t-3h_t}}{h_t} + O(h_t^3), \tag{26}$$

with h_t the time difference between two consecutive frames.

For mechanical problems, should the distribution of external force be known *a-priori*, the deformation (curvature and twist) could be obtained at any given $s = s_0$ through Eq. 23. Such a problem is known as a direct problem. However in this study, the force distribution was unknown while the curvatures were known that made this problem an inverse problem. Thus, the solution schema required localizing the external forces and estimating the magnitude of the localized forces. As the first step of the solution, the following force indicator, Ω, was proposed to localize the external forces.

3.2.6 Force Indicator

The physical intuition of the proposed force indicator in this study was based on the fact that the internal shear force, $\mathbf{n}(s)$, exhibits a discontinuity (sudden change) at points where concentrated external forces are applied. Theoretically at such points, $\mathbf{n}'(s)$ becomes singular. In practice, such singularities were identifiable by local maxima in $\mathbf{n}'(s)$. Therefore, it was hypothesized that the corresponding arc-lengths s_i^c corresponding to the local maxima of $\mathbf{n}'(s)$ were the locations of external forces. Nevertheless, $\mathbf{f}(s)$ was unknown and yet to be solved.

To obtain the location of the external forces, the RHS and LHS of Eq. 21 were differentiated with respect to s. Eq. 27 and 28 express the first and the second derivatives, respectively.

$$-\mathbf{c}'(s)^{\wedge}\mathbf{n}(s) = \mathbf{R}'\mathbf{K}_b \begin{pmatrix} \tau_g \\ \kappa_n \\ \kappa_g \end{pmatrix} + \mathbf{R}\mathbf{K}_b \begin{pmatrix} \tau_g' \\ \kappa_n' \\ \kappa_g' \end{pmatrix}. \tag{27}$$

$$-\mathbf{c}''(s)^{\wedge}\mathbf{n}(s) - \mathbf{c}'(s)^{\wedge}\mathbf{n}'(s) = \mathbf{R}''\mathbf{K}_b \begin{pmatrix} \tau_g \\ \kappa_n \\ \kappa_g \end{pmatrix} + 2\mathbf{R}'\mathbf{K}_b \begin{pmatrix} \tau_g' \\ \kappa_n' \\ \kappa_g' \end{pmatrix} + \mathbf{R}\mathbf{K}_b \begin{pmatrix} \tau_g'' \\ \kappa_n'' \\ \kappa_g'' \end{pmatrix}. \tag{28}$$

For any arbitrary s_i^c with an external force applied on the catheter, the term $\mathbf{n}'(s_i^c)$ becomes singular. This condition necessitates that the RHS of Eq. 28 becomes singular at s_i^c.

To find a proper force indicator for finding s_i^c, the RHS was analytically investigated. Given that curve $\mathbf{c}(s)$ is Lipschitz continuous, its derivatives exist and are real-valued [210]. Also, from the properties of Darboux frames is that τ_g, κ_g, and κ_n are not singular [210]. Moreover, in Darboux frames:

$$\mathbf{R}' = \begin{pmatrix} 0 & -\kappa_g & \tau_n \\ \kappa_n & 0 & -\kappa_n \\ -\tau_g & \kappa_n & 0 \end{pmatrix} \mathbf{R} = \begin{pmatrix} \tau_g \\ \kappa_n \\ \kappa_g \end{pmatrix}^{\wedge} \mathbf{R}, \tag{29}$$

and

$$\mathbf{R}'' = \begin{pmatrix} \tau_g' \\ \kappa_n' \\ \kappa_g' \end{pmatrix}^{\wedge} \mathbf{R} + \begin{pmatrix} \tau_g \\ \kappa_n \\ \kappa_g \end{pmatrix}^{\wedge 2} \mathbf{R}, \tag{30}$$

which implies $\mathbf{R}'$ is real-valued. Therefore, the necessary condition for singularity of the RHS of Eq. 28 is that either of τ_g', τ_g'', κ_n', κ_n'', κ_g', or κ_g'' become singular.

Given that in this study torsional twist was neglected $\tau_g = 0$, only κ_g and κ_n were remained. Also, with the definition of κ_g and κ_n it can be shown that singularities of κ_g' and κ_g'' and κ_n' and κ_n'' happen at similar s_i^c (concentrated external force in the $\mathbf{d}_2$-direction causes singularity in both κ_g' and κ_g'', and concentrated external force in the $\mathbf{d}_3$-direction causes both κ_n' and κ_n'' become singular). Since the second derivative would amplify the numerical singularity, it was used as the condition. To combine these necessary conditions, the second derivative of the square of the total curvature κ (Eq. 17) was used. The rationale was that a singularity in either κ_n or in κ_g would make it singular, thus allow for localizing the external force. Therefore, the force indicator $\Omega(s)$ was defined as:

$$\Omega = \frac{\mathrm{d}^2}{\mathrm{d}s^2}\kappa^2 = \frac{\mathrm{d}^2}{\mathrm{d}s^2}\left(\kappa_g^2 + \kappa_n^2\right). \tag{31}$$

The objective was to find s_i^c, the singularities of Ω, in real-time to localize the external forces. Afterward s_i^c were used in the inverse solution to find the magnitude of the external forces.

3.2.7 Inverse Solution: iFEM

Inverse problems are typically ill-conditioned due to (1) the non-existence, (2) the non-uniqueness, or (3) the discontinuity of the solution [217]. From these factors, the non-existence was not relevant to the problem since the deformations were obtained from physically-deformed catheters; thus, the existence of the solution is guaranteed. It is noteworthy that non-existence usually occurs when there cannot be a physically plausible solution for the equation. Nevertheless, the discontinuity of the solution is intrinsic in this study since the external forces assumed to be point loads at contact points. The mathematical representation of such point loads would be Dirac's sliding delta, $\delta(s-s_i^c)$ [218]. To remedy the discontinuity issue, a few studies have proposed continuous forms to estimate the external forces such as truncated Fourier series [218]. Nevertheless, such approximations have resulted in large errors in the force estimation and localization. The main reason for large errors in those studies is the fact that the proposed interpolation functions could not adequately replicate the point load conditions. To remedy this problem in this study, a sliding Gaussian distribution was proposed. The force interpolation function was of the form:

$$\mathbf{f}(s) = f_2^{\text{Tip}} e^{-\frac{(s-1)^2}{\sigma^2}} \mathbf{d}_2 \Big|_{s=1} + f_3^{\text{Tip}} e^{-\frac{(s-1)^2}{\sigma^2}} \mathbf{d}_3 \Big|_{s=1} + \sum_{i=1}^{n_c} \alpha_{2,i} e^{-\frac{(s-s_i^c)^2}{\sigma^2}} \mathbf{d}_2 + \alpha_{3,i} e^{-\frac{(s-s_i^c)^2}{\sigma^2}} \mathbf{d}_3 \quad (32)$$

which was of a smooth continuous form with multiple maxima at s_i^c and zero values at $s \neq s_i^c$. In Eq. 32, n_c are the number of contact points localized with force indicator, $\alpha_{2,i}$ and $\alpha_{3,i}$ are the interpolation coefficients for the *i*-th contact force along $\mathbf{d}_2$ and $\mathbf{d}_3$ directions, respectively and $\sigma = 1/100$ is a shape controlling parameter which controlled the sharpness of the peaks in $\mathbf{f}(s)$. In addition, two unknown tip forces residing in the normal plane to the catheter were added. The reason was that tip forces were not detectable with the proposed force indicator due to the non-existence of the derivative of the curvature at the tip. Should the catheter be force-free at the tip, the force estimation would find zero values for $f_{2,3}^{\text{Tip}}$.

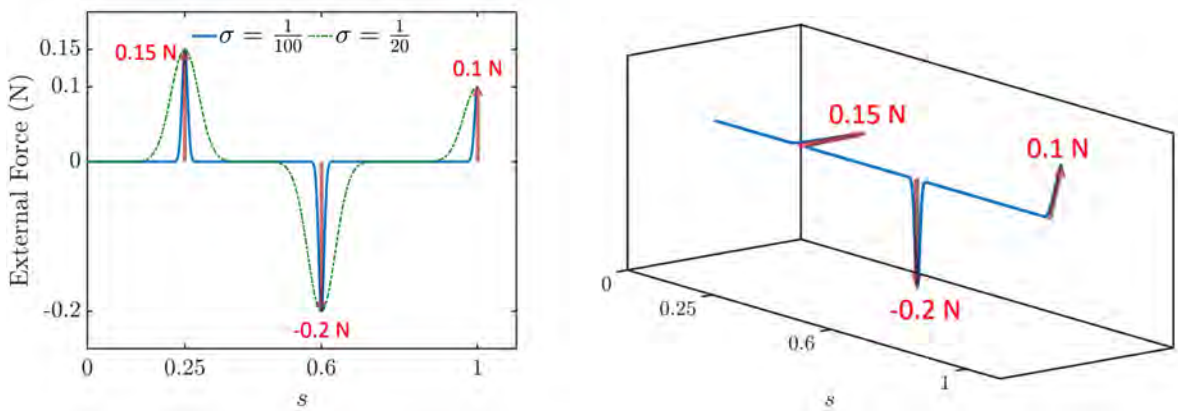

(a) (b)

Figure 3.7: Representative force distributions along the catheter with the proposed smooth force interpolation function with (a) 2D distribution, and (b) 3D distribution.

To exemplify, Fig. 3.7(a) depicts a representative force distribution on the catheter with $L = 500$ mm, $f_2^{\text{Tip}} = 0.1$ N, and two contact forces of $\alpha_{2,1} = 0.15$ N and $\alpha_{2,2} = -0.2$ N acting at $s_1^c = 0.25$ and $s_2^c = 0.6$, respectively. Also, Fig. 3.7(b) depicts a similar force distribution with 3D distribution.

The force estimation problem along flexible beams has previously formulated as a constrained minimization problem with nonlinear constraints [218]. In this study, thanks to the use of a continuous force interpolation, the problem was an unconstrained minimization problem defined as:

$$\text{minimize} \qquad \varepsilon = ||\mathbf{c}(s) - \mathbf{c}^{\star}(s) - \mathbf{u}_{\text{FEM}}||, \tag{33}$$

where $\mathbf{u}_{FEM}$ is the deformation obtained from the FEM solver. In each frame, $\mathbf{c}(s)$ was obtained as described in 3.2.3 and was used in the minimization of Eq. 33.

For solving the minimization problem, various gradient descent methods, such as the Gauss-Newton method, have been proposed [218] However, gradient-based methods suffer from high computation cost (due to their iterative algorithms) and stagnation at local minima. To avoid the computational cost and stagnation issues, a particle swarm optimization (PSO) method was used in this study [219].

The PSO method is a global optimization method with a parallel search algorithm that allowed for

performing the optimization on parallel threads on GPU. The PSO was implemented in C++ and was parallelized with 100 search threads with a maximum iteration of `MAX_ITER`=100. The initial $\alpha_{2,i}$ and $\alpha_{3,i}$ were randomly selected from $[0, 2]$ N, within the reported range of force in RCI procedures [62]. As recommended in [219], the cognitive and social parameters of the PSO were set to 1.5 and the inertial parameter linearly decreasing from 1 to 0.4 over the iterations. The stopping criterion for the optimization $\varepsilon \leq 1$mm or `MAX_ITER`=100, whichever happened first.

3.2.8 Finite Element Formulation

To obtain u_{FEM} in optimization threads, an FEM model of the catheter (as a cantilever beam) with geometric nonlinearity (large deflection) and $n_e = 100$ linear beam elements [133] was implemented in C++ programming language. The GPU-accelerated `Armadillo` linear algebra library was utilized in the FEM solver for fast matrix operations. A mesh-independency test confirmed that $n_e = 100$ was sufficient for the developed model. The formulation of the incremental FEM solver was adopted from [133]. The incremental FEM balance equation for the j-th iteration of the solution in each frame was:

$$ {}^{j}\boldsymbol{\delta}\tilde{\mathbf{u}}_{\text{FEM}} = \left(\mathbf{K}_L + {}^{j}\mathbf{K}_G\right)^{-1} {}^{j}\boldsymbol{\delta}\tilde{\mathbf{f}}_{\text{FEM}}, \tag{34} $$

with j as the iteration number, $\tilde{\mathbf{u}}_{\text{FEM}}$ and $\tilde{\mathbf{f}}_{\text{FEM}}$ as the global nodal displacement and forces, and $\mathbf{K}_L$ and $\mathbf{K}_G$ as the global linear and geometric stiffness matrices. Each 3D beam element had twelve DoFs corresponding to three global displacements, one torsional twist, and two bending angles for each node. Thus, for the i-th element, the elemental displacement and force vectors were:

$$ \tilde{\mathbf{u}}^{i}_{\text{FEM}} = \begin{pmatrix} \tilde{u}^i_1 & \tilde{u}^i_2 & \tilde{u}^i_3 & \tilde{\theta}^i_1 & \tilde{\theta}^i_2 & \tilde{\theta}^i_3 & \tilde{u}^i_4 & \tilde{u}^i_5 & \tilde{u}^i_6 & \tilde{\theta}^i_4 & \tilde{\theta}^i_5 & \tilde{\theta}^i_6 \end{pmatrix}^{\mathsf{T}}, \tag{35} $$

$$ \tilde{\mathbf{f}}^{i}_{\text{FEM}} = \begin{pmatrix} \tilde{f}^i_1 & \tilde{f}^i_2 & \tilde{f}^i_3 & \tilde{m}^i_1 & \tilde{m}^i_2 & \tilde{m}^i_3 & \tilde{f}^i_4 & \tilde{f}^i_5 & \tilde{f}^i_6 & \tilde{m}^i_4 & \tilde{m}^i_5 & \tilde{m}^i_6 \end{pmatrix}^{\mathsf{T}}. \tag{36} $$

In addition the elemental stiffness matrices for the i-th element are provided in Eq. 37 and Eq. 38.

$$
\tilde{\mathbf{K}}_L^i = \begin{pmatrix}
\frac{EA}{L} & 0 & 0 & 0 & 0 & 0 & -\frac{EA}{L} & 0 & 0 & 0 & 0 & 0 \\
0 & \frac{12EI}{L^3(1+\Phi)} & 0 & 0 & 0 & \frac{6EI}{L^2(1+\Phi)} & 0 & -\frac{12EI}{L^3(1+\Phi)} & 0 & 0 & 0 & \frac{6EI}{L^2(1+\Phi)} \\
0 & 0 & \frac{12EI}{L^3(1+\Phi)} & 0 & -\frac{6EI}{L^2(1+\Phi)} & 0 & 0 & 0 & -\frac{12EI}{L^3(1+\Phi)} & 0 & -\frac{6EI}{L^2(1+\Phi)} & 0 \\
0 & 0 & 0 & \frac{GJ}{L} & 0 & 0 & 0 & 0 & 0 & -\frac{GJ}{L} & 0 & 0 \\
0 & 0 & -\frac{6EI}{L^2(1+\Phi)} & 0 & \frac{(4+\Phi)EI}{L(1+\Phi)} & 0 & 0 & 0 & \frac{6EI}{L^2(1+\Phi)} & 0 & \frac{(2-\Phi)EI}{L(1+\Phi)} & 0 \\
0 & \frac{6EI}{L^2(1+\Phi)} & 0 & 0 & 0 & \frac{(4+\Phi)EI}{L(1+\Phi)} & 0 & -\frac{6EI}{L^2(1+\Phi)} & 0 & 0 & 0 & \frac{(2-\Phi)EI}{L(1+\Phi)} \\
-\frac{EA}{L} & 0 & 0 & 0 & 0 & 0 & \frac{EA}{L} & 0 & 0 & 0 & 0 & 0 \\
0 & -\frac{12EI}{L^3(1+\Phi)} & 0 & 0 & 0 & -\frac{6EI}{L^2(1+\Phi)} & 0 & \frac{12EI}{L^3(1+\Phi)} & 0 & 0 & 0 & -\frac{6EI}{L^2(1+\Phi)} \\
0 & 0 & -\frac{12EI}{L^3(1+\Phi)} & 0 & \frac{6EI}{L^2(1+\Phi)} & 0 & 0 & 0 & \frac{12EI}{L^3(1+\Phi)} & 0 & \frac{6EI}{L^2(1+\Phi)} & 0 \\
0 & 0 & 0 & -\frac{GJ}{L} & 0 & 0 & 0 & 0 & 0 & \frac{GJ}{L} & 0 & 0 \\
0 & 0 & -\frac{6EI}{L^2(1+\Phi)} & 0 & \frac{(2-\Phi)EI}{L(1+\Phi)} & 0 & 0 & 0 & \frac{6EI}{L^2(1+\Phi)} & 0 & \frac{(4+\Phi)EI}{L(1+\Phi)} & 0 \\
0 & \frac{6EI}{L^2(1+\Phi)} & 0 & 0 & 0 & \frac{(2-\Phi)EI}{L(1+\Phi)} & 0 & -\frac{6EI}{L^2(1+\Phi)} & 0 & 0 & 0 & \frac{(4+\Phi)EI}{L(1+\Phi)}
\end{pmatrix} \tag{37}
$$

$$
\tilde{\mathbf{K}}_G^i = \frac{T}{L}\begin{pmatrix}
0 & 0 & 0 & 0 & 0 & 0 & 0 & 0 & 0 & 0 & 0 & 0 \\
0 & \frac{1.2+2\Phi+\Phi^2}{(1+\Phi)^2} & 0 & 0 & 0 & \frac{L}{10(1+\Phi)^2} & 0 & -\frac{1.2+2\Phi+\Phi^2}{(1+\Phi)^2} & 0 & 0 & 0 & \frac{L}{10(1+\Phi)^2} \\
0 & 0 & \frac{1.2+2\Phi+\Phi^2}{(1+\Phi)^2} & 0 & -\frac{L}{10(1+\Phi)^2} & 0 & 0 & 0 & -\frac{1.2+2\Phi+\Phi^2}{(1+\Phi)^2} & 0 & -\frac{L}{10(1+\Phi)^2} & 0 \\
0 & 0 & 0 & \frac{J}{Ax} & 0 & 0 & 0 & 0 & 0 & -\frac{J}{A_x} & 0 & 0 \\
0 & 0 & -\frac{L}{10(1+\Phi)^2} & 0 & \frac{L^2(8+10\Phi+5\Phi^2)}{60(1+\Phi)^2} & 0 & 0 & 0 & \frac{L}{10(1+\Phi)^2} & 0 & -\frac{L^2(2+10\Phi+5\Phi^2)}{60(1+\Phi)^2} & 0 \\
0 & \frac{L}{10(1+\Phi)^2} & 0 & 0 & 0 & \frac{L^2(8+10\Phi+5\Phi^2)}{60(1+\Phi)^2} & 0 & -\frac{L}{10(1+\Phi)^2} & 0 & 0 & 0 & -\frac{L^2(2+10\Phi+5\Phi^2)}{60(1+\Phi)^2} \\
0 & 0 & 0 & 0 & 0 & 0 & 0 & 0 & 0 & 0 & 0 & 0 \\
0 & -\frac{1.2+2\Phi+\Phi^2}{(1+\Phi)^2} & 0 & 0 & 0 & -\frac{L}{10(1+\Phi)^2} & 0 & \frac{1.2+2\Phi+\Phi^2}{(1+\Phi)^2} & 0 & 0 & 0 & -\frac{L}{10(1+\Phi)^2} \\
0 & 0 & -\frac{1.2+2\Phi+\Phi^2}{(1+\Phi)^2} & 0 & \frac{L}{10(1+\Phi)^2} & 0 & 0 & 0 & \frac{1.2+2\Phi+\Phi^2}{(1+\Phi)^2} & 0 & \frac{L}{10(1+\Phi)^2} & 0 \\
0 & 0 & 0 & -\frac{J}{Ax} & 0 & 0 & 0 & 0 & 0 & \frac{J}{A_x} & 0 & 0 \\
0 & 0 & -\frac{L}{10(1+\Phi)^2} & 0 & -\frac{L^2(2+10\Phi+5\Phi^2)}{60(1+\Phi)^2} & 0 & 0 & 0 & \frac{L}{10(1+\Phi)^2} & 0 & \frac{L^2(8+10\Phi+5\Phi^2)}{60(1+\Phi)^2} & 0 \\
0 & \frac{L}{10(1+\Phi)^2} & 0 & 0 & 0 & \frac{L^2(2+10\Phi+5\Phi^2)}{60(1+\Phi)^2} & 0 & -\frac{L}{10(1+\Phi)^2} & 0 & 0 & 0 & -\frac{L^2(8+10\Phi+5\Phi^2)}{60(1+\Phi)^2}
\end{pmatrix} \tag{38}
$$

where,

$$
T = EA\frac{(u_4 - u_1)}{L} \tag{39}
$$

$$
\Phi = 24(1+\vartheta)(\frac{A^2}{\pi L^2}) \tag{40}
$$

For small deformation and in the absence of rigid body motion, the geometric elemental matrix would approach zero since $u_1 \ll 1$ and $u_4 \ll 1$. However, with larger deformations, $u_4 - u_1$ (which shows longitudinal deformation of the beam) would increase and augment a geometric stiffness to the global stiffness.

The global stiffness matrices were assembled by adding the corresponding terms of $\tilde{\mathbf{K}}_G^i$ and $\tilde{\mathbf{K}}_G^i$ for each DoF in a 600×600 matrix. In the implementation, each PSO thread had a dedicated FEM solver. In each solver, $\boldsymbol{\delta}\tilde{\mathbf{f}}_{\text{FEM}}$ started from zero and linearly increased in 20 iterations to the force of interest determined by the PSO thread. At the end of the iterations the total displacement of the nodes were obtained through the summation of all the displacement increments in the iterations:

$$\tilde{\mathbf{u}}_{\text{FEM}} = \sum_j {}^j\boldsymbol{\delta}\tilde{\mathbf{u}}_{\text{FEM}}, \tag{41}$$

and $\mathbf{u}_{\text{FEM}}$ was constructed by compiling the deformed nodal positions to be used in Eq. 33.

3.2.9 Solver Verification

To verify the accuracy of the developed FEM solver for beam deflection, three 6-Fr (1 Fr=$1/3$ mm) catheters with flexural rigidities of 3000 Nmm^2 (super stiff), 750 Nmm^2 (stiff), and 200 Nmm^2 (soft) were studied. The geometrical specifications of the catheters are provided in Fig. 3.8(a). Each catheter was solved for three different load cases: (1) concentrated shear force at the tip, uniform shear force, and two concentrated forces perpendicular to the beam at the tip and mid-span. Fig. 3.8(a) depicts the load cases. Afterward, the results of the developed solver were compared with a commercial FEM software (Ansys R17.0, PA, USA). Fig 3.8(b) compares the deformed shape of the beams from the developed solver and the commercial software. In addition, Table 3.1 compares the maximum vertical deflection, total strain energy, and computation time of the simulation for the soft catheter (worst-case scenario) for the developed solver and Ansys.

The post-processing showed that the results of the developed FEM solver were in fair agreement with the results of the commercial software for the load cases tests. The mean relative difference

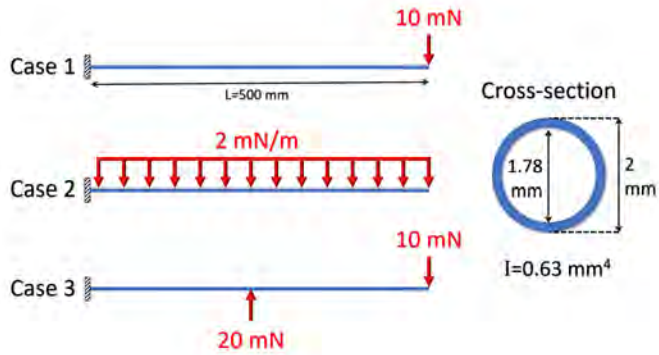

(a)

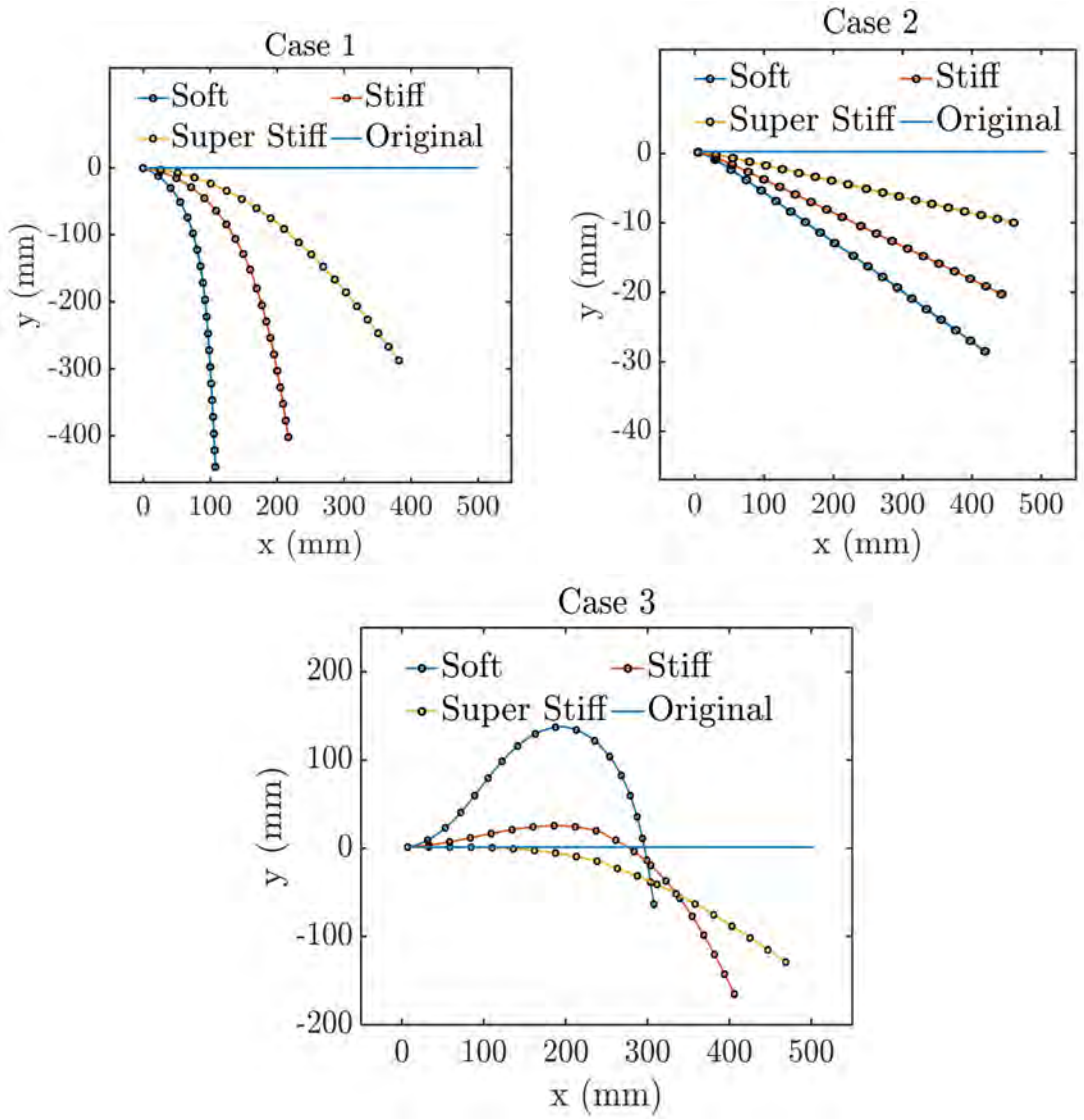

(b)

Figure 3.8: (a) Schematic of the simulated catheter with three load cases, (b) comparison of the shape of the deformed catheter from the developed FEM solver and Ansys R17.0 for three loading scenarios.

Table 3.1: Comparison of the results of the developed FEM solver with Ansys R17.0 for three load cases.

	Case 1		Case 2		Case 3		Mean Difference
	Solver	Ansys	Solver	Ansys	Solver	Ansys	(%)
Maximum Deflection (mm)	-448.1	-457.3	-27.3	-27.6	135.7	136.9	-1.3%
Total Strain Energy (mJ)	2.2	2.3	8×10^{-3}	8×10^{-3}	1.7	1.8	-2.9%
Computation Time (ms)	7	313	2	25	5	261	-95.8%

in the solver results for maximum deflection was 1.29% and was 2.67% for the total strain energy. Also, the results showed that the developed FEM solver was 95.67% faster than the commercial software. The superior performance of the developed software might be related to the utilization of GPU-accelerated libraries for linear algebra and the fact that Ansys uses multiple preamble libraries for data storage and graphical user interface that occupy memory and diminish the performance.

3.2.10 Parameter Identification

The parameters incorporated in the model were the elastic modulus, E, cross-sectional area, A, second moment of cross-sectional area, I, and the Poisson's ratio, ϑ of the catheter. Since the catheters used in this study (RunWay 6Fr, Boston Scientific, MA, USA) were made of metal-braided body, the Poisson's ratio was set to 0.395 as the average of 0.3, commonly used for metals, and 0.49, commonly used for incompressible elastomers.

Moreover, a similar catheter was cut into three samples of 100 mm length for diameter measurement and three-point bending test (3PB), as per ISO 14125 standard [220]. The 3PB test was performed using a universal testing machine (ElectroForce 3200, TA Instruments, DE, USA) with a vertical displacement rate of 20 $^{\mathrm{mm}}/_{\mathrm{min}}$.

Fig. 3.9(a) and (b) show a sample of the catheter under 3PB test and the force-displacement curve of the three samples, respectively. Table 3.2 summarizes the model parameters as used in the solution. In clinical practice, a look-up table of various catheter s may be populated in the software and parameters automatically get set when the operator selects a specific catheter.

Table 3.2: Summary of the measured and set values of the model parameters for RunWay 6Fr catheter (n=3).

Parameter	Method/Definition	Measured value	Set value
A (mm^2)	$\frac{\pi}{4}$(OD^2-ID^2)	OD=2.14 ± 0.17 mm ID=1.85 ± 0.23 mm	2.14
I (mm^4)	$\frac{\pi}{64}$(OD^4-ID^4)	OD=2.14 ± 0.17 mm ID=1.85 ± 0.23 mm	0.45
E (MPa)	$k\frac{\sigma^3}{48I}$	$k = 0.0671 \pm 0.0023$ N/mm	1592.3
ϑ	-	-	0.395

OD: outer diameter — $\sigma = 80$mm: the span of the 3PB test jig
ID: inner diameter — k : flexural stiffness- the slope of force-displacement curve

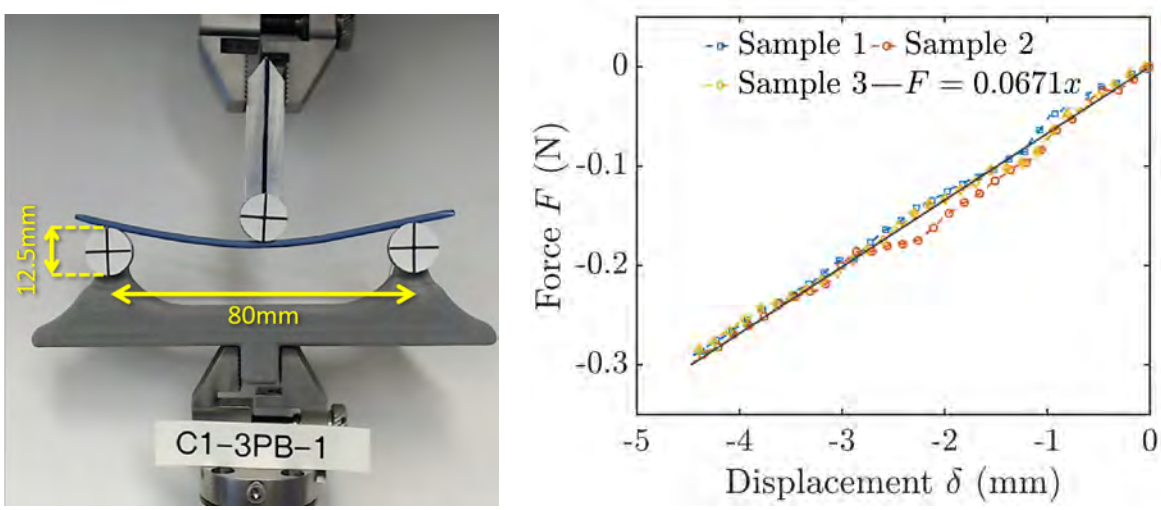

(a) (b)

Figure 3.9: (a) a sample of the catheter under the three-point bending test, (b) force-displacement curves of the three samples under three-point bending test.

3.3 Validation Studies

For the validation of the proposed force localization and estimation method, two studies were performed. The objective of the first study was to investigate the accuracy of the proposed methods on simulated deformed shapes of the catheter. The location and magnitude of the external forces on the simulated catheters were used as the reference to assess the performance of the proposed methods. The objective of the second study was to investigate the performance of the proposed methods on planar deflections of the catheter. Planar deflections of the endovascular catheter usually happen during the intervention of peripheral arteries, e.g., hands and legs, and parts of the cerebral vessels, e.g., neck and parietal arteries. The accurate position and magnitude of the external forces were measured using film force sensors and were used as references for comparison.

3.3.1 Study I: Simulation-based Validation

In Study I, sixteen load cases were simulated in Ansys R17.0 and the image of the deformed shape of the catheter was used for force localization and estimation. To this end, model parameters in Table 3.2 were used for the FEM simulations. The external forces in the load cases were in the range of reported RCI forces in the literature, i.e., less than 0.3 N [62]. Fig. 3.10(a) shows the schematic of the simulated load cases with a representative force. In the simulated load cases, multiple forces at various locations were simulated with 2D and 3D distributions. The details of the load cases are provided in Table 3.3. Fig. 3.10(b) shows deformed shapes of the catheter for four load cases. The catheters were segmented and their spatial curvature were extracted using the method provided in Sec. 3.2.3. Afterward the location of the external forces were identified using the force indicator Ω (Eq. 31) applied on the results of the FEM simulations. Fig. 3.11 shows representative Ω-s for load cases 1 to 4.

The results showed that in all cases, Ω had indicated an initial singularity at the neighborhood of $s = 0$. The reason for that was related to the interpolation inaccuracy at the proximity of $s = 0$. This phenomenon was not remedied in this study as its effect was limited to $s \leq 0.1$. Nevertheless, computational constraints such as tangency enforcement algorithm [210] could be used to avoid it. A promising finding in Study I was that Ω was fairly accurate in localizing the external force at the

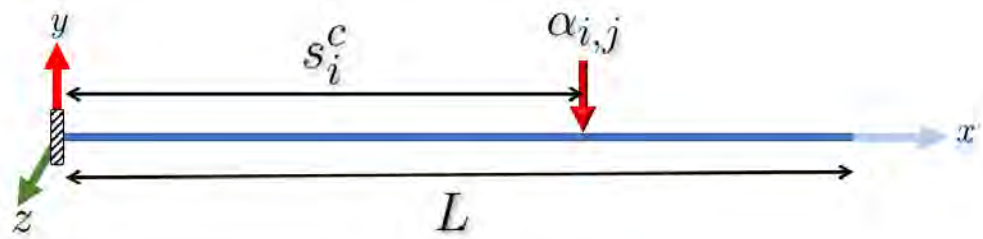

(a)

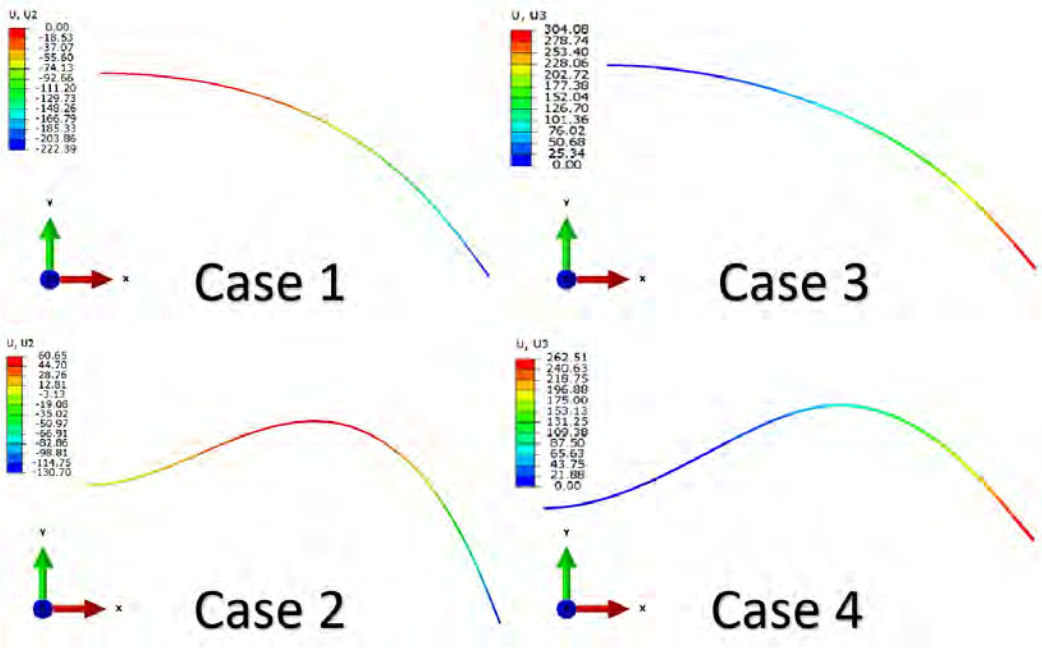

(b)

Figure 3.10: (a) Schematic of the simulated load cases with a representative force and (b) deformed shape of the catheter for four load cases.

Table 3.3: Simulated load cases for Study I.

No.	L (mm)	E (MPa)	2D/3D	Force locations	Force magnitudes (mN)
1	500	6600	2D	$s^{\text{Tip}} = 1$	$f_2^{\text{Tip}} = -15$
2				$s^{\text{Tip}} = 1$, $s_1^c = 0.5$	$f_2^{\text{Tip}} = -15$, $\alpha_{2,1} = 30$
3			3D	$s^{\text{Tip}} = 1$	$f_2^{\text{Tip}} = -15$, $f_3^{\text{Tip}} = 20$
4				$s^{\text{Tip}} = 1$, $s_1^c = 0.5$	$f_2^{\text{Tip}} = -15$, $f_3^{\text{Tip}} = 20$, $\alpha_{2,1} = 30$, $\alpha_{3,1} = -10$
5		1600	2D	$s^{\text{Tip}} = 1$	$f_2^{\text{Tip}} = -15$
6				$s^{\text{Tip}} = 1$, $s_1^c = 0.5$	$f_2^{\text{Tip}} = -15$, $\alpha_{2,1} = 30$
7			3D	$s^{\text{Tip}} = 1$	$f_2^{\text{Tip}} = -15$, $f_3^{\text{Tip}} = 20$
8				$s^{\text{Tip}} = 1$, $s_1^c = 0.5$	$f_2^{\text{Tip}} = -15$, $f_3^{\text{Tip}} = 20$, $\alpha_{2,1} = 30$, $\alpha_{3,1} = -10$
9	200	6600	2D	$s^{\text{Tip}} = 1$	$f_2^{\text{Tip}} = -15$
10				$s^{\text{Tip}} = 1$, $s_1^c = 0.5$	$f_2^{\text{Tip}} = -15$, $\alpha_{2,1} = 30$
11			3D	$s^{\text{Tip}} = 1$	$f_2^{\text{Tip}} = -15$, $f_3^{\text{Tip}} = 20$
12				$s^{\text{Tip}} = 1$, $s_1^c = 0.5$	$f_2^{\text{Tip}} = -15$, $f_3^{\text{Tip}} = 20$, $\alpha_{2,1} = 30$, $\alpha_{3,1} = -10$
13		1600	2D	$s^{\text{Tip}} = 1$	$f_2^{\text{Tip}} = -15$
14				$s^{\text{Tip}} = 1$, $s_1^c = 0.5$	$f_2^{\text{Tip}} = -15$, $\alpha_{2,1} = 30$
15			3D	$s^{\text{Tip}} = 1$	$f_2^{\text{Tip}} = -15$, $f_3^{\text{Tip}} = 20$
16				$s^{\text{Tip}} = 1$, $s_1^c = 0.5$	$f_2^{\text{Tip}} = -15$, $f_3^{\text{Tip}} = 20$, $\alpha_{2,1} = 30$, $\alpha_{3,1} = -10$

midspan. For example, for 2D deformation with force at the midspan (Case 2) the peak of singularity in Ω was at $s = 0.52$ while the external force was at $s_1^c = 0.5$. Similarly for the 3D deformation (Case 4), Ω localized the force at $s = 0.47$ while the reference force was at $s_1^c = 0.5$. A similar trend was observed for all load cases. The mean-absolute error (MAE) of the force localization in 2D cases (n=8) was 0.027 ± 0.008 mm (5.4%) and for 3D cases (n=8) was 0.043 ± 0.013 mm (8.6%). Wilcoxon's signed-rank test with a 5% confidence interval ($p < 0.05$) showed no significant difference between the error of force localization in 2D and 3D cases ($p = 0.00128$).

Another finding was that Ω possessed larger values for 3D deformations, especially near the singularity. The reason might have been due to the superposition of singularity in κ_n and κ_g which both have had singularities at the force locations. In addition, the MAE of force estimation for 2D cases (n=8) was 1.03 ± 0.47 mN (6.8%) at the tip and 2.41 ± 0.33 (8%) at the mid-span while the MAE for the 3D cases (n=8) was 1.07 (7.1%) 3.31 ± 0.74 (11%) at the mid-span. Wilcoxon's signed rank test with a 5% confidence interval ($p < 0.05$) confirmed significant difference between the error of force estimation in 3D cases ($p = 0.218$).

The average computational time for force localization and estimation was 17 ± 5 ms in 2D cases and 41 ± 7 ms in 3D cases which corresponds to minimum refresh rates of 45Hz (2D cases) and 20Hz

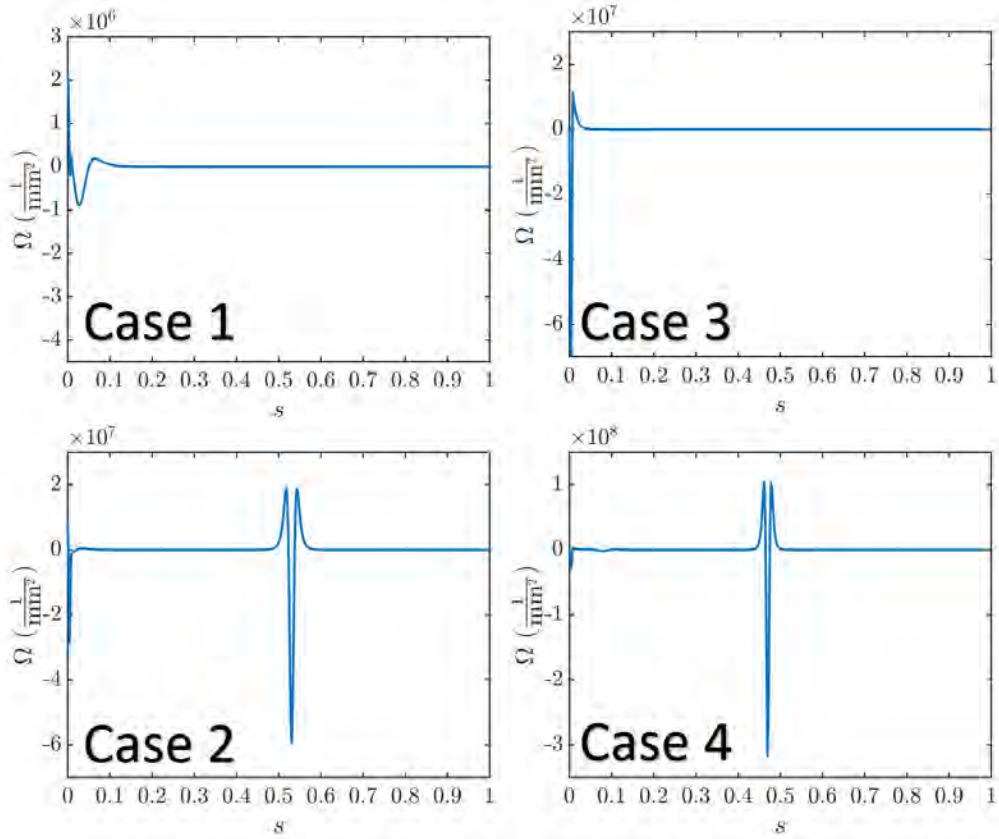

Figure 3.11: Variation of the force indicator for load cases 1 to 4.

(3D cases). Despite the accuracy of force localization and in spite of using simulated deformation images, that were artifact-free, the refresh rate of the proposed method for 3D cases was below the requirements for real-time applications, i.e., 25-30Hz. The main bottleneck of the 3D analysis was matrix inversion that was frequently performed within the PSO optimizer.

3.3.2 Study II: Force Localization and Estimation with Planar Deformation

In study II, the performance of the proposed method for 2D deformations of the catheter were experimentally investigated. To this end, two sets of experiments were performed.

In the first experiment, the image streams of the 100mm-long catheter samples were used to perform force localization and estimation in real-time. In the second experiment, a 3D printed planar vascular model equipped with four force-sensing linear potentiometer (FSLP) (FSLP-2730, Polulu, NV, USA) was used for cannulation. A catheter was inserted into the sensor-equipped vascular model for five repetitions while iFEM was run in parallel to image-acquisition. The FSLPs were calibrated in-house using a 3D printed housing for the forces in the range of 0 to 3 N. The output voltage of each FSLP was linearly proportional to the magnitude and location of the applied force. Eq. 42 shows the multi-linear regression calibration matrix for one of the FSLPs and Fig. 3.12 depicts the calibration verification results for forces in the range of 0 to 3 N. The calibration verification showed that the MAE of the position sensing for four FSLPs was 0.89 ± 0.21 mm (0.89%) and the MAE of force sensing was 0.018 ± 0.014 N (0.6%). FSLP data were acquired using an Arduino MEGA 2560 embedded system.

$$\begin{pmatrix} d_{\text{FSLP}} \\ f_{\text{FSLP}} \end{pmatrix} = \begin{pmatrix} -0.106 & 20.47 \\ 0.956 & 0.363 \end{pmatrix} \begin{pmatrix} v_1 \\ v_2 \end{pmatrix} + \begin{pmatrix} -0.366 \\ -1.905 \end{pmatrix} \tag{42}$$

Fig. 3.13(a) shows the experimental setup used for the first experiment with a checkerboard camera calibration template, Fig. 3.13(b) shows the calibration setup for FSLPs, and Fig. 3.13(c) depicts the experimental setup for validation of 2D force localization and estimation with FSLPs.

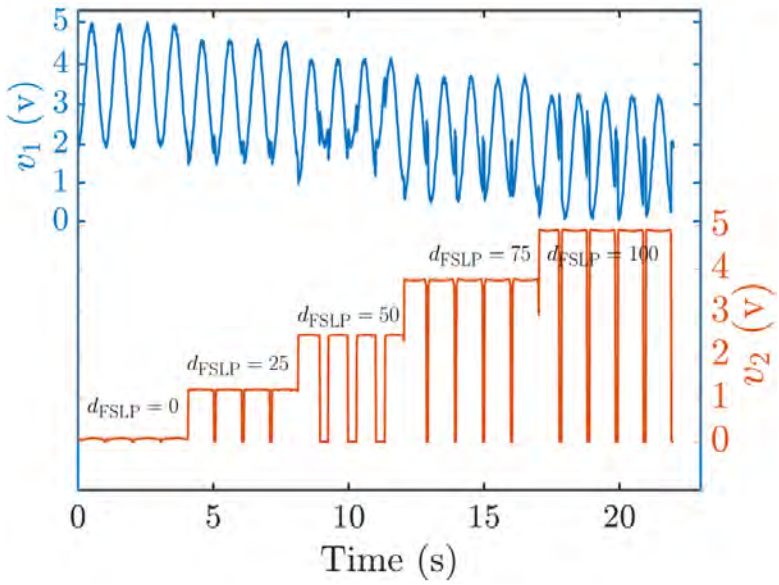

(a)

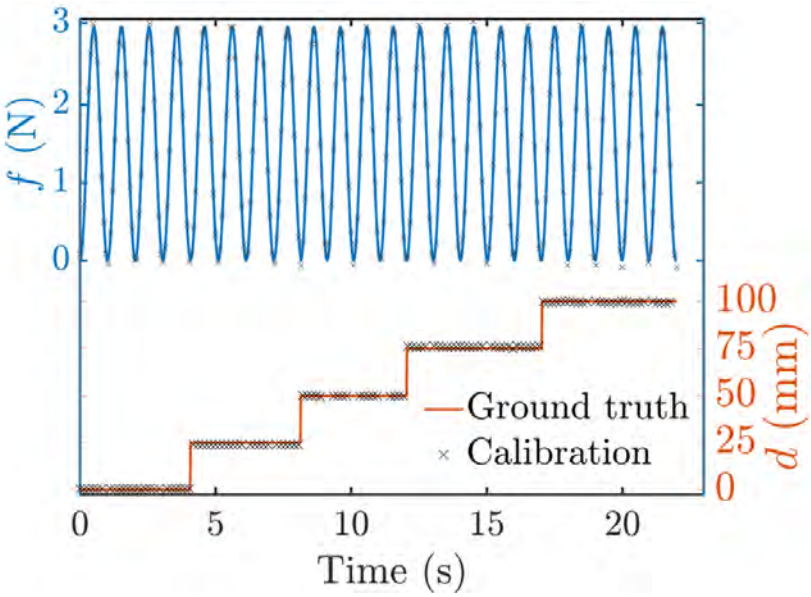

(b)

Figure 3.12: (a) Variation of output voltages of the FSLPs during the calibration test with input force of 0 to 3 N and at $d_{\text{FSLP}} = 0$ to 100 mm, and (b) results of calibration verification and comparison with the ground truth force and location.

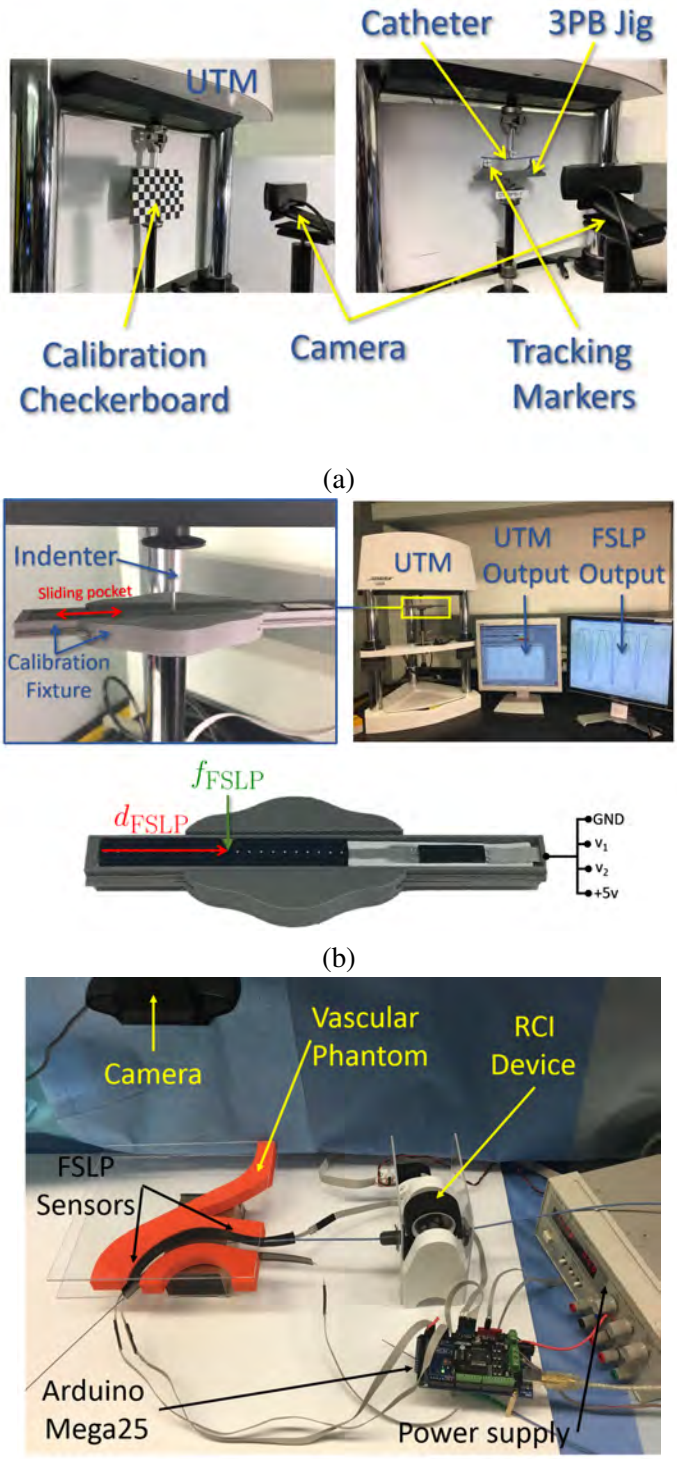

Figure 3.13: Experimental setup used in Study II in (a) 3PB tests, (b) FSLP calibration, and (c) force localization and estimation with FSLPs validation.

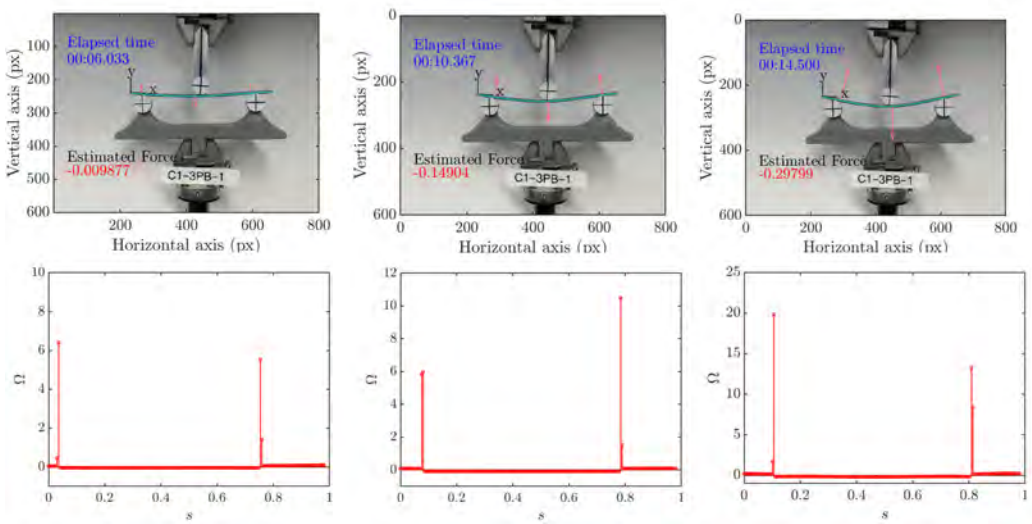

Figure 3.14: Representative snapshots of the output of the iFEM force estimation for 3PB test images and their corresponding force indicators.

Fig. 3.14 shows the result of force localization and estimation on the 3PB test frames with the localized force vectors augmented on the original frames. Also, Fig. 3.15 compares the iFEM estimated mid-span force with the ground truth (UTM output). It is noteworthy that in order to perform the force estimation on the 3PB test images, the sample was assumed as two cantilever beams fixed together at the base and spanning toward left and right. The point of the fixture (of the two beams) was identified at the minimum point of the deflected catheter in each frame. Thus, two parallel force estimation PSO optimizers were used for the left and right beams.

The average computation time per frame for force estimation on the 3PB images was 21 ± 3 ms (refresh rate of 47 Hz) which was slightly more than the computation time of Study I for 2D cases. The reason was due to more time spent on catheter segmentation in 3PB tests. For force localization, the proposed method had a limitation in detecting the force locations for forces less than 0.01 N, however above that the accuracy of force localization increased with larger deflection of the catheter sample. Fig. 3.15(b) shows the variation of the detected forces on the left and right with time.

The MAE of force localization (combined for left and right forces) was 6.7 ± 2.3 mm (6.7% of the length). Furthermore, the MAE of iFEM for force estimation was 0.023 ± 0.017 N with bounded variation around the 10-point moving average of the estimated force. The observed variation was

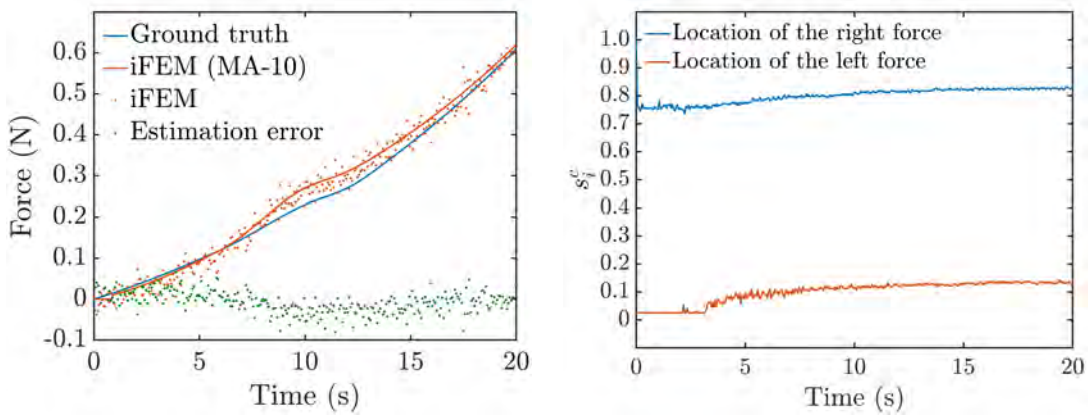

(a) (b)

Figure 3.15: (a) Comparison of the iFEM estimated mid-span force with ground truth for 3PB test, and (b) variation of the position of the identified forces on the catheter sample.

attributed to the flicker of the camera and residual error of the PSO optimization.

Fig. 3.16 shows snapshots of the catheter inserted into the 3D printed planar vascular model with their corresponding Ω-s and localized forces. Also, Fig. 3.17(a–b) depict the measured forces locations with each FSLP and their corresponding contact forces. Also, Fig. 3.17(c–d) compares the estimated total insertion force (iFEM) with the ground truth and distribution of the estimation error, respectively. The total insertion force was estimated as the resultant force of the contact forces and their corresponding frictions along $\mathbf{d}_1$ (tangent to the body of the catheter). The coefficient of friction of the catheter with the surfaces of the FSLPs was 0.617, identified empirically.

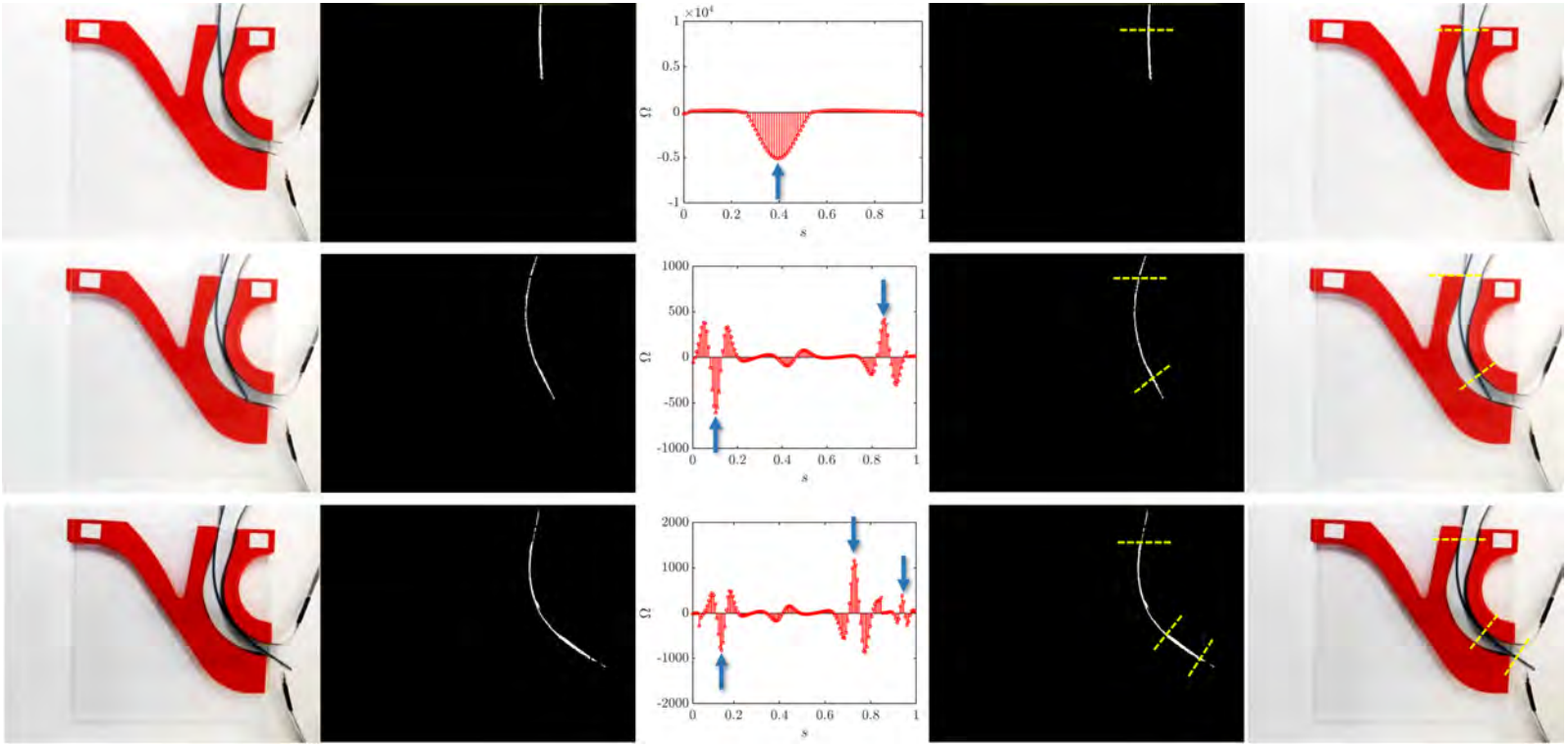

Figure 3.16: Result of force localization on the catheter with planar vascular model.

The average computation time per frame for this experiment was 23 ± 7 ms (refresh rate of 43 Hz) which was in compliance with the requirements of RCI applications, i.e. 25-30Hz. Also, it was observed that the estimated insertion force fairly followed the ground truth in all five repetitions. However, there was a minimum detectable contact force of 0.020 ± 0.011 N, below which the iFEM could not accurately estimate the insertion force. Compared to the insertion forces reported in the literature for RCI applications, i.e., up to 0.3 N, this minimum detectable force would relate to a 7.6% (of full-scale) lower-limit. Another phenomenon observed in the experiments was the occurrence of a whiplash effect. Whiplashes were identified as fast joggings of the catheter off of the vascular walls due to fast catheter insertions and frictional stick-slip of the catheter on the FSLP surfaces. Such whiplashes are not likely to happen during real surgical procedures due to typically slow catheter manipulations and small friction between catheters and vascular surfaces.

In two repetitions (of five) whiplash effects were observed. During the whiplash period (≈ 0.5 s) iFEM has failed to accurately estimate the forces. The reason was that the whiplash effect was a highly dynamic motion (with non-negligible acceleration), thus iFEM has failed to capture it because of its quasi-static formulation. Also, toward the end of three repetitions (of five), the distal contact point of the catheter with the vascular model passed the surface of FSLP-2 which resulted in inaccurate total reference force measurement.

For error analysis, the data in the whiplash period and those acquired while the distal contact point passed FSLP-2 were excluded from the dataset. However, the data related to the non-detected contact forces (< 0.021 N) were included in the analysis. The error analysis showed that the MAE of contact localization was 6.7 ± 1.9 mm while it was 0.020 ± 0.009 N (9.5% of maximum force) for insertion force estimation. Also, Wilcoxon's signed-rank test with $(p < 0.05)$ on five repetitions (total n=778 samples) showed no significant difference between the estimated force and reference force ($p = 0.01476$). In addition, the distribution of error for the pooled errors showed that the median error was 0.007 with a Gaussian distribution with a spread of 0.018 N. This indicates that more than 95% of the data points had an absolute error of less than 0.036 N (11.45% of maximum force).

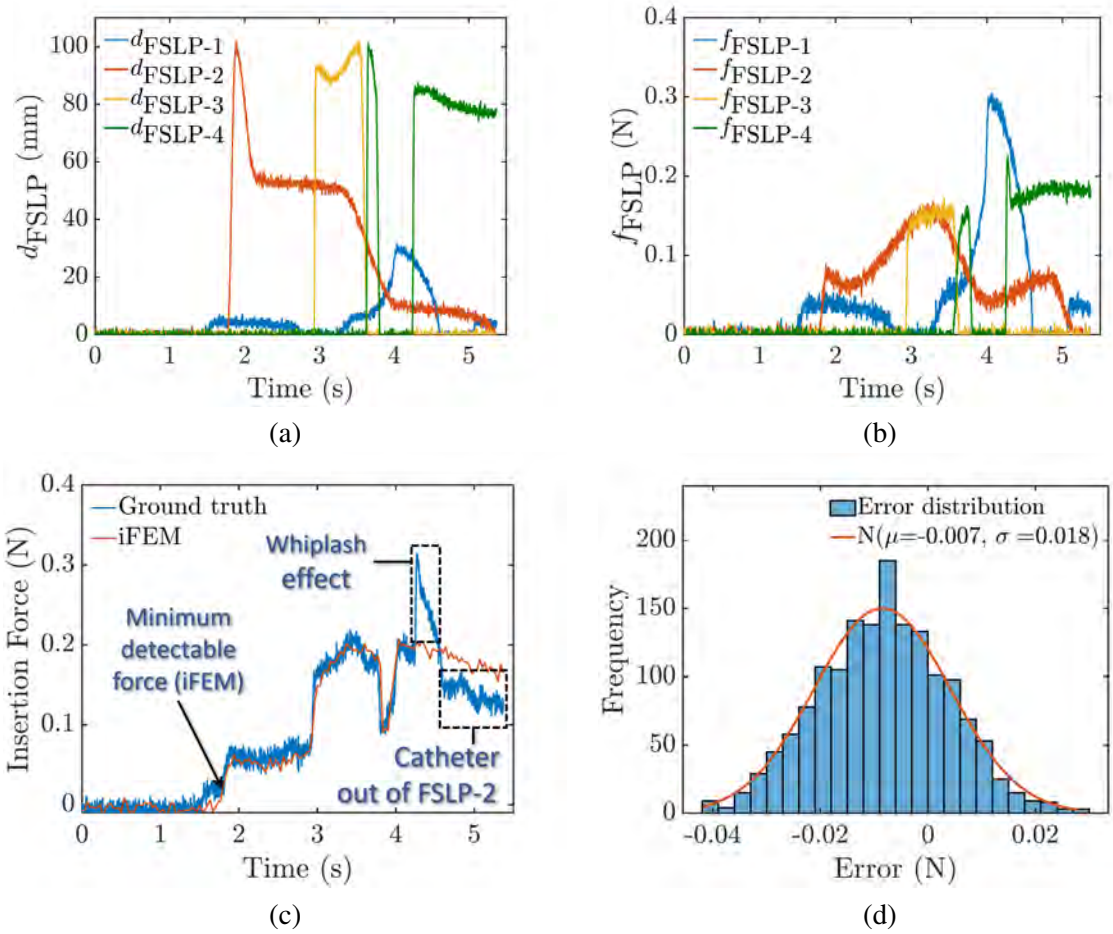

Figure 3.17: Representative data from the second validation experiment in Study II: (a) contact force locations, (b) contact force magnitudes measured with FSLPs, (c) comparison of the total insertion force estimated with iFEM and ground truth, and (d) distribution of error of iFEM estimations.

3.3.3 Study III: Force Estimation with Spatial Deformation

In the third validation study, a surgeon-patient RCI setup was used for investigating the performance of the proposed force estimation method for haptic provision with an RCI system. To this end, an experimental setup with a surgeon unit and a patient unit was developed. The patient unit consisted of a 2-DoF RCI robot with rotation and insertion degrees-of-freedom (Fig. 3.18(a)) and a 5-DoF serial arm (Catalyst 5). The components and the design of the RCI robot is depicted in Fig. 3.18(b). The housing of the RCI robot was 3D printed and was anchored to the robotic arm. The arm was used to align the RCI system with the vascular model as shown in Fig. 3.18(a).

Also, the surgeon unit consisted of a graphical user interface (GUI) to display the images relayed from the patient unit and a haptic interface for providing haptic feedback. The GUI was developed in the C# programming language. The haptic feedback was rendered through controlling the electrical current to a DC motor (3242-024CR, Faulhaber GMbH & Co. KG, Switzerland). The nominal torque constant of the selected motor was $k_T = 41.3$ $^{\text{mNm}}/_{\text{A}}$. For controlling the current a proportional-integral (PI-) controller was implemented. The current feedback was acquired using a current sensor (1122, Phidgets Inc., AB, Canada) at a sampling rate of 1 kHz. Fig. 3.18(c) shows the internal structure of the haptic interface. Since the diameter of the roller coupled to the motor was 40 mm, the desired force (from iFEM) was divided by 20mm (radius of the roller) to obtain the desired torque of the DC motor. In addition and for validation purposes, the vascular model was installed on an ATI-Mini force sensor to measure the total insertion force, F_{ATI}, on the vascular model.

Fig. 3.19(a) shows the system integration architecture in Study III. The communication between the patient and master units was established using a user datagram protocol (UDP) over a local wireless network. The average latency of the communication between the patient and surgeon units was 132 ± 11 ms. Based on the literature, latencies up to 300 ms are imperceptible by surgeons in remote RCI procedures [34, 221]. The force estimation was performed using the proposed iFEM method and the resultant total insertion force was relayed to the PI-controller to render haptic feedback accordingly. The details of the controller design and its performance in force tracking are provided in [67]. The author's investigation in [67] showed that the designed force controller could follow the

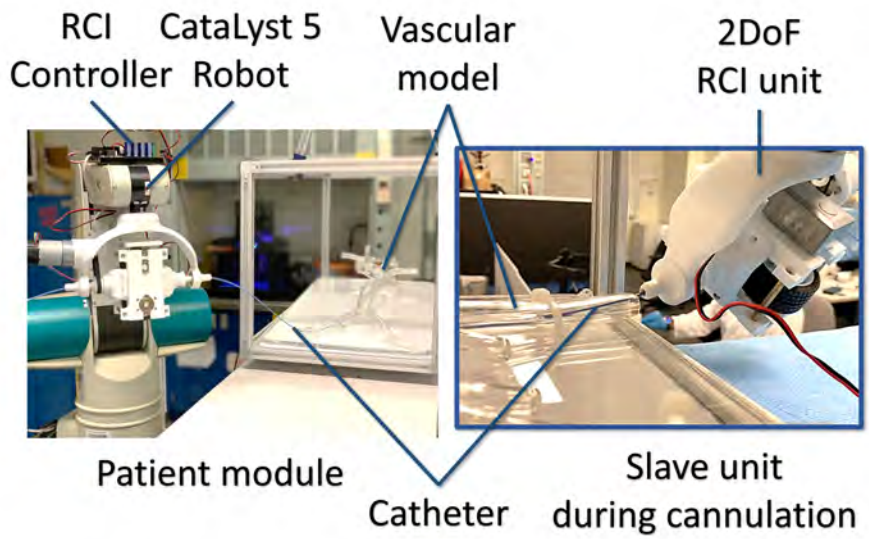

(a)

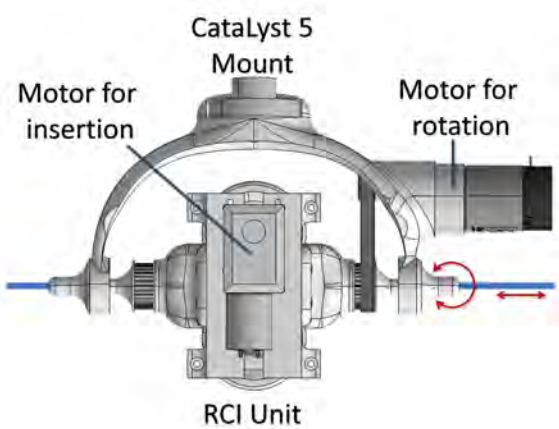

(b)

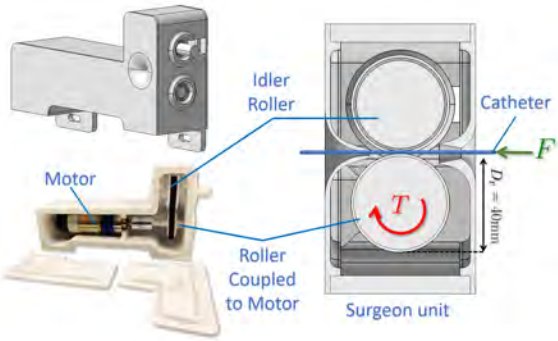

(c)

Figure 3.18: (a) The 2-DoF RCI robot used in Study III, (b) cross-sectional view of the RCI system, and (c) components of the developed haptic interface.

desired force with an MAE of 0.061 ± 0.034 N for dynamic forces up to 0.5 N. Fig. 3.19(b) shows the integrated patient and surgeon units for Study III. Since this study was scoped to investigating the performance of the system, a single-user study was performed. The user was tasked to perform aortic cannulation by inserting the catheter from the femoral artery toward the aortic arch remotely. The user was given 15 minutes to familiarize themself with the system. The user repeated the test five times.

Fig. 3.20 compares the estimated insertion force with the ground truth (F_{ATI}) for the five repetitions. From a qualitative perspective, the estimated forces were in harmony with the ground truth, F_{ATI}. However, iFEM failed to capture the rapid changes in the force, e.g., Repetition 1 and Repetition 5. Such rapid changes were mainly related to the stick-slip friction of the catheter inside the vascular model. However, no major whiplash effect similar to the observed whiplashes in Study II was observed in Study III. Also, it was observed that iFEM has underestimated the total insertion force.

Previously, Rafii *et al.* [42] have shown that the mean force F_{avg}, maximum force F_{max}, force impact over time, FIT, and the number of major peaks in the force NP (above 0.1N), are the statistically significant features (metrics) in the force feedback for the RCI procedures. In addition, the MAE and minimum detectable force F_{min} were used as metrics in this study. The F_{min} metric was defined as the minimum estimated force for which the absolute error of 10-point average of iFEM with respect to F_{ATI} was less than 5% of F_{ATI} for $F_{\text{ATI}} > 0.1N$. For the quantitative analysis, these metrics were compared between the iFEM estimations and ground truth F_{ATI} and were statistically tested using Wilcoxon's signed-rank test with a 5% confidence interval ($p < 0.05$), where possible. Table 3.4 summarizes the comparison of iFEM estimations with the ground truth for five repetitions in Study III.

While the results showed that MAE of iFEM was 7.31% of F_{max} at average for the five repetitions, Wilcoxon's signed-rank test confirmed significant differences between the iFEM and reference measurements. The post-processing showed that the average computation time per frame for all repetitions was 70.4 ms corresponding to a refresh rate of 14 Hz. This computation time was higher than Study I and Study II and was not within the required range for real-time RCI applications, i.e. 25-30 Hz. An implication of the high computation time was in the observed error of iFEM, whereas the iFEM estimations had an accumulated lag over time resulting in the error of asynchrony.

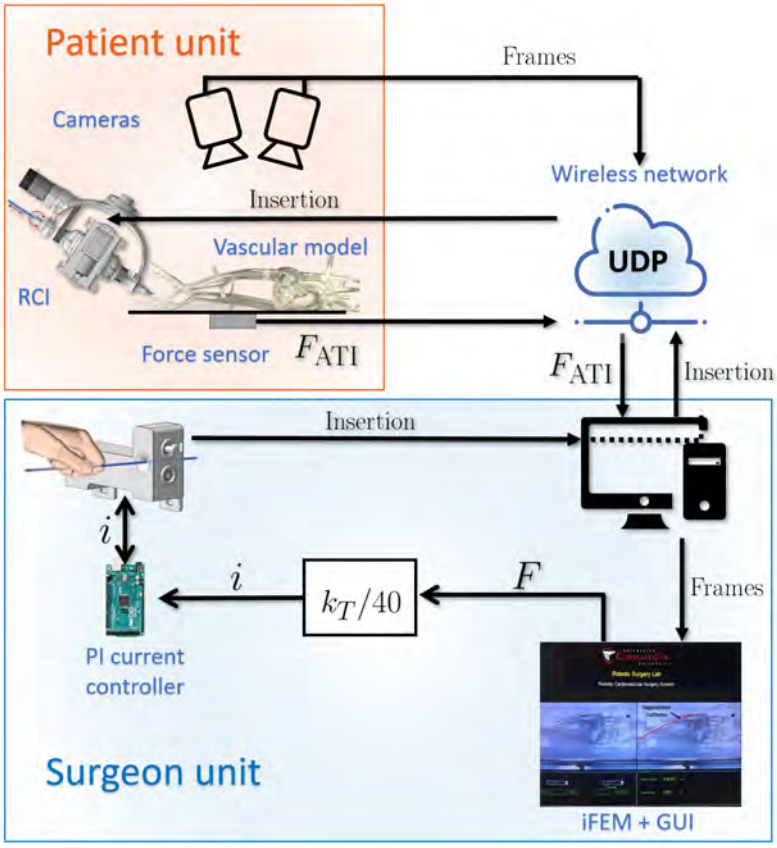

(a)

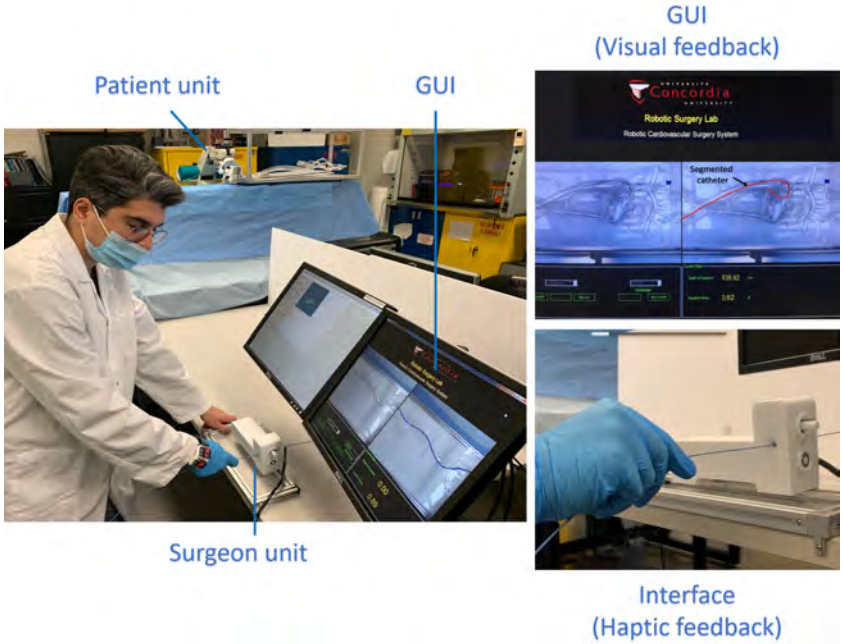

(b)

Figure 3.19: (a) The system integration architecture in Study III and (b) the integrated patient and surgeon units.

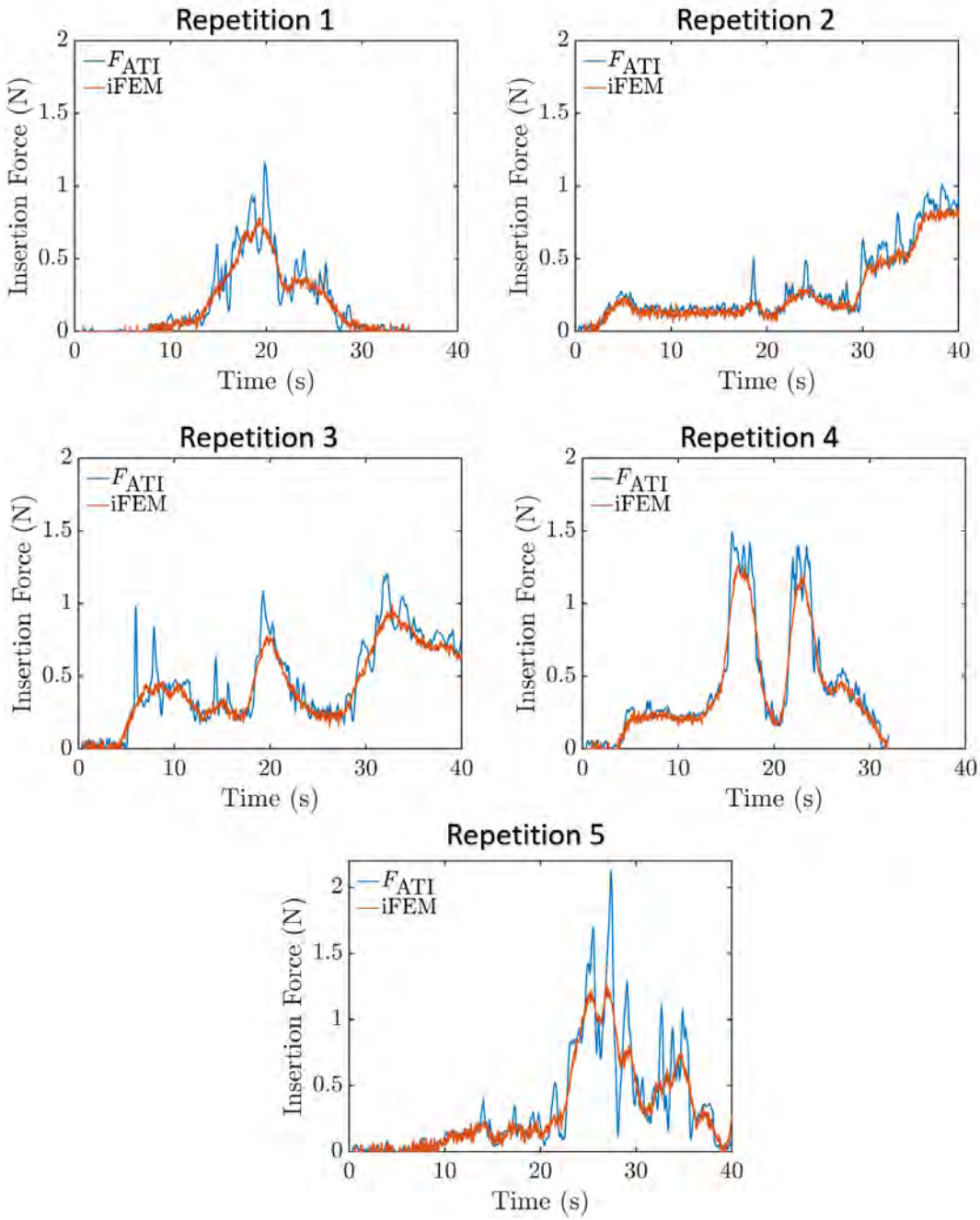

Figure 3.20: Comparison of the estimated total insertion force by iFEM and ground truth in Study III.

Table 3.4: Comparison of the performance metrics of iFEM in Study III for five repetitions.

Metric	Repetition 1		Repetition 2		Repetition 3		Repetition 4		Repetition 5	
	iFEM	F_{ATI}	iFEM	F_{ATI}	iFEM	F_{ATI}	iFEM	F_{ATI}	iFEM	F_{ATI}
Mean Force, F_{avg} (N)	0.179±0.221*	0.199±0.255	0.366±0.214*	0.405±0.2943	0.628±0.255*	0.681±0.295	0.392±0.345*	0.431±0.394	0.283±0.321*	0.316±0.386
Max. Force, F_{max} (N)	0.779*	1.161	0.877*	1.036	0.992*	1.208	1.260*	1.493	1.276*	2.121
MAE, (N)	0.058±0.072*	-	0.062±0.054*	-	0.091±0.088*	-	0.067±0.075*	-	0.097±0.084*	-
Min. Det. Force, F_{min} (N)	0.029	-	0.031	-	0.026	-	0.034	-	0.037	-
No. Peaks, NP	4*	17	6*	15	7*	20	5*	18	14*	22
Force impact, FIT (Ns)	6.064	6.810	10.107	11.578	16.315	17.841	12.456	13.770	13.128	14.738
Computation time ($^{\text{ms}}/_{\text{frame}}$)	65 (15 Hz)	-	69 (15 Hz)	-	75 (13 Hz)	-	72 (14 Hz)	-	66 (15 Hz)	-

*: significant difference was observed between iFEM and F_{ATI} with $p < 0.05$.

The main computational bottleneck for the iFEM was in PSO convergence where more than 78% of the computation time was spent for the PSO optimization. In fact, a maximum of 20×100 iterations (100 PSO iterations with 20 FEM increments in each PSO iteration) were performed for PSO convergence in each frame.

The average minimum detectable force for the five repetitions was 0.031 N (3.1% of F_{max}). In all the repetitions, the minimum detectable force happened fairly early during the procedure. During actual interventions, such small forces are only applied to the catheter at the beginning procedure that the catheter is still in the femur artery. Therefore, the presence of a small minimum detectable force, such as in this study, will not pose a major risk.

3.4 Summary

In this chapter, initially a Bezier-based shape interpolation for catheters was proposed and formulated. Afterward, the kinematics of the deformation of the catheter was derived analytically based on the proposed shape interpolation. Furthermore, the constitutive equations and force balance equations of the catheter were derived based on the differential geometry and continuum mechanics principles. To obtain the unknown forces acting on a deformed catheter with known deformation, an inverse solution based on non-linear finite-element modeling and particle swarm optimization was proposed. In addition, a geometric force indicator was proposed to localize the unknown external forces acting on the catheter. To test the performance of the proposed force localization and estimation method, iFEM, three validation studies were performed. The studies showed that the proposed method was fairly accurate in force estimation and localization for simulated and experimental deformations. In addition, the proposed method was integrated with a haptics-enabled RCI system for aortic cannulation tasks. The proposed integration architecture was modular and showed robustness during the five remote interventions. Despite the accuracy and real-time performance for 2D deformations, the integration study showed that iFEM is computationally expensive for 3D deformations which requires remediation for practical integration.

To address this limitation, an alternative solution for the force estimation inverse problem was developed and validated based on inverse Cosserat Rod model (iCORD). The details of iCORD are provided in the next chapter.

Chapter 4

Real-time Image-based Force Estimation along Endovascular Devices using Inverse Cosserat Rod Model (iCORD) for Robot-assisted Cardiovascular Interventional Surgery

Fast and accurate force estimation is a clinical need for robot-assisted cardiovascular intervention systems, e.g., for enhanced safety or haptic feedback. In this study, an inverse Cosserat rod model was proposed and validated for real-time image-based force estimation on endovascular devices. First, the deformation of conventional endovascular devices was parameterized through 3D Bezier shape modeling. The deformation was used to derive the analytical form of Cosserat rod balance equations. Also, a multi-Gaussian distributed contact force with an unknown number, magnitudes, and loci was used in the balance equations. To find the unknown forces, parallelized particle swarm optimization was used. The accuracy and computational performance of the proposed method were tested in three major interventions on phantom vessels. Mean force, peak force, and force-impact over time were compared between the model estimations and reference data. Wilcoxon signed-rank test with $p<0.05$ revealed no significant difference between the estimations and reference. The proposed method showed accuracy and real-time performance without a dependency on the a-priori knowledge of vascular anatomy.

4.1 Introduction

4.1.1 Background

Endovascular devices (EDs), such as guidewires and catheters, are long and flexible medical devices inserted into the patient's vessels through a small skin incision, i.e., vascular port, to provide minimally invasive access to vessels and heart. To visualize such devices inside the body, continuous X-ray imaging, fluoroscopy, is used. Prolonged hours of X-ray exposure has been shown to be related to skin cancer, cataract, and orthopedic disorders in surgeons [17]. Clinical studies have shown that by using a surgeon–patient robot-assisted cardiovascular intervention (RCI) system, the irradiation to surgeons would decrease by 95% [25]. Recent studies have shown the safety and feasibility of using robot-assisted systems for neurovascular interventions [222, 223] and remote procedures [34, 221, 224].

RCI procedures have shown clinical success in reducing X-ray exposure to surgeons and performing complex procedures. However, the loss of haptic feedback has been reported as the prime technological limitation [17, 62, 225]. The reason for the loss of haptic feedback is that the surgeon uses knobs on a control panel (surgeon module) to control the robot (patient module) to insert and rotate the EDs. Loss of haptic feedback could result in altered situational awareness for the surgeon, over-steering of the devices, and vascular damage, which might cause irreversible sequels for the patient [32, 35].

For example, US FDA's Manufacturer and User Facility Device Experience (MAUDE) system shows that undesirable movements, e.g., MDR 7713735, 7918144, and 6197973, excessive force and kinking of EDs, e.g., MDR 8055503 and 7400392, and over-steering of the control knobs, e.g., MDR 6227199, have been among the adverse events experienced with commercially available RCIs. Although comprehensive post-market surveillance platforms (like MAUDE) are not available worldwide, clinical surveys have emphasized the need for incorporation of haptic feedback in the state-of-the-art RCIs systems, e.g., [32, 62]. The review of the root-cause of the above-mentioned reports suggests that the likelihood of such adverse events could be reduced through the provision of intraoperative haptic feedback [41, 62].

During conventional interventions, the surgeon perceives the distal motion of the ED by cognitive synchronization of the haptic cues (force and motion) from the proximal end of the ED held in hand and the live X-ray [41]. A recent study has shown that the haptic cues are perceived faster than the visual cues by surgeons during interventional surgeries [50]. The haptic cues perceived by the surgeon are contact forces acting on and transferred through the body of the ED and the friction of the ED with the introducer sheath. The latter, however, has been recognized as being undesirable noise and diminishing the haptic cue [41].

4.1.2 Related Studies

To provide surgeons with the force feedback during RCI, researchers have adopted sensor-based and model-based approaches. In a recent literature survey, Hooshiar *et al.* [62] reviewed the approaches and methods for measurement, estimation, and provision of haptic feedback for RCI systems. The survey showed that, despite its higher accuracy, using a sensor, e.g., [226–228], or an array of sensors, e.g., [77], provides limited information about the contact forces on EDs. The reason is that a sensor provides information merely for the sensor-embedded part of the catheter, which might not be adequate to render high-fidelity haptic feedback. As stated earlier, the surgeon's haptic perception depends on the assimilation of total contact forces acting on the catheter.

In addition, embedding a sensor on conventional EDs used for percutaneous cardiovascular (PCI) and neurovascular interventions (NVI), is cumbersome, due to the limitations in size, material, electromagnetic and bio-compatibility, and structural flexibility [229]. Moreover, if the sensor is embedded at the proximal part of the EDs, it would pick up the undesirable noises, e.g., friction with the introducer sheath, which alters the haptic cue [41]. Therefore, a force estimation schema is desirable if it is compatible with conventional EDs and can filter the effect of friction in the insertion force.

As an alternative to the sensor-based force measurement, studies have proposed model-based force estimation schema. Such schema, utilize a shape sensing method, e.g., image-based techniques to obtain the deformation of EDs, e.g., [185, 209]. In such studies, usually a continuous kinematic model for the ED is derived which mathematically expresses the deformed shape of the ED. Afterwards, a dynamic model is solved inversely with optimization techniques to estimate the

unknown forces acted on it [62]. The proposed models in the literature have been mainly based on continuum mechanics [74, 230, 231], multi-body dynamics [51, 232], and differential geometry [156–158, 233]. Such models usually assume simplified deformation forms, such as planar deformation, [71, 73, 74, 230, 231], constant radius bending [172], and piece-wise constant bending catheters [173, 174, 234, 235]. Fig. 4.1 shows the schematic system representation of RCIs with sensor-based and model-based haptic feedback.

Among the modeling approaches, the continuum mechanics-based models produce the most accurate results [62]; however, suffer from the high computational cost and non-unified formulation for small and large deformations of EDs [74]. Comparatively, the multi-body dynamics models are generally computationally efficient and unify large and small deformation formulation; however, require fine geometric discretization to produce physically plausible results for EDs. Such fine geometric discretization may further compromise the computational efficiency. Differential geometry-based models, such as the Cosserat rod model, on the other hand, unify the large and small deformation formulation. Nevertheless, these models rely on the rigorous derivation of a set of nonlinear spatiotemporal partial differential equations to describe the structural behavior of EDs [213, 235–238].

Furthermore, for modeling the deformation of catheters in contact with vasculature, studies have been dependent on *a-priori* knowledge of the vascular anatomy, e.g., [239]. The *a-priori* knowledge of anatomy entails imposing a clinically unnecessary structural scan of vessels, e.g., computational tomography (CT), or magnetic resonance imaging (MRI). To account for the heart motion, real-time non-rigid deformation of the vascular model would be necessary which has a high computational cost and further diminishes the real-time performance of the models. In summary, Table 4.1 provides a comparison between representative studies on mechanical modeling of flexible rods exhibiting large deformation, applicable to EDs. The studies were compared based on their application, modeling approach, theory, solution schema, dimensionality, dependency to *a-priori* CT or MRI, and the use of real-time imaging (shape-sensing).

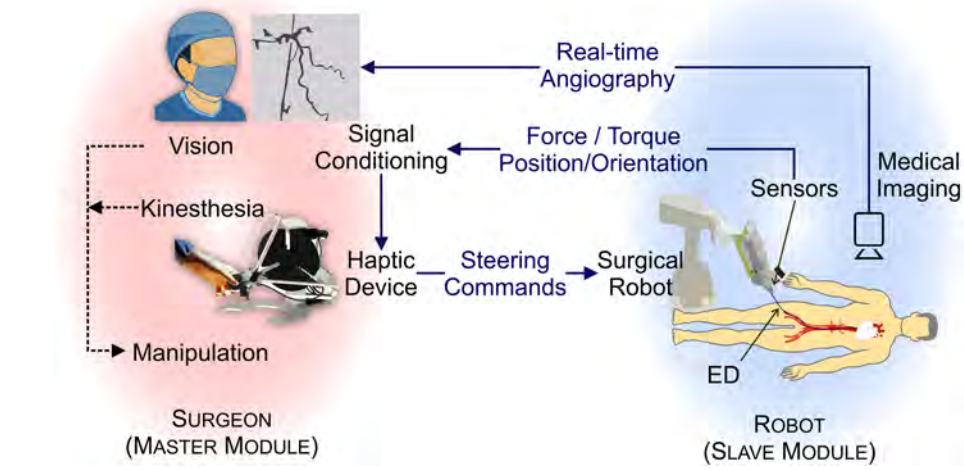

(a)

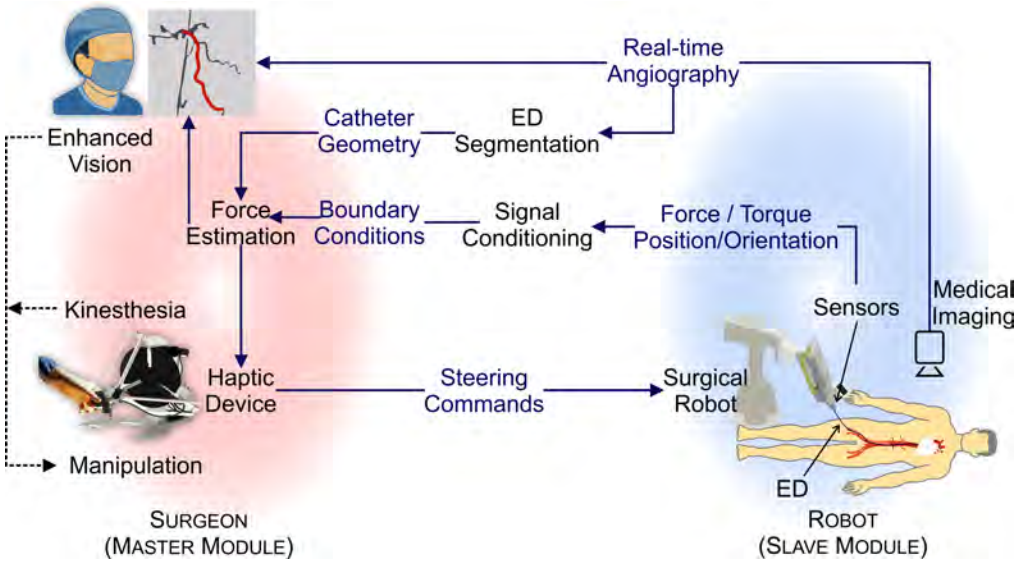

(b)

Figure 4.1: System-level layout of (a) sensor-based and (b) model-based haptics-enabled RCI systems.

Table 4.1: Comparison of representative studies on modeling flexible rods, applicable to force estimation on endovascular devices.

Study	Application	Approach	Theory	Solution	Dimensions	CT/MRI	Markers	Imaging
[157]	Simulation	DG*	Cosserat rod	Explicit integration	3D	✓	×	Simulated
[230]	Force estimation	CM*	Beam theory	Gaussian Mixture Model	2D	×	✓	✓
[231]	Force estimation	MD*	Piecewise circular arc	Newton-Raphson	2D	×	✓	✓
[151]	Simulation	MD	–	Numerical optimization	3D	✓	×	Simulated
[144]	Simulation	MD	Pseudo-rigid body	Numerical optimization	2D	×	×	×
[158]	Simulation	CM	Beam theory	Numerical optimization	3D	✓	×	✓
[235]	Simulation	DG	Cosserat rod	Implicit integration	2D	×	✓	Simulated
[187]	Simulation	CM	Kirchhoff rod	Explicit integration	3D	✓	×	Simulated
[240]	Control and dynamics	DG	Cosserat rod	Explicit integration	3D	×	×	×
[232]	Simulation	CM	Nonlinear beam	NL–FEM*	3D	✓	×	Simulated
[188]	Force estimation	DG	Cosserat rod	Analytical	3D	×	✓	✓
[74]	Force estimation	CM	Nonlinear Beam	NL–FEM	2D	×	×	✓
[241]	Simulation	MD	–	Numerical optimization	3D	✓	✓	✓
[213]	Control and dynamics	DG	Cosserat rod	Explicit integration	3D	×	×	×
[218]	Force estimation	DG	Cosserat rod	Constrained optimization	3D	×	×	✓
[239]	Force estimation	DG	Cosserat rod	Constrained optimization	2D	×	✓	✓
[64]	Control and dynamics	MD	Single circular arc	Analytical	3D	×	✓	✓
[70]	Force estimation	MD	Generalized Kelvin-Voigt	Analytical	3D	×	✓	✓
This study	Force estimation	DG	Cosserat rod	Multi-PSO optimization	3D	×	×	✓

*__DG__: Differential Geometry, __MD__: Multibody Dynamics, __CM__: Continuum Mechanics, __NL-FEM__: Nonlinear Finite Elements Method

By comparing the representative studies, it was evident that most of the studies were focused on forward modeling of the flexible rods, e.g., for either simulation or control purposes. However, a number of studies were focused on force estimation, where deformation is known and forces were to be determined, e.g, [74, 188, 218, 239]. Moreover, none of the representative studies have parameterized the deformation with an analytical form. Derivatives of such analytical parameterization could further facilitate estimation of kinematic variables, e.g., strains and curvature, to be employed in the continuum's conservation equations. While numerical arc-length parameterization, such as employed by Aloi *et al.* [218], may be stable for single-plane deformations, it may incur numerical unboundedness for curvature, in the case of highly tortuous 3D deformed conventional EDs during RCI. Moreover, to the best of the author's knowledge none of the reviewed studies have investigated the feasibility of rendering haptic cue (total insertion force) from real-time imaging without *a-priori* knowledge of anatomy.

4.1.3 Motivation and Contributions

Based on the literature survey, a computational framework for estimation of the haptic forces on flexible EDs without the need for a sensor, simplifying assumptions on its 3D deformation, or using fiducial markers is desirable for model-based haptic provision. Also, the dependence on the *a-priori* knowledge of anatomy is a limiting factor for the clinical usage of force estimation models.

To address this need, in this study, a computational framework (iCORD) for real-time estimation of acting forces on flexible EDs was proposed and validated. To this end, the author exploited the availability of the intraoperative live X-ray fluoroscopy, as a standard-of-care, to extract and parameterize the 3D deformation of a catheter. Afterward, the parameterized deformation was incorporated in the kinematics of a (quasi-) static Cosserat rod model. The contact forces were assumed to have a multiple Gaussian form with an unknown number of contact forces, unknown magnitudes, and loci and were optimized using a multiple particle swarm (multi-PSO) optimization technique. The proposed method was applied to experimental data for three major vascular interventions on a vascular phantom and eventually statistical analysis was performed to compare the results of iCORD with the reference data.

The Cosserat rod model was used to unify the small and large deformation formula. Also,

the analytical form of this model allowed for pre-compiling the balance equations for generalized parametric deformation of EDs, which further decreased the runtime computations leading to a small computational surplus. More specifically, our main contributions in the present study are:

(1) proposing an image-based force estimation framework compatible with the available image modality in practice,

(2) independence of the force estimation from *a-priori* knowledge of anatomy and mechanical properties of the tissue,

(3) inclusion of the frictional effects of the contact forces which allows for the exclusion of friction from the haptic cue,

(4) pre-compilation of the analytical description of the balance equations for runtime computational efficiency,

(5) incorporation of a Jacobian-free and global optimization technique without the need for a well-posed initial guess, and

(6) improvement of the accuracy and computational efficiency of the developed Cosserat-based models for EDs.

In the following, the details of shape extraction, deformation parameterization, inverse problem formulation, and solution schema are provided in Section 4.2. Also, the details of the hardware and software used for validation tests, experimental procedures, results, and statistical analysis are presented and discussed in Section 4.3. Finally, Section 4.4, concludes this article with a summary of the main findings, limitations, and proposed future works.

4.2 Force Estimation Framework

In this section, the details of the image-based deformation extraction, shape parameterization, inverse Cosserat rod model, and the force estimation schema are described.

4.2.1 Image-based Shape Extraction

Since the live X-ray images are available intraoperatively, an image-based shape extraction was proposed. In this study, camera imaging was used to obtain the shape of the flexible catheter through stereo vision. Using the stereo vision, in laboratory experiments, has been validated for catheter shape extraction in the literature, e.g., [185].

Two USB cameras (C920, Logitec Inc., Switzerland), were installed on a frame for providing stereo vision. The cameras were calibrated using MATLAB Stereo Camera Calibration Toolbox (MATLAB R2019b, MathWorks Inc., MA, USA) adopting a pinhole camera model [208]. Fig. 4.2 shows the pose of cameras with respect to the vascular model. The checkerboard calibration and re-projection test confirmed a root-mean-square (RMS) re-projection error of 0.21, 0.07, and 0.35 mm for x, y, and z estimation. Also, the goodness-of-fit for the pinhole model as a mapping from camera coordinates to world coordinates was $\mathrm{R}^2 = 0.97$.

For the experiments, a vascular phantom (SAM plus, Lake Forest Anatomical Inc., IL, USA) with femoral, abdominal, and thoracic aorta was used. Also, a surgeon–patient robotic mechanism, developed previously by Hooshiar *et al.* [74] was used for robotic steering of the catheter.

To segment the catheter, each frame of each camera was converted to gray-scale and was subtracted from the background image obtained with the same camera (image of the setup before inserting the catheter). Afterward, by performing thresholding, adopted from [185, 209], a binary map representing the catheter in each frame was obtained and was used for 3D reconstruction. The 3D reconstruction of the pixels from binary maps were performed using the calibration mapping matrix of stereo-cameras, i.e. $\mathbf{\Psi}_{3\times5}$ obtained from camera calibration; whereas, m segmented pixels in left $({}^{j}u_1, {}^{j}v_1)^T$, and right $({}^{j}u_2, {}^{j}v_2)$ cameras were mapped to the 3D point $\bar{\mathbf{p}}_j$ by triangulation using (43). Equation (44) shows a representative calibration matrix obtained from stereo-calibration.

$$\bar{\mathbf{p}}_j = \mathbf{\Psi} \begin{pmatrix} {}^{j}u_1 \\ {}^{j}v_1 \\ {}^{j}u_2 \\ {}^{j}v_2 \\ 1 \end{pmatrix} \qquad j = 1 \cdots m \tag{43}$$

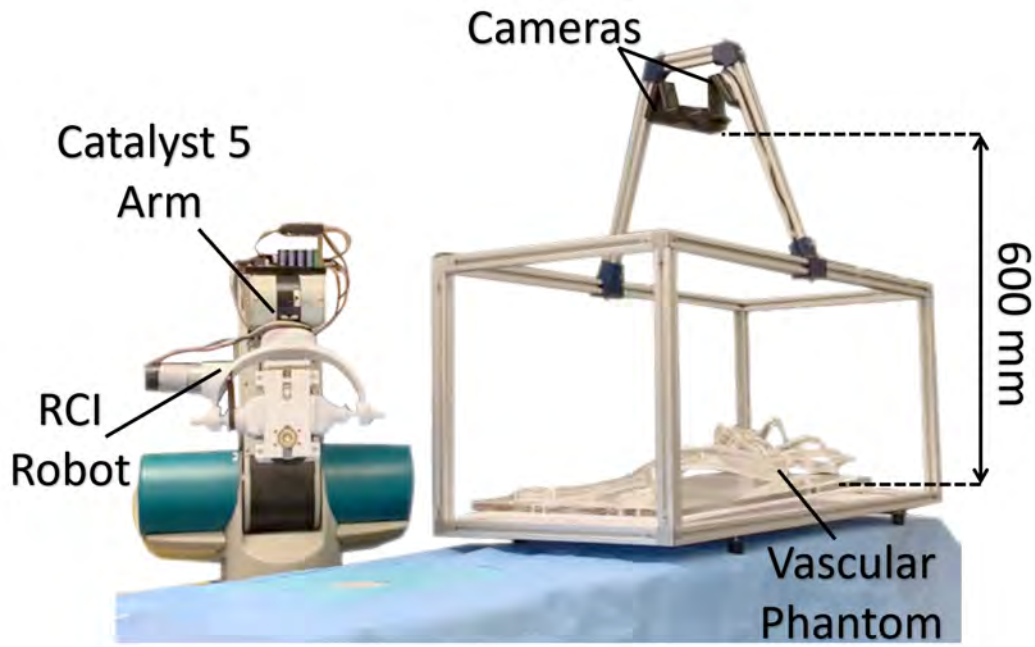

Figure 4.2: Experimental setup with the cameras, RCI system, and vascular phantom.

$$\mathbf{\Psi} = \begin{pmatrix} -0.3248 & -0.0067 & -0.4914 & 0.0015 & 397.4636 \\ -0.1962 & -0.4624 & 0.1996 & 0.3527 & 256.4915 \\ 0.0017 & -0.0513 & 0.0021 & 0.0464 & 600.2752 \end{pmatrix} (\frac{\text{mm}}{\text{px}}) \tag{44}$$

4.2.2 Shape Parameterization

The goal of the shape parameterization was to find a continuously differentiable representation for the shape of the catheter in each frame. The parameterized shape would facilitate the formulation and solution of the inverse Cosserat rod model as it is based on the continuous and differentiable shape of the rod.

Given that the points along the catheter were acquired densely, each $\bar{\mathbf{p}}_j$ was associated with a normalized curve parameter $\bar{s}_j$ defined as:

$$\bar{s}_j = \frac{1}{\bar{L}} \sum_{k=1}^{j} ||\bar{\mathbf{p}}_k - \bar{\mathbf{p}}_{k-1}||, \tag{45}$$

where $\bar{L}$ was the inserted length of the catheter obtained from the RCI device in real-time. Therefore, the discretized centerline $\bar{\mathbf{c}}(\bar{s}_j)$ was defined as a collection of $\bar{\mathbf{p}}_j$s such that:

$$\bar{\mathbf{c}}(\bar{s}_j) = \bar{\mathbf{p}}_j = \begin{pmatrix} \bar{x}_j \\ \bar{y}_j \\ \bar{z}_j \end{pmatrix}, \tag{46}$$

with $\bar{x}_j$, $\bar{y}_j$, and $\bar{z}_j$ in the global coordinates.

On the other hand, centerline shape $\mathbf{c}(s)$ was assumed as a Bezier curve. Bezier curves are Pythagorean–hodograph curves with Bernstein polynomial tuple basis [210], which are widely used for 3D shape reconstruction of curves. A Bezier curve of n–order is a function of normalized length parameter $s \in [0, 1]$ and provides a continuous and differentiable interpolation using $n + 1$ control points $\mathbf{p}_{0\text{–}n}$. Therefore, the centerline $\mathbf{c}(s)$ was parameterized as a Bezier curve of degree n with the form:

$$\mathbf{c}(s) = \begin{pmatrix} x(s) \\ y(s) \\ z(s) \end{pmatrix} = \sum_{i=0}^{n} b_{i,n}(s)\mathbf{p}_i, \tag{47}$$

where, $\mathbf{p}_i = (x_i, y_i, z_i)^T$ represent the i-th control point in global coordinates and $b_{i,n}$ is the $(i-1)$-th Bernstein basis polynomial of degree n with the form:

$$b_{i,n}(s) = \begin{pmatrix} n \\ i \end{pmatrix} (1-s)^{n-i}\, s^i. \tag{48}$$

In general, the control points do not coincide with the curve, however, $\mathbf{p}_0$ and $\mathbf{p}_n$, associated with $s = 0$ and $s = 1$, necessarily reside on the tail and the tip of the curve, respectively. This would further facilitate the localization of the beginning (tail) and the ending (tip) of the catheter in

the reconstructed shape. The matricial form of (47) was:

$$\mathbf{c}(s) = \mathbf{P}\mathbf{b}_n(s) = \begin{pmatrix} \mathbf{p}_0 & \cdots & \mathbf{p}_n \end{pmatrix} \begin{pmatrix} b_{0,n}(s) \\ . \\ . \\ . \\ b_{n,n}(s) \end{pmatrix}. \tag{49}$$

Fitting the discrete shape of the centerline $\bar{\mathbf{c}}(s_j)$ with the Bezier curve $\mathbf{c}(s)$ constituted an unconstrained least-square optimization (LSO) problem defined by (50) with $\mathbf{P}$ unknown.

$$mininmize \sum_{j=1}^{m} \left(\mathbf{P}\mathbf{b}_n(\bar{s}_j) - \bar{\mathbf{c}}(\bar{s}_j)\right)^T \left(\mathbf{P}\mathbf{b}_n(\bar{s}_j) - \bar{\mathbf{c}}(\bar{s}_j)\right), \tag{50}$$

Moore-Penrose pseudo-inverse theorem guarantees the existence and uniqueness of a $\mathbf{P}$ minimizing (50), if and only if:

$$\mathbf{P} = \begin{pmatrix} \mathbf{p}_0 & \cdots & \mathbf{p}_n \end{pmatrix} = \bar{\mathbf{C}}\bar{\mathbf{B}}^T(\bar{\mathbf{B}}\bar{\mathbf{B}}^T)^{-1}, \tag{51}$$

with,

$$\bar{\mathbf{C}} = \begin{pmatrix} \bar{\mathbf{p}}_1 & \cdots & \bar{\mathbf{p}}_m \end{pmatrix} \tag{52}$$

and,

$$\bar{\mathbf{B}} = \begin{pmatrix} \mathbf{b}_n(\bar{s}_1) & \cdots & \mathbf{b}_n(\bar{s}_m) \end{pmatrix}, \tag{53}$$

The computation of (51) is fast and efficient compared to the gradient-based optimization techniques. In each frame, n was selected by the solver so that the error of length estimation for catheter L would be less than 5% compared to the measured inserted length relayed from the RCI device. Also, for further acceleration, the initial n at any time-step was equal to the n at the previous time-step. The length of the parameterized centerline $\mathbf{c}(s)$ was formulated as:

$$L = \int_0^1 \mathrm{d}l = \int_0^1 ||\mathbf{c}'(s)||\mathrm{d}s, \tag{54}$$

where $(\cdot)' = \frac{\mathrm{d}}{\mathrm{d}s}(\cdot)$. Five-node Gaussian quadrature, (55), with Gauss nodes and weights (Table 4.2) would result in *exact* integration of L for $n \leq 10$ [242, 243]. To accelerate the integration, a

Table 4.2: Gauss nodes ξ_k and weights w_k for six-node Gauss quadrature [243].

k	ξ_k	w_k
1	0	0.5689
$2, 3$	± 0.5385	0.4786
$4, 5$	± 0.9062	0.2369

collection of the analytical form of $||\mathbf{c}'(s)||$ for $n \in \{1, 2, 3, \cdots, 10\}$ was compiled offline using recursive Casteljau's algorithm [210] and was used in runtime.

$$L \approx \frac{1}{2} \sum_{k=1}^{5} w_k ||\mathbf{c}'(\frac{\xi_k + 1}{2})||. \tag{55}$$

To test the accuracy of the length estimation, 400 mm of the catheter was inserted in and retracted from the vascular model using the RCI system. In real-time, the reference inserted length was obtained from the encoder on the RCI system, while the estimated length was obtained from using (55). The test was repeated five times.

Fig. 4.3(a) depicts a representative snapshot of the catheter during the test and its parameterized 3D shape, Fig. 4.3(b) compares the reference and estimated lengths, and Fig. 4.3 shows the distribution of the percentage of error in length estimation. The post-processing showed that the root-mean-square error (RMSE) in length estimation was 1.07 ± 0.93 mm.

4.2.3 Kinematics

4.2.3.1 Spatial orientation

The Fernet-Serret (FS-) frame is the most adopted moving frame choice for representing the spatial orientation of parameterized curves. However, the FS-based curvature $\kappa(s)$ is singular at the inflection points of the curve [210].

To alleviate this problem, orthonormal Darboux frame [211, 212] was used in this study to parameterize the spatial orientation of $\mathbf{c}(s)$. Using the definitions $\mathbf{d}_{1\text{–}3}$, $\kappa(s)$, and $\tau(s)$ provided in the Appendix A, the local Darboux frame $\mathbf{R}$ was defined as:

$$\mathbf{R} = \begin{pmatrix} \mathbf{d}_1(s) & \mathbf{d}_2(s) & \mathbf{d}_3(s) \end{pmatrix} \tag{56}$$

Fig. 4.4 depicts the schematic deformed shape of catheter with representative Darboux frames.

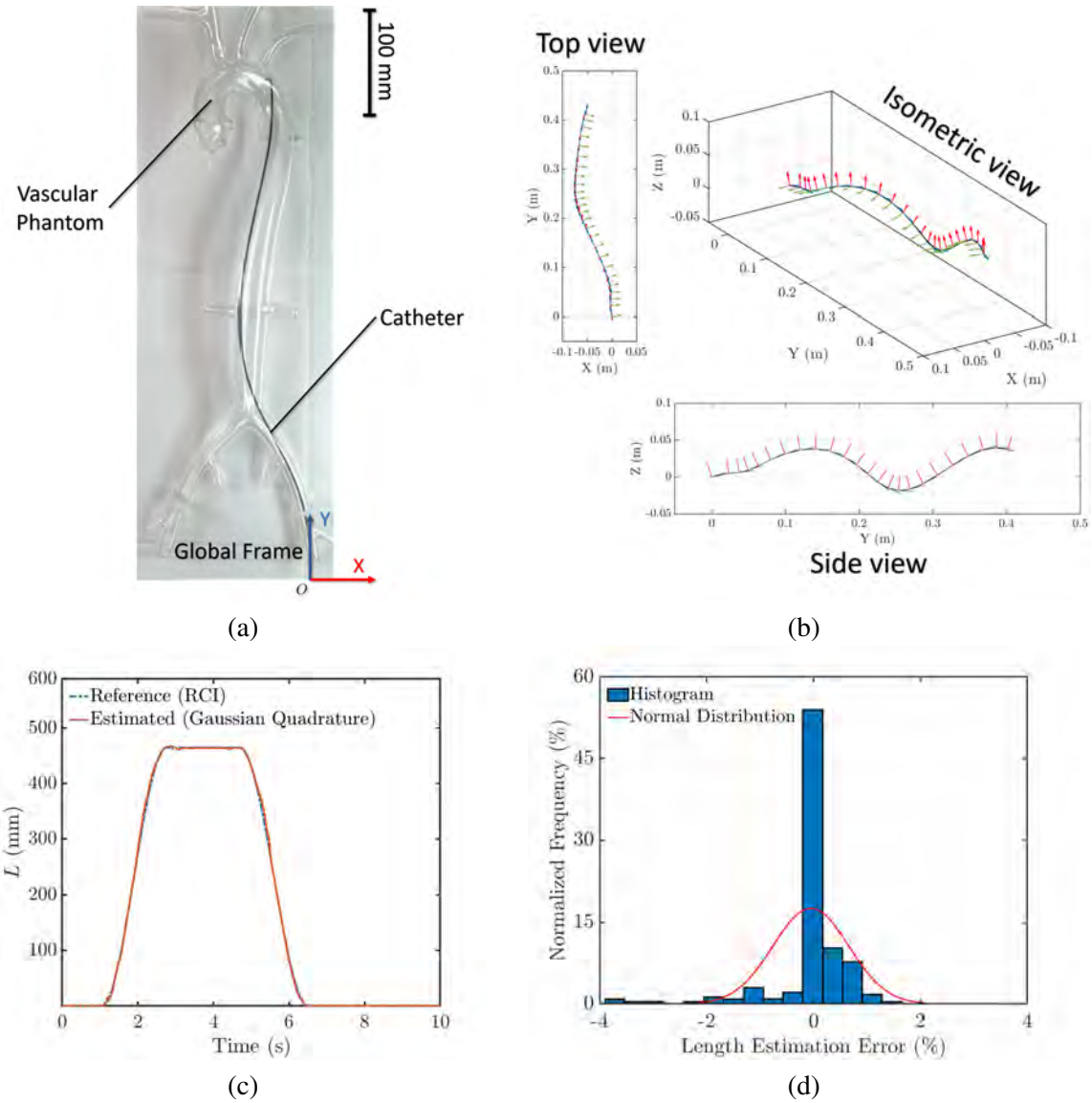

Figure 4.3: (a) Deformed catheter during the length estimation test, (b) 3D reconstructed shape of the deformed catheter with Darboux frames, (c) comparison of the estimated and reference length of insertion, and (d) distribution of length estimation error.

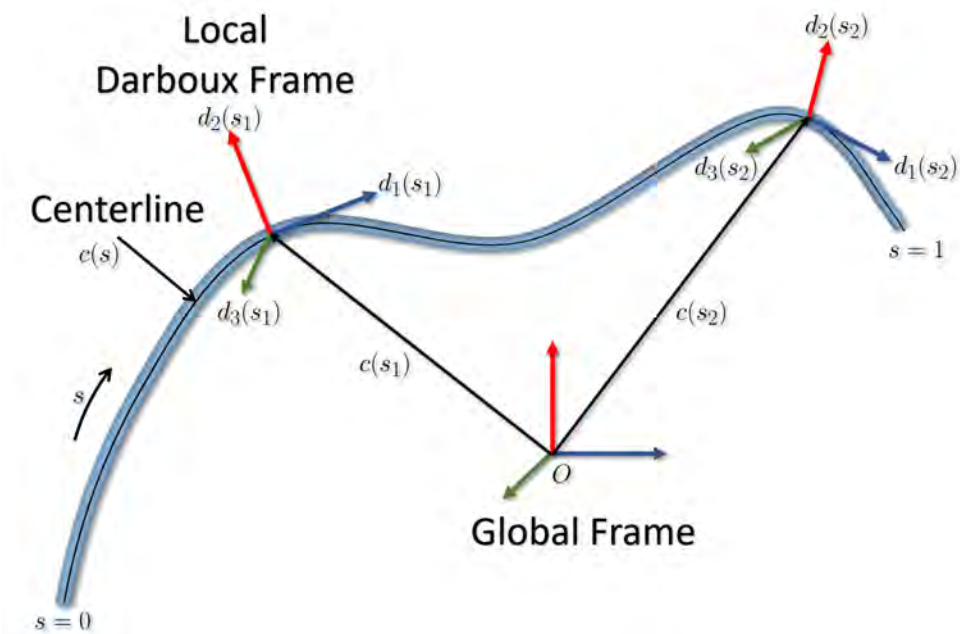

Figure 4.4: Schematic deformed shape of the catheter, $c(s)$ with representative local Darboux frames.

4.2.3.2 Local bending and torsion

Catheters have been modeled as inextensible and slender rods [213, 218]. The inextensibility assumption was enforced by considering the undeformed length of the catheter equal to the deformed length of the centerline, L. The parameterized bending and torsion of the centerline were obtained from the spatial rate of change of the curve orientation, $\mathbf{R}'$. From the differential geometry properties of Darboux frames:

$$\mathbf{R}' = \mathbf{D}\mathbf{R} = \begin{pmatrix} 0 & \kappa_g(s) & \kappa_g(s) \\ -\kappa_n(s) & 0 & \tau_g(s) \\ -\kappa_n(s) & -\tau_g(s) & 0 \end{pmatrix} \mathbf{R}. \tag{57}$$

According to the Cosserat model, the bending and torsion deformation of the parameterized curve is defined as:

$$\mathbf{u} = (\mathbf{R}^T\mathbf{R}')^\vee = (\mathbf{R}^T\mathbf{D}\mathbf{R})^\vee, \tag{58}$$

where, $\mathbf{u}$ is the parameterized vector of bending and torsion of $\mathbf{c}(s)$ in about the axes of the local

frames, and $(.)^\vee$ represents the *vee* operator, a mapping from $\mathfrak{so}(3)$ to $\mathbb{R}^3$ defined as [244]:

$$\begin{pmatrix} 0 & -u_3 & u_2 \\ u_3 & 0 & -u_1 \\ -u_2 & u_1 & 0 \end{pmatrix}^\vee \triangleq \begin{pmatrix} u_1 \\ u_2 \\ u_3 \end{pmatrix}. \tag{59}$$

From a mechanical point of view, at any given s, u_1 measures the torsional shear angle of $\mathbf{c}(s)$ about the local $\mathbf{d}_1(s)$ in Radian per unit length, while u_2 and u_3 are the curvature of $\mathbf{c}(s)$ in the planes constructed by $(\mathbf{d}_3(s), \mathbf{d}_1(s))$ and $(\mathbf{d}_1(s), \mathbf{d}_2(s))$, respectively. Since $\mathbf{u}$ was parameterized with respect to $\mathbf{p}_{0-n}$ and s, a library of $\mathbf{u}$ for $n \in \{2, \cdots, 10\}$ was compiled offline and was used in real-time.

4.2.3.3 Local extension and shear

Local extension and shear were defined as the spatial rate of change in the position of the centerline, $\mathbf{c}(s)$ with respect to its local coordinates, (60).

$$\boldsymbol{\delta} = \mathbf{R}^T \mathbf{c}'(s) \tag{60}$$

With the definition of $\mathbf{c}(s)$, as (49), and $\mathbf{R}$, as (56), it can be shown that $\boldsymbol{\delta}$ is of the form $\begin{pmatrix} \delta_1(s) & 0 & 0 \end{pmatrix}^T$. In fact, δ_1 measures the local longitudinal extension of the catheter along its local $\mathbf{d}_1$ direction. Therefore, the proposed Bezier shape parameterization automatically does not encode the shear and possible warping deformations. However, for non-slender rods, shear and warping effects can be included with a modified parameterization. Discarding shear and warping effects for slender rods, e.g., EDs, have been widely adopted in the previous literature, e.g., [64, 211, 213, 218, 236].

4.2.3.4 Undeformed shape

In general, the undeformed (original) shape of catheter of any form could be parameterized with a unique $\mathbf{c}^\star(s)$. Without loss of generality, the undeformed shape of the catheter $\mathbf{c}^\star(s)$ was assumed to be a straight line of length L along the direction of $\mathbf{d}_1(0)$, i.e., tangent to the deformed shape at tail $(s = 0)$. Therefore:

$$\mathbf{c}^\star(s) = \begin{pmatrix} \mathbf{p}_0 & L\mathbf{d}_1(0) \end{pmatrix} \mathbf{b}_1(s). \tag{61}$$

The undeformed shape $\mathbf{c}^\star(s)$ exhibits zero torsion and bending, thus, $\mathbf{u}^\star = \mathbf{0}$, however, it has spatial extension $\boldsymbol{\delta}^\star = \begin{pmatrix} L & 0 & 0 \end{pmatrix}^T$ in local coordinates. Such an assumption has been adopted in similar studies, e.g., [213, 218, 236].

4.2.3.5 Parameterized deformation

The proposed parameterized deformation of catheter was defined as a twist vector $\boldsymbol{\chi}(s)$ [236] in local coordinates such that:

$$\boldsymbol{\chi}(s) = \begin{pmatrix} \boldsymbol{\delta} - \boldsymbol{\delta}^\star \\ \mathbf{u} - \mathbf{u}^\star \end{pmatrix} \tag{62}$$

The parameterized deformation, $\boldsymbol{\chi}(s)$, satisfies the homogeneous Dirichlet and Neumann boundary conditions, necessary for modeling a cantilever rod. Thus, $\boldsymbol{\chi}(s)$ is admissible as the deformation of the catheter as a cantilever rod. In addition, it can be shown that the proposed deformation is length-preserving for $n \leq 10$:

$$\delta L = \int_0^1 \mathbf{R}\boldsymbol{\delta}(s) \cdot \mathbf{d}_1(s) \mathrm{d}s - L = \int_0^1 ||\mathbf{c}'(s)|| \mathrm{d}s - L = 0, \tag{63}$$

where, δL is the total change in the length of the deformed shape with respect to the undeformed shape. In other words, since generally $\boldsymbol{\delta}(s) \neq \mathbf{0}$, the local elongations in the catheter are compensated with the local compressions and vice versa, resulting in a total $\delta L = 0$.

4.2.4 Constitutive Equations

Medical catheters are usually constituted of a medical-grade Nickel-Titanium (NiTi) alloys coil [214] covered with a thin polymeric drag-reducing sheet. Despite the large geometrical deformation of the catheter, it remains within the limits of the linear elastic region thanks to the super-elastic properties of NiTi alloys [215]. Therefore, the constitutive equations of the catheter in global coordinates are of the following Hookean form:

$$\begin{pmatrix} \mathbf{n}(s) \\ \mathbf{m}(s) \end{pmatrix} = \begin{pmatrix} \mathbf{R} & \mathbf{0} \\ \mathbf{0} & \mathbf{R} \end{pmatrix} \begin{pmatrix} \mathbf{K}_\delta & \mathbf{0} \\ \mathbf{0} & \mathbf{K}_u \end{pmatrix} \boldsymbol{\chi}(s), \tag{64}$$

where, $\mathbf{n}(s)$ and $\mathbf{m}(s)$ are internal forces and moments as a function of s, while, $\mathbf{K}_\delta$ and $\mathbf{K}_u$ are stiffness matrices for elongation–shear and torsion–bending, respectively:

$$\mathbf{K}_\delta = \frac{\text{EA}}{L}\begin{pmatrix} 1 & 0 & 0 \\ 0 & 1 & 0 \\ 0 & 0 & \frac{1}{2(1+\vartheta)} \end{pmatrix}, \tag{65}$$

$$\mathbf{K}_u = \text{EI}\begin{pmatrix} \frac{1}{1+\vartheta} & 0 & 0 \\ 0 & 1 & 0 \\ 0 & 0 & 1 \end{pmatrix}, \tag{66}$$

$$\tag{67}$$

where, $\frac{EA}{L}$, EI, and ϑ are the tensile–compressive stiffness, flexural rigidity, and Poisson's ratio of the catheter.

In the case of non-negligible shear and warping effects, e.g., for non-slender rods, the off-diagonal components of the assembled stiffness matrix would be non-zero.

4.2.5 Force Balance

Fig. 4.5 shows the free-body-diagram of a representative catheter in its deformed shape being cut at an arbitrary point,e.g., $s = s_0$. Previous studies have shown that the inertial effects on the intraluminal catheters are negligible, mainly due to slow insertion and rotation speeds and the small mass of catheters [245]. Based on the fact that intraluminal catheters are coated with hydrophobic materials, the drag deflection from blood flow is negligible compared to the large deformation of the catheter [246]. Also, due to the small external diameter of the catheter, e.g., 7 Fr (2.33 mm), the external torque on the body of catheter is not comparable to the steering torque (at $s = 0$) and bending moments throughout the catheter.

Therefore, the loading on the rod model included external steering moments and forces at $s = 0$ and contact forces $\mathbf{f}(s)$ and contact friction $\mathbf{f}_f(s)$.

Studies have shown that the average coefficient of friction between intraluminal devices and vessels is $\mu_f = 0.04$ with a maximum of 20% uncertainty [216]. Thus, the contact force distribution $\mathbf{f}(s)$ is in the normal plane and toward the centerline. The contact force would generate a frictional force

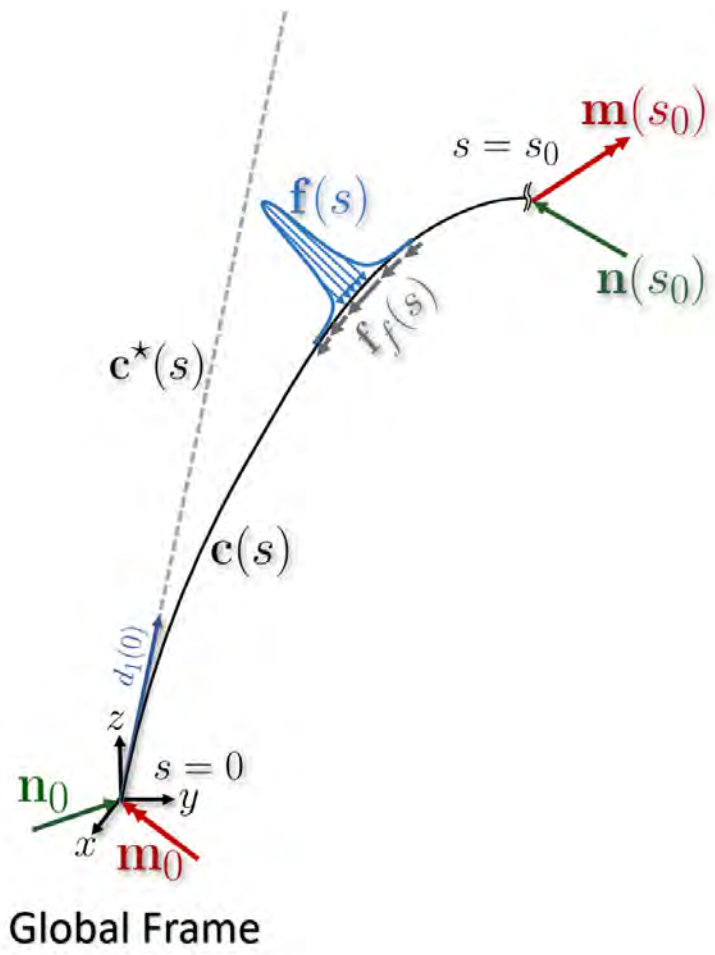

Figure 4.5: Free-body-diagram of a representative catheter in original and deformed shapes cut at a given s_0.

distribution $\mathbf{f}_f$ along $\mathbf{d}_1(s)$ in the opposite direction of the linear velocity of $\mathbf{c}(s)$. The contact force and contact friction in local coordinates were formulated as:

$$\mathbf{f}(s) = \begin{pmatrix} 0 \\ f_2(s) \\ f_3(s) \end{pmatrix}, \tag{68}$$

$$\mathbf{f}_f(s) = -\mathrm{sgn}\big(\dot{\mathbf{c}}(s) \cdot \mathbf{d}_1\big)\mu_f ||\mathbf{f}(s)|| \begin{pmatrix} 1 \\ 0 \\ 0 \end{pmatrix} = -\mathrm{sgn}\big(\dot{\mathbf{P}}\mathbf{b}_n(s) \cdot \mathbf{d}_1\big)\mu_f ||\mathbf{f}(s)|| \begin{pmatrix} 1 \\ 0 \\ 0 \end{pmatrix}, \tag{69}$$

with sgn as the sign function, $\dot{(.)} = \frac{\mathrm{d}}{\mathrm{d}t}$, the temporal derivation operator, and $\dot{\mathbf{P}}$ as the velocity of the control points. The temporal derivative terms were calculated using the third-order backward differentiation formula:

$$\dot{\mathbf{P}} = \frac{\frac{11}{6}\mathbf{P}_t - 3\mathbf{P}_{t-h_t} + \frac{3}{2}\mathbf{P}_{t-2h_t} - \frac{1}{3}\mathbf{P}_{t-3h_t}}{h_t} + O(h_t^3), \tag{70}$$

with h_t the time difference between two consecutive frames.

The force balance equations of the portion of the rod shown in Fig. 4.5 in global coordinates are:

$$\mathbf{n}_0 = \mathbf{n}(s_0) + \int_0^{s_0} (\mathbf{R}(\mathbf{f}(s) + \mathbf{f}_f(s)) + \rho A \mathbf{g})\mathrm{d}s, \tag{71}$$

$$\mathbf{m}_0 = \mathbf{m}(s_0) + \int_0^{s_0} -\mathbf{c}'(s) \times (\mathbf{R}(\mathbf{f}(s) + \mathbf{f}_f(s)) + \rho A \mathbf{g})\mathrm{d}s \tag{72}$$

where $\mathbf{n}_0$ and $\mathbf{m}_0$ represent the steering forces and moments applied at the proximal part of catheter ($s = 0$) and $\mathbf{g} = \begin{pmatrix} 0 & 0 & -g \end{pmatrix}^T$ is the gravity vector in global coordinates with $g = 9.81 m/s^2$.

4.2.6 Problem Formulation

4.2.6.1 Inverse problem

With the shape and deformation ($\mathbf{R}$ and $\boldsymbol{\chi}(s)$) known from the deformation parameterization, the inverse problem was defined as to determine the distribution of unknown contact and steering forces, i.e., $\tilde{\mathbf{f}}(s)$, $\mathbf{n}_0$, and $\mathbf{m}_0$. As discussed in [217], the inverse problems are generally ill-posed due to non-existence, non-uniqueness, or discontinuity of the inverse solution for small perturbations. However,

employing the integral form of the model would improve the posedness of the problem [217]. The residual of the force and moment balance equations for a given $s = s_0$ was defined as:

$$\tilde{\mathbf{r}}_n(s_0) = \mathbf{n}(s_0) + \int_0^{s_0} (\mathbf{R}(\tilde{\mathbf{f}}(s) + \tilde{\mathbf{f}}_f(s)) + \rho A \mathbf{g}) \mathrm{d}s - \mathbf{n}_0, \tag{73}$$

$$\begin{aligned} \tilde{\mathbf{r}}_m(s_0) = \mathbf{m}(s_0) + \int_0^{s_0} -\mathbf{c}'(s) \times (\mathbf{R}(\mathbf{f}(s) + \mathbf{f}_f(s)) + \\ \rho A \mathbf{g}) \mathrm{d}s - \mathbf{m}_0. \end{aligned} \tag{74}$$

$$\tilde{\mathbf{r}}(s_0) = \begin{pmatrix} \tilde{\mathbf{r}}_n(s_0) \\ \tilde{\mathbf{r}}_m(s_0) \end{pmatrix} \tag{75}$$

Also for computational efficiency, (74) was reordered as:

$$\begin{aligned} \tilde{\mathbf{r}}_m(s_0) = \mathbf{m}(s_0) + \int_0^{s_0} \mathbf{c}'(s)^{\wedge T} (\mathbf{R}(\mathbf{f}(s) + \mathbf{f}_f(s)) + \\ \rho A \mathbf{g}) \mathrm{d}s - \mathbf{m}_0. \end{aligned} \tag{76}$$

By evaluating the residuals $\tilde{\mathbf{r}}(s_0)$ for $s_0 = 1$, the residuals would include all the forces acting on the catheter. Therefore, a least-square minimization problem was defined as:

$$minimize \quad \varepsilon = (\tilde{\mathbf{r}}(s_0)|_{s_0=1})^T (\tilde{\mathbf{r}}(s_0)|_{s_0=1}) \tag{77}$$

The variable of interest in this study was the total insertion force $||n_0||$ during cannulation procedures, as the literature indicates insertion force as a determinant haptic cue during interventional surgeries [41, 43].

4.2.6.2 Force interpolation function

In order to evaluate the integral part of (73), the form of $\tilde{\mathbf{f}}(s)$ was required. Recent studies have proposed curvature-based force localization [74], sliding Dirac-δ force localization [218], truncated Fourier approximation [218], and contact treatment with *a-priori* knowledge of vessel geometry [247]. However, the curvature-based method is based on 2D deformation, Dirac-δ requires constrained non-linear optimization, truncated Fourier approximation requires large number of terms to capture sharp changes, e.g., point loads, and contact treatment necessitates *a-priori* knowledge of 3D vessel shape.

Given that the contact happens at small areas along the catheter (contact points), the force interpolation function is required to exhibit individual sharp spikes at contact points, while remains zero at non-contacting points along the catheter. Therefore, the force interpolation function was proposed to be of the form of summation of sliding Gaussian functions, (78).

$$f_i(s) = \sum_{j=1}^{n_c} \alpha_{ij} e^{-(\frac{s-\beta_j}{\sigma})^2}, \quad \sigma = \frac{1}{10}, i = 2, 3. \tag{78}$$

In the proposed interpolation function, $0 < \beta_i \leq 1$ is the offset, which localizes the j-th contact force, while σ controls the spread of the force peak. Also, the spread σ was set to $1/10$. Such a choice of σ would limit the spread of the contact forces to merely $\pm 5\%$ of the length of the catheter at the neighborhood of β_j. Therefore, the inverse problem was reduced to the determination of the number of the contact points n_c, location of the contact points β_j, and the magnitude of the contact forces α_{ij}.

4.2.7 Solution

As stated in Section 4.2.6.1, Eq. 77 constitutes a nonlinear least-square problem. To solve this problem, a gradient descent method, e.g., Gauss-Newton method, would need iterative computation of the Jacobian of the residual ε with respect to fitting parameters β_j and α_{ij}. Moreover, the gradient descent methods is not applicable with the integer variable n_c. Also, the gradient-based solution might stagnate at a local minimum, depending on the initial guess. To avoid these limitations in this study, a particle swarm optimization (PSO) algorithm was used for minimizing (77). The PSO algorithm is a fast-converging, Jacobian-free, and global optimization method [219].

Similar to [218], the aim of the solution was to find the *'worst-case'* loading, which involved the *'least'* number of contact points, i.e., n_c. To this end, a multi-PSO optimizer was implemented to simultaneously start ten parallel PSOs, with $n_c = 1, 2, \cdots 10$, at each frame. Each PSO defined with an inertial coefficient ω linearly decreasing from 1 to 0.4 over iterations, a social coefficient of $c_1 = 1.5$, and a cognitive coefficient of $c_2 = 1.5$ [219]. The stopping criterion for each PSO was reaching a residual norm of $\varepsilon < 0.01$ N or reaching the maximum iteration of `MAX_ITER`$= 100$. The optimizer would finally select the solution, i.e., α_{ij}-s and β_j-s, which satisfied the minimum residual norm with the smallest n_c.

Table 4.3: Summary of the measured and set values of the model parameters for RunWay 6Fr catheter (n=3).

Parameter	Method/Definition	Measured value	Set value
A (mm^2)	$\frac{\pi}{4}$(OD^2-ID^2)	OD=2.14 ± 0.17 mm ID=1.85 ± 0.23 mm	2.14
I (mm^4)	$\frac{\pi}{64}$(OD^4-ID^4)	OD=2.14 ± 0.17 mm ID=1.85 ± 0.23 mm	0.45
E (MPa)	3PB	EI=723.7 $^{MPa}/_{mm^2}$	1592.3
ϑ	-	-	0.395

OD: outer diameter
ID: inner diameter

4.2.8 Model Parameters

The parameters incorporated in the model were the elastic modulus, E, cross-sectional area, A, second moment of cross-sectional area, I, and the Poisson's ratio, ϑ of the catheter. Since the catheters used in this study (RunWay 6Fr, Boston Scientific, MA, USA) were made of metal-braided body, the Poisson's ratio was set to 0.395 as the average of 0.3, commonly used for metals, and 0.49, commonly used for incompressible elastomers.

Moreover, a similar catheter was cut into three samples of 100 mm length for diameter measurements and three-point bending tests (3PB), as per [220]. The 3PB test was performed using a universal testing machine (ElectroForce 3200, TA Instruments, DE, USA) with a vertical displacement rate of 20 $^{mm}/_{min}$.

Fig. 4.6 shows a sample of the catheter under the 3PB test and Table 4.3 summarizes the model parameters as used in the solution. In clinical practice, a look-up table of various intraluminal devices may be populated in the software and parameters automatically get set when the operator selects a specific ED.

4.3 Validation Study

4.3.1 Hardware–Software Integration

Fig. 4.7 shows the system-level hardware-software integration map implemented in this study. For this study, a graphical user interface (GUI) was developed in the C# programming language. The

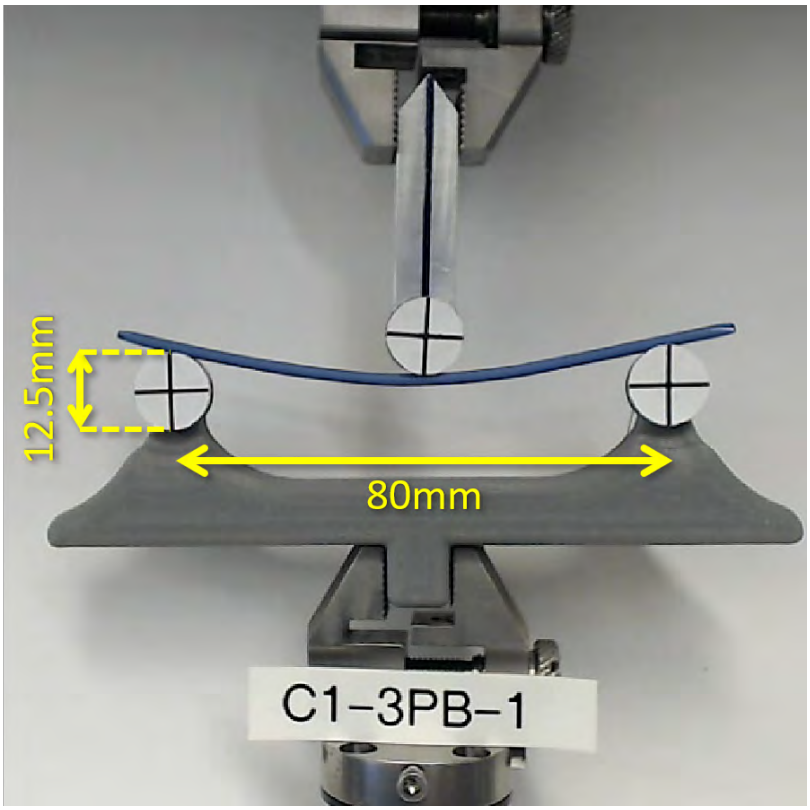

Figure 4.6: Sample of a catheter under the three-point bending test.

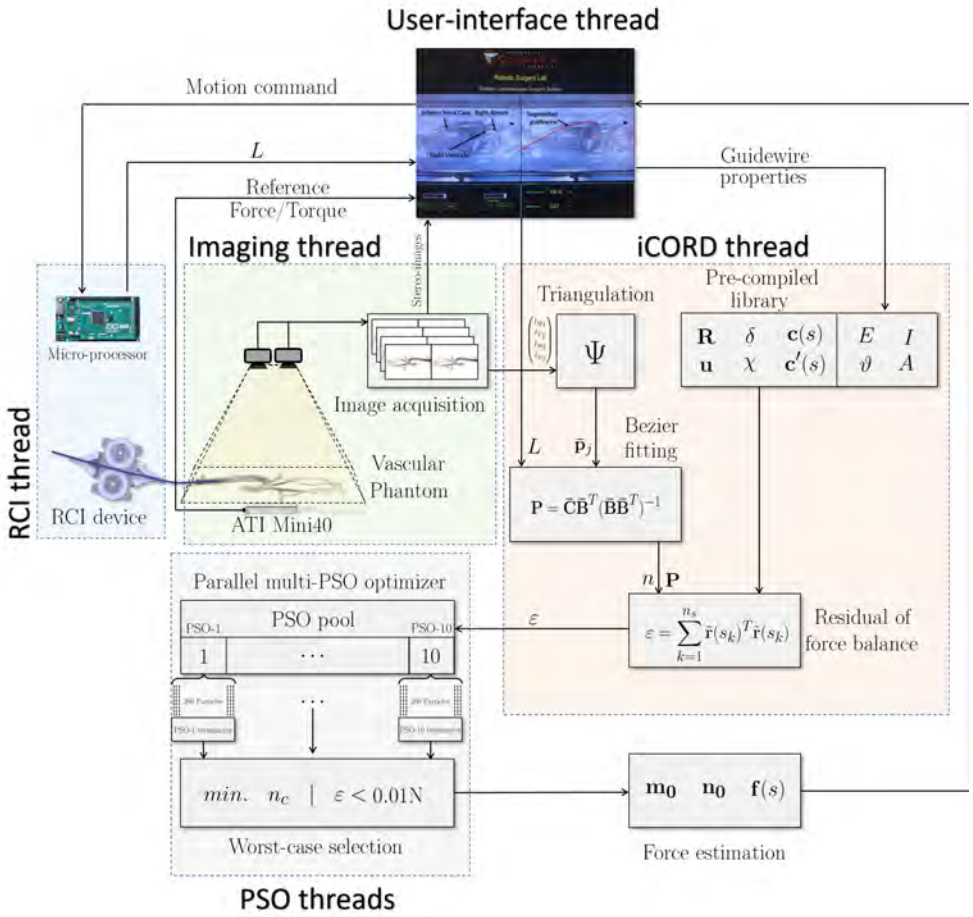

Figure 4.7: System-level representation of the RCI system with iCORD force estimation.

user would enter the mechanical and geometrical properties of the catheter to the GUI. The RCI was also controlled through the GUI, relaying the motion commands to the RCI microprocessor (Arduino Mega, Arduino, MA, USA). The microprocessor firmware was developed in the C++ programming language and controlled the catheter insertion and rotation with two independent PID feedback loops. GUI-RCI connectivity was through a Bluetooth serial protocol (HC-06, Guangzhou HC Information Technology, Co., Ltd., Guangzhou, China).

The stereo frames were acquired at a nominal frame-rate of 30 Hz (actual frame-rate: 27 ± 2Hz) with an HD 1080p (1920×1080 pixels) resolution. The image processing algorithm was developed using the OpenCV library [248] in C++. Also, the matricial operations and Moore-Penrose pseudo inversion were developed using the GPU-accelerated Armadillo linear algebra library [249].

4.3.2 Study Protocol

In order to study the performance of the proposed method for force estimation, the catheter (RunWay 6Fr, Boston Scientific, MA, USA) was steered by the RCI system according to the user motion command to reach three targets. The targets were the left subclavian artery (LSA), brachiocephalic artery (BCA), and ascending aorta (AA), all being commonly practiced catheterization tasks in cardiovascular and neurovascular interventions [43]. The catheter was placed at the entrance of the left femoral artery and steered toward each target for $n = 15$ times, making a total of $n = 45$ tests. The same operator performed all the tests.

During the test, the reference total insertion force was measured using the ATI Mini40 sensor installed below the vascular phantom. The force data from the sensor was recorded in a parallel thread and in synchrony with frame acquisition leading to a sample rate of 27 ± 2Hz. Fig. 4.8(a) depicts the GUI with the schematic RCI, and Fig. 4.8(b) shows the target areas on the vascular model.

4.3.3 Performance Assessment

Considering the free-body-diagram depicted in Fig. 4.5 and equation (71), the total contact force applied to the vascular phantom is equal and in the opposite direction of the total force applied on the catheter by the RCI. Therefore, for the performance assessment, the total insertion force was studied. Similar studies have also considered total insertion force as the performance assessment criterion, e.g., [43].

Fig. 4.9 depicts the data from three sample tests and compares the reference total contact force (measured) with the estimated contact force with the iCORD method for the three targets. In this figure, the *'Raw'* tag refers to un-averaged data and the *'MA10'* refers to the 10-point moving average. The figures are also tagged with numbers, e.g., 1, 2, which refer to the corresponding location of the tip of the catheter in the vascular phantom shown next to each graph.

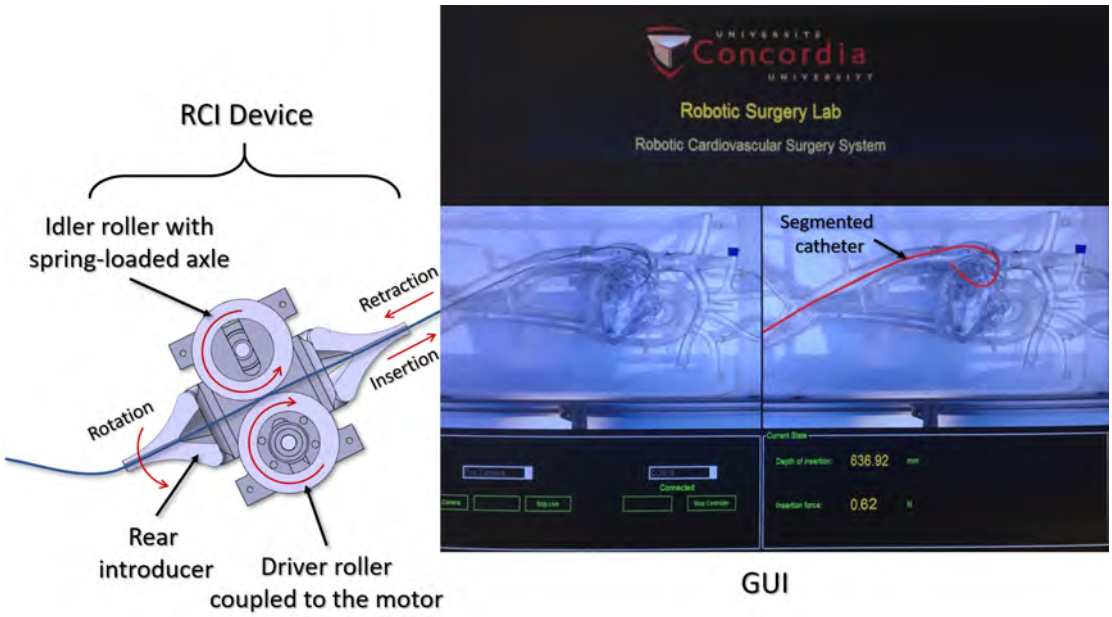

(a)

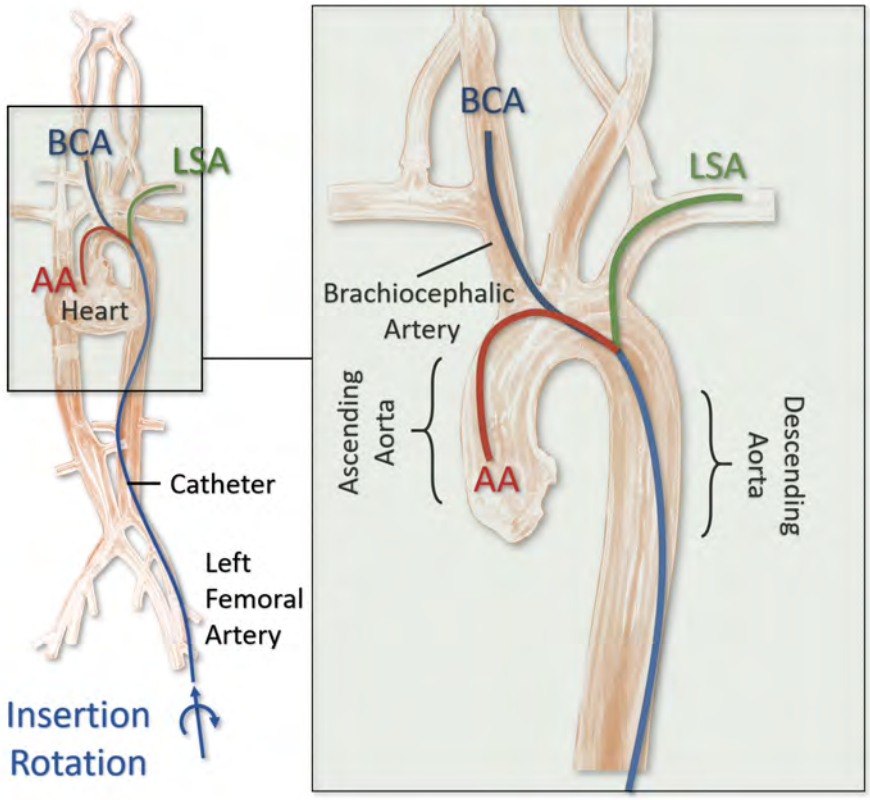

(b)

Figure 4.8: (a) Graphical user interface developed for the experiments with the schematic RCI system and (b) three target areas on the vascular phantom.

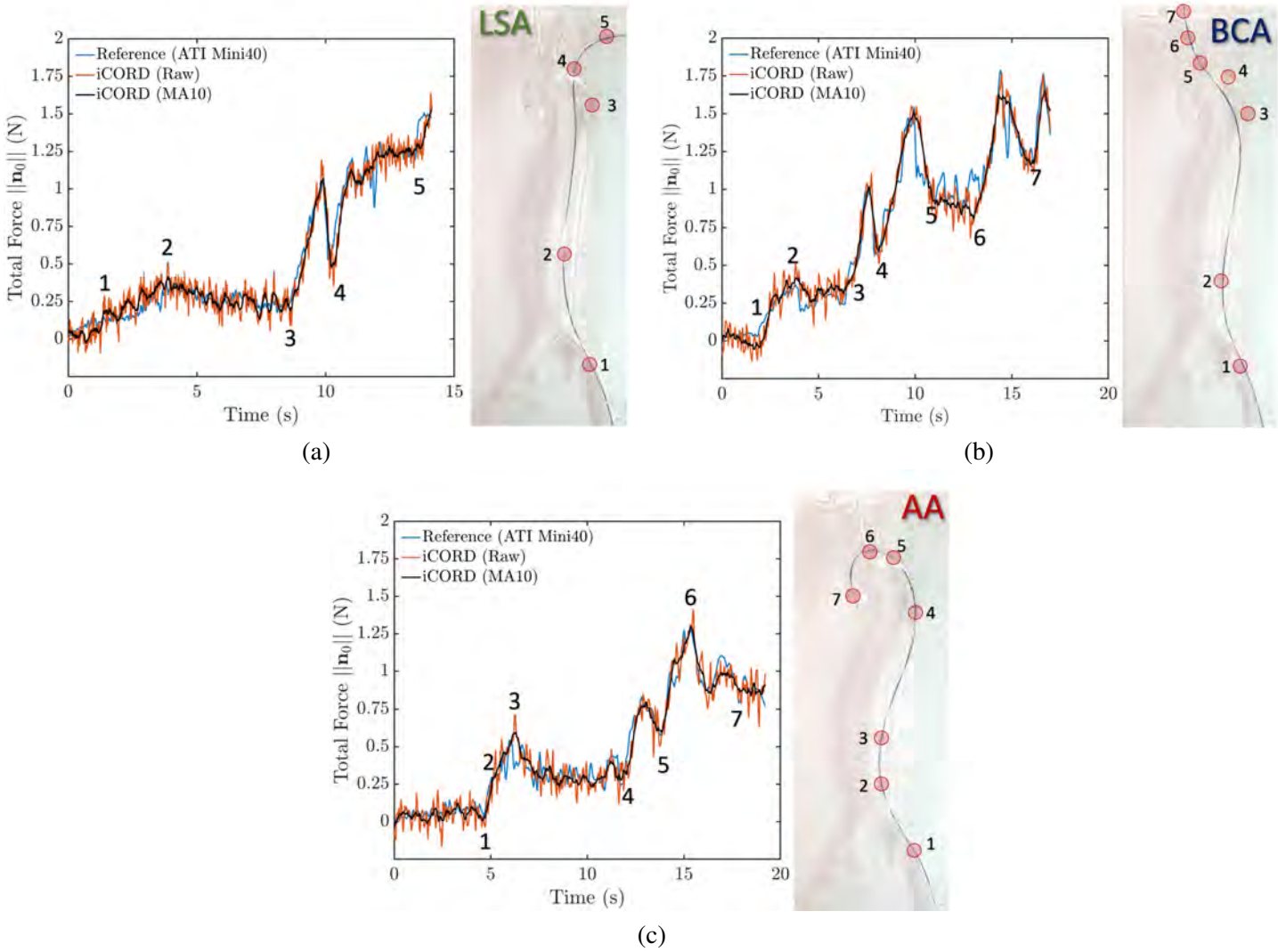

Figure 4.9: Comparison of the measured total contact force and the estimated contact forces for the catheterization tests toward (a) LSA, (b) BCA, and (c) AA target. Tagged points show the locations of the tip of the catheter in the image during insertion and their corresponding point on the force-time graph.

In all the tests, the total contact force showed a sharp peak as the catheter passed the femoral bifurcation and contacted with the aortic wall just above the bifurcation (point 2). In four tests, the tip of the catheter entered the right renal artery causing a secondary peak in force, e.g., point 3 in Fig. 4.9(a). Also, multiple consecutive peaks followed by valleys are evident in the force graph for all the tests, e.g., (4–5, 5–7) in Fig. 4.9(a), (3–4, 4–5, 6–7) in Fig. 4.9(b), and (3–4) in Fig. 4.9(c). Such sharp peaks are related to the stick–slip phenomenon happening due to the friction between the catheter and vascular phantom. Although the tests of this study were performed with dry phantom, similar observation has been previously reported in [216] for wet phantom experiments. The presence of stick-slip in the results shows that the inclusion of friction in the iCORD has successfully contributed to the capturing of the stick–slip phenomenon.

Also, the qualitative comparison with the reference shows that the iCORD estimations were in good agreement with the reference. Moreover, applying a 10-point moving average on the iCORD estimations decreased the noise in the raw iCORD estimations. The main source of noise in the iCORD *Raw* estimations was related to the flicker of the images due to the ambient vibration, as the experimental setup was not set on a vibration canceling platform.

4.3.4 Performance Metrics

Previously, Rafii *et al.* [43] have shown that the mean force, F_{avg}, maximum force F_{max}, force impact over time, FIT, and the number of peaks in the force N_P (above 0.1N), are the statistically significant features (metrics) in the force feedback for the RCI procedures. Therefore for the quantitative analysis the metrics for the iCORD estimations, *raw* and *MA10*, were compared with those calculated for reference. Moreover, the minimum detectable force by iCORD, F_{min}, was defined as the minimum estimated force with less than 5% error from its corresponding reference after the occurrence of the first contact (point 1). Also, the mean-absolute-error (MAE) between estimation and reference was calculated as a measure of accuracy for iCORD estimations. Table 4.4 summarizes the comparison of performance metrics.

In all the experiments, the mean force was overestimated by iCORD compared to the reference, i.e., +9.6% (LSA), +13.3% (BCA), and +10.8% (AA). Higher ranges of the error have been reported in the recent literature, e.g., [188, 218, 230, 239]. A similar over-estimating trend was observed

Table 4.4: Summary and comparison of the performance metrics between iCORD force estimation and reference.

Target	Metric	iCORD (Raw)	iCORD (MA10)	Reference
LSA	Mean Force, F_{avg} (N)	0.57±0.62	0.55±0.57	0.52±0.43
	Max. Force, F_{max} (N)	1.62±0.16	1.58±0.12	1.53±0.21
	Min. Det. Force, F_{min} (N)	0.22±0.09	0.26±0.08	0.01
	No. Peaks, N_p	5	5	5
	FIT (N.s)	8.21±1.48	7.97±1.35	7.44±0.96
	MAE (N)	0.08±0.14	0.06±0.12	–
BCA	Mean Force, F_{avg} (N)	0.85±0.49	0.79±0.55	0.75±0.50
	Max. Force, F_{max} (N)	1.76±0.34	1.71±0.25	1.65±0.26
	Min. Det. Force, F_{min} (N)	0.22±0.10	0.25±0.08	0.01
	No. Peaks, N_P	7	7	7
	FIT (N.s)	13.92±2.07	13.38±2.12	12.78±2.01
	MAE (N)	0.12±0.07	0.09±0.04	–
AA	Mean Force, F_{avg} (N)	0.51±0.49	0.48±0.45	0.46±0.36
	Max. Force, F_{max} (N)	1.36±0.18	1.31±0.17	1.28±0.14
	Min. Det. Force, F_{min} (N)	0.23±0.06	0.27±0.11	0.01
	No. Peaks, N_P	4	4	4
	FIT (N.s)	9.70±1.88	9.23±1.42	8.95±1.61
	MAE (N)	0.10±0.11	0.07±0.05	–

for the maximum force, i.e., +5.8% (LSA), +7.2% (BCA), and +6.3% (AA). However, the error of maximum force was less than the mean force; thus, it was inferred that iCORD estimations were more accurate toward the end of each intervention. This observation might be related to that as the shape of the catheter was more tortuous toward the end, a more specific combination of contact forces was to result in a similar shape and the multi-PSO converged to more accurate results. Another implication of over-estimating the force was its effect of the force-impact over time (FIT), where FIT was over-estimated by 10.3% in LSA, 8.9% in BCA, and 8.4% in AA experiment.

The findings showed that the minimum detectable force of iCORD was within the range of 0.22–0.23 N. Although, the minimum detectable force was higher than the nominal resolution of the reference force sensor (0.01 N), it showed improvement compared with the results of [188, 218, 230], and [239]. Although, using a moving average on the *Raw* data has decreased the noise of iCORD estimations, it has increased the minimum detectable force by 18.2% in LSA, 13.6% in BCA, and 17.4% in AA experiments. On the other hand, it is noteworthy that the minimum detectable force happened early in the procedure (near the femoral bifurcation) where is anticipated as a low-risk region for interventional surgeries.

As for the number of peaks, all the experiments showed similar numbers of peaks in the insertion force compared to the reference. The mean absolute error, was less than the minimum detectable force, which could rule out the advert effect of minimum detectable force on the accuracy of the iCORD estimations. Moreover, the MAE was decreased by applying a 10-point moving average which shows its effective noise cancellation on the iCORD performance. However, without the moving average, the MAE was 5.2%, 7.3%, and 7.8% of the peak force in LSA, BCA, and AA experiments, respectively.

4.3.5 Statistical Analysis

Based on the descriptive statistics provided in Table 4.4, the performance metrics of the iCORD showed levels of deviation from reference values. To determine whether the iCORD performance metrics for *Raw* and *MA10* groups were statistically different from the reference, statistical analyses were performed. To this end, the mean force (n=15), peak force (n=15), and force-impact over time (n=15) were tested for each experiment (three groups) against their corresponding reference values

for significant differences. Non-parametric Wilcoxon signed-rank test with a confidence level of 5% ($p < 0.05$) was selected, as the number of tests was $n \leq 15$ and the distribution of the sample tests was unknown. All the statistical analyses were performed using IBM SPSS Statistics software (v22, IBM Corp., NY, USA).

Fig. 4.10 shows the calculated significance levels for the iCORD and reference data. Since all the p-values were above the confidence level of $p < 0.05$, there was not enough statistical evidence that the performance metrics of iCORD were significantly different from the reference data. This finding further supports the similarity of the iCORD results to the reference data provided in Table 4.4.

4.3.6 Computation Time

The total insertion length for the LSA, BCA, and AA targets were, 524 ± 12 (n=15), 566 ± 23 (n=15), and 573 ± 9 mm (n=15). The post-processing showed that the average total computation time for force estimation increased from 10.9 ± 0.3 ms (BCA) to 24 ± 1 ms (BCA) as the catheter advanced into the phantom. Fig. 4.11(a) depicts the average computation time for force estimation for each target with respect to the inserted length.

In all the tests, the computation time increased exponentially with the inserted length. Such an exponential growth was related to the increasing the number of pixels occupied by the catheter in the frames, thus, increasing the computational cost of Bezier fitting, (51). As another factor, it was observed that by increasing the insertion length, the tortuosity of the catheter increased due to entering the aortic arch and the arteries. Therefore, more PSO iterations were necessary to achieve convergence. Nevertheless the total computation time per frame was less than the real-time ceiling, i.e., 37 ms corresponding to the average frame rate of 27Hz. Therefore, the proposed solution and optimization method were fast enough to satisfy the real-time requirement.

More specifically, Fig. 4.11(b) compares the breakdown of the computation time for image processing (shape extraction and triangulation), Bezier fitting, and convergence time of the multi-PSO optimizer. Comparatively, PSO optimization had the most and Bezier fitting had the least computational cost for the solution.

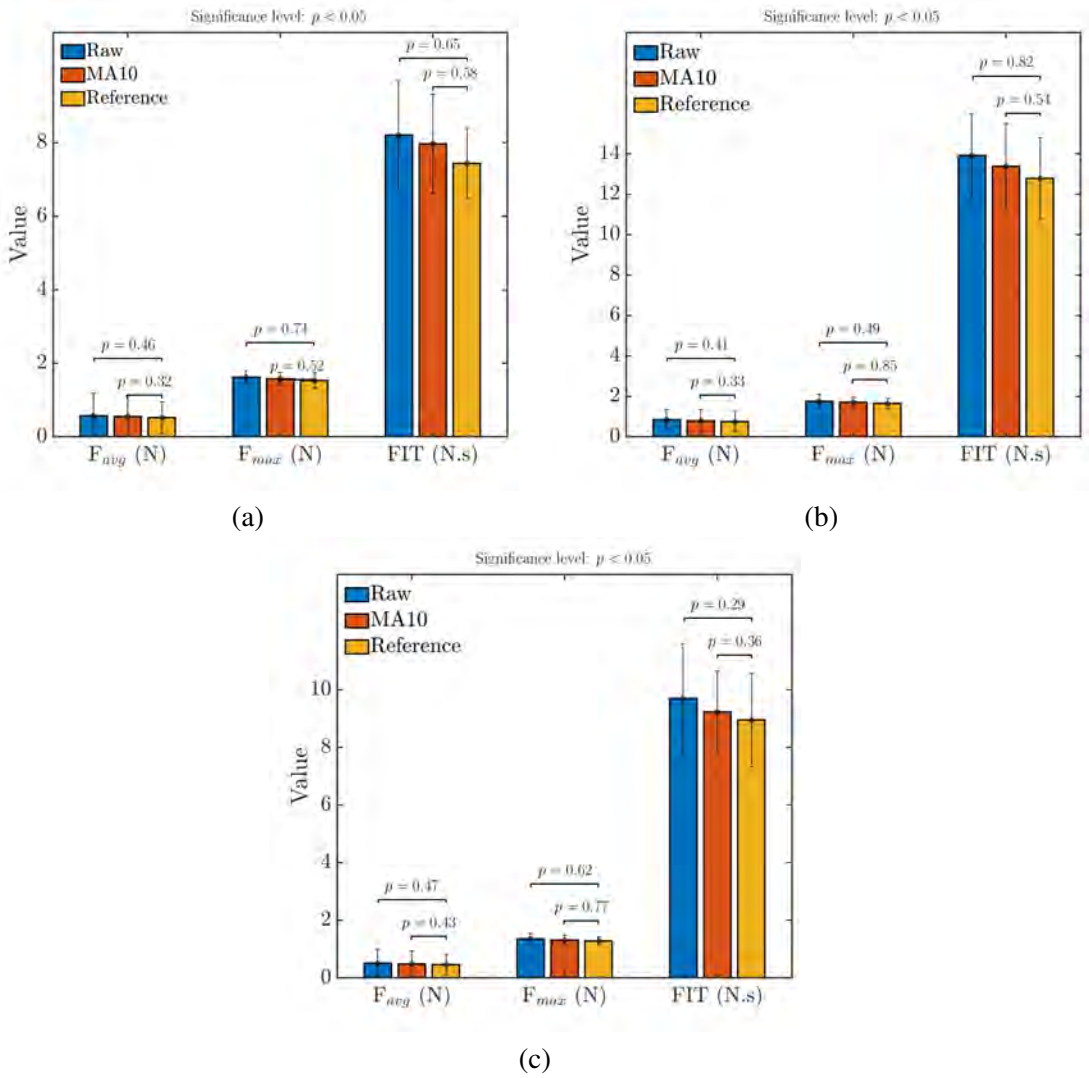

Figure 4.10: Results of the statistical analysis of the performance metrics of iCORD results (*Raw* and *MA10*) with reference data for cannulation of (a) LSA, (b) BCA, and (c) AA. The Wilcoxon signed-rank test for all the comparisons showed no significant difference between the performance metrics of iCORD and reference.

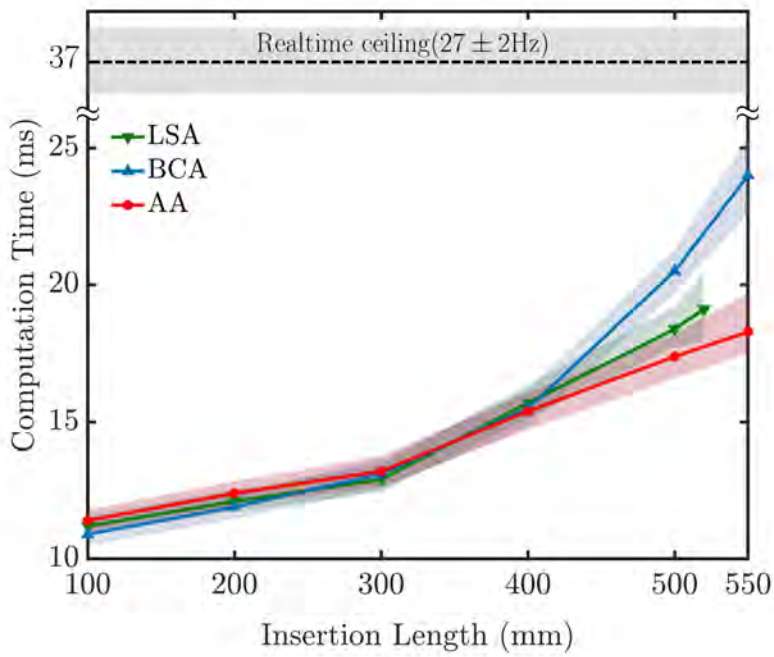

(a)

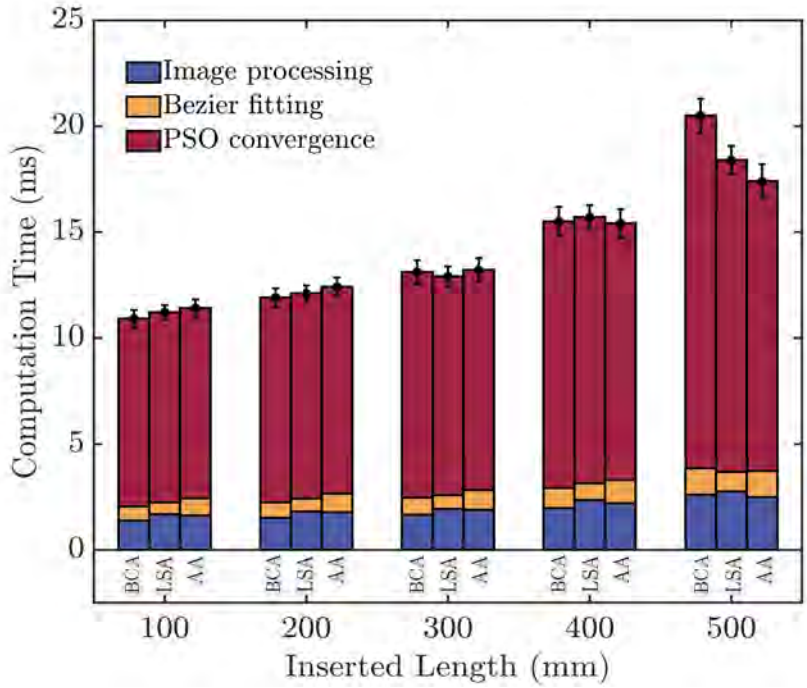

(b)

Figure 4.11: (a) Total computation time for reaching three targets with respect to the inserted length of the catheter and (b) breakdown of computation time for image processing, Bezier fitting, and convergence time of the optimizer.

4.4 Summary

The aim of this study was to propose and validate an inverse Cosserat rod model for endovascular devices for real-time image-based force estimation on EDs. For a continuous and differentiable description of the rod's shape, a fast Bezier shape reconstruction was proposed and validated. Also, the governing equations of the Cosserat rod theory were derived to accommodate the Bezier curve-based kinematics. Moreover, the model incorporated a multiple Gaussian force distribution with an unknown number of forces, with unknown magnitudes and unknown loci. A multi-PSO global optimization schema was proposed and implemented using a GPU-accelerated framework for finding the least number of forces, their magnitude, and loci leading to a similar deformed shape.

The total insertion force was estimated for three arterial cannulations, i.e., LSA, BCA, and AA using the iCORD, while the reference forces were recorded with a pre-calibrated sensor. The statistical analysis of the findings showed that, despite the presence of noise, there was not a significant difference between the estimated performance metrics by iCORD compared to the reference metrics.

The prime contribution of this study was to propose an accurate and fast method for markerless and sensor-free image-based force estimation schema for endovascular devices. Also, *a-priori* knowledge of the vascular anatomy was not required in the proposed method. The author deemed this feature necessary in practice, as it eliminates the need for pre-operative CT-, MRI, or MRA-imaging. Furthermore, the results of this study showed improvement of the minimum detectable force compared to similar studies using shape-based force estimation. Moreover, using a multi-PSO technique allowed for incorporating the number of contact forces as an unknown, which, has not been provided in similar studies. Similar studies have either assumed the number of forces fixed, e.g., [230], or detected the contact points through image-based techniques, e.g., [74].

The real-time performance achieved in this study was mainly due to the utilization of a pre-compiled library of analytical Bezier-based kinematics variables and the parallelized implementation of multi-PSO optimization. To the best of the author's knowledge, such implementation of inverse Cosserat model was not available in the current literature.

Despite the overall slight over-estimation of the performance metrics by the iCORD, the author

deems that it might not compromise the safety of practical use of the iCORD in clinical setups. The reason is that either the iCORD results be used for audio-visual feedback or haptic feedback to the surgeon, such an over-estimation of force will increase the surgeon's caution, thus, does not add to the risk for the patient.

In the present study, stereo-vision was used for obtaining the 3D shape of the catheter in real-time. Although bi-planar fluoroscopy is available in the market and can be used for stereo-vision, this technology is not as abundant as single-plane fluoroscopy. To remedy this limitation, utilization of the recently developed single-camera shape sensing techniques, e.g., [247], can be a significant extension to the iCORD. Another factor for future studies is the sensitivity of the results to uncertainties in the model parameters, e.g., mechanical properties and geometry. Also, in this study, the initial shape of the catheter was assumed as a straight line. Although in this study we utilized a straight catheter, endovascular devices come in various shapes and accurate Bezier-based definition of the initial shape is crucial for accurate results. An extension of this work could be to capture and incorporate the initial shape of the catheter with the same image-acquisition system, prior to the beginning of the surgery. Moreover, integration of the proposed method in a haptics-enabled RCI system is further discussed in the continuation of this thesis.

Although the proposed iCORD method can be used for force estimation on steerable catheters, the proposed solution schema may not be the most optimal for such catheters. The reason is that the deformation of the steerable catheters is typically with a constant bending curvature. Therefore, there is an opportunity to assert this specific type of deformation on the iCORD kinematics and balance equations for finding an analytical solution for force estimation. Also, it was hypothesized that with a fast and robust force estimation on steerable catheters, tactile displays, e.g., [63] and [61], can be used for rendering the contact forces for the surgeon during RCI procedures. Therefore, in the next Chapter the proposed iCORD is adapted to the constant bending curvature of the steerable catheters and an analytical, fast, accurate, and robust force estimation schema for steerable catheters is presented.

Chapter 5

Accurate Estimation of Tip Force on Tendon-driven Catheters using Inverse Cosserat Rod Model (iCORD)

Tip force estimation on tendon-driven catheters is of crucial clinical importance for catheter-based surgeries such as radio-frequency ablation (RFA). Building upon iCORD catheter model, proposed in Chapter 4, a force estimation framework with Bezier spline shape approximation and inverse Cosserat rod model was proposed and validated specifically for RFA catheters. To this end, initially the necessary condition for a Bezier spline to approximate a constant bending radius catheter was derived. Afterward, the kinematics and balance equations of the catheter were derived based on the proposed shape approximation technique and solved to find the tip force. The force estimation problem was formulated as an inverse problem with a functional minimization technique that led to finding an analytical solution the real-time tip force estimation. In the end, the proposed method was experimentally tested for accuracy and computation time. The results showed that the estimated forces were in fair agreement with reference with a mean-absolute error of 0.024 ± 0.020 N and a computation time of 7 ± 5 ms per frame. The exhibited performance was comparable to other studies and was in compliance with the requirements of robot-assisted cardiovascular intervention applications.

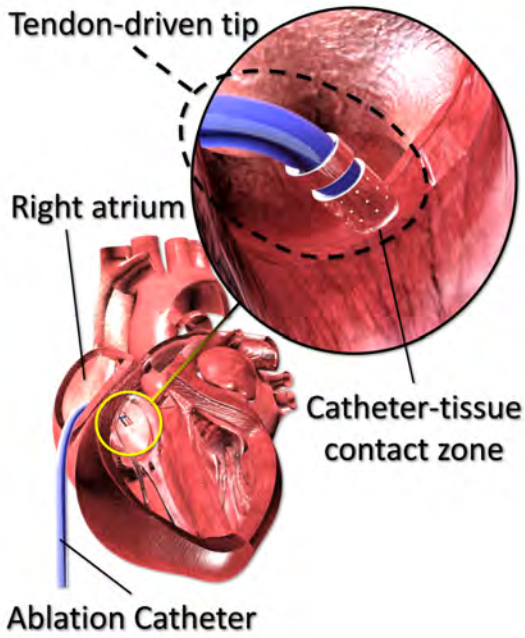

Figure 5.1: The schematic shape of steerable ablation catheters in the right atrium during ablation interventions.

5.1 Introduction

5.1.1 Background

Catheter ablation therapy is the standard-of-care for the treatment of cardiac atrial fibrillation (AFib) [250]. AFib is the cause of cardiac arrhythmia which is the top electrophysiologic disease requiring hospitalizations [250]. Inactivating the over-active cardiac cells, responsible for arrhythmia, is performed by either burning, i.e., radio-frequency ablation (RFA), or freezing, cryo-ablation (CRA). Fig. 5.1 schematically depicts an RFA catheter inside the left atrium. For RFA, a flexible catheter is surgically inserted into the patient's femoral vein and is advanced toward the right or left atrium. Once the tip of the catheter is inside the atrium and in contact with the desired location on the atrial wall, the surgeon performs the ablation to burn the over-active cells. Tip force estimation on tendon-driven catheters is of crucial clinical importance for RFA procedures.

Tendon-driven catheters have a small diameter, e.g, 3–6 mm, thus can be used in minimally-invasive surgeries for endovascular applications. Also, such catheters provide a large workspace for the surgeon as the position of their tip can be controlled by pulling the tendons. For more robust and

dexterous manipulation of the catheters, soft catheters are a favorable choice [251], as they offer flexibility and dexterity. Tendon-driven catheters are a widely-adopted mode of actuation for RFA procedures [252].

A steerable catheter is comprised of a controllable tip part (4–10 cm), a non-steerable body (80–150 cm), and a control handle. The handle typically has a knob mechanism to wind/unwind the tendons which are internally anchored to the tip [252]. Such catheters may also have embedded sensors for direct measurement of contact force at the tip [228, 253]. The limitation of using embedded sensors is in reducing the maneuverability of the catheter, increasing the cost of the catheters, and complicating the design. These have been the technical limitations hindering the wide clinical adoption of sensorized catheters.

On the other hand, a minimum of two tendons is needed to apply bending moment at the tip of such catheters in an agonist-antagonist configuration. Due to non-negligible frictional force between the tendons and the body of the steerable catheters, surgeons usually cannot perceive an accurate measurement of the small forces at the tip of such catheters. In addition for RFA procedures, the range of safe tip force on the catheters is less than 0.3 N [62, 254] and over-steering of catheters is a clinical risk that may lead to tissue perforation and catastrophic outcomes. Also, a minimum tip force of 0.1 N must be maintained at the tip of the catheter in contact with the tissue to attain effective RFA treatment. Therefore, a robust and accurate force estimation method is a clinical need.

5.1.2 Related Studies

To measure the tip forces, researchers have used sensor-based [77, 253] and sensorless approaches. Sensorless methods have been proposed based on continuum mechanics, differential geometry, and particle-based dynamics [62]. Usually, sensorless methods involve deformation estimation through imaging and derivation of kinematics and dynamics equations thereof. Finally, the tip force is obtained through inverse solution techniques [70]. In comparison, the sensor-based methods include less uncertain model parameters, however, require changing the design and structure of the conventional tendon-driven catheters. While sensorless methods are less cumbersome to implement, they

necessitate having accurate modeling of the catheter dynamics and usually involve model parameters with intrinsic uncertainty [62].

The available literature of modeling the mechanics of steerable catheters can be categorized in mechanistic and heuristic (statistical) approaches. As for the mechanistic models, researchers have modeled the deformation of flexible catheters under external load with [255] and without [74] internal tendon actuation. Theoretically, a flexible catheter has infinite degrees-of-freedom (DoFs). However, for simplification, the shape of the catheter has been modeled as a curve [213, 218, 230, 231] with a limited number of DoFs, or a set of rigid segments with elastic joints [46, 195, 256–258]. Recently, accurate results have been obtained for forward dynamics of RFA catheter through employing differential geometry modeling, e.g., Cosserat rod model [213, 218, 259, 260]. However, to the best of the author's knowledge, a differential geometry-based inverse modeling of RFA catheter has not yet been investigated.

Heuristic models such as Gaussian Mixture Models (GMM) and neural networks (NN) have shown favorable real-time performance with low computational cost and the ability to capture the nonlinear effects such as dead-zone and friction [62, 64]. In an early study, Rafii-Tari *et al.* [261] utilized a GMM to obtain the kinematics of catheter maneuvers in an RCI setup. In another effort, Khoshnam *et al.* [120] proposed a Gaussian Mixture Model to estimate the external force on RFA catheters using curvature analysis. Recently, Chi *et al.* [262] encoded the catheter kinematics in a GMM model and used it for kinematic control of catheters. Although GMMs offer the inclusion of nonlinearities, such models require a relatively large dataset and rigorous data preparation for accurate predictions. In addition, redundancy resolution and non-uniqueness are among the serious limitations of heuristic models.

As stated above, sensorless methods of force estimation heavily rely on image-based shape and deformation extraction. Also, the balance equations of steerable catheters employ estimated kinematic variables, e.g., curvature, which typically requires first and second-order differentiation of the shape. Since image-processing provides a pixel-based discretized shape, performing numerical differentiation amplifies the error of resolution or flicker between consecutive frames, thus diminishes the accuracy. Therefore, approximation of the shape with a differentiable shape function is an alternative. As a requirement, such a differentiable shape functions shall have the same dimensionality

as the catheter and satisfy the deformation boundary conditions.

Cosserat rod theory is a widely adopted method to model beams, e.g., catheters, with large spatial deformations [213]. Recently, Aloi *et al.* [218] proposed a Cosserat-based method for estimating force along beams using moving Dirac's delta and truncated Fourier series. Nevertheless, their method involved nonlinear constrained optimization with an iterative solution which is a computationally intensive procedure. Also, Trivisionne *et al.* [247] proposed a force estimation method based on contact mechanics with a constrained optimization solution which required *a-priori* knowledge of anatomy and multiple fiducial markers on the catheter. In another study, Hooshiar *et al.* [74] used a continuum mechanics-based approach for finding the position of contact forces and used those in an inverse finite element method for estimating the contact forces. However, their technique required the computation of a nonlinear geometric stiffness matrix which was computationally expensive. In another study, Jolaei *et al.* [64, 70] proposed a contact mechanics-based method for force estimation. Nevertheless, their method requires real-time tissue characterization to compensate for the cardiac motion.

5.1.3 Motivation and Contributions

In this study, to adapt the proposed iCORD methodology for force estimation for steerable catheters, a Bezier-based shape approximation for tendon-driven catheters was proposed. Afterward, a relationship between the curvature along the catheter and the contact force applied at its tip was obtained using the Cosserat rod theory. Furthermore, the balance equations were re-formed to constitute a generalized norm-minimization problem for which a fast solution is available. In the end, the proposed force estimation method was validated in an experimental test and the error analysis was performed on the results.

The main contributions of this study are:

(1) proposing a continuous and differentiable shape function to derive a generalized analytical form for the catheter deformation,

(2) analytical derivation of the balance equations for the catheter with large deformations, and

(3) proposing a fast and robust analytical method for tip force estimation favorable for image-based force estimation on steerable RFA catheters,

(4) experimental validation of the proposed method and its feasibility assessment through integration with a robotic RFA catheter system.

5.2 Material and Methods

In this section, derivation of the kinematics, constitutive equation, and force balance equation for steerable RFA catheters are provided. The kinematics was a special case of Bezier fitting that fulfilled a single-plane constant bending radius condition [263]. Also, iCORD method proposed in Chapter 4 was adopted for the constitutive and balance equations. In the end, tip force estimation was performed by finding an analytical solution for the balance equations.

5.2.1 Catheter Fabrication and Assembly

The catheter of interest in this study was a tendon-driven steerable catheter with four tendons. Fig. 5.2 shows the fabrication steps and the assembled catheter. The fabricated catheter had a diameter of 6 mm and a length of 40 mm, corresponding to a clinical 18-Fr catheter (1 Fr = $1/3$ mm). The selected length was sufficient to access the interior surface of the right atrium in adults [264].

For the fabrication, a cylindrical mold was rapid-prototyped with a 3D printer (Replicator+, MakerBot, NY, USA). Also, a square platform ($16 \times 16 \times 8$ mm), housing four through-holes, was 3D-printed to provide a platform for the fixed end of the catheter. The through holes were used to accommodate anchorage M2 screws for fixing the mold to the platform and later were used as guides for the four tendons.

The catheter was comprised of a steel compression coil spring with a nominal outer diameter of 5 mm and compressive stiffness of 0.35 $\mathrm{N/mm}$. The spring was installed at the center of the cylindrical mold while silicon rubber material for the body of the catheter (Ecoflex™ 00-20, Smooth-on Inc., PA, USA) was filled in the mold. The use of coil spring enhanced the ability of the catheter to recover to its original shape after deformation. The mold was rested in a vacuum chamber (Best Value Vacs, IL, USA) under 29 mmHg vacuum pressure for discarding the air bubbles (degassing) for 10 minutes. Afterward, the degassed mold was rested at 24°C for final curing. After curing,

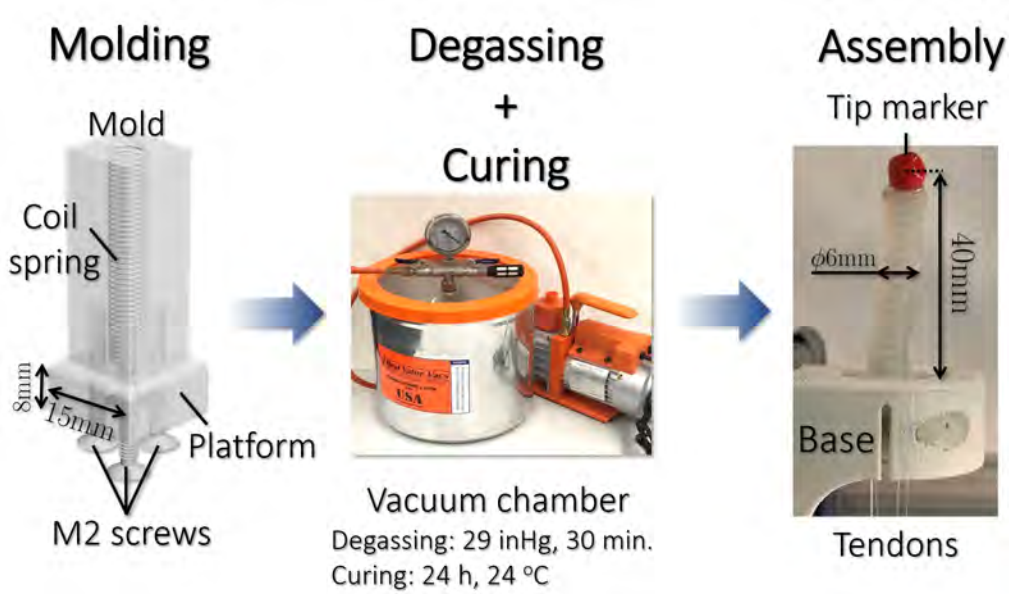

Figure 5.2: Molding, degassing, curing, and assembly steps for prototyping the flexible catheter [64].

the platform was secured in a 3D-printed base. The reason for the base was to make the assembly modular and facilitate the replacement of the catheter and base.

5.2.2 Workspace

Studies have shown that the deformed shape of a steerable catheter is of a constant bending curvature [51, 230]. Moreover, the deformation of such catheters occurs in a single plane, denoted as Γ. Therefore, the shape of the distal section of the catheter was assumed as a circular arc made by co-planar points. The workspace of the catheter was obtained through kinematic analysis in spherical coordinates. Workspace of the catheter was defined as the theoretical locus of the tip of the catheter. Fig. 5.3 depicts the schematic deformed shape of the catheter with $\mathbf{t}$ as the position vector of the tip of the catheter. The original shape of the catheter was assumed to be along the X-axis in Cartesian coordinates. The length-preserving deformation assumption for the catheter [74, 218, 247], necessitates that for all deformations:

$$r\varphi = \mathrm{L} = 40\mathrm{mm}. \tag{79}$$

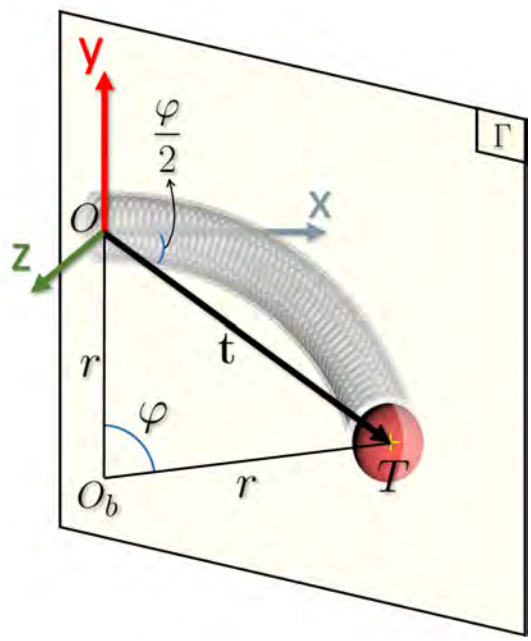

Figure 5.3: Representative deformed shape of the catheter with constant bending radius.

Assuming X-axis as the height axis (zenith direction) in the spherical coordinates, the spherical representation of $\mathbf{t}$ was convened as:

$$\mathbf{t} = \begin{pmatrix} \rho \\ \theta \\ \varphi/2 \end{pmatrix}. \tag{80}$$

From the geometric relations in $\triangle OTO_b$:

$$\rho = ||\mathbf{t}|| = 2r \sin \frac{\varphi}{2} \tag{81}$$

Eliminating r in Eq. 79 and Eq. 81 resulted in:

$$\rho \frac{\varphi/2}{\sin \varphi/2} = \mathrm{L}. \tag{82}$$

In fact, Eq. 82 represents the locus surface of the theoretical workspace of the tip of the catheter in spherical coordinates. The theoretical workspace was visualized for $\varphi \in (-\pi, \pi]$. Since the workspace is independent of θ (inclination direction), the workspace is theoretically axisymmetric with respect to the height direction (X-axis).

In practice, the feasible workspace of the catheter was a sub-domain of the theoretical workspace

due to limitations in the tendons actuation.

The feasible workspace of the catheter was obtained through an experiment by pulling the tendons from their rest position to the feasible extremes, i.e., 10 mm. The position of the tip marker of the catheter was obtained through stereo-vision. Fig. 5.4(a) depicts the theoretical and feasible workspace of the catheter and Fig. 5.4(b) depicts the error distribution of the feasible workspace with the theoretical workspace. Post-processing indicated a maximum absolute error of 0.8 mm (2% of the nominal length of the catheter) between the theoretical workspace and feasible workspace.

Relative small error between the theoretical workspace and experimental observation confirmed the constant bending curvature assumption. Therefore, the force estimation method was developed adopting this special case of deformation.

5.2.3 Shape Interpolation

Real-time x-ray imaging, a.k.a., fluoroscopy, is present during catheterization procedures and can be used to obtain the position of the tip of the catheter. Nevertheless, the author's findings in [64] for a similar catheter showed that the tip position of the catheter can be accurately predicted using the lengths of the tendons. In this study, the shape of the catheter, $\mathbf{c}(s)$, was interpolated using a Bezier spline of the form:

$$\mathbf{c}(s) = \begin{pmatrix} x(s) \\ y(s) \\ z(s) \end{pmatrix} = \begin{pmatrix} \mathbf{p}_0 & \cdots & \mathbf{p}_n \end{pmatrix} \begin{pmatrix} \begin{pmatrix} n \\ i \end{pmatrix} (1-s)^{n-1} s^i \\ \vdots \\ \begin{pmatrix} n \\ i \end{pmatrix} (1-s)^{n-1} s^i \end{pmatrix}. \tag{83}$$

where, $s \in [0, 1]$ is the normalized length parameter, n is the degree of the spline, and $\mathbf{p}_i \in \Gamma$ are the control points determining the shape of $\mathbf{c}(s)$. Previously, the author has derived the kinematics of tendon-driven catheters and have experimentally validated the circular arc shape assumption for the tendon-driven catheters [64].

As depicted in Fig. 5.5(a) the spatial deformation of the tendon-driven catheter was assumed to occur in the Γ-plane. Control points $\mathbf{p}_0 = \mathbf{c}(0)$ and $\mathbf{p}_3 = \mathbf{c}(1)$ determine the base and tip of the

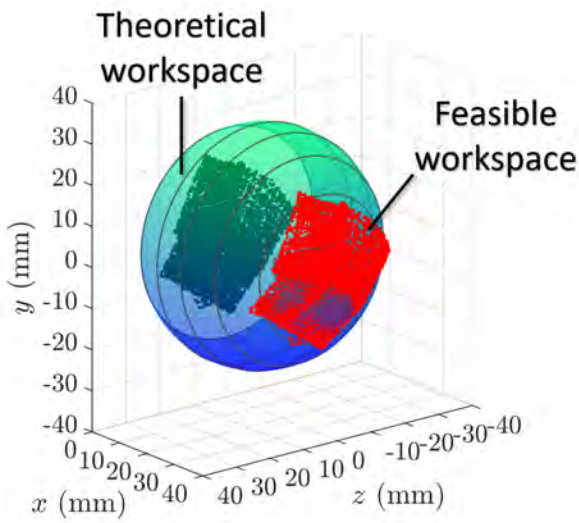

(a)

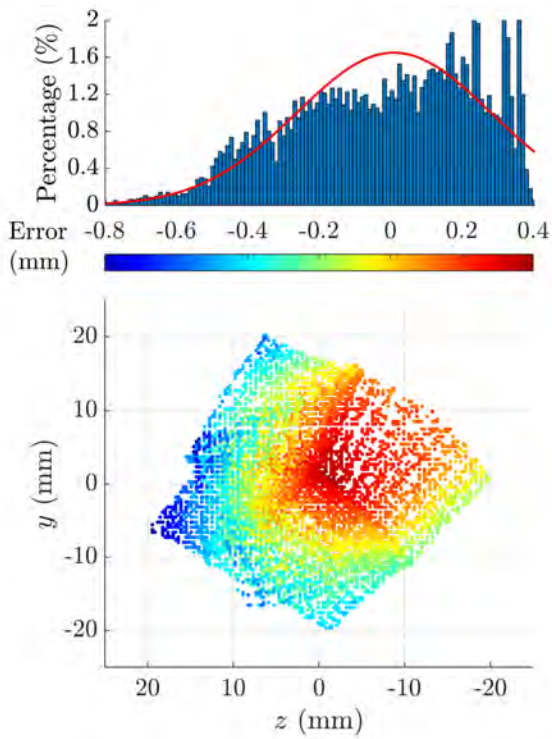

(b)

Figure 5.4: (a) Comparison of the theoretical workspace and the feasible workspace of the catheter, and (b) distribution of the error between the experimental and theoretical workspace.

catheter in global coordinates, respectively. The position of tip and base of the catheter was obtained by real-time image processing and through pinhole camera model calibration described in Chapter 3.

It can be shown that $n = 3$ is the minimum Bezier degree necessary for generating a constant radius circular arc r. Thus, a Bezier spline of degree $n = 3$ was selected for the shape approximation.

To satisfy the Dirichlet and Neumann boundary conditions of the catheter as a cantilever beam, $\mathbf{c}(s)$ shall necessarily satisfy the boundary conditions in Eq. 84–85. In addition, the tip of the Bezier line shall collocate and align with the tip of the catheter from the image (Eq. 86–87). It is noteworthy that in Bezier splines, the first and last control points necessarily reside on the curve.

In the following, it was assumed that the global coordinate system was collocated with the base of the catheter. Also without loss of generality, it was assumed that the deformation occurred in the XY-plane. In case the deformation is in another plane, a linear mapping with a rotation matrix, $\mathbf{R} \in \mathfrak{so}(3)$, could map the local coordinates (in the Γ-plane) to the global coordinates. Therefore:

$$\mathbf{p}_0 = \mathbf{c}(0) = \begin{pmatrix} 0 \\ 0 \\ 0 \end{pmatrix}, \tag{84}$$

$$\mathbf{p}_1 = \lambda \mathrm{L} \begin{pmatrix} 1 \\ 0 \\ 0 \end{pmatrix}, \tag{85}$$

$$\mathbf{p}_3 = \mathbf{c}(1) = \begin{pmatrix} x \\ y \\ 0 \end{pmatrix}, \tag{86}$$

where, x and y are the horizontal and vertical coordinates of the tip in Γ, and $\lambda \in [0, 1]$ is a constant which controls the curvature throughout the Bezier spline. Also, the shape-fitting spline shall be

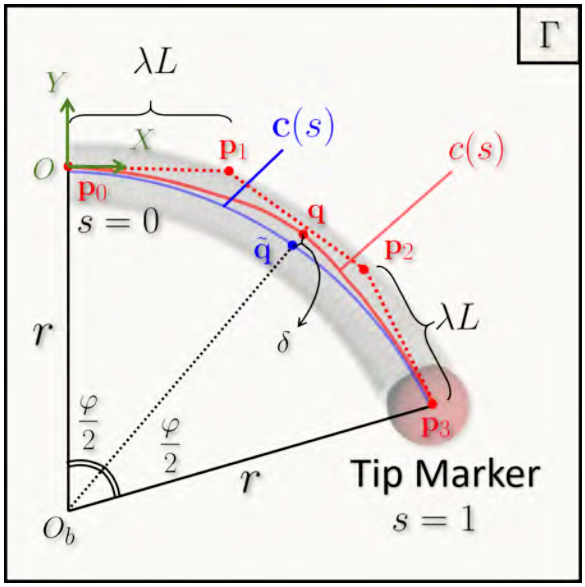

(a)

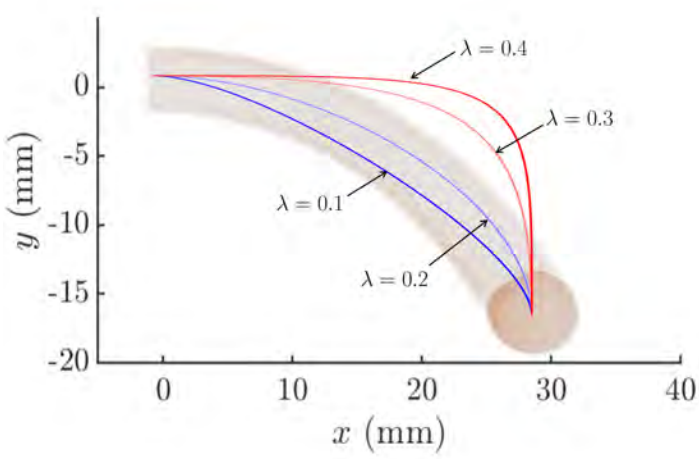

(b)

Figure 5.5: (a) Schematic deformed shape of a typical tendon-driven catheter with the geometric definition of parameters, (b) representative Bezier curves with various λ's for shape approximation.

symmetric with respect to $\overline{\mathbf{O}_b\tilde{\mathbf{q}}}$ bisector. Therefore:

$$||\mathbf{p}_3 - \mathbf{p}_2|| = \lambda \mathrm{L} \Rightarrow \mathbf{p}_2 = \begin{pmatrix} x \\ y \\ 0 \end{pmatrix} - \lambda \mathrm{L} \begin{pmatrix} \cos\varphi \\ \sin\varphi \\ 0 \end{pmatrix} \tag{87}$$

From the derived kinematics above, the bending angle and radius of curvature of the catheter are:

$$r = \frac{x^2 + y^2}{2y} \tag{88}$$

$$\varphi = \frac{\mathrm{L}}{r}. \tag{89}$$

By substituting Eq. 84–87 in Eq. 83, the shape fitting problem was reduced to the determination of λ. In fact, λ is a shape parameter that determines the convexity (radius of curvature) of the Bezier spline.

To find the best fitting λ, it was necessary that the mid-point of $\mathbf{c}(s)$, $\mathbf{q}$, collocate with the mid-arc $\tilde{\mathbf{q}}$. Using the position of $\tilde{\mathbf{q}}$:

$$\tilde{\mathbf{q}} = r \begin{pmatrix} \sin\frac{\varphi}{2} \\ 1 - \cos\frac{\varphi}{2} \\ 0 \end{pmatrix}, \tag{90}$$

the collocation of $\mathbf{q}$ and $\tilde{\mathbf{q}}$ was formulated as:

$$\delta = ||\mathbf{c}(s)|_{s=\frac{1}{2}} - \tilde{\mathbf{q}}||^2 = 0. \tag{91}$$

Analytical solution of Eq. 91 in Maple R2020 software (Maplesoft Inc., ON, Canada) revealed two distinct real roots for Eq. 91. Signum analysis showed that the two roots, λ_1 and λ_2, have the following unconditional property:

$$\lambda_1 \lambda_2 < 0. \tag{92}$$

Given that λ in this problem shall be strictly positive, the admissible solution was:

$$\lambda = \frac{-\sqrt{4(1-\cos\varphi)\left(((r-\frac{x}{2})^2-\frac{y^2}{4})\cos\varphi+y(r-\frac{x}{2})\sin\varphi+r^2+rx-\frac{x^2+y^2}{4}\right)}-y\cos\varphi+(2r-x)\sin\varphi+y}{60(\cos\varphi-1)}. \tag{93}$$

5.2.4 Kinematics

For the described single-plane bending of the catheter, the only kinematic variable was κ_g. With the definitions, provided in Appendix A, κ_g was found as:

$$\kappa_g(s) = -\frac{x'(s)y''(s) - y'(s)x''(s)}{(x'^2(s) + y'^2(s))^{\frac{3}{2}}}, \tag{94}$$

with $(.)' = \frac{\mathrm{d}}{\mathrm{d}s}(.)$ as the derivation operator. For demonstration, Fig. 5.6 depicts circular arcs, their Bezier fittings, and their corresponding κ_g-s. As shown the proposed shape interpolation resulted in fair curvature approximations. However for bendings with $|\varphi| > \pi$, adopting an $n > 3$ would be necessary for accurate curvature approximation. Nevertheless, in the scope of this study the bending angles were fairly smaller than π.

5.2.5 Constitutive Equation

Based on Cosserat rod model for cantilever beams, the relationship between the bending deformation $\boldsymbol{\chi}(s)$ for single-plane bending simplifies:

$$\mathbf{m}(s) = \mathbf{R}\mathbf{K}_u\boldsymbol{\chi}(s) = \mathbf{R}\mathbf{K}_u(\mathbf{u} - \mathbf{u}^\star). \tag{95}$$

The rotation matrix $\mathbf{R}$, bending stiffness $\mathbf{K}_u$, bending deformation $\mathbf{u} - \mathbf{u}^\star$, and geodesic curvatures $\kappa_g(s)$ and $\kappa_g^\star$ were previously derived for a Bezier spline in Chapter 3 and 4. Thus, with the described single-plane bending, the constitutive equation (Eq. 95) simplifies to:

$$\mathbf{m}(s) = \mathrm{EI}\begin{pmatrix} 0 \\ 0 \\ \kappa_g(s) - \kappa_g^\star(s) \end{pmatrix}. \tag{96}$$

with EI as the flexural rigidity of the catheter. The constitutive equation implies that the internal bending moment has only an out-of-plane component perpendicular to Γ (in this case XY-plane). Also, by assuming the initial shape of the catheter as a straight line, $\kappa_g^\star(s) = 0$.

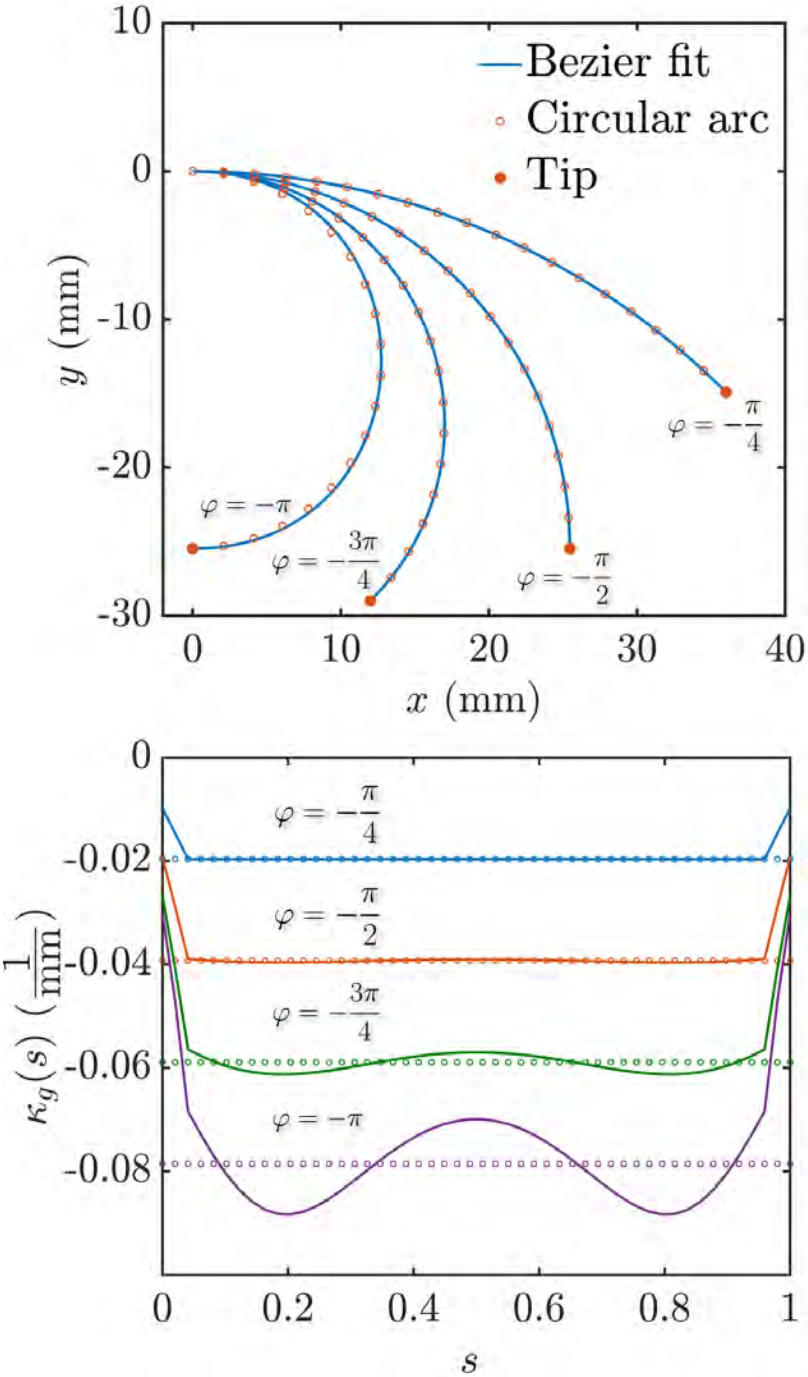

Figure 5.6: Interpolated shapes of circular arcs and their corresponding curvatures.

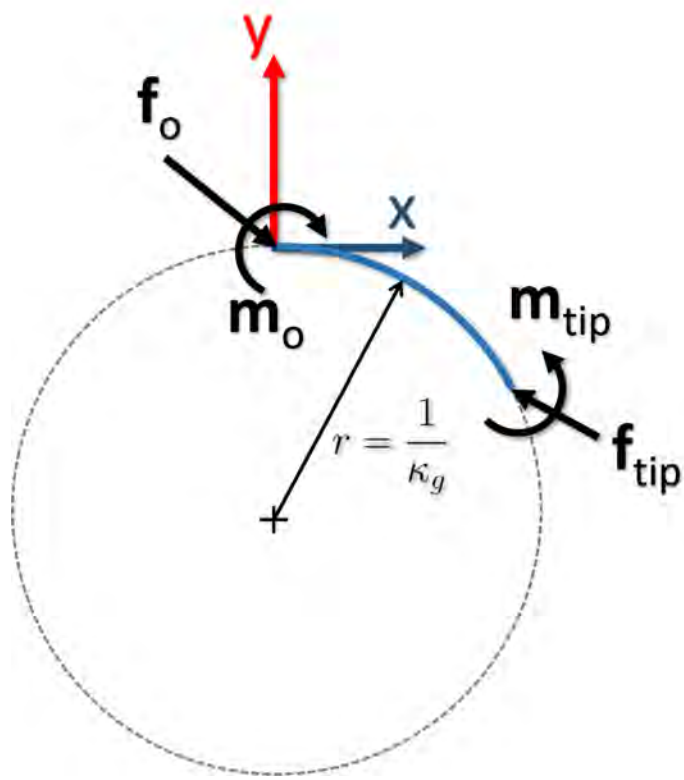

Figure 5.7: The free-body diagram (FBD) of a deformed tendon-driven catheter with constant bending radius deformation.

5.2.6 Moment Balance

Fig. 5.7 shows the free-body diagram (FBD) of a tendon-driven catheter at equilibrium. The catheter is bent as a result of an external tip force $\mathbf{f}^{\text{Tip}}$ and an external tip bending moment $\mathbf{m}^{\text{Tip}}$. The tip force is the contact force between the catheter and the cardiac tissue while the tip moment is applied because of the pulling in the catheter's steering tendons. Quasi-static equilibrium of the FBD depicted in Fig. 5.7 shows that the force and moment at the base of the catheter applied to it from its anchorage are:

$$\mathbf{f}_0 = -\mathbf{f}^{\text{Tip}}, \tag{97}$$

$$\mathbf{m}_0 = -\mathbf{m}^{\text{Tip}} - \begin{pmatrix} x \\ y \\ 0 \end{pmatrix} \times \mathbf{f}^{\text{Tip}}. \tag{98}$$

Also, the moment balance equation at any given point $\mathbf{p}(s) = \begin{pmatrix} x(s) & y(s) & 0 \end{pmatrix}^{\mathsf{T}}$ throughout the catheter is:

$$\mathbf{m}(s) = \mathbf{m}^{\text{Tip}} + \begin{pmatrix} x - x(s) \\ y - y(s) \\ 0 \end{pmatrix} \times \mathbf{f}^{\text{Tip}}. \tag{99}$$

Substituting the constitutive definition of $\mathbf{m}(s)$ from Eq. 96, the balance equation, which relates the shape of the catheter to the unknown tip force, was obtained as:

$$\mathbf{m}^{\text{Tip}} + \begin{pmatrix} x - x(s) \\ y - y(s) \\ 0 \end{pmatrix} \times \mathbf{f}^{\text{Tip}} = \text{EI} \begin{pmatrix} 0 \\ 0 \\ \kappa_g(s) \end{pmatrix}. \tag{100}$$

This equation is a vectorial equation with two trivial scalar equations ($0 = 0$) from the first and second rows and an under-determined scalar equation from the third row:

$$m^{\text{Tip}} + f_y\left(x - x(s)\right) - f_x\left(y - y(s)\right) = \text{EI}\kappa_g(s), \tag{101}$$

with m^{Tip} as the external tip moment applied through pulling the steering tendons, f_x and f_y as the horizontal and vertical components of the tip force in the bending angle, respectively. The tip

bending moment was known in real-time by measuring the torque of the driving motor. Further details on measuring m^{Tip} are provided in Sec. 5.3.2.2.

5.2.7 Inverse Solution

5.2.7.1 Solution schema

As stated earlier, Eq. 101 is under-determined with two unknowns and one equation. However, the balance equation must be satisfied for all the points along the catheter's length, i.e., $s \in [0, 1]$. Therefore, the force estimation was formulated as a minimization problem over $s \in [0, 1]$ domain. This solution approach is regarded as the *exact formulation* in the literature [62]. To find f_x and f_y through minimization, functional $\Pi(f_x, f_y)$ was defined as:

$$\Pi(f_x, f_y) = \int_0^1 \Big(m^{\text{Tip}} + f_y\big(x - x(s)\big) - f_x\big(y - y(s)\big) - \text{EI}\kappa_g(s)\Big)^2 \mathrm{d}s. \tag{102}$$

Functional $\Pi(f_x, f_y)$ represents the summation of the residual of momentum balance equation along the length of the catheter. Minimization of $\Pi(f_x, f_y)$, in fact, enforces Eq. 101 throughout the length of the catheter. The functional was further simplified to Eq. 104 by introducing:

$$\eta(s) = m^{\text{Tip}} - \text{EI}\kappa_g(s), \tag{103}$$

$$\Pi(f_x, f_y) = \int_0^1 \Big(f_y\big(x - x(s)\big) - f_x\big(y - y(s)\big) + \eta(s)\Big)^2 \mathrm{d}s. \tag{104}$$

The tip force applied on the catheter is from contact with the environment. By assuming a frictionless contact, for the sake of simplicity, and given that contact forces are perpendicular to the surface of the contacting bodies, the tip force was assumed to be perpendicular to $\mathbf{c}(s)$ at the tip. This assumption has been experimentally validated for steerable catheters in [51]. The condition necessitated:

$$f_x \cos\varphi + f_y \sin\varphi = 0 \rightarrow f_x = -f_y \tan\varphi. \tag{105}$$

Using Eq. 105, functional Π simplified to:

$$\Pi(f_y) = \int_0^1 \left(f_y\Big(x - x(s) + \tan\varphi\big(y - y(s)\big)\Big) + \eta(s)\right)^2 \mathrm{d}s. \tag{106}$$

The necessary condition for minimizing $\Pi(f_y)$ was:

$$\frac{\partial}{\partial f_y}\Pi(f_y) = 0, \tag{107}$$

which expanded to:

$$f_y \int_0^1 \Big(x - x(s) + \tan\varphi\big(y - y(s)\big)\Big)^2 \mathrm{d}s = -\int_0^1 \eta(s)\Big(x - x(s) + \tan\varphi\big(y - y(s)\big)\Big)\mathrm{d}s. \tag{108}$$

Therefore, external forces f_x and f_y were obtained as:

$$f_y = -\frac{\int_0^1 \eta(s)\Big(x - x(s) + \tan\varphi\big(y - y(s)\big)\Big)\mathrm{d}s}{\int_0^1 \Big(x - x(s) + \tan\varphi\big(y - y(s)\big)\Big)^2 \mathrm{d}s}, \tag{109}$$

$$f_x = -f_y \tan\varphi. \tag{110}$$

Given that the parametric expressions of $x(s)$, $y(s)$, and $\kappa_g(s)$ were obtained through kinematic analysis with the proposed shape interpolation, the integrals in Eq. 109 were evaluated in real-time using RK4 method. The parameters involved in the integrals were $\mathbf{p}_{0-3}$, $\kappa_g(s)$, m^{Tip}, x, and y which were determined in each frame.

A special case of catheter shape is $y(s) = y$ that happens when the catheter is with a straight-line shape. In this case, Eq. 109 may indicate non-zero force if $\eta(s) \neq 0$. In fact, simultaneous $y(s) = y$ and $\eta(s) \neq 0$ happens when there is an external bending moment at the tip without a change in the shape, which indicates the presence of a resistance force at the tip against the deformation.

5.2.7.2 Existence and uniqueness

Unless $f_y = 0$, Eq. 106 is a quadratic and strictly positive function of f_y. Therefore, irrespective of x, y, φ, and $\eta(s)$, there exists only one $f_y \in \mathbb{R}$ which unconditionally minimizes Π. Fig. 5.8 shows the variation of Π with respect to $\eta(s)$ and f_y for a representative bending angle, i.e., $\varphi = -\pi/6$. As depicted, the Π-surface is convex and has one global minimum for any given $\eta(s)$. Similar variation of Π was observed for other bending angles.

5.2.8 Model Parameters

The model parameters required in the proposed method are the length of the catheter, L, and its flexural rigidity EI. The length of the prototyped catheter, measured with a caliper three times,

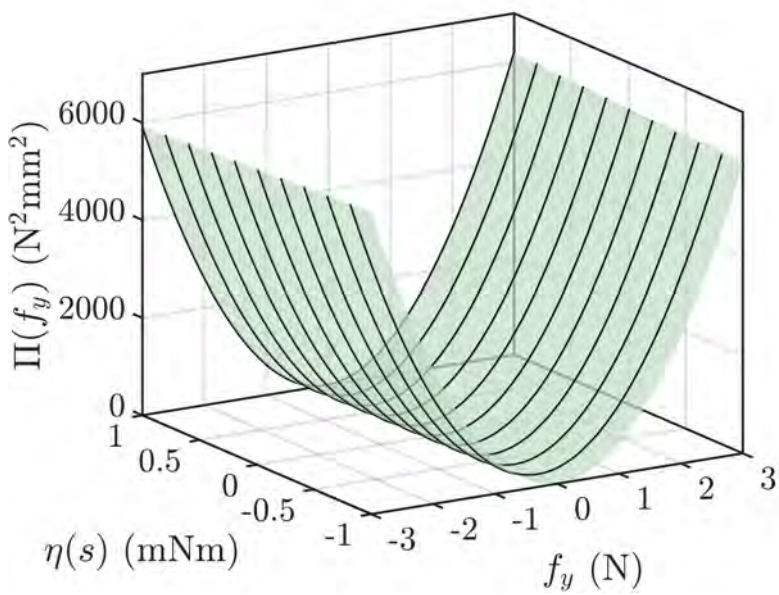

Figure 5.8: Variation of Π with respect to f_y and $\eta(s)$ and the contours of constant $\eta(s)$ shows the uniqueness and existence of f_y for various $\eta(s)$.

was 40.71 ± 0.25. To obtain the flexural rigidity a cantilever bending test was performed on the prototyped catheter and repeated three times. A test jig was designed and 3D printed to provide a cantilever test fixture. Fig. 5.9(a) shows the prototyped catheter under the cantilever test.

Given that the prototyped catheter was not slender, a Timoshenko beam model for the determination of EI was adopted. The flexural rigidity of a prismatic Timoshenko beam with a circular cross-section from cantilever bending test was obtained using [265]:

$$\mathrm{EI} = \frac{k_c}{6}\left(\frac{\pi r_c^2 \mathrm{L}(4+5\vartheta)}{4} + 2\mathrm{L}^3\right), \tag{111}$$

with $k_c = 0.011$ N/mm as the slope of the experimental force-displacement curve (Fig. 5.9(b)), ϑ as the Poisson's ratio, and r_c as the radius of the cross-section of the beam. Because of the hyperelastic material used in the prototyped catheter, ϑ was assumed 0.49, representing a nearly incompressible material, and r_c was 3 mm. The estimated EI was obtained as $\mathrm{EI} = 238.01$ Nmm^2.

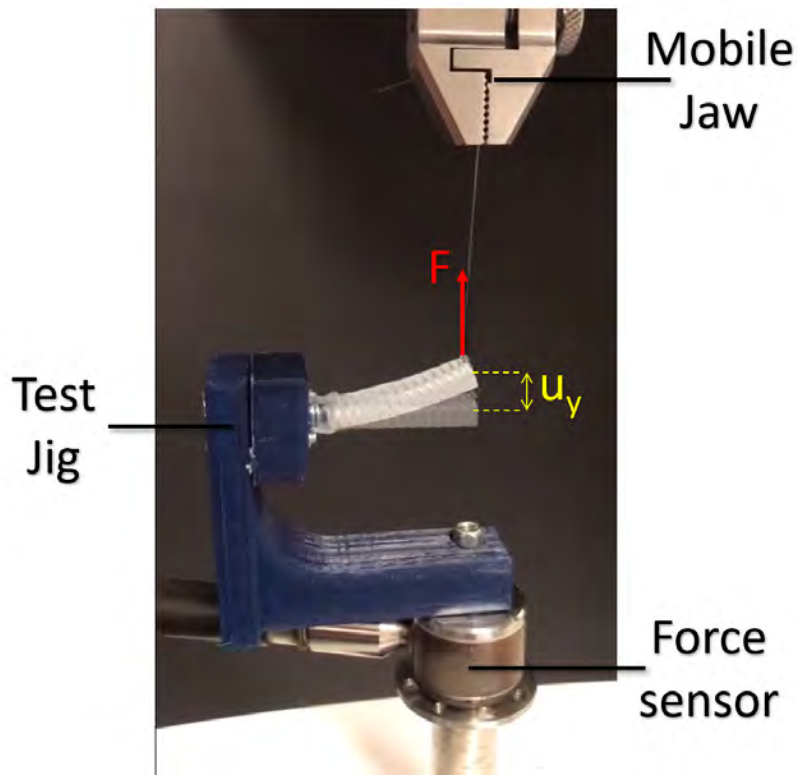

(a)

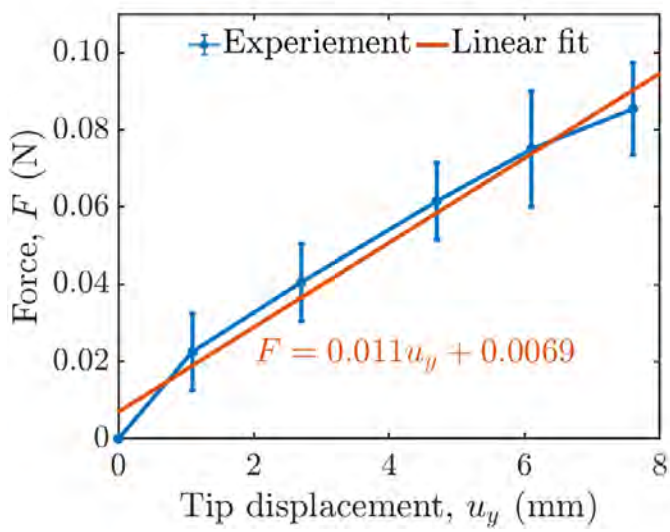

Figure 5.9: (a) the prototyped catheter under cantilever bending test and (b) the force-displacement curve of the bending test.

5.3 Validation Studies

To assess the performance of the proposed force estimation method, a simulation-based validation study and an experimental study were performed. In the simulation-based validation, three different catheters with various tip moment and forces were simulated in commercial finite-element analysis software (Ansys R17.0, PA, USA). The objective of the first study was to assess the accuracy of the proposed tip force estimation method. In the second study, the performance of the proposed force estimation method was investigated in experiments with a prototyped steerable catheter (described in Sec. 5.2.1) with two different tip moments while it was in contact with a moving tissue phantom. The objective of the second experimental study was to assess the accuracy of the proposed method while integrated with a representative robot-assisted catheter actuation system. To this end, a tendon-driven catheter control system, previously co-developed and validated by the author, was used to drive the catheter [70]. In the following, the details of the validation studies, protocol, and results are provided.

5.3.1 Study I: Simulation-based Validation

5.3.1.1 Simulation Protocol

The constructed finite-element models of the catheter were similar to the prototyped 18-Fr catheter, i.e. 40 mm length and 6 mm diameter. Three simulations with flexural rigidities of 238, 500, and 750 Nmm^2 were performed. In each simulation, initially the catheter was subjected to an external tip moment of -18 mNm to have an initial downward deflection. After the initial bending, a monotonically-increasing tip force with a final magnitude of 0.3 N was applied perpendicular to the tip of the deformed catheter to decrease its curvature. This loading scenario simulated the clinical condition when the tip of the steerable catheter is in contact with the heart while the heart's wall moves due to the beating.

For each simulation, the deformed shapes of the catheter were exported for 0.1 N, 0.2 N, and 0.3 N as images to be used for force estimation. The shape extraction and force estimation were performed on the images of the deformed catheters. The shape extraction and force estimation algorithms were developed in Matlab R2020 (Mathworks Inc, MA) according to the proposed method. For the force estimation, the tip moment was assumed as an *a-priori* knowledge, i.e., $m^{\text{Tip}} = -18$ mNm. In the

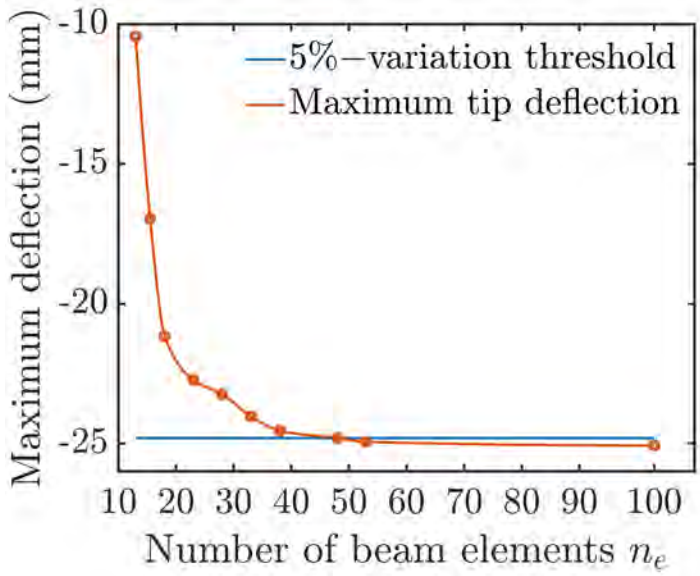

Figure 5.10: Variation of the maximum tip deflection with the number of elements in Study I.

end, the estimated force on each image was compared with the forces used in the finite-element simulation.

The finite-element model of the catheter was constructed using quadratic `beam` elements with large deflection. The minimum number of elements leading to less than 5% variation in the maximum tip deflection, subjected to $m^{\text{Tip}} = -18$ mNm, was $n_e = 48$. Thus, the model was meshed with $n_e = 50$ elements. Fig. 5.10 depicts the variation of the tip deflection with the number of elements.

5.3.1.2 Results

Fig. 5.11 shows the deformed shape of the catheters after the initial $m^{\text{Tip}} = -18$ mNm and after tip forces of 0.1 N, 0.2 N, and 0.3 N. The images in Fig. 5.11 were used as inputs in the Bezier interpolation and force estimation algorithms in Matlab. In this regard, Fig. 5.12 depicts a representative input image to the Bezier interpolation algorithm and the output interpolated Bezier spline.

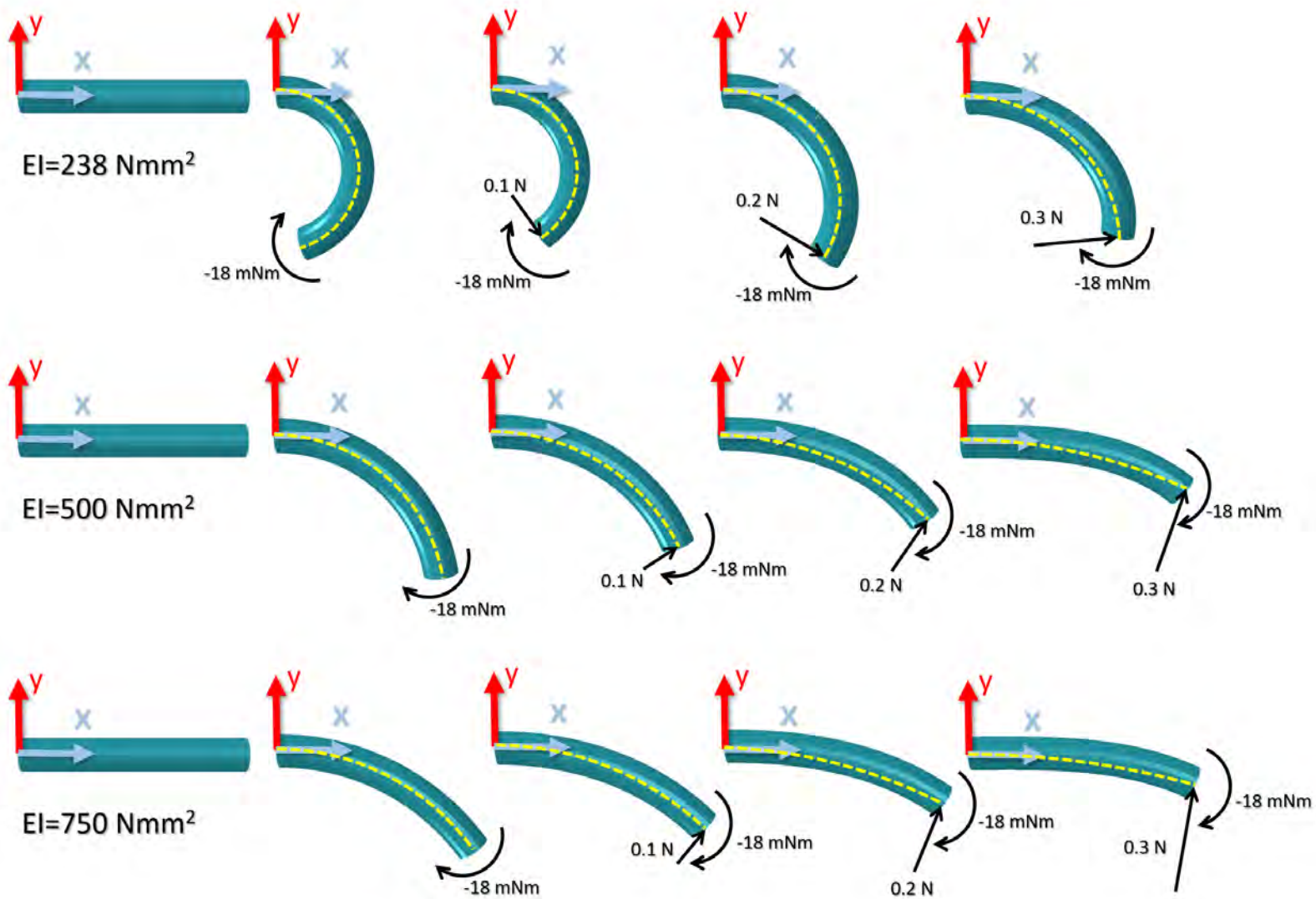

Figure 5.11: Deformed shape of the catheters subjected to the initial $m^{\text{Tip}} = -18$ mNm, and tip force of 0 N, 0.1 N, 0.2 N, and 0.3 N.

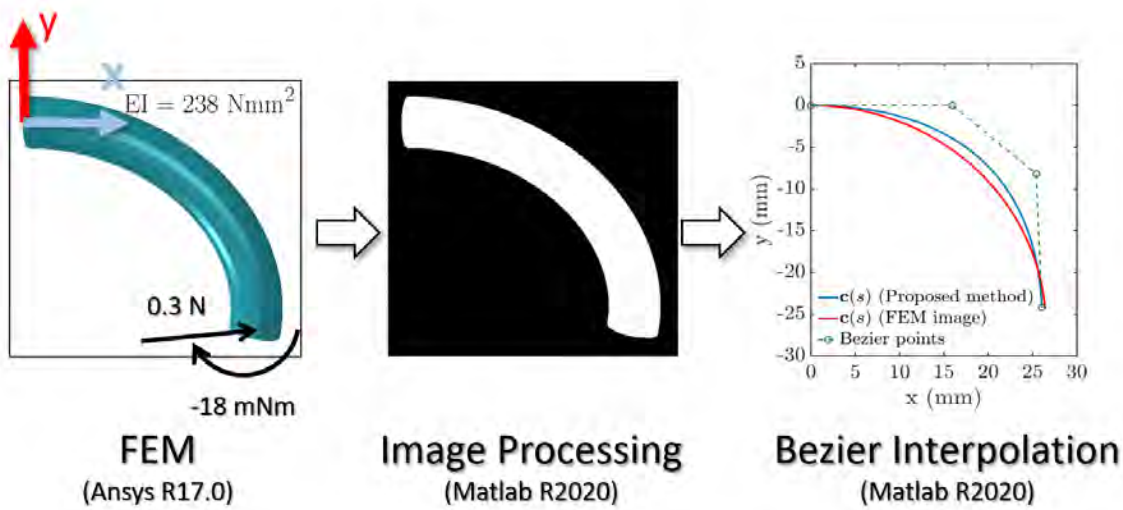

Figure 5.12: Representative input image to the shape extraction algorithm and the output interpolation result for EI $= 238$, $m^{\text{Tip}} = -18$ mNm, $f^{\text{Tip}} = 0.3$ N, and $\lambda = 0.396$.

For each image of the deformed catheter (n=12), first λ was obtained using the proposed shape interpolation method (Eq. 93). Afterwards by using λ (output of Bezier interpolation), $x(s)$ and $y(s)$ were reconstructed and used in Eq. 109 to estimate the force. Table 5.1 summarizes the results of shape interpolation and force estimation in terms of the magnitude and angle (with respect to $+x$-axis) of estimated forces.

The comparison of the estimated forces with the reference forces showed that the force estimation had an average error of 0.013 ± 0.010 N (4.3% of the maximum force). Also, the shape interpolation had an average bending angle error of $-0.3^\circ \pm 1^\circ$ (0.2% of the maximum bending angle). Another observation was that in all the cases the proposed method had slightly overestimated the tip force. However, the error in angle estimation varied in different load-cases. The reason for the slight overestimation might have been in the fact that after initial bending, the tip force tends to change the distribution of the internal moment to a non-uniform state. With that, the bending radius along the catheter slightly changes and violates the assumption of constant bending radius. Also, the overestimation error has increased with the flexural rigidity. Nevertheless, the least overestimation was observed in EI $= 238$ Nmm^2, which is the flexural rigidity of the prototyped catheter in this study.

Table 5.1: Comparison of the estimated force and reference force in Study I.

EI (Nmm^2)	λ	Tip Force ($\|\|\mathbf{f}^{Tip}\|\|$)			Force Angle (φ)		
		Reference (N)	Estimated (N)	Error (N)	Reference (°)	Estimated (°)	Error (°)
238	0	0.0	0.000	0.000	0 -161.2	-162.8	-1.6
	0.483	0.1	0.107	0.007	-143.7	-145.1	-1.4
	0.414	0.2	0.218	0.018	-121.6	-122.9	-1.3
	0.396	0.3	0.322	0.022	-82.3	-82.3	-1.0
500	0.376	0.0	0.000	0.000	-76.2	-77.1	-0.5
	0.365	0.1	0.112	0.011	-57.5	-56.8	+0.7
	0.321	0.2	0.216	0.016	-36.3	-34.9	+1.4
	0.290	0.3	0.317	0.027	-20.1	-19.4	+0.7
750	0.311	0.0	0.000	0.000	-52.1	-53.0	-0.9
	0.288	0.1	0.111	0.011	-37.9	-36.9	-1.0
	0.262	0.2	0.222	0.022	-22.1	-21.7	+0.6
	0.233	0.3	0.325	0.025	-9.7	-9.2	-0.5
Mean±SD	-	-	-	0.013±0.010	-	-	-0.3±1.0

5.3.2 Study II: Experimental Validation

5.3.2.1 Setup and Protocol

To actuate the steerable catheter, a tendon drive system was used in this study. The author has previously co-developed an integrated mechatronic system with a learning-based method for the tip position control of this system in [64, 70]. The system used a learning-based method with artificial neural networks (ANN) and support vector classification (SVC) for position and tension control on the tendons of the steerable catheter. It was capable of controlling the tip position with an MAE error of 0.46 mm. The details of the control methods are provided in [64] and [70] for further solicitation but is not part of the contributions of this study.

In summary, the system had mechanical, electrical, and software modules. Fig. 5.13(a) shows the components of the mechanical module of the catheter control system. Four independent stepper motors were used to control the length and tension of the tendons to attain the desired tip position. Fig. 5.13(b) depicts the software architecture used for the feedback control of the motors, trajectory error estimation, and data storage. The software module was composed of two components: the user interface (UI), running on a PC workstation, and the firmware (FW), uploaded on the microprocessors. The UI was used to acquire the user inputs, i.e., the desired tip position (and tendon tensions)

and to perform real-time data acquisition and storage. The FW was used to perform low-level tendon length and tension control based on the user inputs from UI. In this study, the tip position of the catheter, i.e., $\begin{pmatrix} x & y \end{pmatrix}^{\mathsf{T}}$ was obtained through stereo-vision and triangulation. For shape interpolation in this study, the trajectory of the tip marker (red sphere at the tip of the catheter) was tracked in real-time using the two USB cameras (800×600 pixels resolution, model C920, Logitec, Lausanne, Switzerland) with a stereo-calibration adopted from [185, 209]. The stereo-vision verification on a checkerboard template (depicted in Fig. 5.13(b)) showed an error of ± 0.26 mm in detecting the corners of the squares in the template.

5.3.2.2 Estimation of tip bending moment m^{Tip}

To control the tip position of the catheter, four nylon tendons were anchored to its tip and were driven using four independent NEMA-11 stepper motors. The nominal continuous torque of each motor was between 0-18 mNm. In this experiment, the motor applied two torques of -9, and -18 mNm by being driven under uni-polar and bi-polar modes, respectively. Therefore, considering the diameter of the motor–tendon pulley, i.e., 3 mm, the motor would apply a tensile force of 3 and 6 mN to the active tendon. The offset of tendon anchorage from the neutral axis of the catheter was also 3 mm, thus it would exert a pure bending moment, m^{Tip}, of -9 and -18 mNm to the tip of the catheter.

To achieve a more realistic condition, i.e., the motion of the heart, the phantom was fixed on a linear motor which was controlled to move sinusoidally with a frequency of 1 Hz and with a total amplitude of 6 mm. An ATI Mini40 force sensor (ATI Inc., NC, USA) was installed on the moving platform below the tissue phantom to measure the contact force for comparison. For this experiment, the linear actuator performed a total of 20 reciprocations while the catheter was in contact with the tissue, i.e., 10 reciprocations with each tip moment. Fig. 5.14(b) shows a snapshot of the catheter in contact with the tissue phantom (Ecoflex 00-10, Smooth-On Inc., PA, USA) during the test. Ecoflex 00-10 elastomer has similar mechanical properties to the heart tissue and has previously been widely used as heart tissue phantom, e.g., [76]. While the tip bending moment on the catheter was kept constant, the bending angle φ and curvature $\kappa_g(s)$ changed in response to variations of the tip contact force $\mathbf{f}^{\text{Tip}}$. Similar to Study I, the shape of the catheter was extracted from

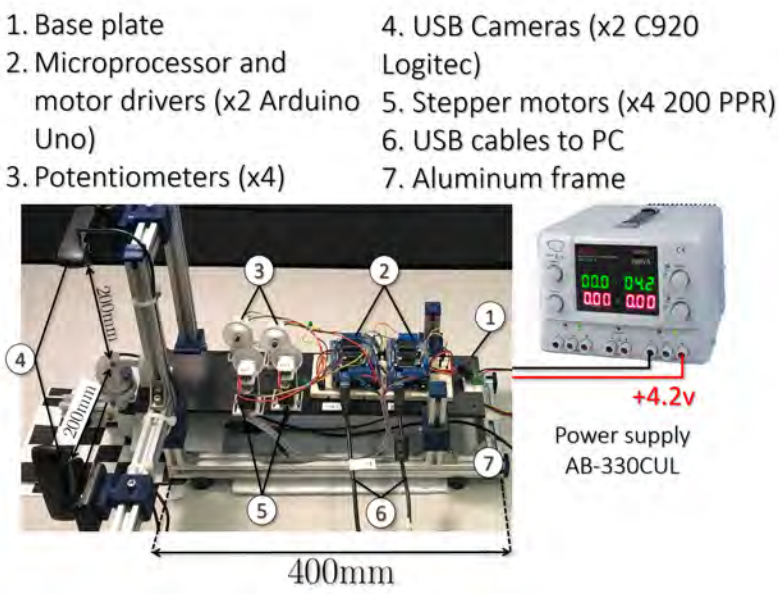

(a)

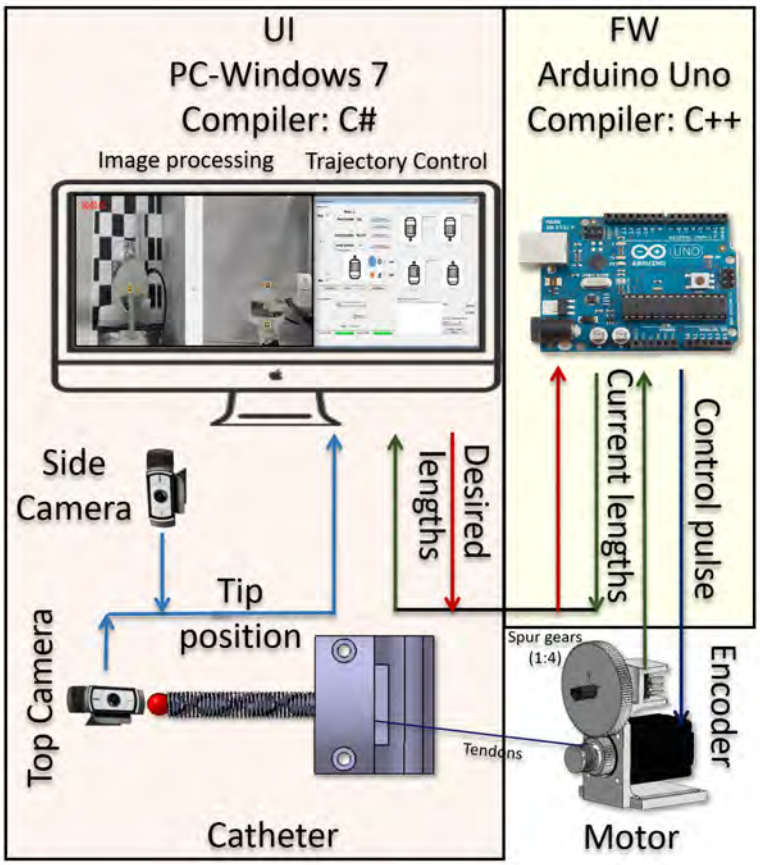

(b)

Figure 5.13: (a) Components of the mechanical and electrical modules of the catheter control system, and (b) software architecture of the user interface (UI) and firmware (FW).

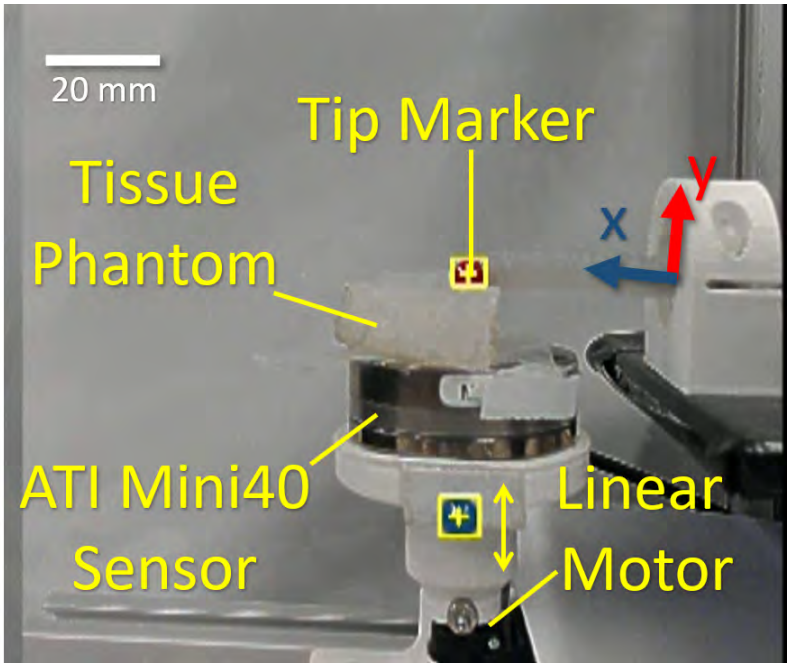

Figure 5.14: Configuration of the catheter, tissue phantom, and the linear motor during the validation study from the camera view.

real-time images and was subjected to Bezier shape interpolation revealing λ and φ. Afterward, λ and φ were used to obtain $\kappa_g(s)$ in each frame to be used in tip force estimation (Eq. 109).

5.3.2.3 Results

Fig. 5.15(a) shows the tip position and its average curvature $\bar{\kappa}_g(s)$ along the catheter with time during the experiment for $m^{\text{Tip}} = -9$ mNm and $m^{\text{Tip}} = -18$ mNm. The post-processing showed that the average curvature varied in the range of $[-0.0142, -0.0003]$ and $[-0.0175, -0.0006]$ for $m^{\text{Tip}} = -9$ mNm and $m^{\text{Tip}} = -18$ mNm, respectively. Also, Fig. 5.16 compares the magnitude of the reference force with the estimated force, $||\mathbf{f}_{tip}||$. The range of reference contact force was 0.095–0.304 N for $m^{\text{Tip}} = -9$ mNm and was 0.476–0.711 N for $m^{\text{Tip}} = -18$ mNm. The absolute error of force estimation with respect to the reference was 0.024 ± 0.020 N (7.9% of the maximum force) and 0.041 ± 0.027 N (5.8% of the maximum force). Furthermore, it was observed that the force estimation error increased with increasing the tip forces. Fig. 5.17 depicts the variation of the force estimation error with the tip force. As described in Sec. 5.3.1.1, as the tip force increased

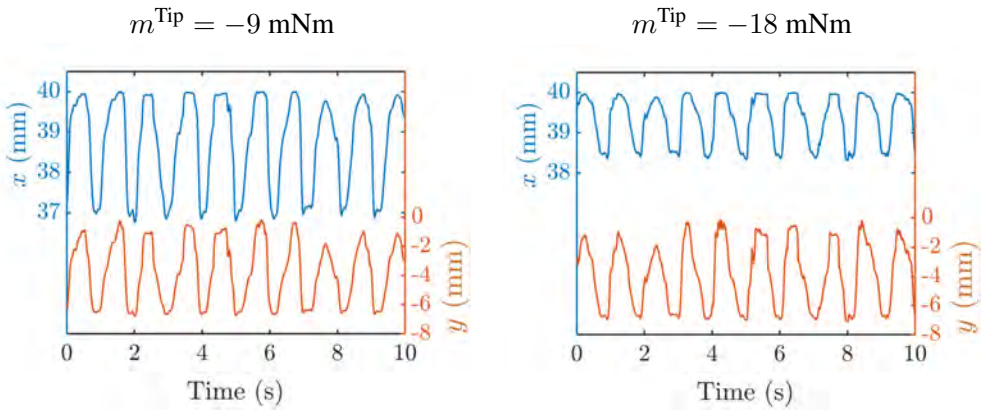

(a)

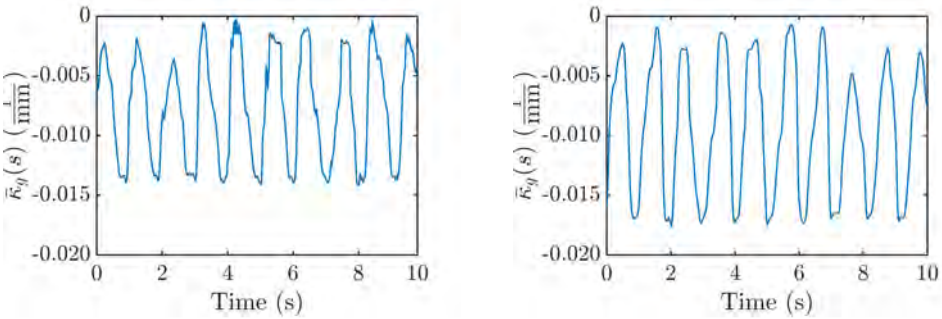

(b)

Figure 5.15: (a) Tip position of the catheter and (b) variation of average curvature along the catheter during the two experiments of Study II.

the bending radius along the catheter deviates from the constant bending radius assumption. Thus, the proposed method resulted in a larger estimation error. A similar trend was observed in Study I on the simulated deformation. Nevertheless, the average relative error of the experiments was 7.9% and 5.8% for the two tip bending moments.

In addition, the error exhibited an accumulation of two normally distributed errors N_1 and N_2 (Fig. 5.16(c)). Since the average error in N_1, i.e., -0.011 N is comparable to the nominal resolution of the ATI Mini40 sensor, i.e. 0.01 N, it might be related to the variation of the reference measurements. The second error distribution N_2 had an average error of 0.03 N, which might be related to the flicker of the tip marker extraction in image-processing. Another source of error could be the error in estimating EI, the model parameter.

Another finding was that the average computational time of the proposed force estimation method was 0.007 ± 0.005 s, corresponding to a minimum refresh rate of 83 Hz. Typically, intraoperative imaging devices, e.g., fluoroscopy, have frame-rates of 25-30 Hz. Therefore, the proposed method complies with the required frame-rate. Typically, a force estimation error of less than 10% is required for the robot-assisted cardiovascular intervention systems [62]. The proposed method showed improved accuracy compared to other image-based methods in the literature, e.g., [70, 74, 218, 247].

5.4 Summary

In this chapter, an image-based method for real-time tip force estimation on tendon-driven steerable RFA catheters was proposed and validated. The proposed method was an extension of the Cosserat rod-based method proposed in Chapter 4. Since the RFA catheters exhibit single-plane deformation the proposed Cosserat model in Chapter 4 was simplified to accommodate the single-plane deformations. In this study, the tip position of the catheter, i.e., $\begin{pmatrix} x & y \end{pmatrix}^{\mathsf{T}}$ was obtained through stereo-vision and triangulation. Afterward, the tip position was used to estimate the curvature along the catheter and both were used in the proposed force estimation framework.

The simulation-based and experimental validation studies showed the feasibility of integrating the proposed method with tendon-driven catheter actuation systems. Also, the validation studies showed

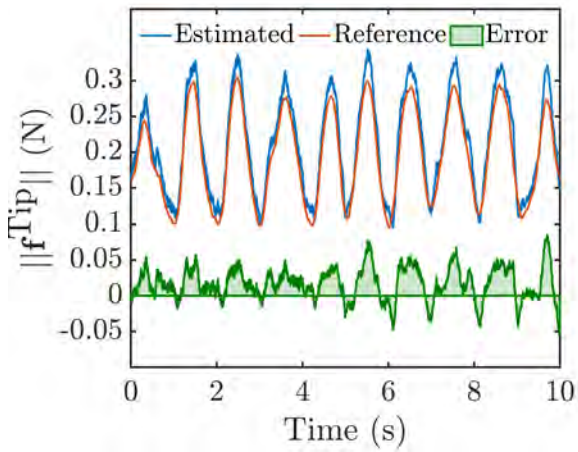

(a)

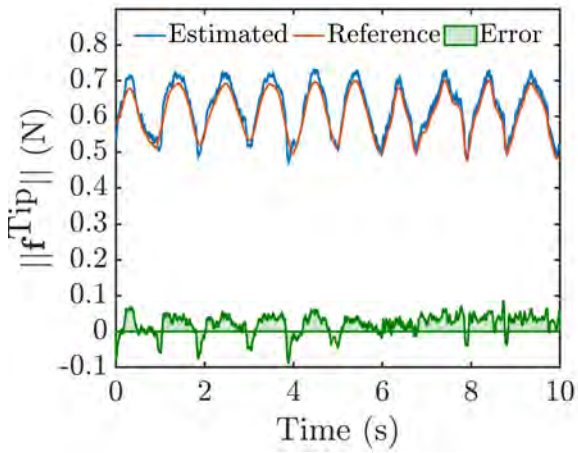

(b)

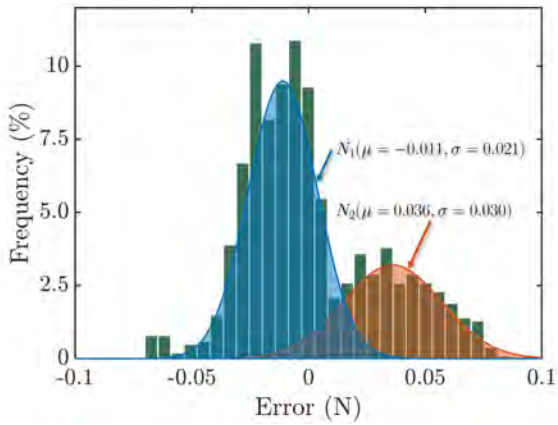

(c)

Figure 5.16: (a) comparison of the estimated tip force with the reference force for $m^{\text{Tip}} = -9$ mNm, (b) comparison of the estimated tip force with the reference force for $m^{\text{Tip}} = -18$ mNm, and (c) distribution of the force estimation error.

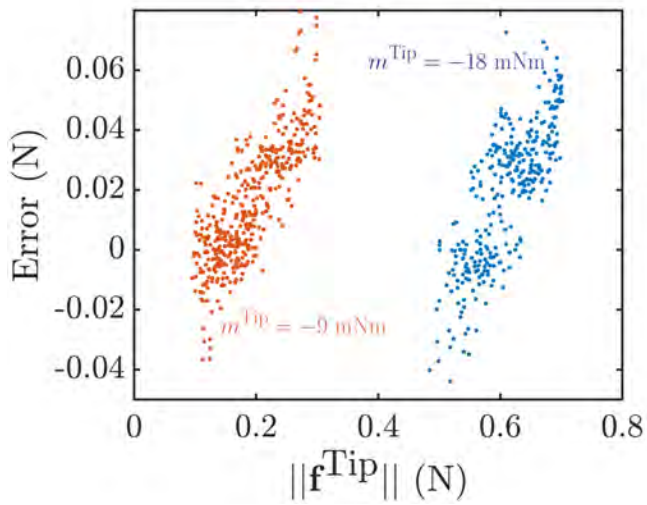

Figure 5.17: Variation of force estimation error with tip force.

acceptable accuracy of the proposed method in estimating the tip force under dynamic conditions. Although in this study the tip position of the catheter was obtained through stereo-vision, the utilized catheter actuation system is capable of accurate estimation of the tip position [64]. Thus, as an extension in future studies and for more usability tip position estimation from tendon lengths can be adopted. Researchers can also utilize a real-time filter, e.g., Kalman filter, for robust tip position estimation. Moreover, studying the effects of out-of-plane deflection on the accuracy of the results is a potential extension of this work.

As discussed in Chapter 1 and Chapter 2, one of the main limitations of the state-of-the-art of robot-assisted cardiovascular interventions is the lack of tactile and haptic feedback. In this regard, the proposed force estimation method facilitates obtaining accurate tip force information for surgeons intraoperatively without a need for extra hardware and hindering their surgical procedure. The author has previously shown the feasibility of rendering tactile force feedback for robotic RFA procedures in [63]. The proposed force estimation method can be integrated in the proposed system in [63] as the input block for the desired force for tactile rendering.

After proposing sensor-free force estimation methods for steerable and non-steerable endovascular devices, the next chapter introduces a drift-free rotation measurement system to decouple the rotation measurement and insertion measurement in the surgeon interface. This development facilitated the design of an intuitive surgeon module.

Chapter 6

An Integral-free Rotation Measurement Method via Stereo-accelerometery with Application in Robot-assisted Catheter Intervention

The spatial orientation of rotating objects is typically measured by utilizing inertial measurement units and requires temporal integration of angular velocities. The integration of the angular velocities accumulates the measurement noise and results in erroneous orientation estimation, thus necessitates real-time error compensation. Moreover, the inertial measurement units have an intrinsic limitation in measuring the spatial yaw angle. In this study, an integral-free 3D orientation estimation framework based on stereo-accelerometry and sensor fusion is proposed and validated. Afterward, a wearable device, *MiCarp* for robot-assisted interventional surgery was designed, prototyped, and investigated for accuracy and real-time performance. To achieve real-time performance, the derived equations were solved offline and an artificial neural network was trained and implemented in *MiCarp* . The accuracy and computational performance of the proposed method were compared with a representative integral-based method. The validation studies showed that the proposed method had a mean-absolute-error of $1.7 \pm 2.4°$, a measurement range of $\pm 180°$, and a real-time refresh rate of up to 117 Hz. Also, the feasibility of integrating the proposed device with a representative robotic intervention system was investigated. The proposed wearable device showed the capability of robust capturing of multiple successive rotations for an arterial cannulation task on a vascular model.

6.1 Introduction

6.1.1 Background

Favorable clinical outcomes and reduction of risk factors such as X-ray exposure to surgeons and patients, dexterous manipulation of surgical instruments, and precise implantation of intraluminal stents, have led to the fast expansion of robot-assisted catheter intervention (RCI) for treating neuro-, cardio-, and peripheral vascular diseases [27, 221–224, 266, 267].

Catheterization is performed under live X-ray imaging for visualizing the shape and trajectory of the endovascular devices inside the patient's body. During manual catheterization, first a catheter, i.e., long flexible hollow tube, is inserted into a large vessel at the patient's groin or forearm through a small skin incision, a.k.a. vascular port. Afterward, it is manually maneuvered inside the vessels toward the preoperatively planned target vessel, e.g., cerebral, cardiac, or peripheral vessels. The catheter provides a conduit for other surgical instruments, e.g., vascular balloons and stents, to reach the target vessel.

Catheter navigation is cumbersome and time-consuming due to the complexity of anatomy, multiple branching, tortuosity of the vasculature, and flexibility of the catheters. Therefore, a series of insertion/retraction and rotations are required to navigate the catheter on a desirable path. By experience and training, surgeons develop the necessary neuro-motor skills, a.k.a. intuition, to control the trajectory of catheters through manual maneuvers [42, 268]. Fig. 6.1(a) shows a schematic of manual catheterization.

A robot-assisted catheter intervention (RCI) system typically has a master-slave robotic configuration. The surgeon controls the robot remotely and through the knobs on the control panel, while the robot performs the insertion and rotation tasks according to the surgeon's commands (Fig. 6.1(b)). The commercially-available RCI systems work under velocity control mode, while conventional catheterization is a position control task [62].

Studies have assessed such user interfacing is not intuitive for the majority of surgeons [17]. The cognitive load of mapping a position-control task to a velocity-control practice has led to long learning-curve for the surgeons [17, 32]. Specifically, US FDA's Manufacturer and User Facility Device Experience (MAUDE) database show that undesirable movements, e.g., MDR 7713735,

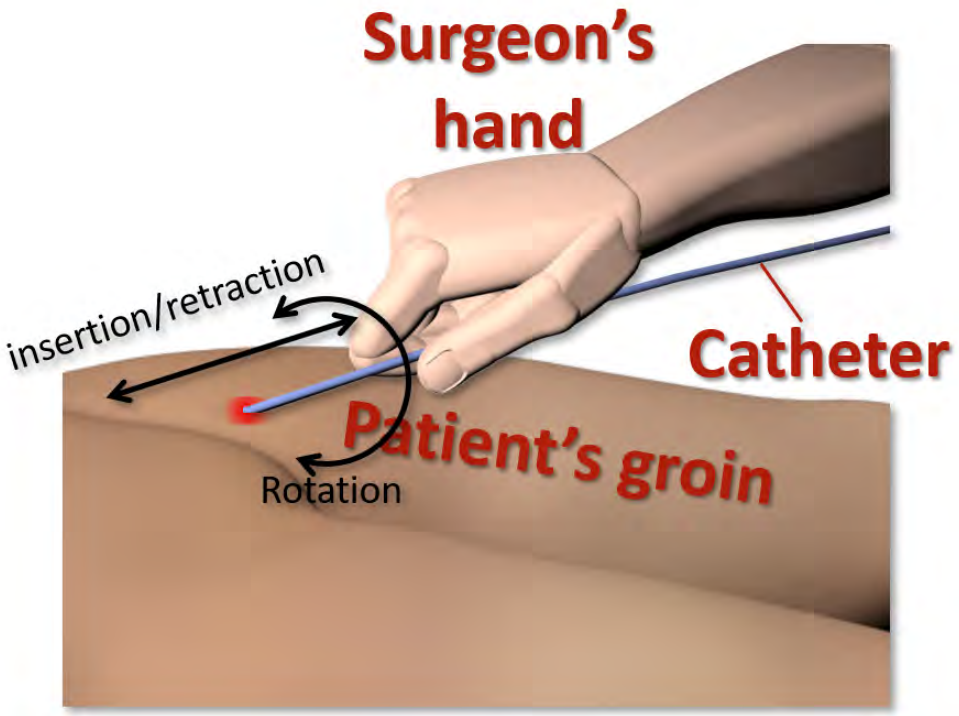

(a)

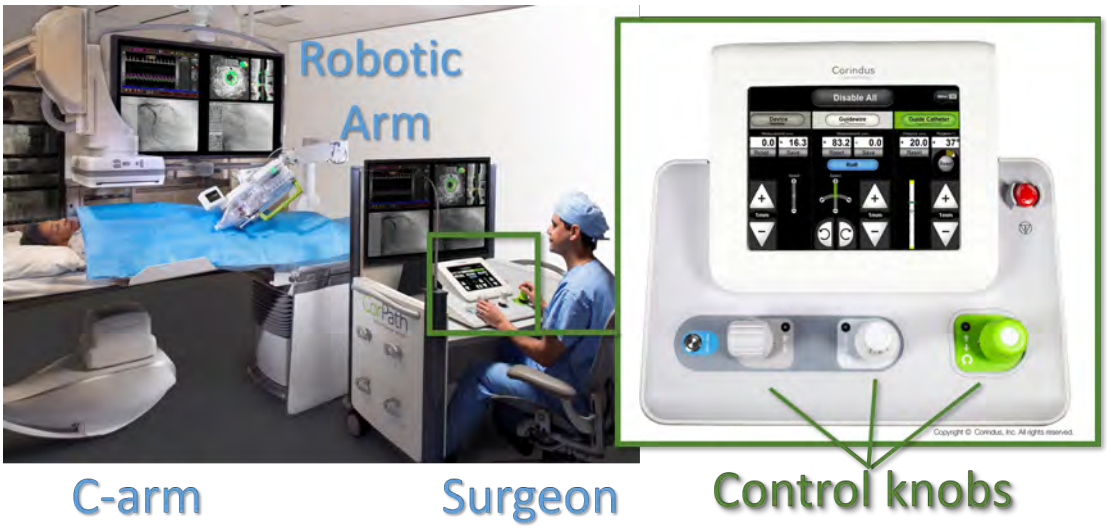

(b)

Figure 6.1: (a) Surgeon's hand navigating a catheter inside the patient's body by insertion/retraction and rotation through a femoral access approach and (b) the control panel of a commercially available RCI system (courtesy of Corindus Inc., MA, USA).

7918144, and 6197973, excessive force and kinking of endovascular devices, e.g., MDR 8055503 and 7400392, and over-steering of the control knobs, e.g., MDR 6227199, have been among the adverse events experienced with commercially-available RCI systems.

For more intuitive master module design, researchers have proposed alternative user interfaces. During an interventional surgery, the surgeon's maneuvers are divided into insertion–retraction and rotation. The surgeon moves a catheter along its insertion alignment (Fig. 6.1); therefore, this maneuver can be categorized as translation along a fixed axis combined with rotation about the same axis in 3D space. In a recent literature survey [62], the author has shown that the majority of the studies have followed the interface design proposed by Xiao *et al.* [198]. Their design was composed of a linear stage for acquiring the insertion and a fixed-axis rotary mechanism for rotation acquisition. A prominent advancement of their study was to enable the RCI system to track the position, as opposed to the early RCI systems which worked under velocity control.

Similarly, Dagnino *et al.* [54] and Chi *et al.* [269] proposed novel haptics-enabled user interfaces based on a design principle adopted from [198]. Despite its compact design, their design mandated utilization of multiple serial sensors and encoders to measure the translational and rotational motions. Therefore, the surgeon needed to slide and rotate all the components together on the linear stage. Inevitably, the user should overcome the intrinsic inertia of the whole system for moving the slider on the surface. Considering the small range of haptic forces during vascular cannulation tasks, i.e. $0.1 - 2$N [54], one would argue that the inertia of the components would affect both the user haptic perception and haptic rendering. A comprehensive review of the proposed designs for RCI systems, including a comparison of advantages and limitations of various designs of the state-of-the-art surgeon modules can be found in our recent survey in [62].

6.1.2 Motivation

The motivation of this study was to propose a new rotation measurement method with a fully decoupled rotation measurement module from the insertion measurement module for the surgeon module of RCI systems. In this study, a wearable solution is provided to decouple the rotation angle acquisition from the insertion measurement and haptic feedback on the surgeon interface module. The

use-case of the proposed device is for teleoperated RCI systems. The proposed system is intended to be integrated with the surgeon's module of RCI systems and measure the successive rotations of a dummy catheter used at the surgeon module. We speculate that the use of a dummy catheter, similar to the catheter simultaneously being used at the patient module, increases the intuition of catheter steering for the surgeon. Also, the decoupling of the inertia of the rotation measurement module from the insertion measurement module may allow for more accurate haptics-enabled user interface development in the future.

6.1.3 Related Studies

Inertial measurement unit (IMU) sensors have been widely used for estimating the 3D orientation of moving objects [270, 271]. To obtain the roll, pitch, and yaw spatial angles of a moving object, typically the angular velocities measured by an IMU are temporally integrated [270]. However, not only would integration accumulate the noise over time and cause drift, but also the sensors readings are not accurate for the yaw velocity [270]. Therefore, the temporal drift of the integral-based methods results in erroneous orientation estimation. Studies have proposed various methods for drift compensation and yaw correction. Kalman filtering has been widely used for orientation estimation, e.g., [272–278]. The general procedure with Kalman filtering is to use a statistical model of the measurement noise (covariance matrix) followed by performing a weighted average between the new measurement and previous estimation. For example, in an early study Marins *et al.* [279] used an extended Kalman filter for orientation estimation of body limbs using IMUs. They used a quaternion-based representation of rotation and exploited a gradient-descent-based method to correct the constructed orientation frame from IMU angular velocities. Their method was not of fast refresh rate mainly due to the iterative nature of the gradient-descent approach. Yun *et al.* [280] enhanced their study by applying Kalman filtering on a quaternion estimator based on the well-known QUEST method, originally introduced in [281]. In continuation, various error estimation and compensation methods have been proposed for optimal attitude estimation and orientation filtering. Majority of the pertinent literature have proposed methods based on optimal correction of the attitude with respect to the geomagnetic field [282–285] and various flavors of probabilistic filtering, e.g., extended complementary filter (ECF) [286, 287], unscented Kalman filtering (UKF) [288, 289],

Table 6.1: Comparison of representative studies on orientation estimation and filtering of body limbs.

Study	Application	No. of Sensors	Filtering Method	RMS Error(°)
[295]	Hand	1	EKF	6.0
[296]	Hand	1	EKF	2.8
[297]	Forearm	3	EKF	3.5
[298]	Hand	1	EKF	9.9
[293]	Extremities	1	ML	4.0
[287]	Hand	1	CF	5.0
[291]	Hand	1	ML	-

Lie-group (LG)-UKF [290], and machine-learning (ML-) based filtering [270, 291–293].

A common limitation of error compensation techniques is the need for probabilistic modeling of error (covariance matrix), which unless obtained from an adequately-large *a-priori* data, may lead to ill-conditioned orientation estimation [294]. Another factor to take into consideration is the effect of electromagnetic interference with the magnetic sensors in IMUs. Magnetic sensors of IMUs are typically used for geomagnetic field-based error compensation. Operation rooms are usually equipped with strong magnetic field generating medical devices such as imaging devices. The magnetic interference may adversely affect the geomagnetic field sensors of IMUs and lead to unreliable sensor readings and drift compensation. Therefore, an integral-free rotation measurement method, that does not require drift compensation, would be of high clinical significance for surgical applications, e.g., teleoperated RCI. To summarize, Table 6.1 compares a representative list of studies on orientation estimation and filtering for body limb orientation estimation.

6.1.4 Objective and Contributions

The objective of this study was to propose, validate, and demonstrate the feasibility of an IMU-based wearable device for integration with the surgeon module of RCI systems. To this end, an alternative integral-free rotation measurement method was developed which allowed for physical decoupling of the insertion measurement module from the rotation measurement module. By such decoupling, the inertia of the rotation acquisition system would not interfere with the insertion measurement system. The proposed system in this study is a wearable device on the wrist that the surgeon could wear and perform the rotation and insertion maneuvers as she/he used to do in the non-robotic

conventional surgeries. Given the limitations of the integral-based orientation estimation, we have developed a method based on stereo-accelerometry to avoid the integration drift and the need for attitude resetting in real-time. The contributions of this study are:

(1) developing a wearable device to decouple the inertia of the rotation measurement from the user interface for RCI applications,

(2) proposing an integral-free method to measure the spatial orientation of wrist through stereo-accelerometry and sensor fusion,

(3) proposing a fast, easy, and one-time calibration for the proposed device,

(4) artificial neural network (ANN-) based implementation of the proposed sensor fusion for fast real-time applications, and

(5) demonstration of the feasibility of integrating the proposed wearable device for RCI applications.

In the following, the design of *MiCarp* , rigorous derivation of the stereo-accelerometry principle as the proposed sensor fusion technique, orientation estimation, off-line solution, and learning-based implementation of the solution is provided in Sec. 6.2, followed by the results of two validation studies in Sec. 6.3 and concluding remarks in Sec. 6.4.

6.2 Material and Method

In this section, the geometric design, integral-free orientation estimation algorithm, mathematical model, solution schema, and the neural-network-based implementation of the system are provided.

6.2.1 Wearable Design and Components

Fig. 6.2(a) represents the geometric design of *MiCarp* as a wearable device with a strap band to secure it on the surgeon's wrist.*MiCarp* was comprised of two Wemos-D1 mini (Wemos Electronics) embedded boards with ESP-8266EX 2.4 GHz WiFi modules, two 6 degree-of-freedom (DoF) IMU sensors (SEN-13944, SparkFun Electronics, CO, USA), a 3D printed housing, a film pressure sensor (RP-C7.7-LT, DFRobot Inc, China), and a velcro strap. The two IMUs were installed with a relative

roll angle of 120° with respect to each other. Each microprocessor was powered by two serial 3V Lithium battery (LiCB CR2477, LiCB Co. Ltd., China).

Each IMU sensor was connected to a Wemos board and was registered as a client on a local WiFi network. The film pressure sensor was intended for detecting the grasping event and was to be strapped to the surgeon's thumb or index figure. The operational voltage of the pressure sensor was 5v. The voltage of the pressure sensor would drop from 5v with the onset and increasing of the grasping pressure. A grasping event was defined to trigger once the voltage of the pressure sensor would drop by 50%, indicating a grasping force of approximately 250 g. The pressure sensor was pulled up and interrogated by one of the Wemos Mini D1-s. Also, the Wemos boards interrogated the IMUs and broadcasted the acceleration data $\mathbf{a}_i = \begin{pmatrix} a_{x_i} & a_{y_i} & a_{z_i} \end{pmatrix}^T$ via a user-datagram-protocol (UDP) protocol at a frequency of 150 Hz. The received data was logged and processed in real-time using the graphical user interface (GUI) developed in C#.

6.2.2 Stereo-accelerometry and Sensor Fusion

In the proposed wearable device, two IMUs were used. The reason for using two IMUs was to allow for accommodating the proposed stereo-accelerometry and sensor fusion technique in this section. As discussed in Sec. 6.1.3, using a single accelerometer and integrating the *yaw* velocity may result in unreliable estimations [270], which requires drift compensation. With the proposed method, the *yaw*-angle, and consequently the surgeon's wrist rotation angle, was obtained through an integral-free rotation estimation technique via stereo-accelerometry, i.e., using two non-coplanar IMUs. Each IMU, denoted by i, provided the rate of change of its orientation ($\boldsymbol{\omega}$), in terms of the rate of change in roll (φ), pitch (θ), and yaw (ψ) angles with respect to its local coordination system $O_i : x_i - y_i - z_i$ in the form of:

$$\boldsymbol{\omega}_i = \begin{pmatrix} \dot{\varphi}_i & \dot{\theta}_i & \dot{\psi}_i \end{pmatrix}^T . \tag{112}$$

Also, each IMU measures the spatial linear accelerations in the form of:

$$\mathbf{a}_i = \begin{pmatrix} a_{x_i} & a_{y_i} & a_{z_i} \end{pmatrix}^T g, \tag{113}$$

where g is the gravitational acceleration, $g = 9.81 m/s^2$. Each measured $\mathbf{a}_i$ are expressed in their corresponding local coordinate systems as shown in Fig. 6.2(a).

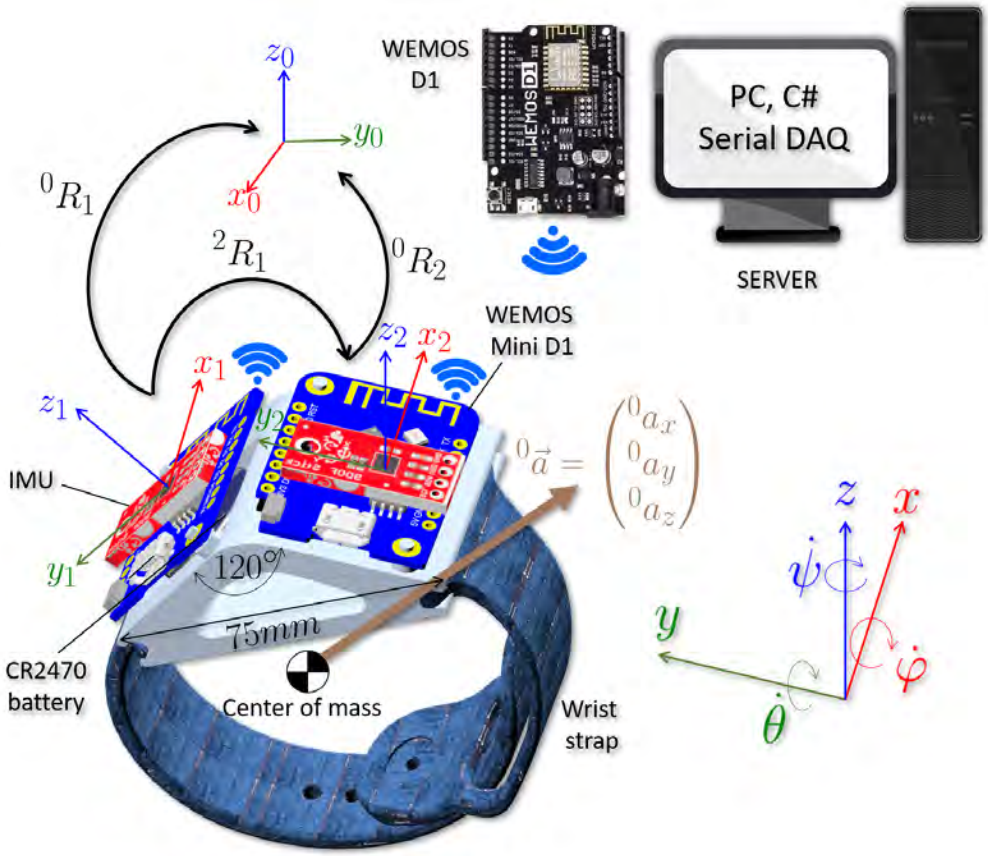

(a)

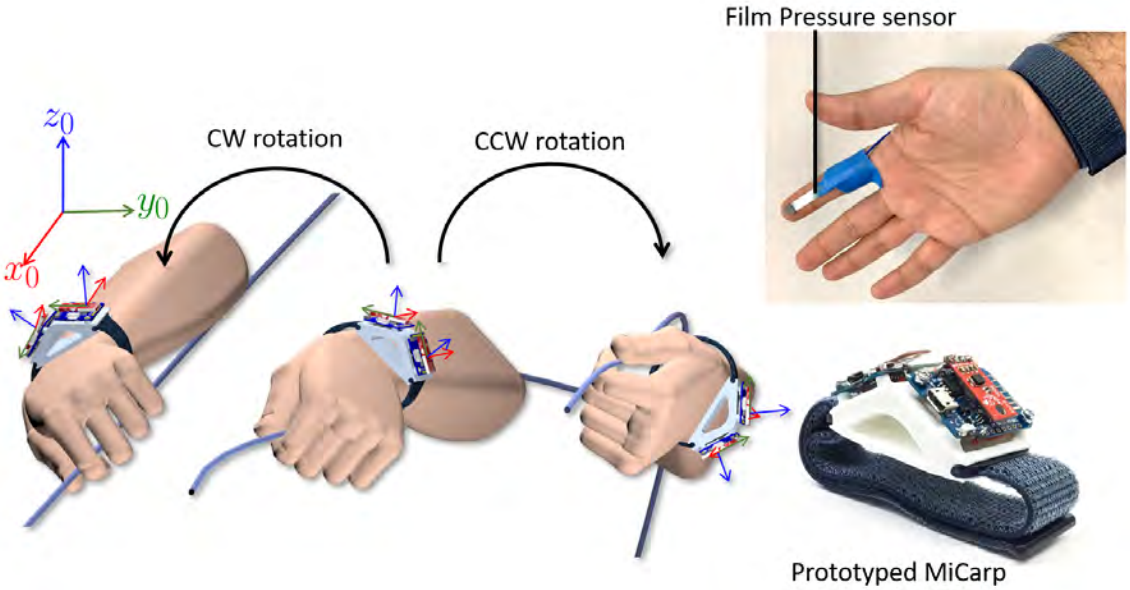

(b)

Figure 6.2: (a) 3D design and rotation angles of *MiCarp* for stereo-accelerometry and (b) schematic use-case of MiCarp in catheter rotation and the prototyped *MiCarp* with the film pressure sensor.

The proposed method for estimating the orientation of *MiCarp* in global coordinates used the linear accelerations measured by the two IMUs in their local coordination systems, i.e., $\mathbf{a}_i$ and $\mathbf{a}_2$. Since the global linear acceleration $\mathbf{a}_0$ experienced by the two IMUs are identical, the local-to-global transformation of local accelerations for both IMU sensors shall be identical. Also, given that the components of the assembly were mechanically locked together, the device would always be in a rigid-body-motion in space (Fig. 6.2(a)). Therefore:

$$\mathbf{a}_0 = {}^0\mathbf{R}_1\mathbf{a}_1, \tag{114}$$

and,

$$\mathbf{a}_0 = {}^0\mathbf{R}_2\mathbf{a}_2, \tag{115}$$

where, ${}^0\mathbf{R}_1$ and ${}^0\mathbf{R}_2$ are unique $\mathfrak{so}(3)$ mappings projecting the local acceleration to global acceleration for IMU-1 and IMU-2, respectively. Eliminating $\mathbf{a}_0$ between Eq. 114–115 yields:

$${}^0\mathbf{R}_1\mathbf{a}_1 = {}^0\mathbf{R}_2\mathbf{a}_2. \tag{116}$$

Any given rotation matrix $\mathbf{R}$ is necessarily orthonormal, thus, $\mathbf{R}^T\mathbf{R} = \mathbf{R}\mathbf{R}^T = \mathbf{I}_3$, where $\mathbf{I}_3$ is the identity matrix of rank-3, and ${}^i\mathbf{R}_j^{-1} = {}^i\mathbf{R}_j^T = {}^j\mathbf{R}_i$. Therefore, by using the successive rotations conventions, Eq. 116 was reordered as:

$$\mathbf{a}_1 = {}^1\mathbf{R}_0{}^0\mathbf{R}_2\mathbf{a}_2 = {}^1\mathbf{R}_2\mathbf{a}_2. \tag{117}$$

Similarly,

$$\mathbf{a}_2 = {}^2\mathbf{R}_0{}^0\mathbf{R}_1\mathbf{a}_1 = {}^2\mathbf{R}_1\mathbf{a}_1 = {}^1\mathbf{R}_2^T\mathbf{a}_1, \tag{118}$$

6.2.3 Calibration

Since the relative orientation of the two IMUs, i.e., ${}^1\mathbf{R}_2$ does not change with *MiCarp* 's motion, ${}^1\mathbf{R}_2$ is intrinsic and can be identified through a one-time experimental calibration. The unknown

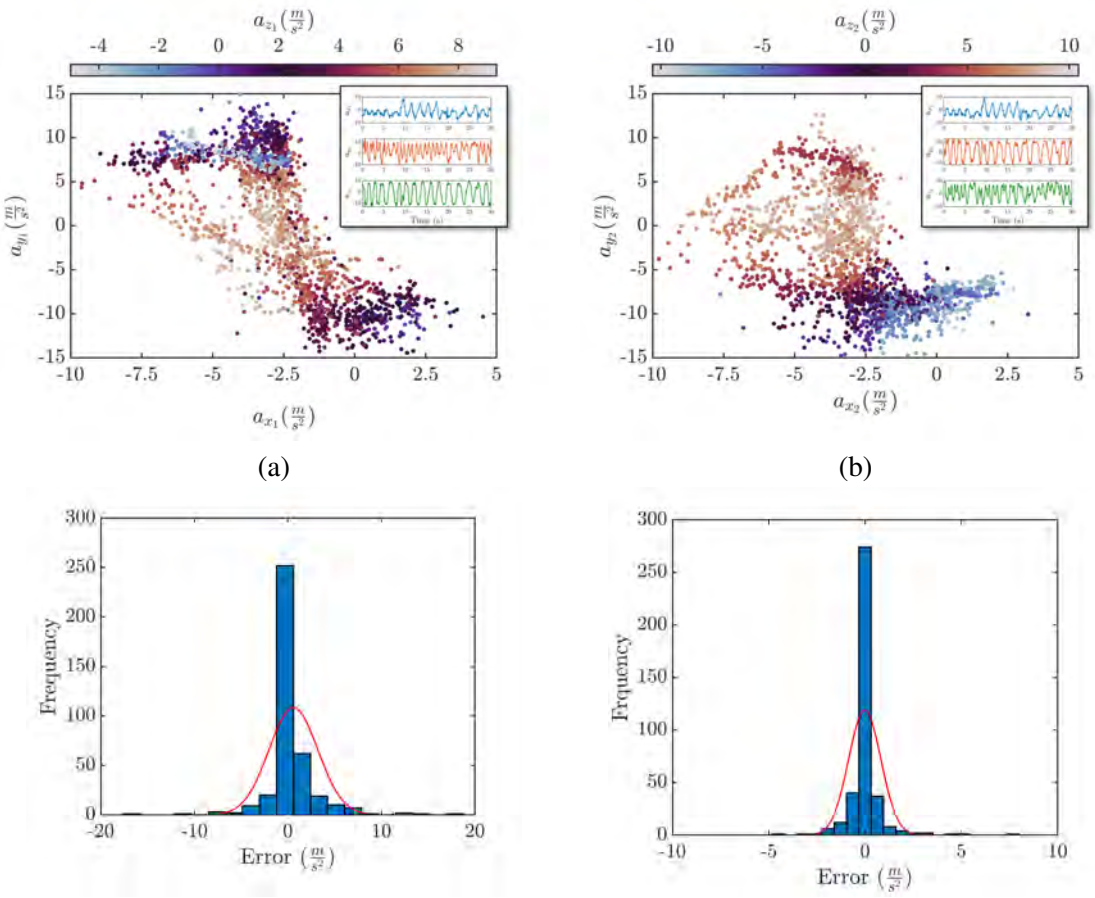

Figure 6.3: Training acceleration data from (a) IMU-1, and (b) IMU-2, used for calibrating *MiCarp* , (c) distribution of error in reconstructing (c) $\mathbf{a}_1$, and (d) $\mathbf{a}_2$ using the identified ${}^1\mathbf{R}_2$.

${}^{1}\mathbf{R}_2$ was assumed with the form:

$$
{}^{1}\mathbf{R}_2 = \begin{pmatrix} r_{11} & r_{12} & r_{13} \\ r_{21} & r_{22} & r_{23} \\ r_{31} & r_{32} & r_{33} \end{pmatrix} \tag{119}
$$

where, r_{ij} shall satisfy the six independent orthonormality conditions imposed by:

$$
{}^{1}\mathbf{R}_2^{T}{}^{1}\mathbf{R}_2 = \mathbf{I}_3, \tag{120}
$$

The identification of ${}^{1}\mathbf{R}_2$ constituted a constrained nonlinear least-square minimization defined as:

$$
\begin{aligned}
\text{minimize} \sum_{k=1}^{n_c} \left(\mathbf{a}_{1,k} - {}^{1}\mathbf{R}_2\mathbf{a}_{2,k}\right)^T \left(\mathbf{a}_{1,k} - {}^{1}\mathbf{R}_2\mathbf{a}_{2,k}\right) + \\
\sum_{k=1}^{n_c} \left(\mathbf{a}_{2,k} - {}^{2}\mathbf{R}_1\mathbf{a}_{1,k}\right)^T \left(\mathbf{a}_{2,k} - {}^{2}\mathbf{R}_1\mathbf{a}_{1,k}\right), \\
\text{subjected to} \qquad {}^{1}\mathbf{R}_2^{T}{}^{1}\mathbf{R}_2 - \mathbf{I}_3 = \mathbf{0}_3,
\end{aligned} \tag{121}
$$

where, n_c denotes the number of sample data used for calibration. Eq. 121 was constructed symmetrically with respect to ${}^{1}\mathbf{R}_2$ and ${}^{2}\mathbf{R}_1$ to avoid bias toward either of the IMUs. Since the adopted minimization method is a numerical approach, there will always be a residual error in the acceleration reconstructions. Therefore, a symmetrical error construction was adopted to make sure the obtained ${}^{2}\mathbf{R}_1$ fairly minimizes both the errors of reconstructing $\mathbf{a}_1$ from a_2 and vice versa. Studies have proposed semi-analytical methods for optimal ortho-normalization of the obtained rotation matrices, e.g., [294], however, such ortho-normalization has not been implemented in this study for the computational efficiency. For the experimental calibration, *MiCarp* was moved randomly in space for 30 s, within its nominal range of motion, while $\mathbf{a}_1$ and $\mathbf{a}_2$, $\boldsymbol{\omega}_1$ and $\boldsymbol{\omega}_2$ were recorded. A total of 9000 synchronized $(\mathbf{a}_1, \mathbf{a}_2) \in \mathbb{R}^{3\times 2}$ were obtained during the calibration and were randomly split for calibration ($75\%, n_c = 6750$) and verification ($25\%, n_v = 2250$). The minimization problem was solved by adopting the Levenberg-Marquardt algorithm in Matlab Optimization Toolbox

(R2019b, Mathworks Inc., MA, USA) and resulted in the following orientation matrix:

$$
{}^{1}\mathbf{R}_2 = \begin{pmatrix} 0.99988 & 0.00247 & 0.01572 \\ 0.00247 & 0.55961 & 0.82875 \\ 0.01572 & -0.80729 & 0.58994 \end{pmatrix} \tag{122}
$$

Fig. 6.3(a–b) show the data used for identification of ${}^{1}\mathbf{R}_2$ and Fig. 6.3(c–d) depict the distribution of error of reconstructing $\mathbf{a}_1$ and $\mathbf{a}_2$ using ${}^{1}\mathbf{R}_2$. The mean-absolute error for reconstructing $\mathbf{a}_1$ and $\mathbf{a}_2$ were $0.046 \pm 0.42\frac{m}{s^2}$ and $0.008 \pm 0.48\frac{m}{s^2}$, respectively.

6.2.4 Orientation Estimation

After calibration, in order to estimate the orientation of *MiCarp* in the global coordinates, i.e., $\begin{pmatrix} \varphi & \theta & \psi \end{pmatrix}^T$, ${}^{0}\mathbf{R}_1$ was multiplied from left in Eq. 117 which resulted in:

$$
{}^{0}\mathbf{R}_1\mathbf{a}_1 - {}^{0}\mathbf{R}_2{}^{2}\mathbf{R}_1\mathbf{a}_1 = ({}^{0}\mathbf{R}_1 - {}^{0}\mathbf{R}_2{}^{2}\mathbf{R}_1)\mathbf{a}_1 = \mathbf{0}. \tag{123}
$$

Since $\mathbf{a}_1$ is not always zero, the following condition was necessary:

$$
{}^{0}\mathbf{R}_1 = {}^{0}\mathbf{R}_2{}^{2}\mathbf{R}_1. \tag{124}
$$

It is noticeable that Eq. 124 shall always be satisfied, concurring with the mathematical implications of matrix rotation. Any given rotation matrix, e.g., ${}^{0}\mathbf{R}_1$ and ${}^{0}\mathbf{R}_2$, can be decomposed into three ordered successive *roll-pitch-yaw* rotations about the global axes [244]. With ${}^{2}\mathbf{R}_1$ as *a-priori* knowledge, Eq. 124 was re-written as:

$$
\mathbf{R}_{x_0}(\varphi_1)\mathbf{R}_{y_0}(\theta_1)\mathbf{R}_{z_0}(\psi_1) = \mathbf{R}_{x_0}(\varphi_2)\mathbf{R}_{y_0}(\theta_2)\mathbf{R}_{z_0}(\psi_2){}^{2}\mathbf{R}_1, \tag{125}
$$

where,

$$
\mathbf{R}_{x_0}(\varphi_i) = \begin{pmatrix} 1 & 0 & 0 \\ 0 & \cos\varphi_i & -\sin\varphi_i \\ 0 & \sin\varphi_i & \cos\varphi_i \end{pmatrix} \quad i = 1, 2 \tag{126}
$$

$$\mathbf{R}_{y_0}(\theta_i) = \begin{pmatrix} \cos\theta_i & 0 & \sin\theta_i \\ 0 & 1 & 0 \\ -\sin\theta_i & 0 & \cos\theta_i \end{pmatrix} \quad i = 1, 2 \tag{127}$$

$$\mathbf{R}_{z_0}(\psi_i) = \begin{pmatrix} \cos\psi_i & -\sin\psi_i & 0 \\ \sin\psi_i & \cos\psi_i & 0 \\ 0 & 0 & 1 \end{pmatrix} \quad i = 1, 2 \tag{128}$$

Adopting the method proposed in [287] the *roll* and *pitch* angles of each IMU were obtained as:

$$\begin{aligned} \theta_i &= \arctan 2(-a_{x_i}, \sqrt{a_{y_i}^2 + a_{z_i}^2}) \quad i = 1, 2 \\ \varphi_i &= \arctan 2(a_{y_i}, a_{z_i}) \quad i = 1, 2 \end{aligned} \tag{129}$$

where $\arctan 2$ is the two-argument inverse tangent function. The only unknowns remaining are the *yaw* angles ψ_1 and ψ_2.

Yaw-angle estimation has been a challenge since the readings of IMU sensors are typically not reliable for $\dot{\psi}$ [270]. To avoid the integration of $\dot{\psi}$ for *yaw*-estimation the following derivation was performed. Eq. 125 was multiplied by $\mathbf{R}_y(\theta_1)^T\mathbf{R}_x(\varphi_1)^T$ from left resulting in:

$$\mathbf{R}_{z_0}(\psi_1) = \mathbf{R}_{y_0}(\theta_1)^T\mathbf{R}_{x_0}(\varphi_1)^T\mathbf{R}_{x_0}(\varphi_2)\mathbf{R}_{y_0}(\theta_2)\mathbf{R}_{z_0}(\psi_2)^2\mathbf{R}_1, \tag{130}$$

in which the only unknown were ψ_1 and ψ_2. Expansion of Eq. 130 resulted in nine nonlinear equations containing ψ_1 and ψ_2. The symbolic mathematical derivation of Eq. 130 was performed in Maple 2020 (MapleSoft Inc., ON, Canada) and was of the close-form:

$$\mathbf{R}_{z_0}(\psi_1) = \mathbf{\Lambda}(\psi_2) = \begin{pmatrix} \Lambda_{11}(\psi_2) & \Lambda_{12}(\psi_2) & \Lambda_{13} \\ \Lambda_{21}(\psi_2) & \Lambda_{22}(\psi_2) & \Lambda_{23} \\ \Lambda_{31} & \Lambda_{32} & \Lambda_{33} \end{pmatrix}, \tag{131}$$

Since $\mathbf{\Lambda}(\psi_2)$ is a multiplication of orthonormal matrices, it trivially satisfies the orthognormality condition. The orthonormality conditions were:

$$\Lambda_{11}^2(\psi_2) + \Lambda_{12}^2(\psi_2) + \Lambda_{13}^2 = 1, \tag{132}$$

$$\Lambda_{21}^2(\psi_2) + \Lambda_{22}^2(\psi_2) + \Lambda_{23}^2 = 1, \tag{133}$$

$$\Lambda_{31}^2 + \Lambda_{32}^2 + \Lambda_{33}^2 = 1, \tag{134}$$

$$\Lambda_{11}^2(\psi_2) + \Lambda_{21}^2(\psi_2) + \Lambda_{31}^2 = 1, \tag{135}$$

$$\Lambda_{12}^2(\psi_2) + \Lambda_{22}^2(\psi_2) + \Lambda_{32}^2 = 1, \tag{136}$$

$$\Lambda_{13}^2 + \Lambda_{23}^2 + \Lambda_{33}^2 = 1. \tag{137}$$

Also, from Eq. 130:

$$\begin{pmatrix} \cos\psi_1 & -\sin\psi_1 \\ \sin\psi_1 & \cos\psi_1 \end{pmatrix} = \begin{pmatrix} \Lambda_{11}(\psi_2) & \Lambda_{12}(\psi_2) \\ \Lambda_{21}(\psi_2) & \Lambda_{22}(\psi_2) \end{pmatrix} \tag{138}$$

which necessarily resulted in $\Lambda_{33}^2 = 1$. The choice of $\Lambda_{33} = 1$ or $\Lambda_{33} = -1$ was arbitrary. Λ_{33} was selected as $\Lambda_{33} = 1$ to convene the clockwise rotations of *MiCarp* as positive angles. Moreover, Eq. 138 and Eq. 132–137 necessitated:

$$\Lambda_{11}^2(\psi_2) + \Lambda_{12}^2(\psi_2) = 1 \rightarrow \Lambda_{13} = 0, \tag{139}$$

$$\Lambda_{11}^2(\psi_2) + \Lambda_{21}^2(\psi_2) = 1 \rightarrow \Lambda_{31} = 0, \tag{140}$$

$$\Lambda_{21}^2(\psi_2) + \Lambda_{22}^2(\psi_2) = 1 \rightarrow \Lambda_{23} = 0, \tag{141}$$

$$\Lambda_{12}^2(\psi_2) + \Lambda_{22}^2(\psi_2) = 1 \rightarrow \Lambda_{32} = 0. \tag{142}$$

Finally the two independent nonlinear equations relating ψ_1 and ψ_2 were obtained as:

$$\mathbf{f}(\psi_1, \psi_2) = \begin{pmatrix} \cos\psi_1 - \Lambda_{11}(\psi_2) \\ \sin\psi_1 - \Lambda_{21}(\psi_2) \end{pmatrix} = \mathbf{0}, \tag{143}$$

subjected to the admissibility conditions:

$$\mathbf{c}(\psi_1, \psi_2) = \begin{pmatrix} \Lambda_{11}(\psi_2) - \Lambda_{22}(\psi_2) \\ \Lambda_{12}(\psi_2) + \Lambda_{21}(\psi_2) \end{pmatrix} = \mathbf{0}. \tag{144}$$

$\mathbf{f}(\psi_1, \psi_2)$ is a system of nonlinear equations subjected $\mathbf{c}(\psi_1, \psi_2)$ constraints. To obtain the *yaw* angles, the equations were numerically solved with *roll* and *pitch* angles recorded during the calibration of *MiCarp* . The solution was performed in Matlab Optimization Toolbox using the sequential quadratic programming (SQP) algorithm. SQP is a widely used method for minimization problems with nonlinear constraints [299]. The computational performance SQP method has been shown to be superior to other methods [299]. Fig. 6.4 shows the obtained ψ_1 and ψ_2 for the calibration experiment. The computational time for estimating ψ_1 and ψ_2 was 244 ± 72 ms, corresponding to a maximum refresh rate of 3.2 Hz. As RCI applications require a minimum 25 Hz of refresh rate [62], this solution was not fast enough for the proposed application.

6.2.5 Learning-based Orientation Estimation

To decrease the computational surplus for orientation estimation, the calibration data was used to calculate the *yaw* angles offline (Eq. 143) and an artificial neural network (ANN) was trained with *roll* and *pitch* angles $\begin{pmatrix} \varphi_1 & \varphi_2 & \theta_1 & \theta_2 \end{pmatrix}$ as inputs and their corresponding ψ_1 and ψ_2 as outputs. ANNs are typically computationally economic as they only require primary mathematical operations and are easy to implement in microprocessors for seamless sensor fusion applications.

As depicted in Fig. 6.5(a), the developed ANN was a three-layer feed-forward neural network (FFNN) with an input layer with four neurons for $\begin{pmatrix} \varphi_1 & \varphi_2 & \theta_1 & \theta_2 \end{pmatrix}$, an output layer with two neurons (ψ_1 and ψ_2) and a hidden layer with ten neurons. The output of each neuron was coupled to a rectified linear unit (ReLU) activation function. Single-hidden-layer FFNNs have been widely used for regression problems [300]. The selected number of neurons in the hidden layer, i.e., ten neurons, was the minimum leading to a mean-absolute-error of less than 5° in ANN validation.

The calibration data was split randomly into training and verification datasets with a 75:25 percent ratio. Before training the ANN, the input data was normalized using Eq. 145–146.

$$\tilde{\theta}_i = \frac{\theta_i - \bar{\theta}_i}{\theta_{i_{max}} - \theta_{i_{min}}} \quad i = 1, 2, \tag{145}$$

$$\tilde{\varphi}_i = \frac{\varphi_i - \bar{\varphi}_i}{\varphi_{i_{max}} - \varphi_{i_{min}}} \quad i = 1, 2. \tag{146}$$

The training and verification of ANN were performed in Matlab Neural Network Toolbox (R2019b, Mathworks Inc., MA, USA). Fig. 6.5(b) shows the correlation between the output of the ANN for

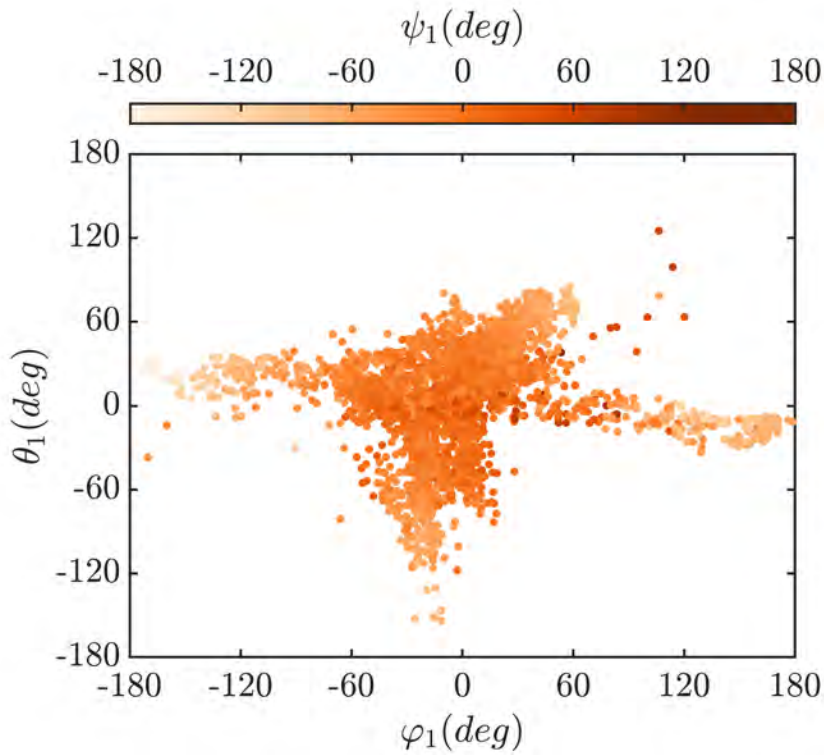

(a)

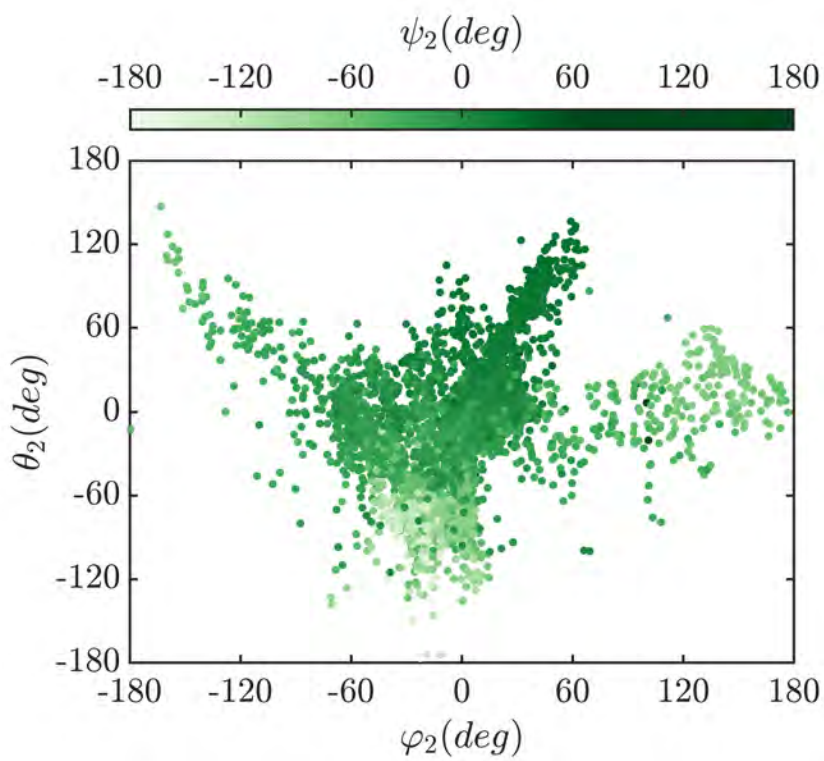

(b)

Figure 6.4: Results of *yaw* angle estimation for (a) ψ_1 and (b) ψ_2 using the calibration data.

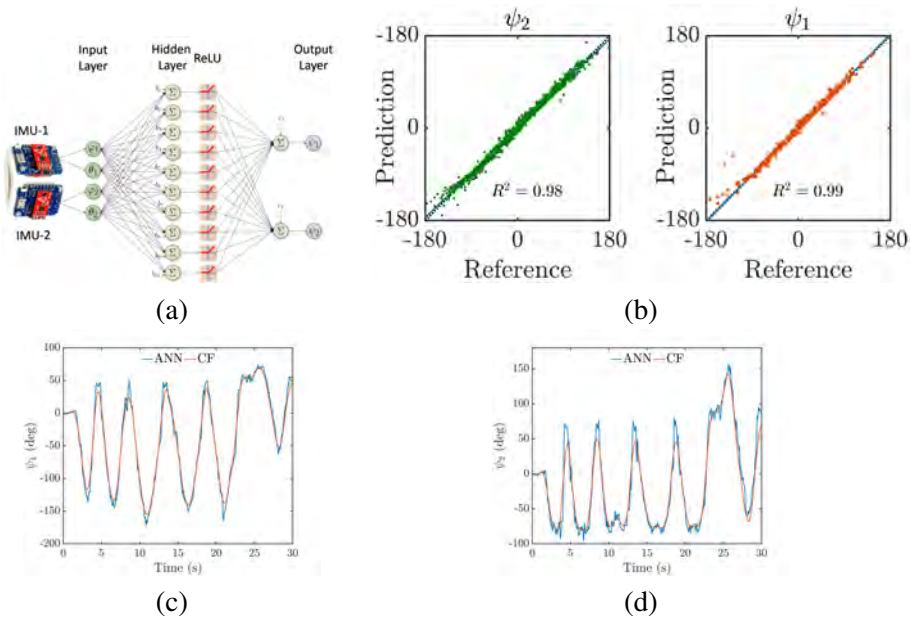

Figure 6.5: (a) Architecture of the feed-forward neural network used to predict *yaw* angles from *roll* and *pitch* angles, (b) the correlation of the ANN prediction with the reference *yaw* angles (from Eq. 143), (c) comparison of the estimated ψ_1 with the CF-based method with the proposed method, and (d) comparison of the estimated ψ_2 with the CF-based method with the proposed method.

yaw angles between the reference (offline solution) and ANN predictions for the verification dataset. The mean absolute error (MAE) of the predictions were $1.5 \pm 2.9°$ and $1.1 \pm 2.3°$ for ψ_1 and ψ_2, respectively. Also, the results showed a strong correlation between the reference and prediction with goodness-of-fit of $R^2 = 0.99$ and $R^2 = 0.98$, respectively.

In addition, a *yaw*-estimation was performed on data obtained for 30s in a second similar experiment to the calibration. For comparison, the *yaw*-angle of both IMUs were estimated adopting a representative complementary filtering (CF) method proposed in [287] and was compared with our proposed method (Fig. 6.5(c–d)).

The comparison showed that the mean absolute error of *yaw*-estimation was $3.5 \pm 4.1°$ for ψ_1 and $3.8 \pm 3.3°$ for ψ_2 using the CF-based method. Also, the computation time for a single yaw estimation with CF compensation was 17 ± 4 ms. Taking, the result of Eq. 144 as the reference, the proposed method was more accurate and faster than the CF-based technique for yaw-estimation. The observed error of the CF-based estimation was consistent with errors reported in [287]. The larger computation surplus of the CF-based technique compared to the ANN-based method was

related to the additional computations required for geomagnetic-based rough yaw estimation and integral drift compensation.

6.3 Validation Studies

To study the performance of the proposed system, two experimental validation studies were performed. The objective of the first study was to investigate the accuracy of the proposed device in rotation estimation, while the second study was aimed at demonstrating the feasibility on integrating *MiCarp* with a representative teleoperated RCI system.

6.3.1 Study I: Rotation Estimation

Fig. 6.6(a) shows the experimental setup used in the validation study. During the test, the user secured *MiCarp* on his wrist using its elastic band and rotated a cardiac catheter (RunWay 6Fr, Boston Scientific, MA, USA) in a qualitatively similar fashion to the maneuvers performed during RCI applications. The proximal part of the catheter was coupled to a rotary quadrature encoder (SEN0230, DFRobot Co., Shanghai, China) while the user was holding the distal part of the catheter. The reference rotation angle of the catheter, measured with the encoder, α_m, was recorded in a PC workstation through an Arduino Uno data acquisition (DAQ). Meanwhile, the *roll-pitch-yaw* angles of IMU-1 and IMU-2 were acquired from *MiCarp* through the UDP protocol on a local WiFi network initiated by Wemos-D1.

Upon starting the test, the initial global orientation of *MiCarp* was recorded as offset and was deducted from the real-time angles to measure the relative change in the angles of IMU-1 and IMU-2. For comparison with α_m, the global roll-pitch-yaw angles of *MiCarp* were used to find its spatial angle, α_c using the mapping between the global rotation matrices of IMU-1 and IMU-2 ($\mathbf{R}_1$ and $\mathbf{R}_2$) to their axis-angle representations [244]. For any given rotation matrix $\mathbf{R}$ of the form:

$$ {}^{0}\mathbf{R}_i = \mathbf{R}_x(\varphi_i)\mathbf{R}_y(\theta_i)\mathbf{R}_z(\psi_i) = \begin{pmatrix} r_{i_{11}} & r_{i_{12}} & r_{i_{13}} \\ r_{i_{21}} & r_{i_{22}} & r_{i_{23}} \\ r_{i_{31}} & r_{i_{32}} & r_{i_{33}} \end{pmatrix} \quad i = 1, 2, \tag{147} $$

the spatial angle is obtained as:

$$\alpha_i = \arccos(\frac{\text{Tr}({}^0\mathbf{R}_i) - 1}{2}) \quad i = 1, 2, \tag{148}$$

where, Tr$(.)$ was the trace operator which is the scalar summation of the major diagonal components of the matrix. Also, since at each time instance two α_i corresponding to $\mathbf{R}_1$ and $\mathbf{R}_2$ would be obtained, the rotation angle α_c was defined as:

$$\alpha_c = \frac{\alpha_1 + \alpha_2}{2}, \tag{149}$$

the average of the spatial rotation angles from two IMUs.

Fig. 6.6(b) shows the results of the validation study. The results exhibited a fair agreement between the *MiCarp* estimated angles and reference values (encoder). More specifically, the MAE of the *MiCarp* angles with respect to the reference was $1.7 \pm 2.4°$, resulting in a maximum relative error of 2.27% of $180°$. Nevertheless, the *MiCarp* angle showed sharp spikes in a few points which were related to the time instances when one of the IMUs sent a false zero data.

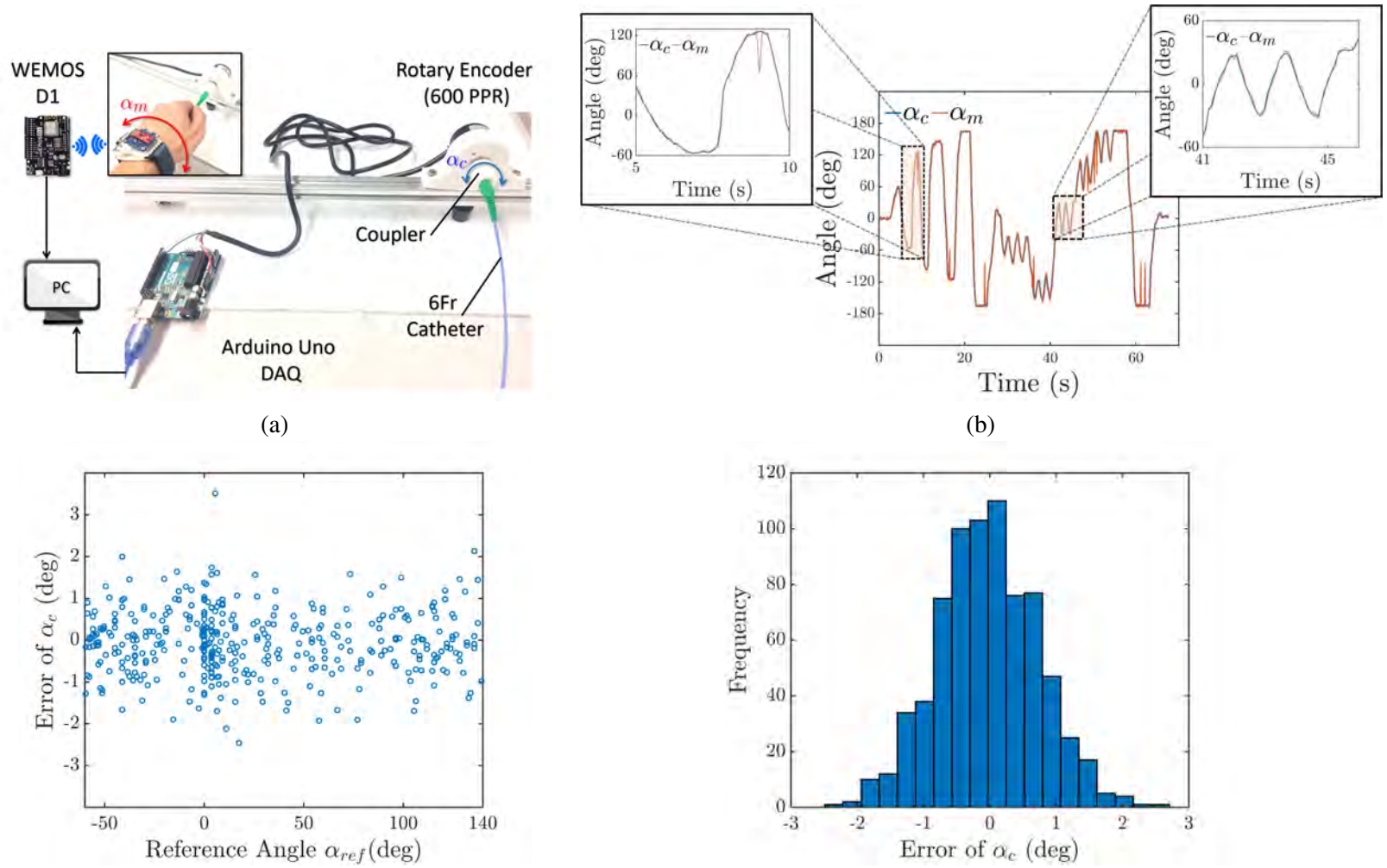

Figure 6.6: (a) Experimental setup used for testing *MiCarp* 's performance for RCI applications, (b) comparison of *MiCarp* rotation angle measurement versus the encoder rotation angle as the reference, (c) error of α_c with respect to the reference angle, and (d) distribution of error of α_c.

Anthropometric studies with IMU-based measurement techniques have shown that the normal ranges of motion of the human wrist in pronation and supination are 60° and 140°, respectively [301]. In this study, the zero angle was defined when the surface of MiCarp facing the ground with a clockwise direction convened as positive rotation ($\alpha_c > 0$). Therefore, the range of α_c would translate to $\alpha_c \in [-60, 140]$. Fig. 6.6(c–d) depict the distribution and range of the measurement error of the proposed method for validation study-I. It was observed that the error was bounded in [-2°, 2°] for $\alpha_c \in [-60, 140]$. The author considers the observed error band within the acceptable range for RCI applications.

Another prominent finding was that *MiCarp* exhibited a refresh rate of 111 ± 6 Hz with a latency of 11 ± 5 millisecond compared to the reference data. The computation time for ANN to find α_m from the angles was 2.1 ± 0.3 ms ($\approx$ 417 Hz). However, the exhibited refresh rate, i.e., 111 ± 6 Hz, was limited by the refresh rate of the IMU sensors. Nevertheless, the required minimum refresh rate for RCI application is 30 Hz [62], *MiCarp* showed an acceptable performance for such applications. The average overall latency for a single rotation measurement, i.e., the time elapsed between acceleration acquisition to the estimation of α_c, was 12.8 ± 0.5ms. The latency was calculated on data acquired for 90s from the uninterrupted operation of *MiCarp* ($\approx 10^4$ samples).

6.3.2 Study II: Integration with RCI

To demonstrate the feasibility of using the proposed wearable device for RCI applications, it was integrated with a representative RCI system, previously developed by the author in [74]. Fig. 6.7 depicts the patient module, surgeon module, and the RCI unit of the RCI system used in this study. The RCI unit of the patient module was a 2-DoF robot with 3D-printed housing. The motors were controlled under position control mode, with internal PID controllers, to follow the measured rotations and insertion at the master module. *MiCarp* was integrated with the master module (PC) via a UDP connection. The master module was also equipped with a rotary quadrature encoder coupled with two idler wheels to measure the length of insertion of the dummy catheter. The master and slave units were both subscribed to a common server as UDP clients similar to the connectivity specifications of Study-I and calibration.

For avoiding unwanted motion being transmitted to the RCI unit, the measured rotation and

insertion length would only be transmitted from surgeon to patient module if the grasping state was ON. As stated in Sec. 6.2.1, ON-state, indicating the grasping event, was triggered if 50% voltage drop was measured on the film pressure sensor. In addition, for allowing successive rotations, *MiCarp* GUI would transmit $\Delta\alpha_c$, defined as the amount α_c had changed from the latest ON-state triggering. This way, the user (surgeon) was able to release and re-grasp the catheter for successive rotations. In addition, should the surgeon's finger slip over the catheter, the grasping force would drop, the grasping state would be set to OFF, and the RCI system would diable the rotation tracking operation.

To simulate a teleoperated RCI procedure, the CataLyst robot (Fig. 6.7(a)) was remotely controlled using its C500C controller (Thermo Fisher Scientific Inc., WA, USA) to align the RCI unit with the entry angle of the femoral vein of the vascular model (SAM plus, Lake Forest Anatomical Inc., IL, USA). Afterward, one user performed a femoral cannulation task. The surgical task in this experiment was to advance the catheter from the femoral artery toward the aortic arch while wearing *MiCarp* and rotating the catheter multiple times in clockwise and counter-clockwise rotations arbitrarily. The user was wearing *MiCarp* with the pressure sensor strapped to his index finger (similar to Fig. 6.2(b)).

Fig. 6.8 shows the rotation angles measured by *MiCarp* at the surgeon unit and the rotations performed by the RCI at the patient unit. The results showed that *MiCarp* was successfully integrated with the representative RCI system. Also, the logic for detecting re-grasping by film pressure sensor was successful and avoided rotation of the RCI unit (patient module) while grasping state was OFF. The mean-absolute error of the RCI unit in tracking the incremental rotations $\Delta\alpha_c$ measured by *MiCarp* was $2.3° \pm 2.4°$. Moreover, *MiCarp* exhibited fair robustness in measuring catheter rotations. This experiment showed the feasibility of using *MiCarp* as a rotation measurement modality in RCI systems.

6.4 Summary

In this study, an integral-free orientation measurement system was proposed, prototyped, and validated. The proposed method was based on stereo-accelerometry and sensor fusion techniques. The proposed sensor fusion technique necessitated a one-time calibration of the prototyped system.

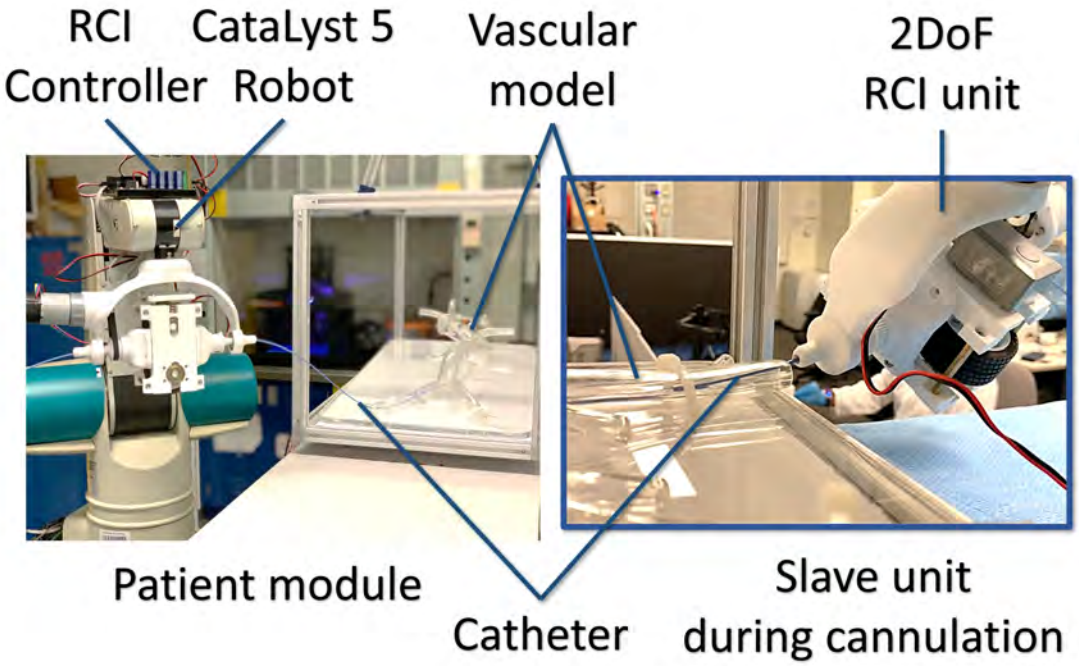

(a)

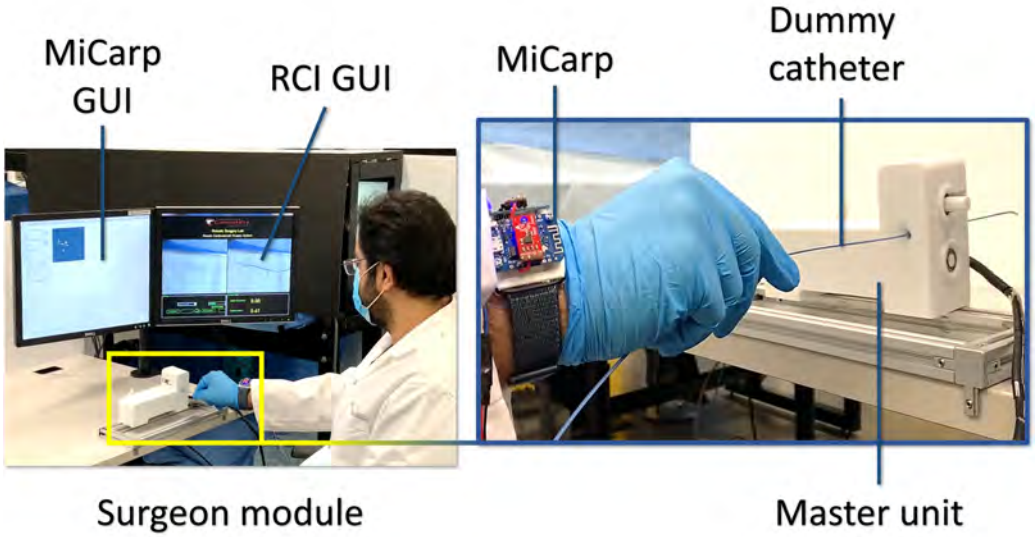

(b)

Figure 6.7: Setup used in validation study-II:(a) patient module, (b) surgeon module with integrated *MiCarp* .

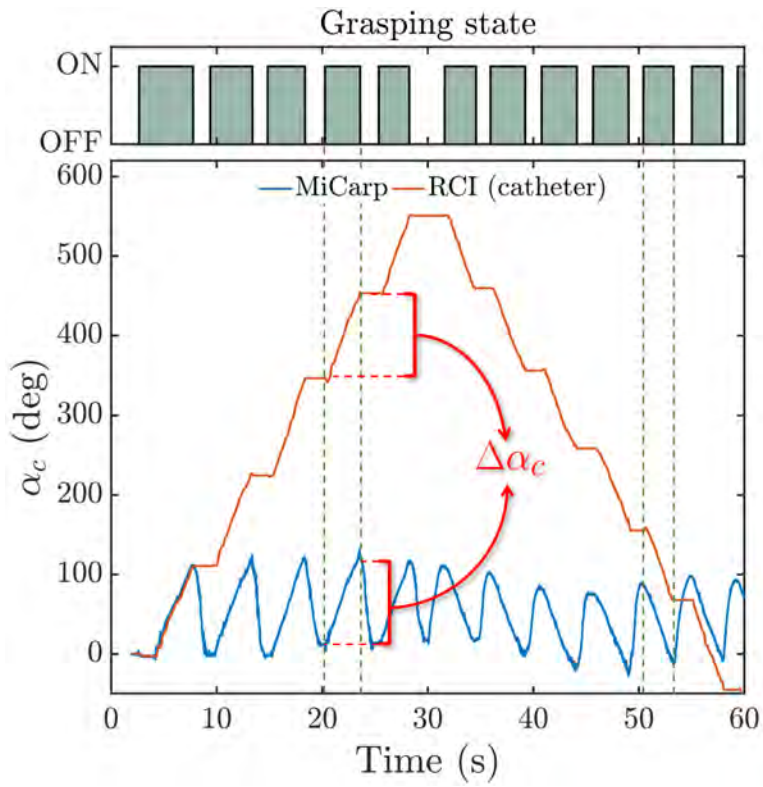

Figure 6.8: Grasping state and comparison of the measured catheter rotation α_c by *MiCarp* at the surgeon module with the performed catheter rotation at the patient module.

Also, it constituted a nonlinear constrained minimization problem which was solved numerically based on the calibration data. To reduce the computational time for real-time applications, the results of the minimization were used to train an ANN, which was afterward implemented in microprocessor on *MiCarp* . The proposed method eliminated the need for integration-based *yaw*-angle estimation from the angular velocities obtained from the IMUs. Also, it only utilized the linear acceleration signals from the IMUs which merely requires using simple fast 3-DoF IMUs.

The main contribution of this study was to validate the proposed integral-free sensor fusion technique without drift compensation. Also, the implementation of the method with a learning-based technique reduced the computational surplus which resulted in a maximum refresh rate of 117 Hz. Moreover, stereo-accelerometry resulted in establishing a direct mathematical relationship between the linear accelerations and orientation. Typically with IMUs, orientation is obtained through integration of the three angular velocities measured by the IMU. However, with the proposed methodology in this study, only three linear acceleration data were enough for estimating the orientation. The proposed system has the potential to be used in other applications such as radio-frequency ablation [64, 70], surgical haptic feedback [61, 63], laparoscopic surgery [253], remote tissue characterization [61, 63, 71, 76], virtual reality, and human motion analysis.

In this study, the mathematical formulation was performed based on fundamental spatial rotation definitions. Investigation of alternative formulations, such as quaternion algebra and filtering [276, 279, 302], nearest rotation matrix estimation [303, 304], and orientation filtering [287, 294, 305] are among possible expansions of this work. One of the limitations of the proposed system was that the robustness of orientation measurement by *MiCarp* could be affected by the false zero data transmitted from IMUs. To tackle this limitation, the utilization of a real-time classification-based fault detection algorithm to reject the false zeros can be explored. Another limitation of the proposed system was in detecting the rotation of the catheter using fingers. Steering fine catheters and guidewires with thumb and index finger with minimal rotation of wrist is possible. Considering the utilization of a custom-designed housing for *MiCarp* , researchers are encouraged to study alternative housing structures for other applications. Given the small size and low cost of IMUs, utilization of more than two IMUs and using smaller or different shape of the housing is possible without changing the orientation measurement methodology.

Another improvement of this study could be replacing the ANN with another nonlinear learning-based regression model such as support-vector-regression (SVR) [228] to decrease the overall error of the method. The proposed calibration schema could also be improved by adopting a uniform sampling technique over the training dataset for calibration and ANN. A uniform sampling technique could reduce the bias of training. Nevertheless, for a sufficiently large sampled data with uniform distribution, obtaining a large dataset size would be necessary. It is noticeable that although the medical catheters are typically circumferentially-reinforced (braided) to transfer rotations with minimal torsional deformation, it is likely that such deformations affect the accuracy of rotation measurement by *MiCarp* .

Building upon the proposed decoupled rotation measurement system in this chapter, the next chapter introduces a haptics-enabled intuitive surgeon interface for RCI applications.

Chapter 7

Magnetostriction-based Force Feedback for Robot-assisted Cardiovascular Surgery using Smart Magnetorheological Composites

Magnetorheological elastomers are a class of smart materials with controllable deformation by an external magnetic field. Recent studies have shown the feasibility of using magnetorheological composites for force feedback applications. In this study, a new haptic feedback system for regulating torque through contact friction was proposed, constitutively modeled, and experimentally validated. To this end, an analytical constitutive model for the composite was proposed and solved and was used to find the contact stress between the composite and a ferromagnetic shaft. Afterward, the proposed device was prototyped and a series of validation studies with three types of magnetorheological composites was performed. The validation studies showed that the analytical predictions for resistant torque were in fair agreement with the experimental results. Also, the proposed device was capable of generating and controlling a resistant torque of up to 115.5 ± 0.7 mNm and haptic force of up to 5.77 N. The system showed favorable performance for haptic feedback applications in robot-assisted cardiovascular interventions.

7.1 Introduction

7.1.1 Background

Cardiovascular diseases (CVDs) are the first cause of mortality, hospitalization, and medical prescription worldwide [306]. The most prevalent CVDs are cardiac artery stenosis (CAS) [306]. CAS's are caused by the build-up of fatty or calcified plaques in the coronary arteries and compromise the blood flow downstream to the heart. They may eventually result in cardiac ischemia, cardiac arrest, and can be fatal.

CAS's are controlled through medication in mild cases, however, need surgical intervention in moderate and severe cases. Minimally invasive cardiac intervention, a.k.a. percutaneous coronary intervention (PCI), is a widely-accepted standard approach for CAS's [12, 307]. Compared to open-heart surgery, PCI is preferred due to the health benefits for the patient such as small incision length, shorter anesthesia time, less infection rate, and shorter recovery time [307].

Despite the benefits, the PCI approach exposes severe health risks to the surgeon and staff due to the continuous use of X-ray for intraoperative imaging and visualization. Radiation-related orthopedic diseases, cataracts, and skin cancer are prevalent in cardiac surgeons [18, 20, 308]. Also, low geometric precision, restricted dexterity, stent misplacement, and imprecise localization of stenosis are known as limitations of PCI [19].

Robot-assisted Cardiovascular Intervention (RCI) was introduced to alleviate the PCI limitations by using a master–slave robotic configuration [36, 62]. Fig. 7.1 shows an RCI system in the operation room. Early evaluations confirmed the effectiveness of the RCI systems in reducing occupational hazards for surgeons and staff [29], improving the accuracy of stent placement [309], and decreasing the X-ray exposure to the surgeon [25]. However, utilization of a remote surgical platform separated the surgeon and intraluminal surgical devices, which further led to poor hand–eye coordination [310], compromised perception of vascular anatomy, and most importantly, loss of haptic perception [62, 308]. The latter has also led to compromised situational awareness for the surgeon and has increased the risk of vascular rupture due to over-steering of the surgical instruments[41, 62]. Loss of haptic feedback is known as the prime limitation of this robotic technology impeding its reliability and wide acceptance amongst the clinicians [40, 45, 310].

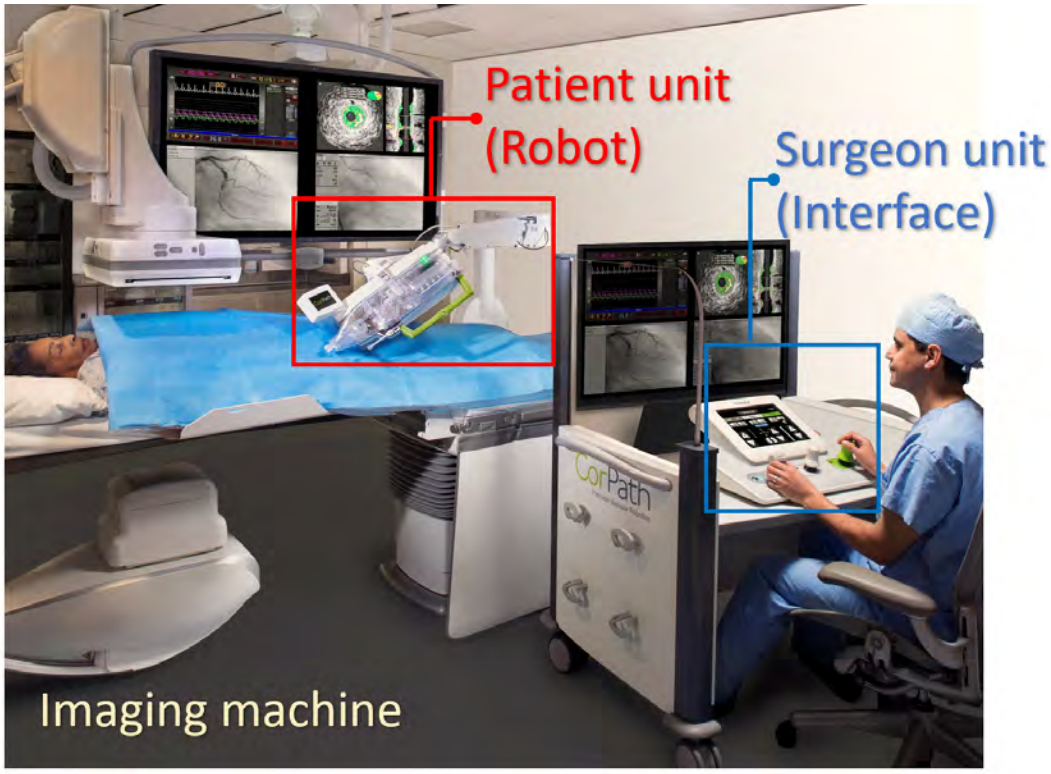

Figure 7.1: Typical system components of an RCI system with patient unit (slave), surgeon unit (master), and imaging machine (Courtesy of Corindus Inc., Waltham, MA, USA).

Recent developments have enabled surgeons to perform long-distance robot-assisted interventions [221]. Given the risks associated with compromised situational awareness in RCI, the provision of haptic feedback is of utmost importance in long-distance telerobotic vascular interventions.

7.1.2 Related Studies

Various modalities of haptic rendering have been proposed in the literature for the integration of haptic feedback to RCI platforms [62]. Bark *et al.* have shown that haptic rendering through application and transfer of torque results in consistent haptic rendering [311]. The haptic signals in RCI systems are the insertion force and rotational torques. Studies have shown that insertion force feedback can increase the safety of RCI procedures [42, 43]. Studies have proposed sensor-based [67, 77, 88, 89, 312] and model-based [64, 66, 69–71, 74, 76, 313] methods for measurement of the insertion force during RCI procedures. For haptic rendering in RCI systems, researchers have adopted three different approaches, i.e., active, semi-active, and passive [62]. The active approach

typically requires using a controllable torque- (or force-) generating component, e.g., a DC motor or a shape-memory alloy (SMA). Typically haptic feedback is rendered by continuous control of the current passing through the torque-generating element. With a proper assembly with a kinematic mechanism, e.g., capstan mechanism, the active approach can provide the required workspace and exhibit the required haptic capacity. While active haptic rendering is known for its accuracy and fast dynamic response, it suffers from high power consumption and instability at the extremes of force capacity [62, 63].

For passive haptic rendering, an adjustable frictional medium is usually used to regulate the resistance against the motion and to generate desired levels of resistant force or torque [206, 207, 314]. Passive rendering is relatively simple to implement and is fairly stable. However, the dynamic range of passive haptic rendering is limited and strongly depends on the intrinsic material properties of the haptic element. Given that the intrinsic material properties are not controllable and change in time, by mechanical wearing, this approach has a limited scope of application [53, 63].

With the emergence of smart materials with controllable mechanical properties, the use of semi-active haptic rendering has gained momentum. For semi-active haptic rendering, a smart material with controllable mechanical properties, such as magnetorheological fluids (MRF), magnetorheological elastomers (MRE), or electroactive polymers (EAP), is used. The smart material is used as an integral part of a kinematic mechanism, e.g., in joints or links, and haptic feedback is rendered by controlling its mechanical properties. For example, the mechanical properties of MRFs and MREs can be controlled by controlling the external magnetic field [63, 312, 315, 316].

More specifically for robot-assisted surgery, Mazursky *et al.* proposed a slim haptic actuator conveying both kinesthetic and vibrotactile information to the user [317]. Although their system could simultaneously provide kinesthetic and tactile feedback, its accuracy was compromised due to the lack of a feedback control loop. In another effort, Kanjanapas *et al.* [318] proposed a wearable two-degree of freedom (DOF) pneumatic soft linear tactor to provide force feedback through intermittent pneumatic compression on the wrist. Although their design was complex and not simple to manufacture, it was capable of rendering zero-force and stiffness which led to a large bandwidth for the rendered feedback. Nevertheless, the use of a pneumatic system requires a continuous pressure

supply for sustained forces (required for RCI applications) which limits the applicability of pneumatic systems for RCI applications.

MRFs have also been used as the media for force feedback applications, e.g., [319–321]. Typically With MRFs, two large electrical coils are used to generate a magnetic field. MRFs exhibit controllable viscosity with an external magnetic field. The current in the coils is usually in the range of 1-10 Amp [312]. While MRFs provide sufficient force range for RCI applications, they suffer from handling issues (due to their fluidic state), usability in clean areas (e.g., operation rooms), and exhibit large heat generation (due to the power consumption of the coils). Heat accumulation in MRFs drastically changes the magneto-fluidic properties of the MRFs and may lead to inaccurate force rendering [63]. Moreover, MRF-based systems cannot generate zero friction on catheters due to their passive viscosity, i.e., intrinsic viscosity in the absence of an external magnetic field.

As a new modality, the utilization of MREs as haptic media has recently been proposed by the author [63, 72, 322]. In the previous studies, the author has proposed using a pair of rare-earth permanent magnets (N52) were used in a feedback loop to control the stiffness and force of a composite MRE. Their system was capable of generating feedback forces in the range of 0-10 N with an acceptable refresh rate (63 Hz). Their MRE-based force feedback system was in compliance with the functional and physical requirements of haptic displays for robot-assisted surgery. In addition to their fast response, the mechanical properties of MREs are temporally stable and reversible under operational conditions [323]. A more comprehensive literature survey on the approaches and methods of haptic provision for RCI applications can be found in [62]. Table 7.1 compares different haptic and tactile rendering methods proposed in the literature.

7.1.3 Haptic Feedback for RCI: Requirements

The proposed haptic rendering in this study is categorized under the semi-active approach. In this study, the resistant torque on a ferromagnetic shaft is regulated through regulating the contact stress (and friction) between the shaft and an MRE hollow cylinder (Fig. 7.2). Based on the reviewed literature, a haptic interface for robot-assisted interventional surgery shall exhibit a force range of 0-2 N [62], with a resolution of 5% of full-scale, i.e., 0.1 N. For this study, we coupled the output

Table 7.1: Comparison of representative studies proposing haptic rendering for the minimally invasive surgery applications.

Study	Haptic cue	Principle	Advantages	Limitations
Culjat *et al.* [324] (2008)	Stiffness	Pneumatic	MR-safe, range, simple, low profile	Zero passive stiffness, specific for da Vinci robot
Dargahi *et al.* [53] (2012,2016)	Force	DC motor	Fast, cheap, simple	range, not MRI-safe, electrically active
Oh *et al.* [325, 326] (2013)	Force	MRF*	Passive stiffness, simple, range	Electrically active, not MRI-safe
Han *et al.* [327] (2018)	Stiffness	EAP†	MRI-safe, passive stiffness	Complex, electrically active
Yanatori *et al.* [328] (2019)	Stiffness	SMA‡	Passive stiffness, simple	Electrically active, not MRI-safe, range
Mazursky *et al.* [317] (2019)	Force	MRF	Passive stiffness, simple, range, low profile	Electrically active, not MRI-safe
Hooshiar *et al.* [63] (2020)	Force	MRE	Passive stiffness, simple, range, low profile electrically passive	not MRI-safe

*MRF: Magneto-rheological fluid †EAP: electro-active polymer ‡SMA: shape-memory alloy

shaft of the proposed system to a 40 mm roller to translate the resistant torque to a linear force. Therefore, the required torque range to generate a linear force of 0-2N was 0-40 mNm with a resolution of 2 mNm. Moreover, the system shall be repeatable within its operational force range with a standard-deviation of repetitions less than 5% of full-scale (4 mNm).

7.1.4 Novelty and Contributions

The novelty of this work is in the utilization of an MRE as a torque regulating media. To the best of the author's knowledge, this haptic modality has not yet been studied. Based on the feasibility of using MREs for force and stiffness feedback [63, 322], the author has proposed an MRE-based torque feedback mechanism with potential application in haptic feedback devices for robot-assisted interventions. The specific contributions of this study are:

(1) multi-physics modeling of the magnetoelastic behavior of the MRE and ferromagnetic output shaft,

(2) analytical solution of the developed magnetoelastic model for the magnetostriction phenomenon in the MRE,

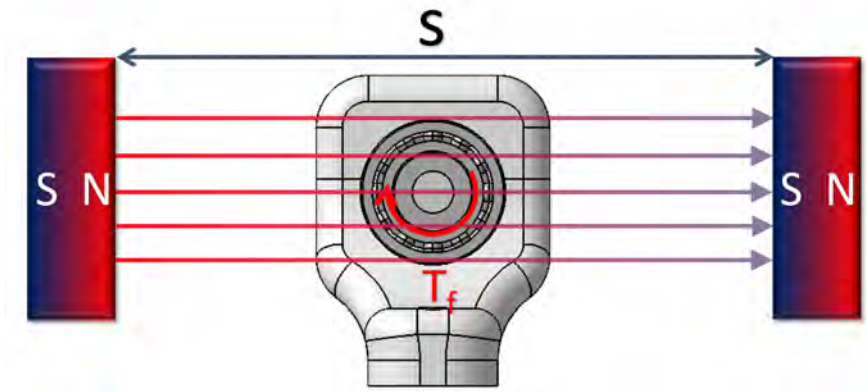

(a)

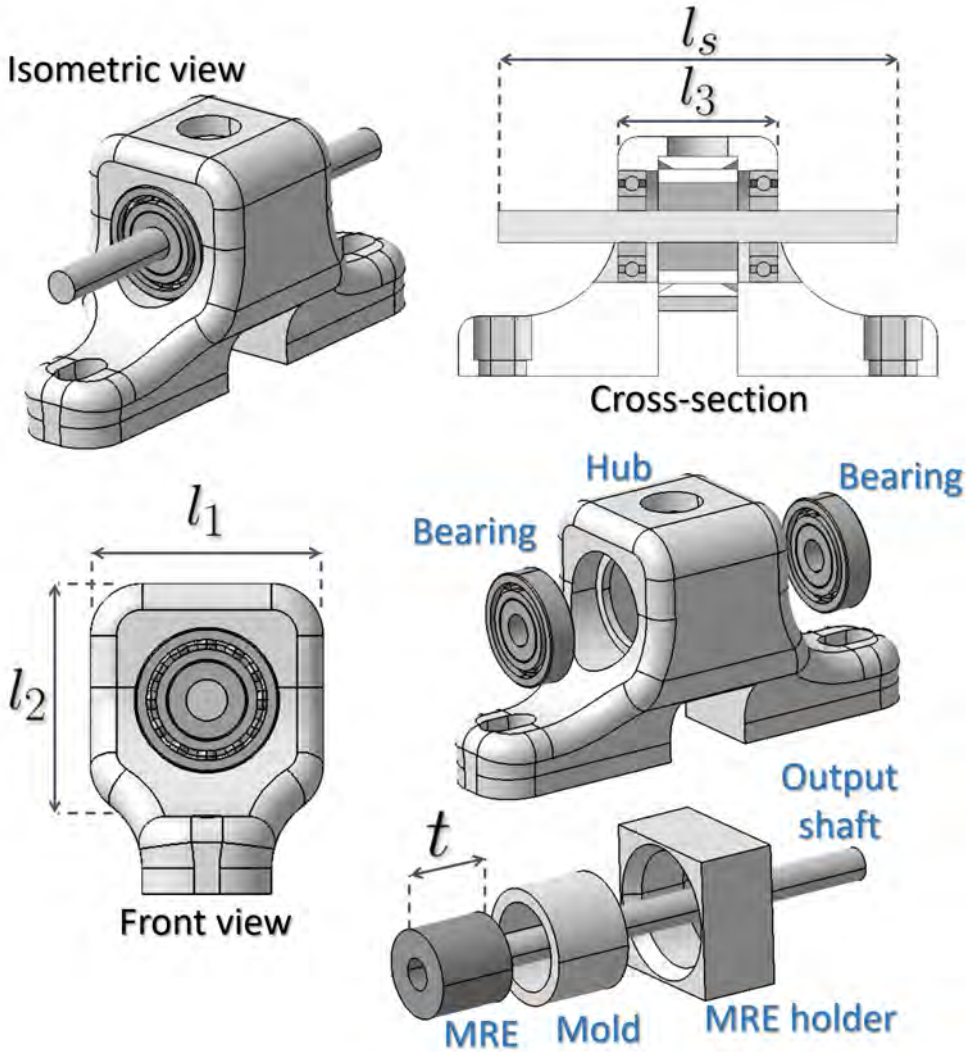

(b)

Figure 7.2: (a) Schematic placement of TorMag in external magnetic field, and (b) components of the proposed MRE-based torque feedback system.

Table 7.2: Geometrical dimensions used in the design of the proposed torque feedback system, TorMag.

	MRE Cylinder			Shaft	Housing		
Dimension	R_o	R_i	t	l_s	l_1	l_2	l_3
(mm)	11	4	20	75	40	45	40

(3) proposing and prototyping a novel MRE-based mechatronics system for insertion force feedback considering the requirements of RCI applications,

(4) generation of a radial magnetic field using permanent magnets without a need for coils,

(5) integration of the proposed system with a representative RCI system and experimental validation with respect to the requirements of RCI.

In the following, the concept, multi-physics modeling, and solution schema are described in Sec. 7.2. Also, the results of three validation studies are presented and discussed in Sec. 7.3, followed by the key findings, concluding remarks, and future extensions in Sec. 7.5.

7.2 Material and Methods

7.2.1 System Design

The conceptual design of the proposed system is based on controlling the frictional torque between a an MRE and a ferromagnetic shaft (iron). It was hypothesized that the contact stress between the MRE and the shaft could be regulated by changing the external magnetic field. The external magnetic field induces magnetization in the ferromagnetic output shaft which pulls the MRE radially leading to the generation of contact stress. The contact stress at the interface generates a frictional resistant torque against the motion of the output shaft, which was exploited for haptic force rendering.

Also, depending on the application, the proposed system can be coupled to a gearbox for torque scaling or torque conversion to force feedback during RCI procedures [62]. The geometrical dimensions used in this study are summarized in Table 7.2. Due to the circumferential symmetry, a homogeneous radial contact stress σ_i is present at the interface of the output shaft and the MRE.

The system also used two rare-earth permanent magnets to generate the external magnetic field. The author has previously used such a dual-magnet configuration for generating a stationary magnetic field in the absence of a ferromagnetic shaft [63, 322]. As will be discussed in Sec. 7.2.4, the proposed configuration of the permanent magnets, MRE, and iron output shaft, would result in a fairly radial magnetic field within the MRE.

7.2.2 MRE Fabrication

The range of torque (force) generation of the proposed system depends on the volume fraction of the ferromagnetic particles filler in the MRE composite, geometrical design and contents of the MRE, geometry and magnetic properties of the shaft, and the strength of magnets. In this study, three isotropic MRE composites with silicon rubber (matrix) and iron particles (filler) were fabricated using the three-stage method provided in [322, 329].

For the matrix, silicon rubber (Ecoflex™, Smooth-On Inc., PA, USA) with a shore-hardnesses of 00-50 was used as the matrix. The silicon rubber was composited with 10%, 20%, and 40% volume percentage of Carbonyl iron powder (CIP) (SQ, BASF, Germany) according to the contents specifications summarized in Table 7.3. The CIP had a nominal average particle diameter of 45 μm with less than 5% variation. Also, Slacker™ (silicon oil) and silicon thinner were used as additives in the emulsions to enhance their moldability. After mixing, the emulsions were degassed in a vacuum chamber (Best Value Vacs, IL, US) at 29 inHg vacuum pressure for 5 minutes to release the entrapped air in the MREs during the mixing. Finally, the emulsions were directly molded in 3D-printed MRE holders (Fig. 7.3(a)) and were rested to set in standard laboratory conditions for 24 h.

The author's recent findings in [322], indicate the initial shear moduli of $G_0 = 81$ kPa,$G_0 = 183$ kPa, and $G_0 = 281$ kPa for MRE-10, MRE-20, and MRE-40, respectively. Similar ranges of shear moduli have been reported in the literature, e.g., [330, 331].

7.2.3 Prototype

The hub and the MRE holder of TorMag were prototyped using a 3D-printer (Replicator+, MakerBot Industries, LLC, NY, USA) with poly-lactic acid (PLA) filaments. A magnetic field controller,

Table 7.3: Density, mass, and volume percentage of the contents of the fabricated MREs.

Material	Contents per 100 cc volume %vol., mass			
	Ecoflex 0050 $\rho_{SR} = 1.04\frac{g}{cc}$	Slacker $\rho_{SL} = 0.97\frac{g}{cc}$	Silicone thinner $\rho_{ST} = 0.97\frac{g}{cc}$	CIP $\rho_{CIP} = 7.87\frac{g}{cc}$
MRE-10	80%, 83.2g	5%, 4.9g	5%, 4.9g	10%, 78.7g
MRE-20	70%, 72.1g	5%, 4.9g	5%, 4.9g	20%, 157.4g
MRE-40	50%, 52.0g	5%, 4.9g	5%, 4.9g	40%, 314.8g

previously developed and validated by the author in [63], was used for control of the separation between the two magnets. Two DC motors (JGY370-12V, BringSmart Intelligent Tech. Co. Ltd., Fujian, China) (Motor-1 and -2) with a 1:60 worm gear were used to control the magnets individually. The details of the PID feedback controller are provided in 7.3.3.1. The PID controller was capable of controlling the magnet separation with an error of less than 1mm [63]. Fig. 7.3(b–c) show the components of TorMag and the assembled prototype.

7.2.4 Magnetic Field: Simulation and Verification

It was hypothesized that the presence of an iron shaft at the mid-span of two magnets would absorb and amplify the magnetic field generated by the magnets. To simulate and visualize the trajectory of the magnetic field, a 3D steady-state magnetic analysis was performed using COMSOL Multiphysics© 5.3a (COMSOL AB, Stockholm, Sweden). The magnetic field was generated by two Neodymium N52 permanent magnets ($2\times2\times1/2$ in, CMS Magnetics Inc., TX, USA) with a coercive force of 875 kAm and remanence of 1.45 T. The iron shaft was modeled as Cobalt-iron alloy with an isotropic relative permeability of 18000 $^{H}/_{m}$. The MRE was modeled as a ferromagnetic media with a linear magnetization [332–334].

The constitutive equation relating the magnetic field intensity **h** to the magnetic flux density **b** within the MRE was:

$$\mathbf{b} = \mu_0 \mu_r \mathbf{h}, \tag{150}$$

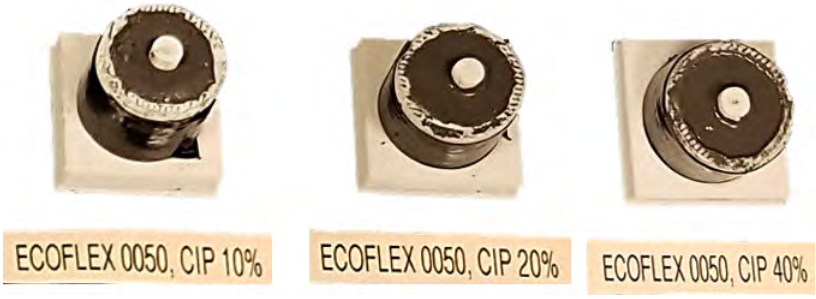

(a)

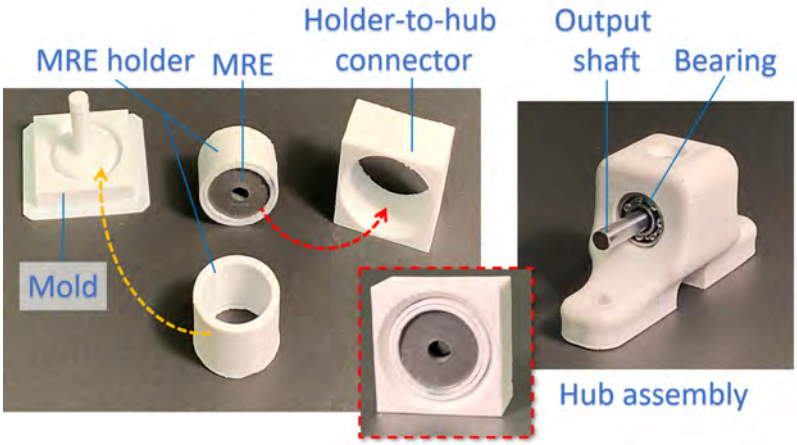

(b)

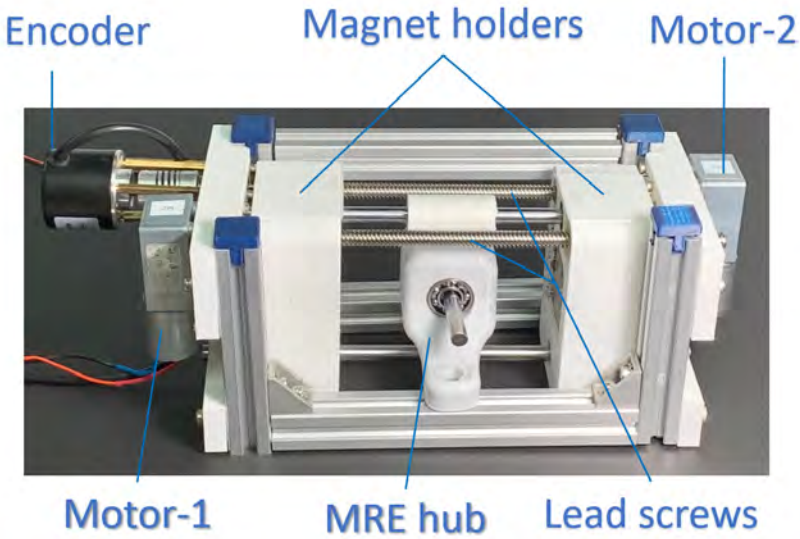

(c)

Figure 7.3: (a) Molded MREs in 3D-printed molds, (b) MRE mold and hub connector assembly, and (c) prototyped TorMag with 3D printed hub.

where $\mu_0 = 4\pi \times 10^{-7} H/m$ is the permeability of vacuum and μ_r is the relative magnetic permeability of the MRE. Recent experimental studies, e.g., [335], suggest that isotropic MREs similar to this study typically exhibit a relative permeability of $\mu_r \approx 2 - 4$ with linear variation with respect to CIP volume fraction.

In cylindrical coordinates, the magnetic field intensity **b** would be of the form:

$$\mathbf{b} = b_R(R, \theta, Z)\hat{\mathbf{e}}_R + b_\theta(R, \theta, Z)\hat{\mathbf{e}}_\Theta + b_z(R, \theta, Z)\hat{\mathbf{e}}_Z, \tag{151}$$

where $\hat{\mathbf{e}}_{(.)}$ and $b_{(.)}$ are the directional unit vectors and directional components of the magnetic field, respectively.

To obtain the variation of the magnetic field with changing the separation gap s, the simulation was repeated for separation gaps of $s = 45, 55, 65, 75, 85, 95$ mm. Fig. 7.4(a-c) depict the distribution of the magnetic field intensity for three representative magnet separations. In all cases, the proximity of MRE to the iron shaft and the fact that magnetic trajectory shall enter and depart perpendicular to the surfaces of ferromagnetic media ($\mathbf{n} \cdot \mathbf{b} = 0$, with **n** as the unit normal of each surface), the field lines have passed through the MRE in mostly radial trajectories. Meanwhile, the iron shaft has amplified the magnetic field locally has increased the magnetic field induced within the MRE. However, the magnetic field has almost halved by distance from the iron shaft within the MRE, i.e., from R_i toward R_o, (Fig. 7.4(e)). Also, Fig. 7.4(e) shows that the magnetic field within the MRE is inversely proportional to the separation between the magnets, whereas, the smaller separation gaps have resulted in larger magnetic fields. The maximum magnetic field within the MRE was 782 mT for $s = 45$ and was 111 mT for $s = 95$ mm. Experimental measurement of the magnetic field using a Gauss-meter (GM2, AlphaLab Inc., PA, USA) verified the results of the simulation for magnetic field within the MRE (Fig. 7.4(d–e)). The average error between the simulation and experiment for the magnetic field was 14 ± 21 mT with maximum error observed for $s = 45$, i.e., 21 ± 32 mT.

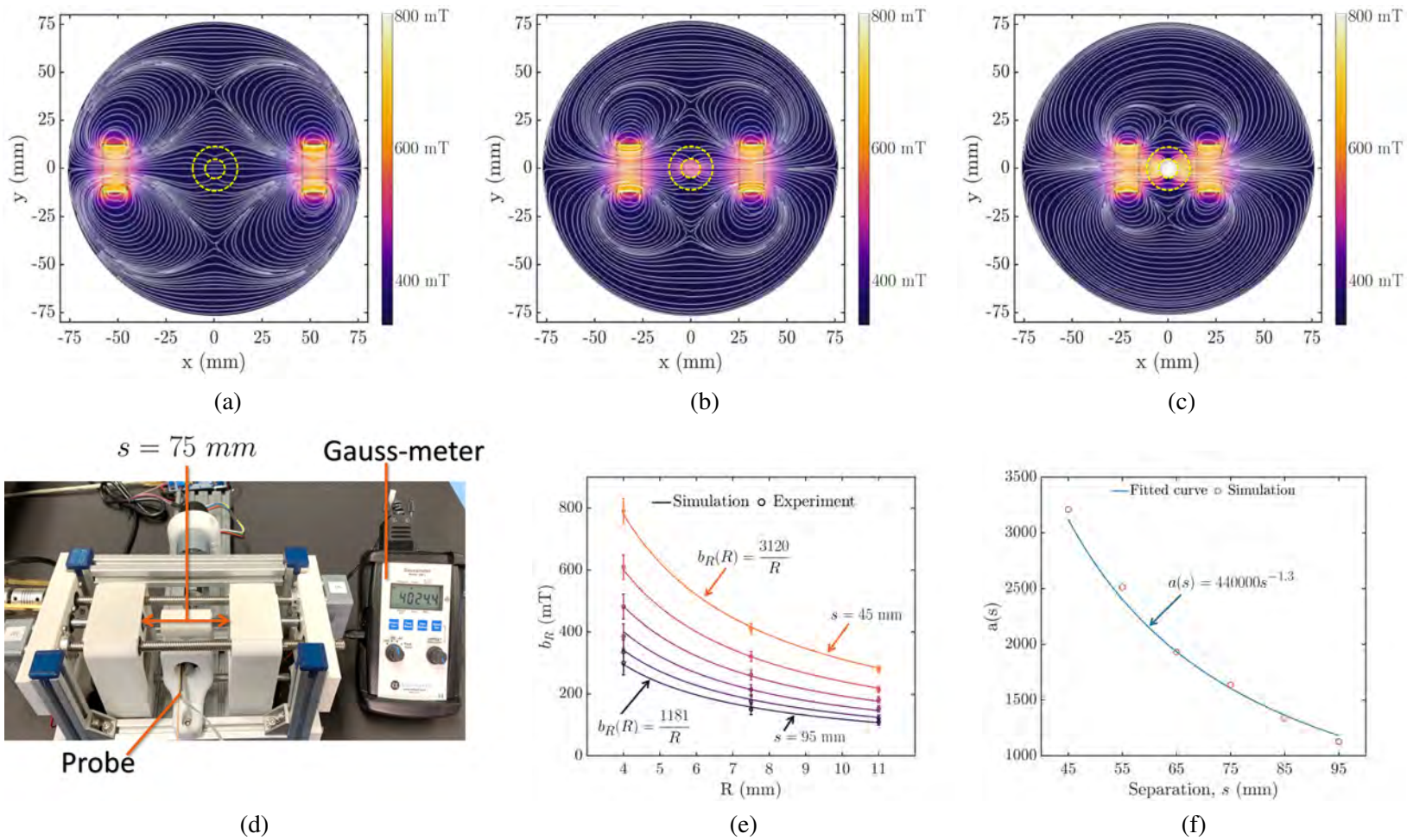

Figure 7.4: Distribution of the magnetic field intensity with magnets separation (a) $s = 95$mm, (b) $s = 55$mm, (c) $s = 45$mm, and (d) experimental setup used for verifying the results of magnetic field simulation for $s = 75$mm, (e) comparison of the simulation and experiment results for the variation of the radial magnetic field within the MRE, and (e) variation of fitting parameter $a(s)$ with magnet separation s.

Table 7.4: The extremal values of magnetic field within the MRE and the best fitting parameters for variation of radial magnetic field in Eq. 152.

Separation s (mm)	Range of b_R $R = R_i$ (mT)	$R = R_o$	Fitting Parameters $a(s)$	Goodness-of-fit
45	792	279	3120	0.998
55	603	210	2403	0.998
65	479	177	1935	0.995
75	402	152	1606	0.994
85	341	126	1365	0.992
95	300	111	1181	0.990

To find an analytical representation for b_R to be used in the magnetoelastic model, the radial component of the magnetic field within the MRE was approximated as:

$$b_R(R, s) = \frac{a(s)}{R}, \tag{152}$$

where $a(s)$ was a $s-$dependent fitting parameter. Table 7.4 summarizes the fitting parameter for various gap separations s. Also, Fig. 7.4(f) shows the change in the fitting parameter a obtained from the simulation with s and the fitted $a(s)$. The curve fitting was performed in the Curve Fitting Toolbox of Matlab (R2019b, Mathworks Inc., MA, USA) and two representative fitted curves for the magnetic field are shown on Fig. 7.4(e).

The post-processing showed that the maximum circumferential variation of b_R has happened at the outer surface $R = R_o$. The variation of b_R in Θ-direction (circumferential direction), would result in shear strain within the MRE and which cannot be accounted for if b_Θ is neglected. However, with the proposed design in 7.2.1, the outer surface of the MRE would be fixed inside the holder block, thus the shear strains caused by the circumferential variations of b_R would be zero at $R = R_o$ and negligible at $R_i \leq R < R_o$. More specifically, the maximum ratio of b_θ to b_R was observed at $R = R_o, \Theta = \frac{\pi}{2}$), where ${}^{b_\theta}/_{b_r} = 0.21$ while the volumetric average absolute ratio of b_θ to b_R was $\vartheta = 0.0416$ for the entire volume of the MRE. ϑ was obtained using:

$$\vartheta = \frac{1}{V_{\text{MRE}}} \int_{R_i}^{R_o} \int_{-\pi}^{\pi} \int_{-\frac{t}{2}}^{\frac{t}{2}} \frac{|b_\theta|}{|b_R|} r \mathrm{d}z \mathrm{d}\theta \mathrm{d}r = 0.162, \tag{153}$$

where $V_{\text{MRE}} = \pi t(R_o^2 - R_i^2)$. From a physical point of view, ${}^{|b_\theta|}/_{|b_R|}$, represents the tangent of

the acute angle between the radial and circumferential components. Therefore, $\vartheta = 0.162$ would correspond to an average acute angle of $\approx 9°$. By neglecting this variation, the magnetic field was assumed to be radial with a negligible circumferential component.

7.2.5 Magnetic Compatibility: Maxwell Equations

To assure the approximated magnetic field does not violate the necessary magnetic compatibility conditions, i.e., Maxwell equations, these equations were tested with the approximated b_R. Maxwell equations for the MRE were [336]:

$$\nabla \times \mathbf{h} = \mathbf{0}, \tag{154}$$

$$\nabla \cdot \mathbf{b} = 0, \tag{155}$$

where, $\nabla \times (.)$ is the curl operator, and $\nabla \cdot (.)$ is the divergence operator in cylindrical coordinates. Using Eq. 152 in the Maxwell equations and assuming $b_\Theta = 0$, it can be shown that b_Z is necessarily constant. This condition was in agreement with the numerical findings from the simulation. The maximum longitudinal magnetic field (b_Z for $s = 45$ mm) was $b_Z = 19.5 \pm 2.54$ mT (13% change) and its minimum (b_Z for $s = 95$ mm) was $b_Z = 1.22 \pm 0.04$ mT (3.3% change) within the MRE. The reason for the observed small changes in b_Z might be due to the effect of the presence of b_Θ. However, since b_Θ was assumed absent, b_Z was modeled as a univariate linear function of s:

$$b_Z = 0.37(45 - s) + 1.22. \tag{156}$$

7.2.6 Resistant Torque

As stated in Sec. 7.2.1, during rotation of the output shaft (iron shaft) it would bear a frictional torque caused by the contact stress σ_i at its interface with the MRE. Considering the dynamic coefficient of friction μ_d and assuming the Coulomb friction model (dry friction), the magnitude of the frictional resistant torque T_r was obtained as:

$$T_r = \zeta|\sigma_i|, \tag{157}$$

where, σ_i is the true (Cauchy) stress at the interface and $\zeta = \lambda_3(R_i)2\pi t R_i^2 \mu_d$ was the traction coefficient. Assuming the output shaft in a quasi-static balance (i.e., the shaft has negligible rotational

inertia compared to the operational torque), a steady-state torque of equal magnitude but in the opposite direction of T_r is required to keep the shaft rotating. In the following sections, magnetoelastic modeling is described to find an analytical relationship between T_f and s. Such an analytical model is desirable for finding the required magnet separation to control (keep) a desired resistant torque on the output shaft, e.g., for haptic feedback applications.

7.2.7 Magnetoelastic Modeling

The decreasing trend of the magnetic field with R causes a distributed body force on MRE material toward the iron shaft. Studies have shown that for a hyperelastic magnetorheological composite, the state of stress is dependent on the stored strain energy in it due to mechanical deformation and the stored magnetic energy due to its presence in a magnetic field [337]. Thereby, σ_i shall take the form of:

$$\sigma_i = f(\Omega^\star, \mathbf{b}), \tag{158}$$

where, $\Omega^\star$ is the total amended free energy function incorporating both mechanical strain energy and magnetic energy contributions.

7.2.7.1 Geometry and domain

Fig. 7.5 shows a schematic initial and deformed geometries of the MRE and the free-body diagram of the output shaft. The MRE is in contact impending with the shaft. The geometric properties of the MRE and shaft are provided in Table 7.2.

Hereinafter, $\mathbf{X} = \begin{pmatrix} R & \Theta & Z \end{pmatrix}$ denote the material (original) cylindrical coordinates of the points inside the MRE with $R \in [R_i, R_o]$, $\Theta \in [-\pi, \pi]$, $Z \in [-\frac{t}{2}, \frac{t}{2}]$ and $\mathbf{x} = \begin{pmatrix} r & \theta & z \end{pmatrix}$ denote the spatial (deformed) coordinates system.

7.2.7.2 Kinematics

It was assumed that there exists a one-to-one, smooth and differentiable mapping χ from material to spatial shape of MRE such that $\mathbf{x} = \chi(\mathbf{X})$. For the assumed mapping $\chi(\mathbf{X})$, there is a deformation gradient $\mathbf{F}$ defined as:

$$\mathbf{F} = \frac{\mathrm{d}\mathbf{x}}{\mathrm{d}\mathbf{X}} \quad \Rightarrow \quad \mathrm{d}\mathbf{x} = \mathbf{F}\mathrm{d}\mathbf{X}. \tag{159}$$

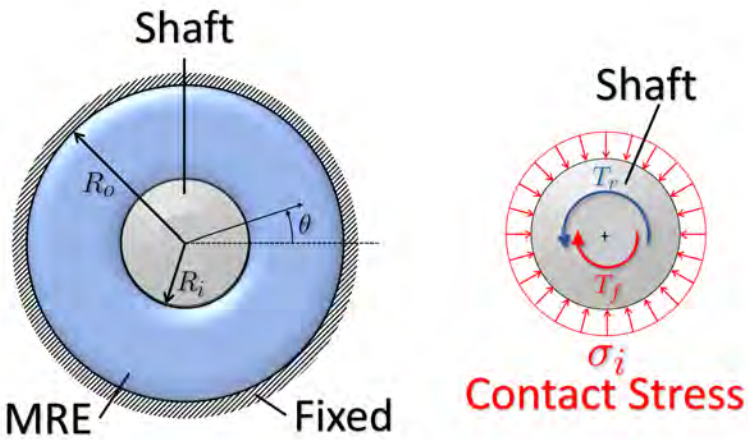

(a)

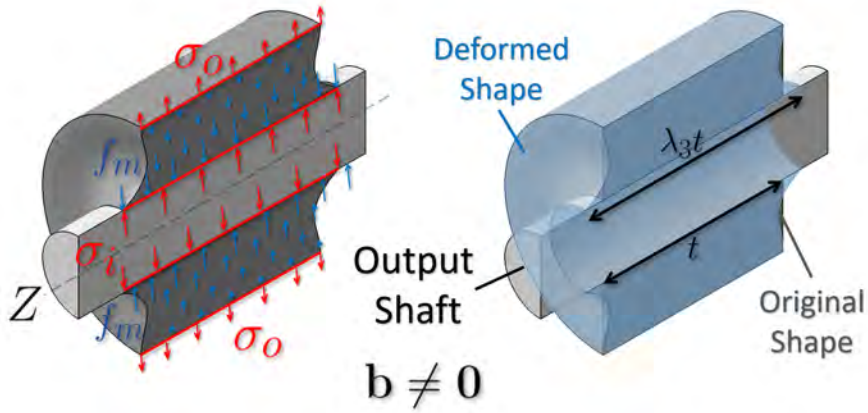

(b)

Figure 7.5: (a) Geometry of the transverse cross-section of the shaft and MRE with fixed boundary conditions at outer radius (left) and the free-body diagram of the output shaft (right), (b) schematic distribution of body force and stress at the boundaries of MRE (left) and illustration of the deformed and original shape of the MRE.

The radial, circumferential, and longitudinal stretches are $\lambda_r, \lambda_\theta$ and λ_z. Because of the monotonically decreasing radial magnetic field within the MRE, the material points are pulled toward the shaft. The present deformation is a special case of inflation of a hollow cylinder introduced in [332] with the additional boundary condition $\lambda_1(R_o) = 1$. Therefore, the principal stretches $\lambda_{1,2,3}$ in cylindrical coordinates [338] are:

$$\lambda_1 = \lambda_R = \frac{\mathrm{d}r}{\mathrm{d}R}, \tag{160}$$

$$\lambda_2 = \lambda_\Theta = \frac{r}{R}, \tag{161}$$

$$\lambda_3 = \lambda_Z = \frac{2z}{t}. \tag{162}$$

Therefore, the deformation gradient F is:

$$\mathbf{F} = \begin{pmatrix} \lambda_1 & 0 & 0 \\ 0 & \lambda_2 & 0 \\ 0 & 0 & \lambda_3 \end{pmatrix}. \tag{163}$$

Typically, MREs are made of hyperelastic rubbers which are incompressible. The incompressibility assumption necessitates:

$$\lambda_1\lambda_2\lambda_3 = 1 \Rightarrow \lambda_3 = (\lambda_1\lambda_2)^{-1}. \tag{164}$$

Also, the Right Cauchy-Green deformation tensor, $\mathbf{C} = \mathbf{F}^\mathsf{T}\mathbf{F}$ was obtained as:

$$\mathbf{C} = \begin{pmatrix} \lambda_1^2 & 0 & 0 \\ 0 & \lambda_2^2 & 0 \\ 0 & 0 & (\lambda_1\lambda_2)^{-2} \end{pmatrix}. \tag{165}$$

The magnetoelastic constitutive equations of MREs are expressed in terms of the magnetoelastic deformation invariants. The three scalar invariants of tensor $\mathbf{C}$ were obtained according to [338] as:

$$I_1(\mathbf{C}) = \mathrm{Tr}\mathbf{C} = \lambda_1^2 + \lambda_2^2 + (\lambda_1\lambda_2)^{-2}, \tag{166}$$

$$I_2(\mathbf{C}) = \frac{I_1(\mathbf{C})^2 - I_1(\mathbf{C}^2)}{2} = \frac{(\mathrm{Tr}\mathbf{C})^2 - (\lambda_1^4 + \lambda_2^4 + \lambda_3^4)}{2}, \tag{167}$$

$$I_3(\mathbf{C}) = \det \mathbf{C} = \lambda_1^2\lambda_2^2\lambda_3^2 = 1, \tag{168}$$

where $\mathrm{Tr}(.)$ is the trace operator from $\mathbb{R}^{3\times3}$ to $\mathbb{R}$, summating the diagonal components of $(.)$ into a scalar. Also, three magnetoelastic invariants, $I_{4,5,6}$ were obtained according to [332] as:

$$I_4 = \mathbf{b}\cdot\mathbf{b} = \frac{a^2}{R^2} + b_Z^2, \tag{169}$$

$$I_5 = (\mathbf{Cb}).\mathbf{b} = \frac{a^2\lambda_1^2}{R^2} + b_Z^2(\lambda_1\lambda_2)^{-2}, \tag{170}$$

$$I_6 = (\mathbf{C}^2\mathbf{b}).\mathbf{b} = \frac{a^2\lambda_1^4}{R^2} + b_Z^2(\lambda_1\lambda_2)^{-4}. \tag{171}$$

It is noteworthy that $I_{1,2}$ only depend on the mechanical stretches $\lambda_{1,2}$ while $I_{4,5,6}$ depend on both the mechanical stretches and magnetic field.

7.2.7.3 Constitutive model

Since both the mechanical stretch and magnetic field contribute to the total free energy stored in the MRE, the mechanical energy is amended with the magnetic energy [332]. Therefore, the total potential energy function $\Omega^\star$ is:

$$\Omega^\star = \Omega + \Psi, \tag{172}$$

where Ω is the strain energy density function, and Ψ is the magnetic energy density function defined as [335]:

$$\Psi = \frac{1}{2}(\mu_0\mu_r)^{-1}(\mathbf{Cb})\cdot\mathbf{b} = \frac{1}{2}(\mu_0\mu_r)^{-1}I_5. \tag{173}$$

Various forms have been adopted in the literature for Ω to model the hyperelastic behavior of MRE, e.g., Ogden [72], Mooney-Rivlin [339]. In this study, as the MRE is mainly under compression, the principal stresses are compressive, thus, a two-term Mooney-Rivlin model was adopted. Studies have previously shown that this constitutive model can sufficiently capture the stretch-stress behavior of hyperelastic cylinders under radial stretch [339–341]. The adopted form of Ω was:

$$\Omega = C_{10}(I_1 - 3) + C_{01}(I_2 - 3), \tag{174}$$

where C_{10} and C_{01} are the material constants of the MRE in the absence of a magnetic field. It is noteworthy that for an incompressible hyperelastic material the initial shear modulus can be obtained through $G_0 = 2(C_{01} + C_{10})$. The total nominal stress tensor of MRE, combining the effects of elastic stress (due to the elastic deformation) and Maxwell stress (due to the magnetic

body force) was obtained as [332]:

$$\mathbf{T} = 2\Omega_1^\star \mathbf{\Lambda} + 2\Omega_2^\star (I_1 \mathbf{\Lambda} - \mathbf{\Lambda}^2) - p\mathbf{I} + 2\Omega_5^\star \mathbf{b} \otimes \mathbf{b}, \tag{175}$$

where

$$\Omega_i^\star = \frac{\partial \Omega}{\partial I_i} \Rightarrow \Omega_1^\star = C_{10}, \Omega_2^\star = C_{01}, \Omega_5^\star = \frac{1}{2}(\mu_0 \mu_r)^{-1}, \tag{176}$$

and $\mathbf{\Lambda} = \mathbf{F}\mathbf{F}^\mathsf{T}$, $\mathbf{I}$ a 3-by-3 identity matrix, p a Lagrange multiplier enforcing the incompressibility constraint, and $\otimes$ as the outer product operator such that $\mathbf{b} \otimes \mathbf{b} = \mathbf{b}\mathbf{b}^\mathsf{T}$.

Since $\mathbf{F}$ is diagonal, $\mathbf{\Lambda} = \mathbf{F}\mathbf{F}^\mathsf{T} = \mathbf{F}^\mathsf{T}\mathbf{F} = \mathbf{F}^2 = \mathbf{C}$. Therefore, the constitutive equation (Eq. 175) simplifies to:

$$\mathbf{T} = 2C_{10}\mathbf{F}^2 + 2C_{01}(I_1 \mathbf{F}^2 - \mathbf{F}^4) - p\mathbf{I} + (\mu_0 \mu_r)^{-1} \mathbf{b} \otimes \mathbf{b}. \tag{177}$$

Tensor $\mathbf{T}$ is diagonal and its diagonal components simplify to:

$$T_{11} = 2C_{01}\lambda_1^2 + 2C_{10}(\lambda_1^2\lambda_2^2 + \lambda_2^{-2}) + (\mu_0\mu_r)^{-1}\frac{a^2}{R^2} - p, \tag{178}$$

$$T_{22} = 2C_{01}\lambda_2^2 + 2C_{10}(\lambda_1^2\lambda_2^2 + \lambda_1^{-2}) - p, \tag{179}$$

$$T_{33} = 2C_{01}\lambda_1^{-2}\lambda_2^{-2} + 2C_{10}(\lambda_1^{-2} + \lambda_2^{-2}) + (\mu_0\mu_r)^{-1} b_Z^2 - p. \tag{180}$$

From the boundary conditions, the MRE does not bear a longitudinal force, thus T_{33} shall be zero. Therefore, Lagrangian multiplier p was determined as:

$$p = 2C_{01}\lambda_1^{-2}\lambda_2^{-2} + 2C_{10}(\lambda_1^{-2} + \lambda_2^{-2}) + (\mu_0\mu_r)^{-1} b_Z^2. \tag{181}$$

Substituting p in Eq. 178–179, the magnetoelastic constitutive relations between the kinematic variables $\lambda_{1,2}$, and nominal stress $\mathbf{T}$ were obtained:

$$T_{11} = 2C_{01}(\lambda_1^2 - \lambda_1^{-2}\lambda_2^{-2}) + 2C_{10}(\lambda_1^2\lambda_2^2 - \lambda_1^{-2}) + (\mu_0\mu_r)^{-1}\left(\frac{a^2}{R^2} - b_Z^2\right), \tag{182}$$

$$T_{22} = 2C_{01}(\lambda_2^2 - \lambda_1^{-2}\lambda_2^{-2}) + 2C_{10}(\lambda_1^2\lambda_2^2 - \lambda_2^{-2}) - (\mu_0\mu_r)^{-1} b_Z^2, \tag{183}$$

$$T_{33} = 0. \tag{184}$$

The derived magnetoelastic constitutive equations show that at any given $\lambda_{1,2}$ increasing the magnetic field (through decreasing the distance s between the magnets) would decrease T_{11} toward more

negative (compressive) stresses within the MRE. This intuition confirms the hypothesis of this study that with decreasing the distance s, compressive stress at the interface of the output shaft and MRE would increase.

From the boundary conditions, the material points on the inner and outer radii of the MRE do not translate in R-direction during any deformation. Also, since the MRE is glued at the outer diameter to the MRE holder, the material points located at $R = R_o$ do not translate in $Z-$direction, thus, according to the definitions of $\lambda_{2,3}$ (Eq. 161–162):

$$\lambda_2(R_i) = 1, \tag{185}$$

$$\lambda_2(R_o) = 1, \tag{186}$$

$$\lambda_3(R_o) = 1. \tag{187}$$

Therefore, due to the incompressibility constraint:

$$\lambda_1(R_o)\lambda_2(R_o)\lambda_3(R_o) = 1 \Rightarrow \lambda_1(R_o) = 1. \tag{188}$$

With $G_0 = 2(C_{10} + C_{01})$ as the initial (linear) shear modulus [338] of the MRE and applying the boundary conditions for $R = R_i$, the constitutive equations (Eq. 182–183) necessitate:

$$T_{11}(R_i) = G_0(\lambda_1^2(R_i) - \lambda_1^{-2}(R_i)) + (\mu_0\mu_r)^{-1}\left(\frac{a^2}{R_i^2} - b_Z^2\right), \tag{189}$$

$$T_{11}(R_o) = (\mu_0\mu_r)^{-1}\left(\frac{a^2}{R_o^2} - b_Z^2\right). \tag{190}$$

Given that the value of a/R_o is larger than b_Z, $T_{11}(R_o)$ is always positive indicating a tensile force at the outer boundary of the MRE. This tensile force is the reaction force against the pulling magnetic force toward the output shaft on the MRE. Nonetheless, Eq. 189 still involves the unknown λ_1. To determine λ_1, the full description of T_{11} was obtained through utilizing the force balance principle on the MRE.

7.2.7.4 Force balance on the MRE

The force balance equation on the MRE is:

$$-T_{11}(R_i)\lambda_3(R_i)A_i + T_{11}(R_o)A_o + F_m = 0, \tag{191}$$

where, $\lambda_3(R_i)A_i = 2\pi R_i t \lambda_1^{-1}(R_i)$ is the true (deformed) surface area of the MRE at the inner radius, $A_o = 2\pi R_o t$ is its the surface area at the outer boundary, and f_m is the magnetic body force per unit volume [337] defined as:

$$f_m = \frac{\mu_r - 1}{2\mu_0\mu_r}\nabla(\mathbf{b}\cdot\mathbf{b})\cdot\hat{\mathbf{e}}_R = -\frac{\mu_r - 1}{\mu_0\mu_r}\frac{a^2}{R^3}. \tag{192}$$

The total radial magnetic force on the MRE in the deformed shape was obtained through volumetric integration of f_m over the MRE:

$$F_m = -2\pi a^2 \frac{\mu_r - 1}{\mu_0\mu_r}\int_{R_i}^{R_o} t\lambda_3 \frac{\mathrm{d}R}{R^2}. \tag{193}$$

Since the description of λ_3 in terms of R is unknown, the following trapezoidal approximation was used to evaluate the integral:

$$t\lambda_3 = \frac{t\lambda_3(R_o) + t\lambda_3(R_i)}{2} = \frac{t\lambda_1(R_i) + t}{2\lambda_1(R_i)}, \tag{194}$$

$$\Rightarrow F_m \approx -2\pi t a^2 \frac{\mu_r - 1}{\mu_0\mu_r}\left(\frac{\lambda_1(R_i) + 1}{2\lambda_1(R_i)}\right)\left(\frac{1}{R_i} - \frac{1}{R_o}\right). \tag{195}$$

Upon substituting F_m in Eq. 191, and $T_{11}(R_i)$ from the constitutive equation (Eq. 189) the following nonlinear balance equation in terms of $\lambda_1(R_i)$ was obtained:

$$\begin{aligned} G_0(\lambda_1^2(R_i) - \lambda_1^{-2}(R_i)) + (\mu_0\mu_r)^{-1}\left(\frac{a^2}{R_i^2} - b_Z^2\right) = \lambda_1(R_i)(\mu_0\mu_r)^{-1}\left(\frac{a^2}{R_iR_o} - \frac{R_o}{R_i}b_Z^2\right) - \\ t a^2 \frac{(\lambda_1(R_i) + 1)(\mu_r - 1)}{2\mu_0\mu_r}\left(\frac{1}{R_i^2} - \frac{1}{R_iR_o}\right), \end{aligned} \tag{196}$$

which can be re-arranged as:

$$G_0(\lambda_1^2(R_i) - \lambda_1^{-2}(R_i)) = \lambda_1(R_i)\Gamma_1 + \Gamma_2, \tag{197}$$

with,

$$\Gamma_1 = (\mu_0\mu_r)^{-1}\left(\frac{a^2}{R_oR_i} - \frac{R_o}{R_i}b_Z^2\right) - t a^2 \frac{\mu_r - 1}{\mu_0\mu_r}\left(\frac{1}{R_i^2} - \frac{1}{R_iR_o}\right)$$

$$\Gamma_2 = -(\mu_0\mu_r)^{-1}\left(\frac{a^2}{R_i^2} - b_Z^2\right) - a^2 \frac{\mu_r - 1}{\mu_0\mu_r}\left(\frac{1}{R_i^2} - \frac{1}{R_iR_o}\right).$$

Using the two-term Taylor expansion at the neighborhood of $\lambda_1 = 1$ (Eq. 198) with an error in the order of $O(\lambda_1(R_i)^3)$, the following admissible solution was obtained:

$$\lambda_1^2(R_i) - \lambda_1^{-2}(R_i) \approx 4(\lambda_1(R_i) - 1) - 2(\lambda_1(R_i) - 1)^2, \tag{198}$$

$$\lambda_1(R_i) = \frac{\left(8G_0 - \Gamma_1 - \sqrt{(\Gamma_1 - 4G_0)^2 - 8G_0(\Gamma_1 + \Gamma_2)}\right)}{4G_0}. \tag{199}$$

Eq. 199 shows the coupled effects of the mechanical properties (G_0) and magnetic field (a, b_Z) on $\lambda_1(R_i)$. Fig. 7.6(a) and Fig. 7.6(b) show the variation $\lambda_1(R_i)$ and σ_i for various magnet separations and shear moduli. Numerical evaluation shows that for any given a, σ_i is always negative (compressive) and its magnitude is monotonically decreasing with s.

Following a derivation similar to Eq. 199, and numeric integration of:

$$\frac{\mathrm{d}r}{\mathrm{d}R} = \lambda_1(R), \tag{200}$$

with boundary condition:

$$\frac{\mathrm{d}r}{\mathrm{d}R}|_{R_i} = \lambda_1(R_i), \tag{201}$$

and integration increment of $\delta R = 0.05$mm, $r(R)$ was obtained for $R \in [R_i, R_o]$. Estimation of $r(R)$ led to the estimation of $\lambda_{1,2,3}$ (Eqs.160–162) and prediction of the shape of the deformed MRE. Fig. 7.7 depicts the variation of the estimated stretches for MRE-40 and the deformed shape of MRE-10 as two representatives.

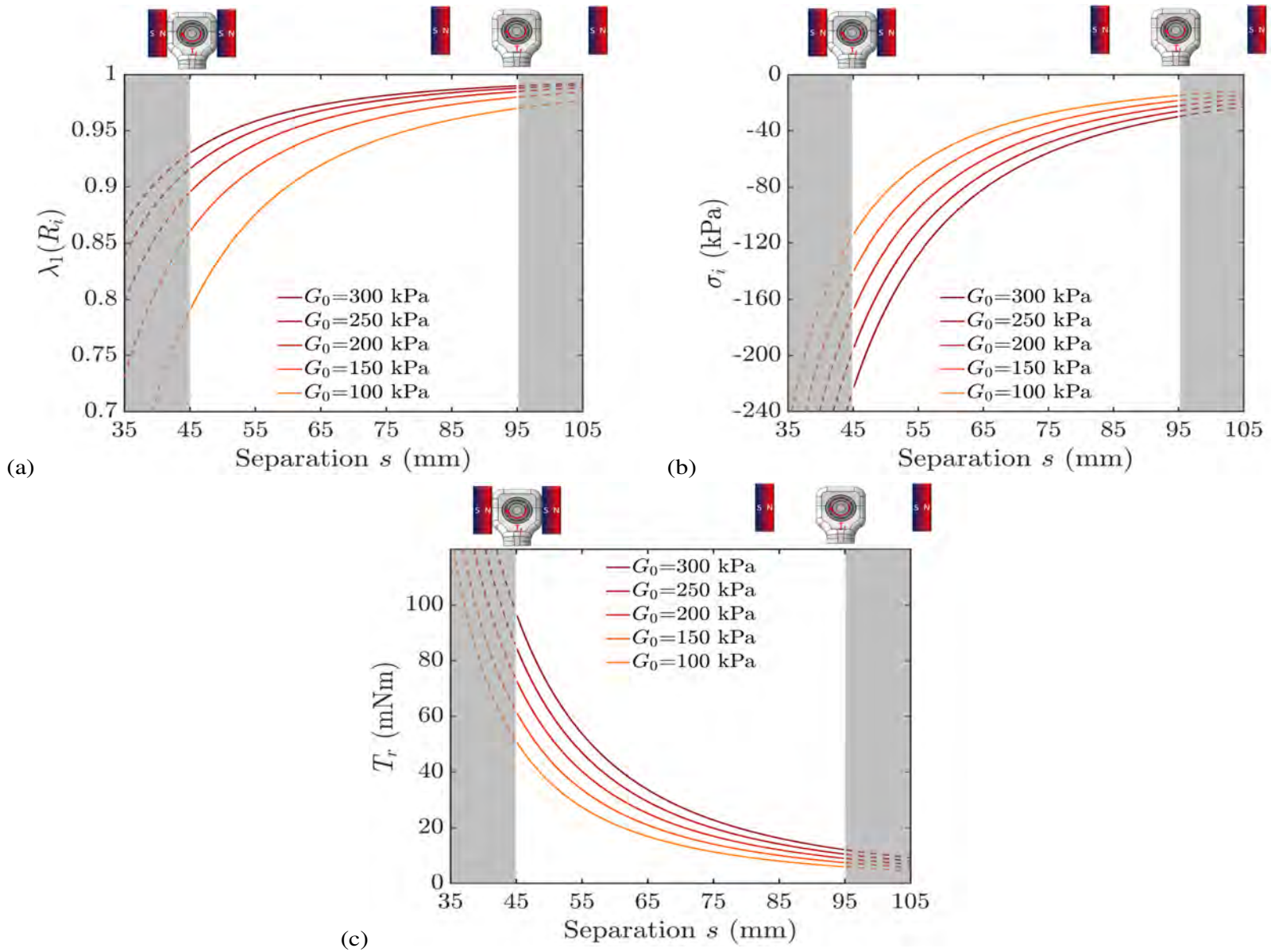

Figure 7.6: Variation of (a) radial stretch $\lambda_1(R_i)$, (b) contact stress σ_i, and (c) resistant torque T_r, with changes in the magnets separation s. Shaded areas are out of the operational range of the prototype system.

7.2.8 Torque and Magnet-separation Relationship

The true stress σ_i at the interface is dependent on the deformation of the MRE through $|\sigma_i| = -\lambda_1^{-1}(R_i)T_{11}(R_i)$. The important physical interpretation of this phenomenon is that for a given magnetic field, softer MREs exhibit more deformation (and larger contact area with the shaft) which increases the capacity of generating resistant torque. In addition, the larger deformation (in softer MREs) will lead to more magnetic pulling force since the MRE particles translate toward the shaft. Nevertheless, softer MREs typically exhibit larger hysteresis which may diminish the repeatability of the system [63, 329, 342].

The relationship between T_r and s was obtained by introducing Eq. 189 in Eq. 157 and using the expression of a and b_Z in terms of s:

$$T_r = -\xi\lambda_1^{-1}(R_i)T_{11}(R_i), \tag{202}$$

$$T_r = -\xi G_0(1-\lambda_1(R_i)^{-4}) + (\mu_0\mu_r\lambda_1^2(R_i))^{-1}\left(\frac{a^2}{R_i^2} - b_Z^2\right). \tag{203}$$

Fig. 7.6 shows the variations of the resistant torque with magnets separation for various shear moduli.

7.3 Validation Studies

To validate the theoretical derivations and to investigate the feasibility of the proposed system, three validation studies were performed. The objective of the first study was to assess the validity of the radial stretch predicted by Eq. 199. The second study was aimed at comparing the effects of the magnetic field and CIP volume fraction on the torque generation capacity of the prototyped device. The third study was a demonstration of how TorMag can be integrated to a representative RCI system for haptic feedback provision.

7.3.1 Study I: Magnetic Field and Magnetostriction

Fig. 7.8 shows the test setup used in study-I (and study-II). The radial positions, r, of four visible markers on the MRE were acquired through an image-based technique. To this end, a CCD camera (resolution 512×512 pixel, WAT-902H Ultimate, Watec, France), equipped with a 55-mm telecentric lens (TEC-M55, Computar Inc., NC, USA), was used. Four markers were placed in each

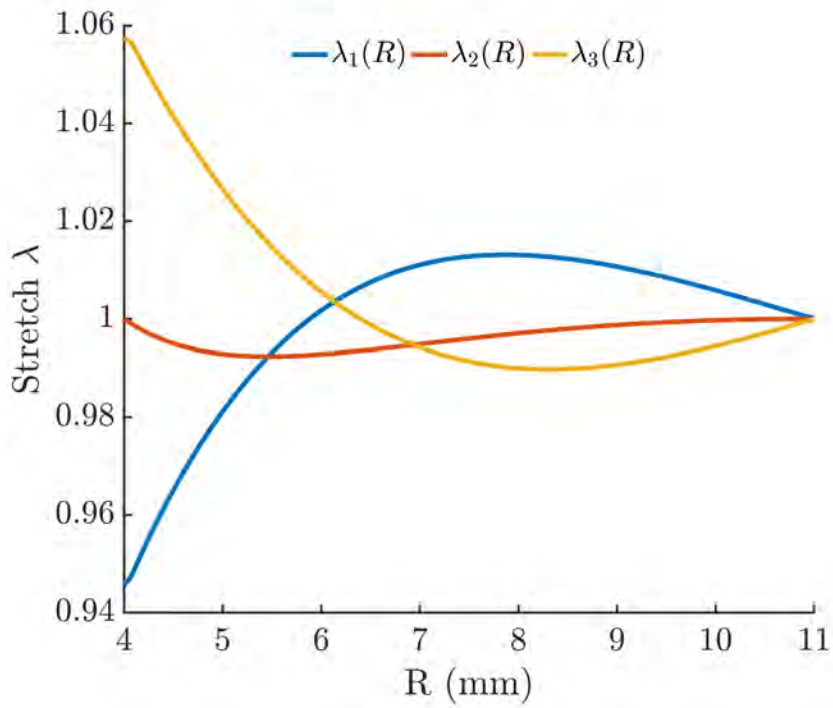

(a)

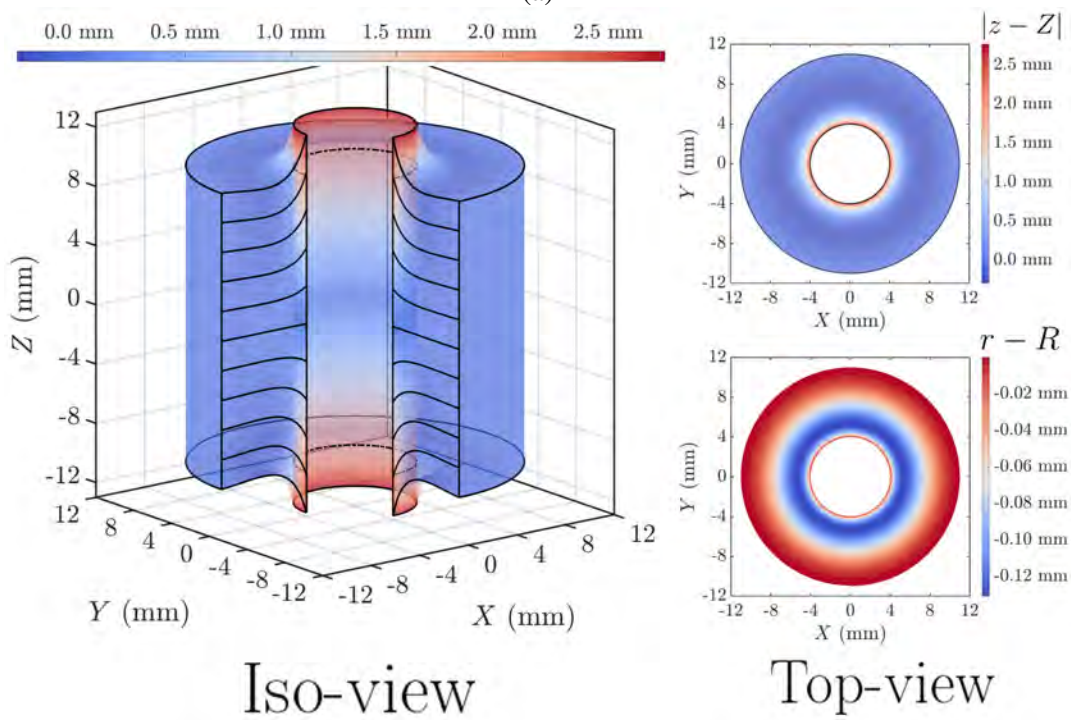

(b)

Figure 7.7: (a) Variation of the mechanical stretches with R in MRE-40, and (b) simulated deformed shape of MRE-10. Dark lines visualize the trajectory of principal stretches.

MRE sample after molding, approximately at $R = 6$mm and $R = 9$mm. Since the markers were placed manually, their placement was not precise. Nevertheless, their initial positions were measured through image processing.

The radial displacement measurement of the four makers, $r - R$ was based on the Pyramid Lucas-Kanade (PLK) optical-flow measurement method proposed in [343] and was developed in C# programming language (EmguCV 4.4.0). Algorithm 3 summarizes the implemented radial displacement measurement procedure. Three MRE samples of each MRE type, MRE-10, MRE-20, and

Algorithm 3 Algorithm for finding the deformed position of the markers in the MRE images

Input: *Calibration Matrix of the Camera* ▷ Pin-hole camera model
Input: *Initial image of the MRE at s=95* ▷ Original shape
Input: *Image of the MRE at* $s \neq 95$ ▷ Deformed shape
Output: r_i ▷ $i = 1, 2, 3, 4,$

1: **procedure** INITIALIZATION
2: Load the image of the undeformed MRE,
3: Find the centroid of the output shaft: $\mathbf{O} = (O_x, O_y)^T$,
4: Find the centroid of the four markers: $\mathbf{M}_i = (X_i, Y_i)^T$ ▷ $i = 1, 2, 3, 4,$
5: Find the radial position of the four markers with respect to $\mathbf{O}$:
$R_i = ||\mathbf{M}_i - \mathbf{O}||$ ▷ $i = 1, 2, 3, 4,$
6: **end procedure**
7: **procedure** DEFORMATIONMEASUREMENT(R_i,M_i,$\mathbf{O}$)
8: Load the image of the deformed MRE
9: Find the displacement field $\mathbf{u}$ at $\mathbf{O}$, and $\mathbf{M}_i$ by PLK method
10: Find the radial position of the markers after deformation
$r_i = ||(\mathbf{M}_i + \mathbf{u}_i) - (\mathbf{O} + \mathbf{u}_O)||$ ▷ Output $i = 1, 2, 3, 4,$
11: **end procedure**

MRE-40 were studied for radial displacement with the magnets at the $s = 45$mm and $s = 95$mm. Fig. 7.8(b) shows a representative image of the detected markers in MRE-10. The deformed radial position of the four markers in each sample were compared with the theoretical findings. Fig. 7.8(c) shows the theoretical and experimental results for the radial position and displacement of the four markers and boundaries of MRE-10. Table 7.5 compares the theoretical and experimental displacement of the markers M_{1-4} for the three MRE types.

The observed average error between the theory and experiment was 0.01 mm (8%) for MRE-10 and 0.01 (9%) for MRE-20, while it was 0.02 mm (26%) for MRE-40. While the findings were in fair

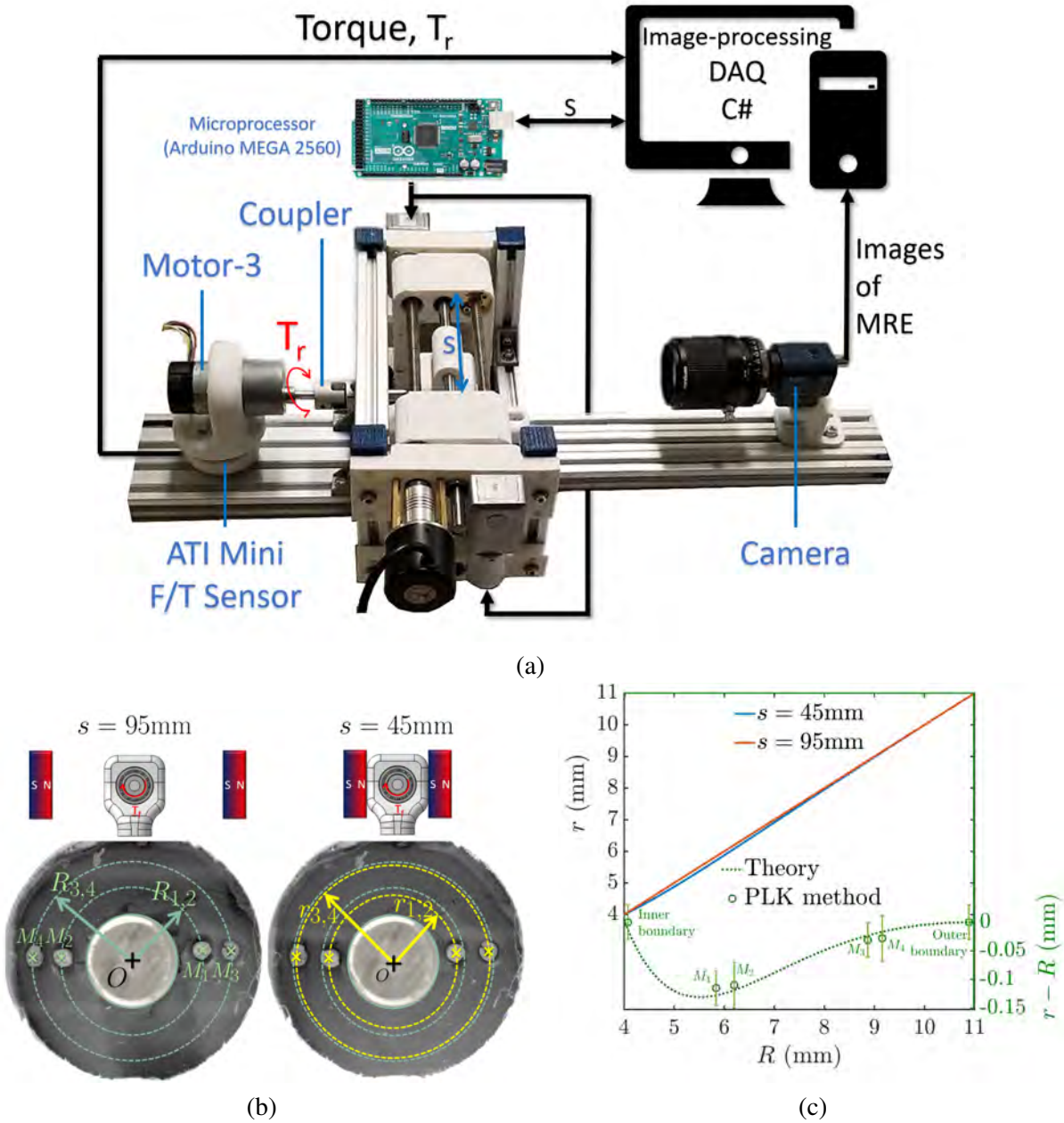

Figure 7.8: (a) Experimental setup used in validation study-I and -II. Data-acquisition (DAQ) was performed in the PC workstation. Microprocessor was used for feedback control of the magnet separation. The camera captured the deformed shape of the MRE, (b) representative images of the markers and output shaft in MRE-10 with $s = 45$mm and $s = 95$mm, and (c) comparison of the theoretical and experimental radial position and displacement of the MRE-10.

agreement with the theory for MRE-10 and MRE-20, the large error for MRE-40 was related to the limitation of the PLK method in detecting deformation below the camera's field-of-view resolution, i.e., 0.01 mm. Nevertheless, the experimental results show a similar trend of variation to the predicted trend from the theoretical model, e.g. (Fig. 7.8(c)).

7.3.2 Study II: Torque Generation

The objective of Study II was to validate the torque generation capacity of the developed system for the proposed application. As discussed in Sec. 7.1.3, the torque feedback system for robot-assisted interventional surgery shall be capable of generating up to 40 mNm of torque with a resolution of 2 mNm. To assess the system performance, the output shaft of TorMag was coupled to a 12v DC motor (37D-4754, Polulu Robotics and Electronics, NV, USA) for generating continuous rotation on the output shaft. A zero-backlash Oldham-type coupler (9845T57, McMaster-Carr, IL, USA) was used to couple the motor to the output shaft. The DC motor was driven under velocity feedback control with a 20 rpm rotational speed [114]. In addition, a 3D-printed mount was designed and rapid-prototyped to firstly align the motor shaft with the output shaft of TorMag and secondly to attach an ATI-Mini40 force-torque sensor (SI-20-1, ATI Inc., MD, USA) to the motor. The Mini40 sensor was used to measure the torque generated by the motor to maintain its rotational speed in the presence of the resistant torque, T_r generated by the MRE. Since the only external torque applied to the motor was from the MRE, the total torque, i.e., $T_r^\star = \sqrt{T_x^2 + T_y^2 + T_z^2}$ was calculated during the test and was recorded for post-processing. (*) indicates the measured values. A total of nine tests (three samples of each MRE) with magnets at six separations, i.e., $s = 95, 85, \cdots, 45$ mm were performed. The separation of the magnets was decreased from $s = 95$ in 10-mm steps and was maintained stationary between the steps. Fig. 7.9(a) depicts the temporal variation of the resistant torque averaged for each MRE and Fig. 7.9(b) shows the variation of the resistant torque with magnet separation. Also, Table 7.6 summarizes the resistant torques and the total range of torque generation of TorMag for the three MRE types.

The average resistant torque at all magnet separations was the highest for MRE-40 and the lowest for MRE-10. As discussed in the magnetoelastic modeling, this phenomenon is attributed to two factors. Firstly, increasing the CIP volume fraction has increased the G_0 of the MREs, which was

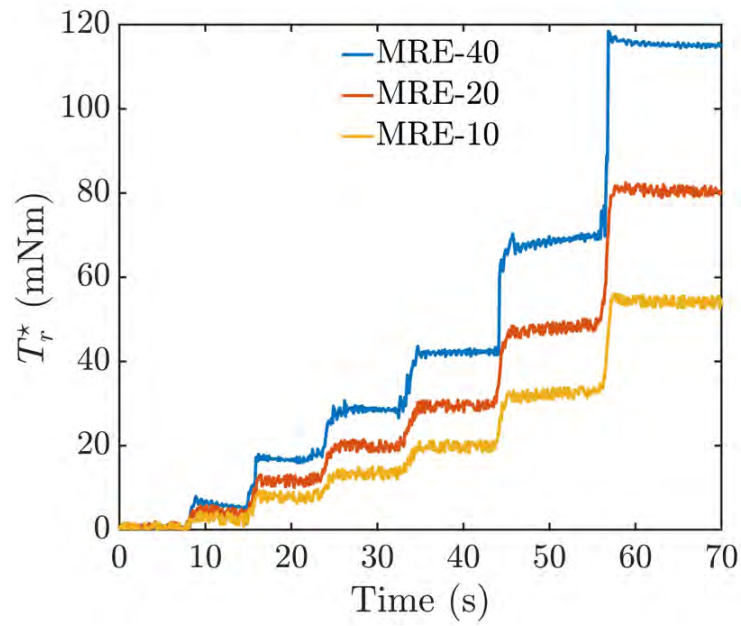

(a)

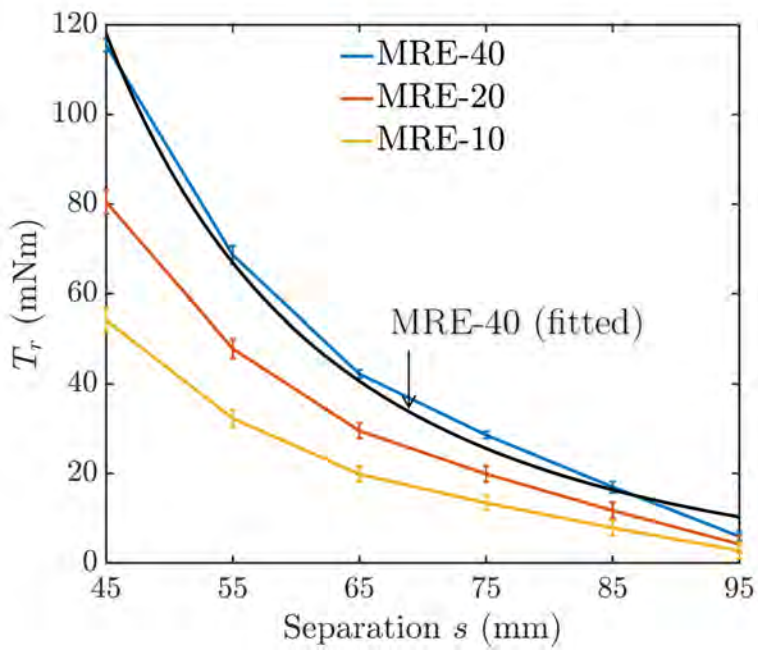

(b)

Figure 7.9: (a) Temporal variation of the resistant torque $T_r^\star$ averaged for the three MRE types, and (b) the variation of the resistant torque with magnet separation.

Table 7.5: Theoretical and experimental radial displacement of the four markers with magnets at $s = 45$mm.

MRE Type	Theory				Experiment (PLK)				Error
	r_1 (mm)	r_2 (mm)	r_3 (mm)	r_4 (mm)	r_1 (mm)	r_2 (mm)	r_3 (mm)	r_4 (mm)	Mean±SD (mm)
MRE-10	-0.1245	-0.1245	-0.0197	-0.0197	-0.1100	-0.1200	-0.0300	-0.0300	0.01±0.004
MRE-20	-0.1105	-0.1105	-0.0175	-0.0175	-0.0900	-0.1000	-0.0200	-0.0200	0.01±0.009
MRE-40	-0.0765	-0.0765	-0.0161	-0.0161	-0.0500	-0.0500	-0.0100	-0.0200	0.02±0.013

Table 7.6: Resistant torque, T_r generated by TorMag with various magnet separations.

	Magnet Separation						Range
	$s = 45$mm (mNm)	$s = 55$mm (mNm)	$s = 65$mm (mNm)	$s = 75$mm (mNm)	$s = 85$mm (mNm)	$s = 95$mm (mNm)	(min-max) (mNm)
MRE-10	2.8±0.8	7.7±0.6	13.4±0.8	19.8±0.7	32.3±0.7	54.2±1.2	(2.9-54.2)
MRE-20	4.2±0.7	11.7±0.8	19.9±0.9	29.5±0.9	47.8±0.8	80.4±1.3	(4.2-80.4)
MRE-40	5.9±0.5	17.0±0.6	28.6±0.4	42.2±0.5	68.6±1.0	115.5±0.7	(5.9-115.5)

shown to increase the contact stress and consequently the resistant torque (Fig. 7.6(b–c)) (mechanical effect). Secondly, increasing the CIP volume fraction has increased the relative permeability of the MREs μ_r (magnetic effect) [335]. As the magnetic field strength is linearly proportional to the permeability, the magnetic force, contact stress, and resistant torque has increased in the MREs with larger CIP volume fraction.

The error observed between the model predictions and experimental results for T_r may be related to the uncertainties associated with geometrical, mechanical, and magnetic model parameters. Nevertheless, the observed trends of variation of T_r with s for the three types of MREs were similar to the model results.

The results showed that TorMag with MRE-40 was capable of generating the required torque for RCI applications, i.e., 100mNm. Also, the maximum standard-deviations of T_r between the re-tests for MRE-10, MRE-20, and MRE-40 were 1.2, 1.3, and 1.0 mNm, respectively. Furthermore, the average step change in the resistant torque (for 1-mm change in s) was 0.13, 0.22, and 0.5 mNm, respectively. Therefore, the repeatability (standard-deviation of re-tests) and resolution (average change for 1-mm change in s) was compliant with the required performance.

7.3.3 Study III: Force Feedback Rendering and System Integration

In Study III, we integrated the prototyped torque generation system with the surgeon unit of a representative RCI system. Given its fair compliance with the torque requirements discussed in Sec. 7.3.2, MRE-40 was used for the torque feedback validation.

The utilized RCI system has been previously developed by the author for telerobotic RCI applications [74]. The RCI system had a surgeon unit (haptic interface) and a patient unit (robot) configured with a master-slave telerobotic configuration. It was capable of replicating the insertion and rotations measured at the surgeon unit and replicate those at the patient unit. A 6Fr surgical catheter (RunWay, Boston Scientific, MA, USA) was used in the surgeon unit, while a similar catheter was used at the patient unit to perform interventional tasks. For simulation, a phantom vascular model (Sam-Plus, Lake Forest Anatomicals Inc., IL, USA) was used. The vascular model was installed on an ATI-Mini40 sensor to measure and relay back the insertion forces. Fig. 7.10 shows the implemented system for the validation tests, patient and surgeon units of the RCI system, and the cross-sectional view of the surgeon unit.

Previously, the author has co-developed model-free controllers, e.g., PID [63], and data-driven artificial neural network (ANN-) controllers [68] for controlling the mechanical properties of MREs for force feedback applications. In this study and as an extension, the developed magnetoelastic model (Eq. 202) was used to fit the experimental data for a physics-based controller design. To this end, the Curve Fitting Toolbox of Matlab (R2019b, Mathworks Inc, MA, USA) was used to find the empirical constants for fitting T_r and s in Eq. 203 for MRE-40. The fitting function was adopted from the analytical solution of the magnetoelastic model of the MRE in Eq. 203:

$$T_r = -\alpha_1 \left(1 - \left(\alpha_2 - \alpha_3 s^{-2.6}\right)^{-4}\right) + \alpha_4 s^{-2.6}, \tag{204}$$

with $\alpha_1 = 7.73, \alpha_2 = 11, \alpha_3 = 0.07, \alpha_4 = 2.5 \times 10^6$ as the fitting constants. The fitting had a goodness-of-fit of $R^2 = 0.995$ with a root-mean-square error (RMSE) of 3.2 mNm.

During the tests, a user repeated a descending aorta cannulation task for three repetitions. The user was tasked to advance the catheter teleoperatively from the femoral artery to the aortic arch of the

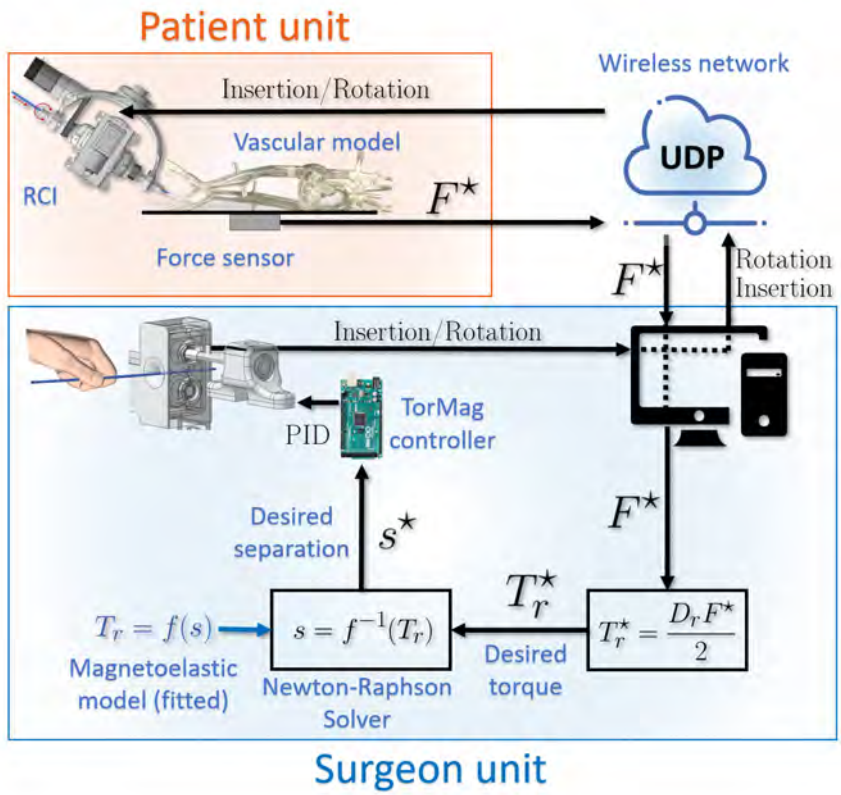

(a)

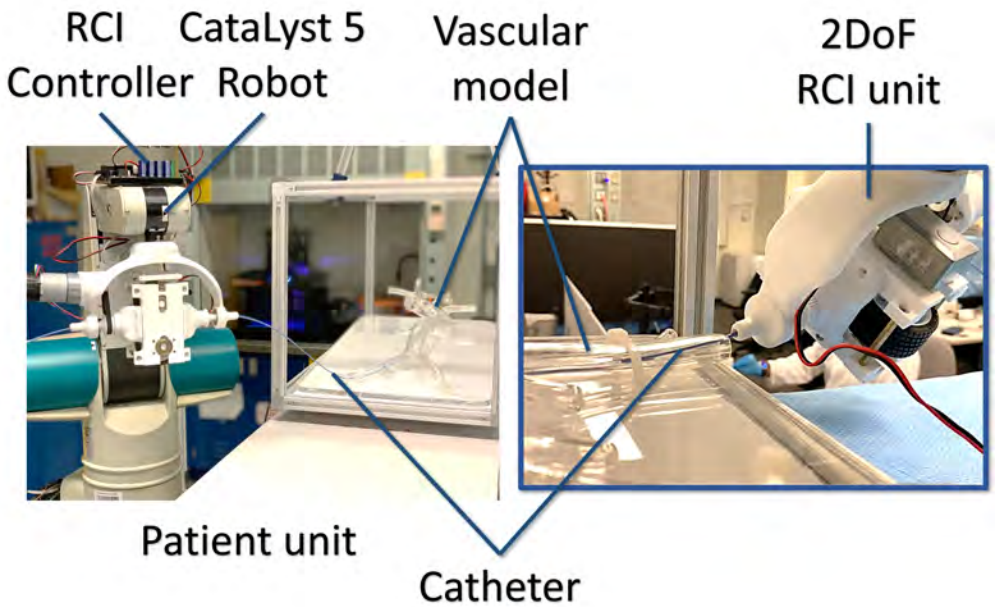

(b)

Figure 7.10: Setup used in Study III: (a) the implemented system for Study III, (b) patient unit.

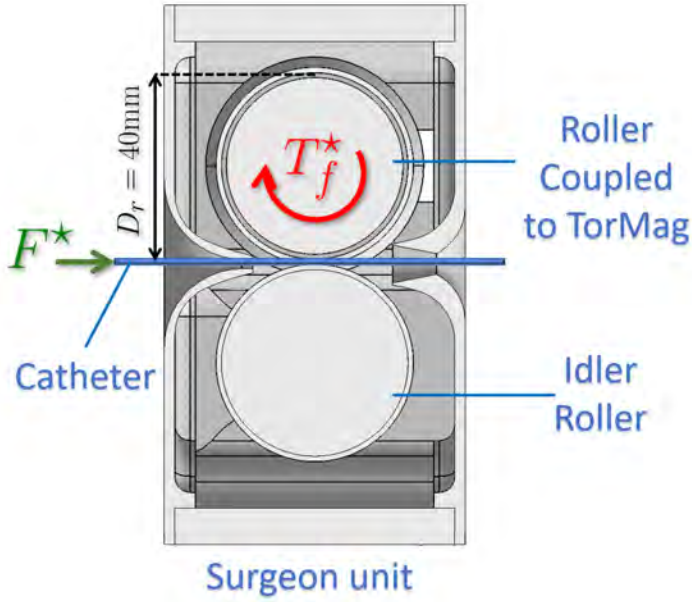

(c)

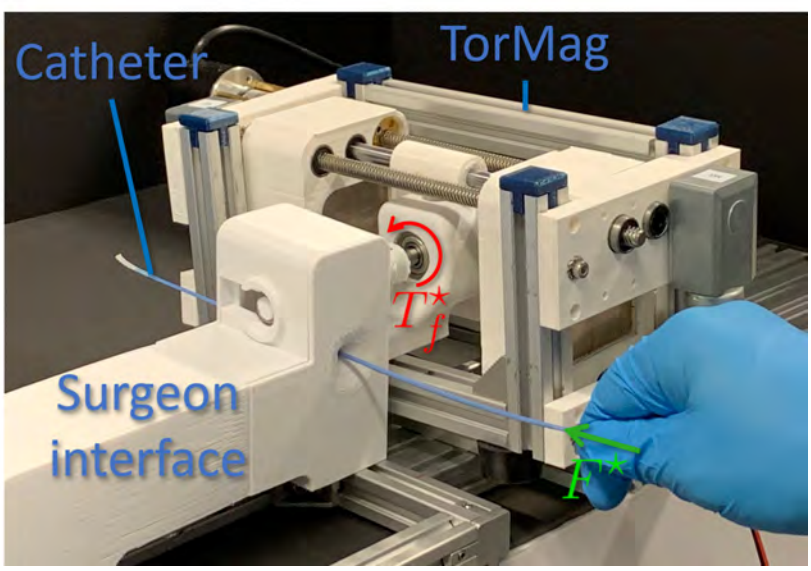

(d)

Figure 7.10: (contd.) Setup used in Study III: (c) schematic cross-sectional view and coupling of TorMag with the surgeon unit, and (d) the surgeon unit during the test.

vascular model. Meanwhile, the total insertion force $F^\star$ was continuously measured at the patient unit and transmitted to the surgeon unit via a user-defined protocol (UDP) over a local wireless network communication channel. Using the design specifications of the surgeon unit (D_r in Fig. 7.10(c)), the required torque $T_r^\star$ to replicate $F^\star$ (measured at the patient unit) was calculated in real-time using:

$$T_r^\star = \frac{D_r F^\star}{2}. \tag{205}$$

Using $T_r^\star$, the desired magnet separation $s^\star$ was obtained by solving Eq. 204. The numerical solution of Eq. 204 was performed using a Newton-Raphson method with the latest $s-$feedback value as the initial guess. During the tests, the surgeon unit was installed on an ATI-Mini40 force sensor and the total insertion force from the user, F_{ATI} was recorded as the reference for comparison.

7.3.3.1 Controller Design and Assessment

For real-time control of the magnet separation $s^\star$, a closed-loop proportional-integral-derivative (PID) control system was designed and implemented. As stated above, the desired magnet separation was obtained based on the required $T_r^\star$ to generate the desired feedback force $F^\star$.

To tune the PID coefficients, $k_{P,I,D}$, the $z-$space transfer function of the magnet driving mechanism was required. To this end, the symmetric step response of motors was obtained for a step pulse input of $\pm$12V with a pause of 1.5sec and full reversal. For system identification, the separation between magnets, s, was considered as the output and voltage on the motors as the input. It is noteworthy that Motor-1 and Motor-2 of TorMag were driven with a common voltage feed to assure the symmetric motion of the two magnets. Fig. 7.11 shows the step response of the motors. System Identification Toolbox of Matlab was used to fit a third-order discrete transfer function (Eq. 206) to the symmetric step response. The third-order transfer function was chosen to relate the gap separation to the voltage without a need for integrating the velocity. The model fitting result showed a goodness-of-fit $R^2 = 0.96$.

$$H(z) = \frac{S(z)}{V(z)} = \frac{-0.107}{1 - 0.942z^{-1} - 0.483z^{-2} + 0.425z^{-3}}, \tag{206}$$

where, $H(z)$ is the transfer function of the magnets driving system, $S(z)$ is the $z-$transform of the magnets separation (output), and $V(z)$ is the $z-$transform of the input voltage.

Using $H(z)$, the magnet separation controller was modeled in Matlab Simulink environment and PID Tuner was used to obtain the $k_{P,I,D}$ such that a set of response requirements were met. The response requirements were rise-time, settling-time, overshoot percentage, and steady-state error. The values used as the requirements were adopted from the literature[62]. The PID tuner showed that PID coefficients of $k_P = 2.751$, $k_I = 0.035$, and $k_D = 0.193$ satisfied the requirements. In addition to the simulation, the PID controller was deployed on an Arduino Mega-2560 embedded board and was used for experimental verification on the prototyped device. For experimental verification, the input $s^\star$ was a unit step pulse with 1.5 s pulse-width starting from $t = 1$ s.

Table 7.7 summarizes the PID coefficients, requirements for the system response, model predictions, and the verification performance of the system for unit step pulse. As summarized in Table 7.7, the response of the control system met the requirements set on rise-time, settling-time, error, and overshoot. The rise-time of the system was approximately 0.12 s for unit step change in the input.

Derivative of empirical Eq. 204 with respect to s indicated that one-millimeter change in the magnet separation would result in 7.12 mNm change (maximum) in the resistant torque at $s = 45$ mm and 0.5 mNm (minimum) for $s = 95$ mm. These rates correspond to a resistance torque gradient in the range of $[4.16, 59.33]$ mNm/s for $s \in [45, 95]$ mm and an insertion force gradient in the range of $[0.21, 2.96]$ N/s for $s \in [45, 95]$. In fact, the obtained range of insertion force gradient and the range of insertion force determine the feasible range of force generation capability of the developed force feedback system. For practical purposes, it is vital that the feasible range of force generation at the surgeon unit adequately cover the range of force variation at the patient unit. Further comparison on this matter was performed on the experimental data.

Fig. 7.12(a–c) compares the insertion forces measured at the patient unit with the feedback force at the surgeon unit for three repetitions. The three repetitions were performed in order to assess the capability of the proposed system to operate under various force range and force gradient ranges. In addition, Fig. 7.13(a–c) compare the phase-portrait of $F^\star$–$\dot{F}^\star$ with the feasible range of the prototyped device.

The mean-absolute errors between the desired force, $F^\star$ and the feedback force, F_{ATI} were

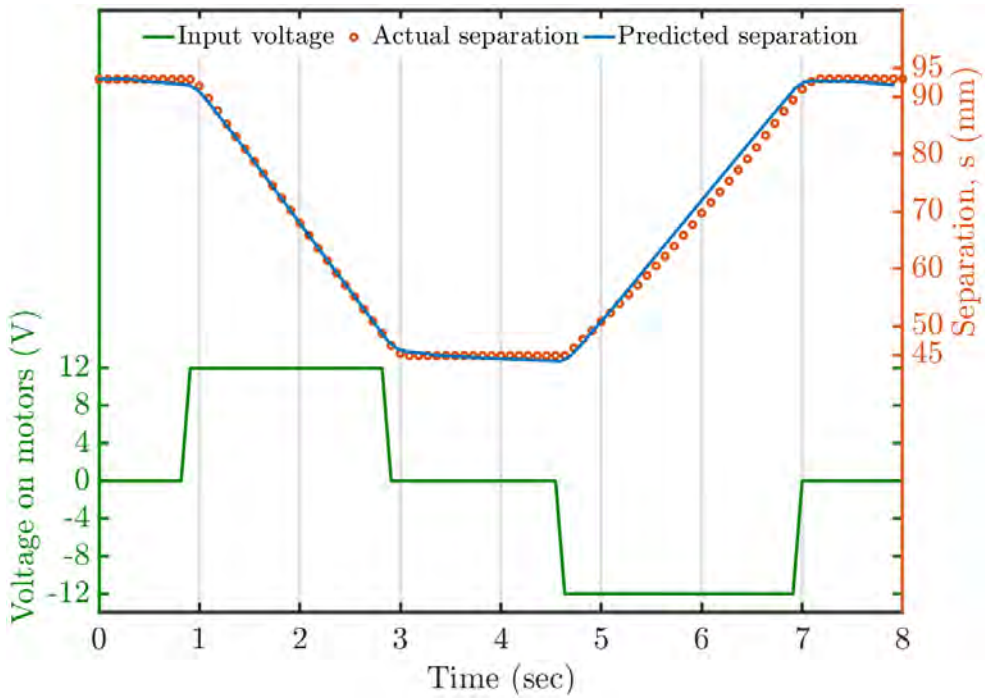

(a)

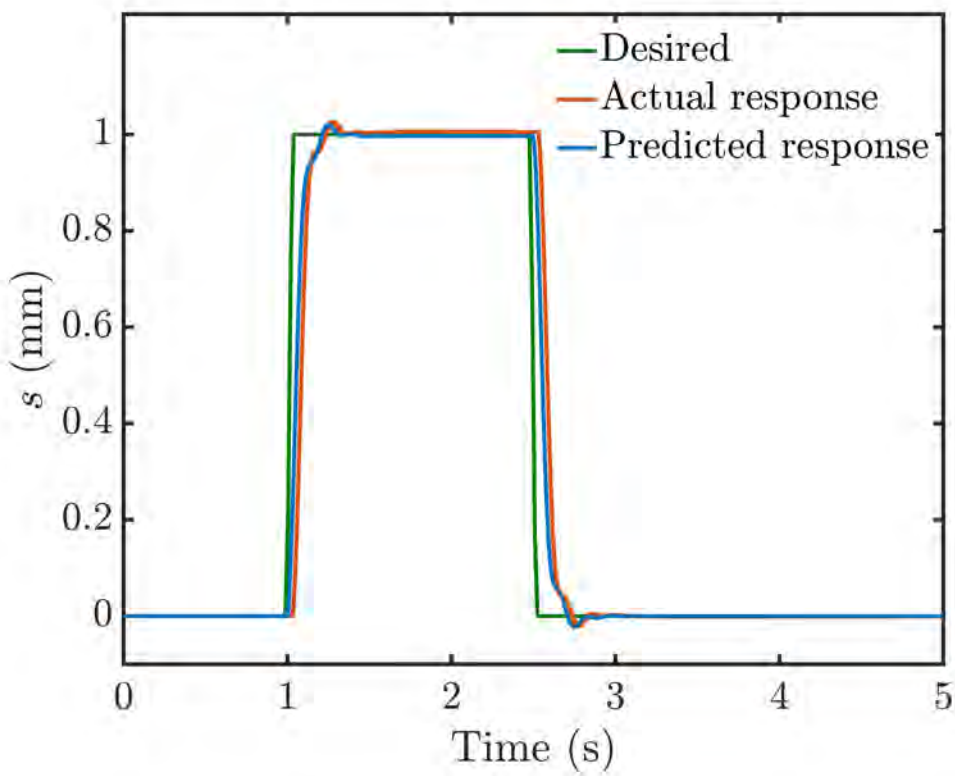

(b)

Figure 7.11: (a) Comparison of the step response of motors and the fitted discrete model (R^2=96%), (b) step response of the motors with PID controller.

Table 7.7: Selected PID coefficients and system response for a unit step input with reversal.

k_P=2.751, k_I=0.035, k_D=0.193				
	Required	Predicted	Actual	Passed
T_r	$\leq$0.3s	0.10	0.12	✓
$T_{5\%}$	$\leq$0.5s	0.22	0.34	✓
PO	$\leq$5%	1.3%	2.4%	✓
e_{ss}	$\leq$2%	0.0%	0.6%	✓

T_r: Rise-time
$T_{5\%}$: Settling-time to 5%-band
PO: Overshoot percentage
e_{ss}: Steady-state error

0.06±0.07 N, 0.05±0.09, and 0.06±0.09 N for repetition 1 to 3, respectively. The range of the generated force by TorMag in the three repetitions was 0.49–2.66 N.

In all the repetitions, $F^\star$ was almost at zero at the beginning of the test but sharply raised as soon as the RCI system entered the catheter into the vascular model (femoral artery). At the beginning of the tests, TorMag was not successful in rendering a zero-force condition due to the limitation of maximum magnet separation. This limitation can be resolved by increasing the range of magnet separation, e.g., 120 mm. A similar limitation was observed in the phase-portraits, where the initial near-zero forces were outside the feasible range of TorMag.

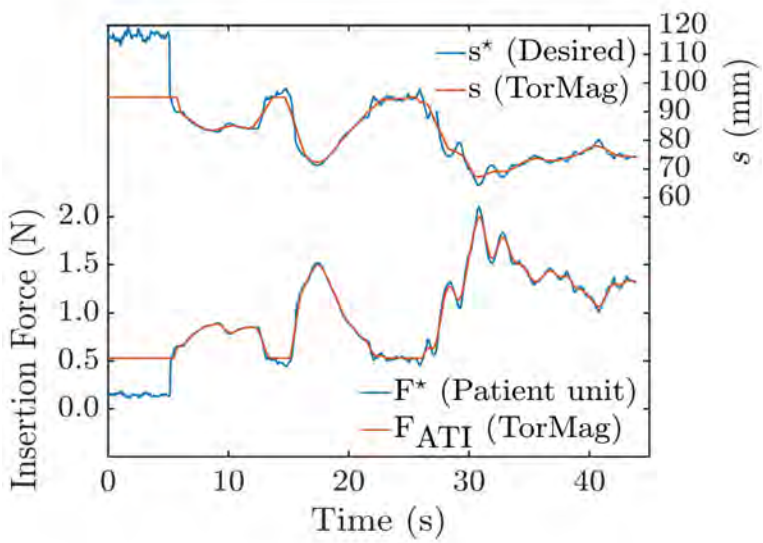

(a)

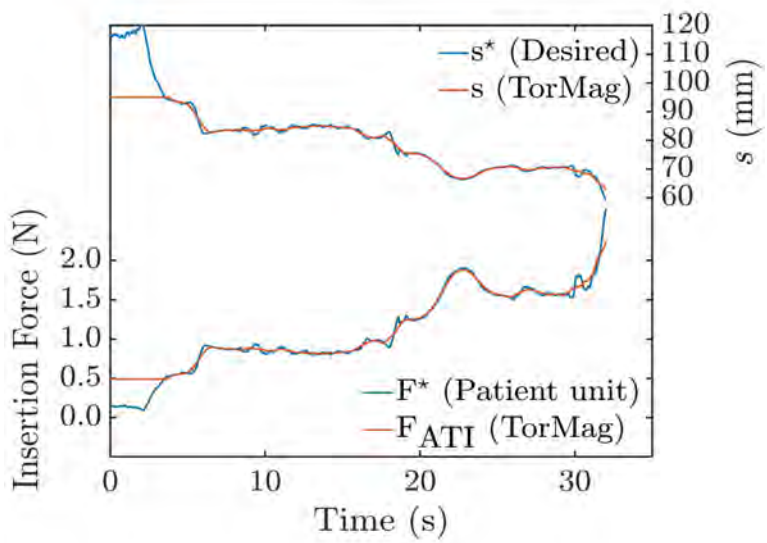

(b)

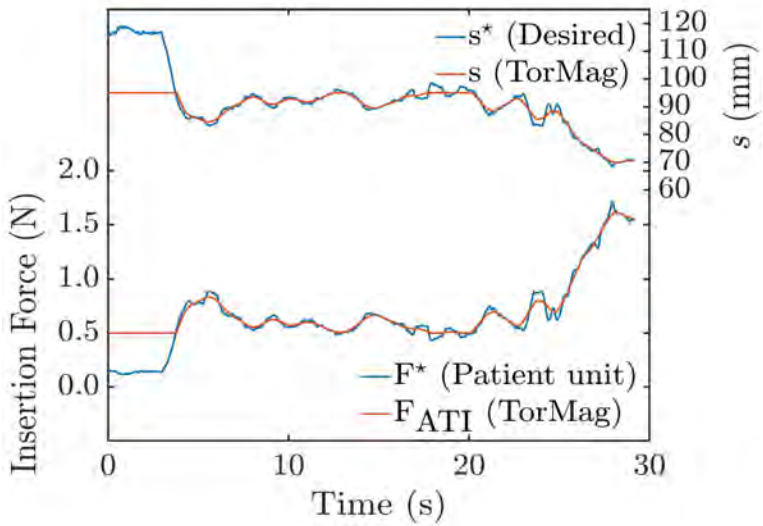

(c)

Figure 7.12: Comparison of the measured insertion force at the patient unit with the feedback force at the surgeon unit in (a) aorta cannulation 1, (b) aorta cannulation 2, and (c) aorta cannulation 3.

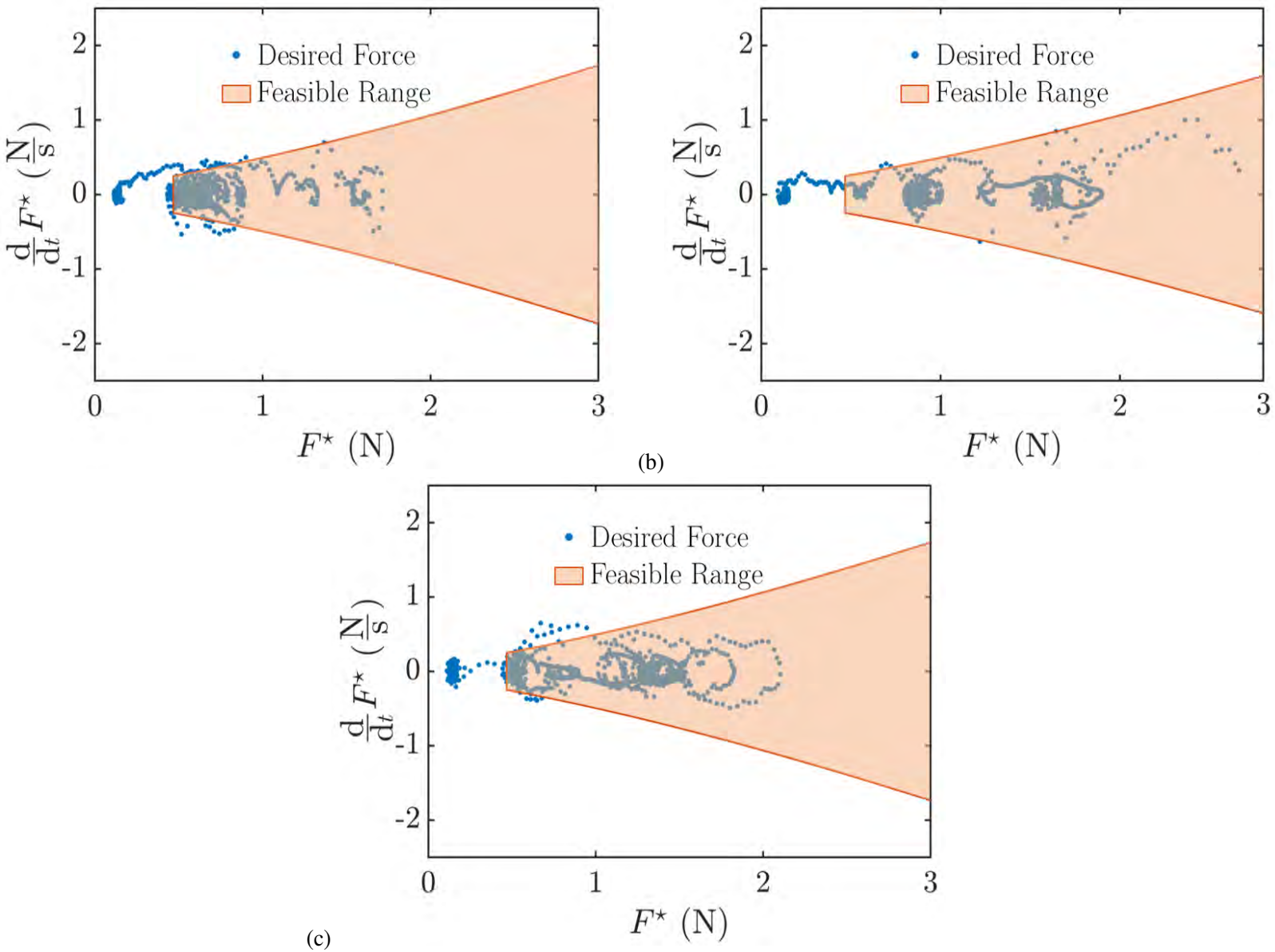

Figure 7.13: Comparison of the phase-portraits of the measured insertion force at the patient unit with the feasible force generation area of TorMag in (a) aorta cannulation 1, (b) aorta cannulation 2, and (c) aorta cannulation 3.

Moreover, Fig. 7.13(a–c) shows that the majority of the desired forces in the repetition tests, especially with a less than 0.5 N magnitudes, reside within the feasible range of TorMag. More specifically, only 11%, 12%, and 9% of all the desired forces were outside the feasible range for cannulation tests 1, 2, and 3, respectively.

In addition, the minimum magnet separation observed in the experiments was 63.13 mm, which is well above the minimum reachable separation of the magnets, i.e., 45 mm. This shows that the maximum desired force during the the cannulation tests, i.e., 2.663 N, was well below the maximum force generation capacity of TorMag, i.e., 5.765 N. The findings of Study II (Fig. 7.9(b)) suggest that TorMag can generate forces up to 5.765 N (115.5 mNm of torque) which can further be exploited for other applications. Nevertheless, larger insertion forces may be required to render the force feedback in more complex cannulation tasks, e.g., coronary cannulation. The integrated RCI system exhibited a refresh rate of 173±11 Hz, which is in compliance with the minimum refresh rate required for RCI applications, i.e., 30 Hz [62]. Also, the time delay from the patient unit to the surgeon unit was 143±11 ms due to the network communication delay. Recent findings suggest that surgeons may not perceive the delays of less than 250 ms in RCI interventions [344]. A comparison of the specifications of the developed system with representative studies is provided in Table 7.8. The comparison showed that the proposed system had better accuracy compared to the representative studies. Also, rendering zero-force is possible in TorMag by increasing the structural range of the magnet separation limit.

7.4 Feasibility of Haptic Rendering with Image-based Force Estimation

To assess the feasibility of haptic rendering with the iCORD image-based force estimation method proposed in Chapter 4, the phase-portraits of the estimated forces in the validation study of Chapter 4 were compared with the feasible range of TorMag (Fig. 7.14). The comparison showed that the feasible range of the prototyped device was adequate for 67%, 83%, and 79% of the estimated force points in cannulations of the aorta, subclavian, and left brachiocephalic arteries, respectively. Similar to the observations in Study III, the lower limit of the prototyped device in force rendering, i.e., ≈ 0.5 N, was above the initial near-zero insertion forces.

Table 7.8: Comparison of the performance of representative studies with the specifications TorMag.

Study	Application	Approach	Haptic Interface	Workspace	Haptic Range	Error	Rendering zero-force
Chen *et al.* [345]	RCI	Passive Friction disk	Custom	∞ (continuous insertion)	0-12 N	0.8 N (6.67%)*	Yes
Bao *et al.* [195]	RCI	Active DC Motor	Touch X (3D Systems Corp.)	160×120×120 mm	0-2.5 N	0.05 N (2.0%)	Yes
Guo *et al.* [89]	RCI	Active DC Motor	Phantom Premium (3D Systems Corp.)	381×267×191 mm	0-0.5 N	0.04 N (8.0%)	Yes
Yin *et al.* [86]	RCI	Semi-active MRF	Custom	∞ (continuous insertion)	0-0.25 N	0.016 N (6.4%)	No
This study	RCI	Semi-active MRE	Custom	∞ (continuous insertion)	0-5.765 N	0.06 N (1.0%)	Possible

*: Error percentage was calculated relative to the reported full-scale range.

One way to remedy this limitation is to increase the maximum magnet separation limit to reduce the minimum magnetic field (and frictional force). Given that TorMag has a relatively large unused feasible force range (up to 5.77 N), the output shaft of TorMag can be coupled with a reduction gear train to decrease its minimum rendered force. Nevertheless, such a reduction gear train will also reduce the maximum rendered force.

One of the major contributions of this study is that the limitations of the force generation in TorMag can be remedied through rigorous use of the validated magnetoelastic model in a structural optimization process; whereas, dimensions of the MRE and TorMag device can be used as design variables and the sufficiency of the minimum and maximum rendered force for RCI applications as the design objectives.

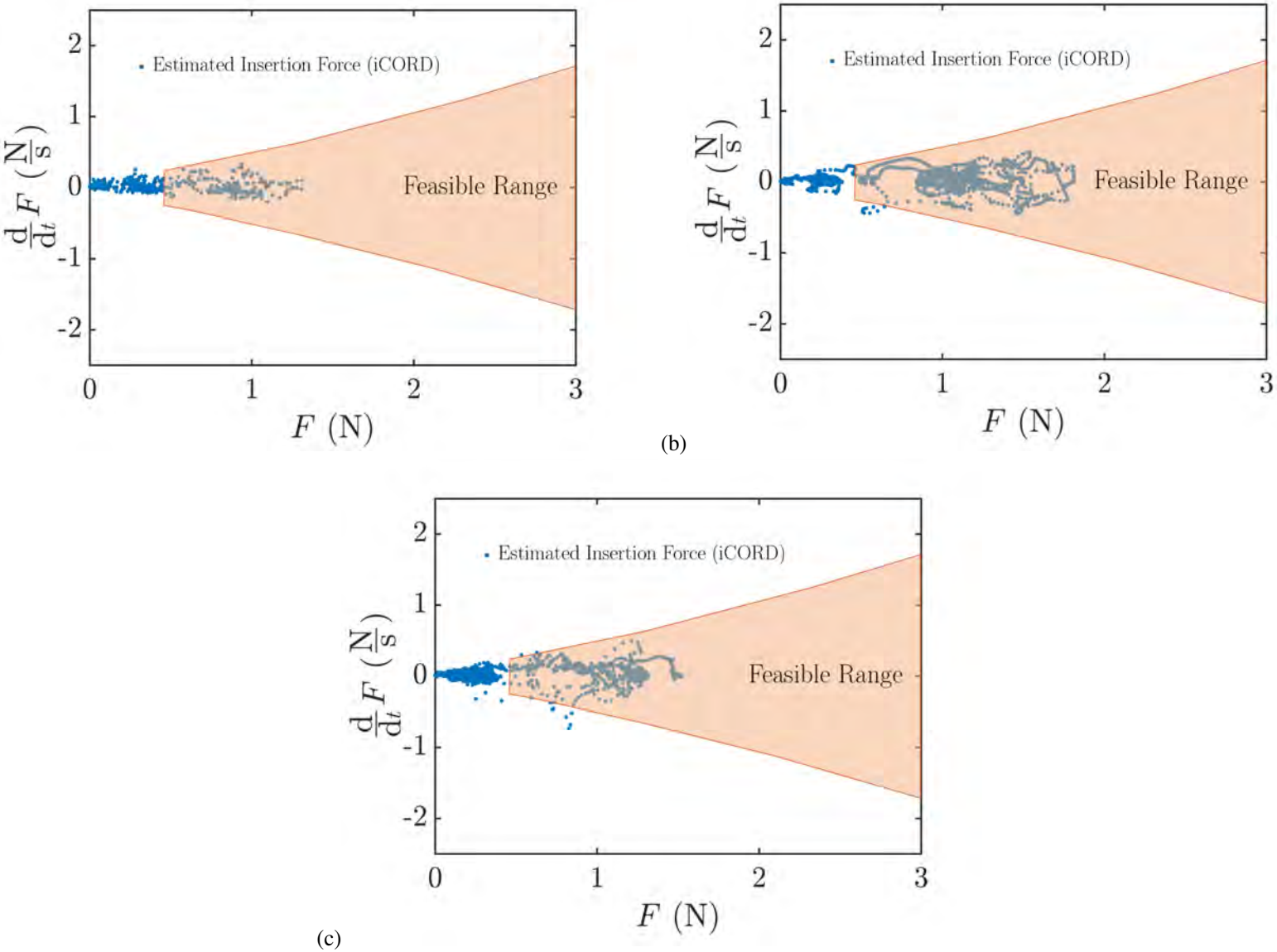

Figure 7.14: Comparison of the phase-portraits of the image-based estimated insertion forces in the validation study of Chapter 4 with the feasible range of force generation of TorMag in (a) aortic artery cannulation, (b) subclavian artery cannulation, and (c) left brachiocephalic artery.

7.5 Summary

In this study, a novel magnetostriction-based force feedback modality based on frictional torque generation between a ferromagnetic shaft and a hollow cylindrical MRE was proposed, analytically modeled, and experimentally validated for RCI applications. The constitutive model developed in this study allowed for analytical modeling and explanation of the magnetostriction phenomenon used in the force rendering. Also, it was used as a phenomenological calibration form for the prototyped TorMag to predict the rendered force from a given magnet separation. In addition, three validation studies verified the findings of the constitutive model for deformation of the MRE, validated the specifications of TorMag with respect to the requirements of RCI applications, and demonstrated the feasibility of integrating TorMag with RCI systems.

A major contribution of this study was developing the analytical model for magnetostriction. This model can be used in future studies for model-based optimization of MRE and TorMag structures. Although the model included simplifying assumptions such as pure radial magnetic field, and linearization of λ_1 at the neighborhood of $\lambda_1(R_i) = 1$, its results were fairly in agreement with the experimental observations.

The comparison of the specifications of TorMag with representative studies in the literature showed its overall superior performance in terms of accuracy, workspace, and range of force rendering. Moreover, the comparison of the feasible force generation range of the proposed device was compared with the experimental data in this study and the results of Chapter 4. In addition, the feasibility of integration of TorMag with the image-based force estimation method (iCORD) in Chapter 4 was investigated. The feasible range of force generation of the prototyped system was fairly large. However, the lower limit of force generation was not small enough to render the near-zero forces observed during the cannulation studies. Given that the minimum detectable force in the image-based force estimation method was 0.22 N, at least a similar lower limit of force generation is required for the proposed device.

The modular design of TorMag and the simplicity of changing the MRE insert (MRE mold) allow for using TorMag for multiple applications with various haptic ranges. Also, TorMag showed robustness in maintaining haptic force without active energy consumption which is a unique feature

compared to other active and semi-active modalities.

The proposed system can be further improved by providing a larger separation range for the magnets to allow for zero-force rendering. Also, the use of other magnets, e.g., serialized magnets [72], can increase the force capacity of TorMag for other applications. In addition, TorMag with its current magnet separation control mechanism is relatively bulky, thus structural optimization is necessary for further developments. Moreover, the performance of TorMag for RCI applications was studied for a simple cannulation task, thus extended user experience study in more complex cannulation tasks is required for a more comprehensive performance assessment.

Chapter 8

Conclusions and Future Works

8.1 Conclusions

In this doctoral research, first the design requirements for various robot-assisted cardiovascular intervention procedures, e.g., PCI, PPI, RFA, and NVI, were identified and set as design requirements for the proposed technology for haptic feedback provision. The design requirement identified in Chapter 2 were the need to use insertion force as the haptic cue with an operational range of 0–2 N, with an error of less than 10% of full-scale, and a minimum refresh rate of 25 Hz.

Based on the design requirements and to avoid introducing an additional technology-related step to the surgical workflow, a new image-based haptic rendering system design was proposed that required developing sensor-free force estimation methods, decoupling the rotation measurement from insertion measurement system, and developing an intuitive surgeon interface compatible with commercially available catheters.

In continuation, a force estimation method based on the inverse finite-element method (iFEM) was developed, integrated with a representative RCI system, and was tested for catheterization tasks. This method met the accuracy requirement, i.e., error less than 10% of full-scale, however its refresh rate was not acceptable for real-time RCI applications. Therefore, a second force estimation method based on the inverse Cosserat rod model (iCORD) was developed and tested for cannulation tasks. The iCORD method met requirements set in the research objectives, i.e., was purely image-based, independent of the a-priori knowledge of the patient's anatomy, with less tha 10% error of full-scale. Also, it was compatible with both non-steerable catheters and steerable catheters by the improvements proposed in Chapter 5. To the best of the author's knowledge, this research was the

first to introduce iCORD. Compared with the available literature, iCORD exhibited improved accuracy for sensor-free force estimation on endovascular devices.

In addition, the proposed device in Chapter 6 met the requirements set in the research objectives, i.e., exhibited zero temporal drift, showed robustness in multiple and continuous rotations of the endovascular device, was accurate with less than 10% error, and had a refresh rate of 111 Hz. The proposed stereo-accelerometry and integral free rotation measurement were unprecedented. The validation study confirmed the elimination of the need for attitude resetting and use of geomagnetic field leading to reduction of computation time by 88% and estimation error by 64%.

Moreover, the proposed surgeon interface in Chapter 7 showed acceptable performance compared to the requirement in the research objectives. It was haptics-enabled with the ability to generate controllable insertion force feedback. Also, various shapes and sizes of endovascular devices could be used with it and combined with the proposed rotation measurement system it provides un unbounded workspace for rotation and insertion degrees of freedom. In terms of force generation capacity, the validated multi-physics-based analytical model showed that rendering zero force is feasible with the proposed haptics rendering modality. However, the prototyped system requires structural optimization to attain zero-force rendering capability.

In the end, a comparison of the phase-portraits of the insertion force between the proposed surgeon interface and the proposed force estimation method (iCORD) showed the feasibility of integrating these two components in the proposed RCI system design.

Based on the aforementioned comparison of the performance with the objectives, at component and system levels, the proposed components, i.e., force estimation, rotation measurement, and haptic rendering, and the integrated system showed compatibility with the design requirements as a feasible technology to address the need for the provision of haptic feedback for RCI systems.

8.2 Future Works

This research can potentially be expanded and improved by:

(1) integration with a medical fluoroscopy device to validate the proposed shape interpolation under various contrast, brightness, and motion artifact conditions. Such integration will allow

for further modifications of the shape interpolation methodology for complex 3D deformations of the endovascular devices based on procedural conditions. Also, replacing the stereo-vision method used in this research with a single-camera 3D shape estimation, e.g., [247] or through deep-learning, would be a significant expansion of the proposed shape interpolation method.

(2) direct solution of the iCORD governing equations to provide a simulation platform for medical education and learning-based force estimation. Currently, direct solution (finding deformation from known external forces) of the temporospatial dynamic equations of the Cosserat rod model is performed numerically, e.g., shooting method [213], and are not computationally efficient for the iterative inverse solution. With the analytical kinematics derivation proposed in this research, there is a possibility to explore an efficient solution schema for the direct solution. An efficient direct solver will allow for simulating numerous loading conditions and building an atlas of deformation–loading. Thanks to the expansion of deep-learning techniques, such an atlas can be utilized to train a network for finding the most similar force distribution to a given deformation. Applications of such an atlas can be expanded to developing a virtual-reality-based engine for procedural simulation intended for medical education and skill transfer, as well as, for haptic rendering and single-camera shape estimation.

(3) investigating the performance of the proposed force estimation methods for non-straight endovascular devices, e.g., catheters with an initial curvature. A simplifying assumption throughout this research was to assume the initial shape of the endovascular devices as straight lines. Accordingly, the utilized devices in the validation studies were of an initial straight shape. Nonetheless, in practice multiple initial forms and shapes exist in the market. Although, the proposed force estimation methods accommodate the non-straight devices theoretically, their practical performance with such devices requires further validation.

(4) investigating the performance of other shape interpolation methods for th derivation of the kinematics of endovascular devices, e.g., Legendre polynomials. It was observed in the development of the force estimation methods that the mathematical properties of interpolation polynomial, e.g., De Casteljau's theorem, were utile to simplify the formulation and enhance

the performance. For example, using Legendre polynomials allows for recursive derivation of geometric terms and simplifies the analytical integrations,

(5) structural and material optimization of the proposed haptic rendering modality using the proposed magnetoelastic model, e.g., finding optimal magnet separation and dimensions of the MRE insert for a maximal force rendering range. As the obtained magnetoelastic model for the haptic force indicated, the material properties and size of the MRE, size and magnetic properties of the permanent magnets, and structural design of the magnet separation mechanism affect the rendered force. In this study, the feasibility of force feedback generation was shown. However, fine-tuning of the feasible range of the force generation capacity requires model-based optimization for which the use of the magnetoelastic model is essential.

(6) using multiple serial MRE insert and individual magnet pairs with smaller sizes along the ferromagnetic shaft of the proposed haptic rendering device to allow for zero-force rendering and finer force control. As an extension of the proposed mechanism for magnetoelastic force generation, using multiple smaller units of the magnet controller could be a possibility to reduced the size of the system while improving its force generation feasible range.

Bibliography

[1] World Health Organization (WHO). Cardiovascular diseases (cvds) factsheets. http://www.who.int/mediacentre/factsheets/fs317/en/, September 2016. Accessed: 2016-09-30.

[2] Zhu-Ming Zhang, Pentti M Rautaharju, Ronald J Prineas, Carlos J Rodriguez, Laura Loehr, Wayne D Rosamond, Dalane Kitzman, David Couper, and Elsayed Z Soliman. Race and sex differences in the incidence and prognostic significance of silent myocardial infarction in the atherosclerosis risk in communities (aric) study. *Circulation*, pages 2141–2148, 2016.

[3] Jay H Lubin, David Couper, Pamela L Lutsey, and Hiroshi Yatsuya. Synergistic and non-synergistic associations for cigarette smoking and non-tobacco risk factors for cardiovascular disease incidence in the atherosclerosis risk in communities (aric) study. *Nicotine & Tobacco Research*, page ntw235, 2016.

[4] J Fritz, S Strohmaier, G Nagel, H Concin, and H Ulmer. Overweight/obesity and coronary heart disease: Age dependencies in metabolic mediation. *Atherosclerosis*, 252:e16, 2016.

[5] Ioanna Tzoulaki, Paul Elliott, Vasilis Kontis, and Majid Ezzati. Worldwide exposures to cardiovascular risk factors and associated health effects current knowledge and data gaps. *Circulation*, 133(23):2314–2333, 2016.

[6] Yoshio Iwashima, Tetsuya Fukuda, Fumiki Yoshihara, Hiroshi Kusunoki, Masatsugu Kishida, Shin-ichiro Hayashi, Satoko Nakamura, Kei Kamide, Takeshi Horio, and Yuhei Kawano. Incidence and risk factors for restenosis, and its impact on blood pressure control after percutaneous transluminal renal angioplasty in hypertensive patients with renal artery stenosis. *Journal of hypertension*, 34(7):1407–1415, 2016.

[7] Farah Rehan, Alina Qadeer, Irfan Bashir, and Mohammed Jamshaid. Risk factors of cardiovascular disease in developing countries. *International Current Pharmaceutical Journal*, 5(8):69–72, 2016.

[8] Antonio Gomez-Outes, M Luisa Suarez-Gea, Gonzalo Calvo-Rojas, Ramon Lecumberri, Eduardo Rocha, Carmen Pozo-Hernández, Ana Isabel Terleira-Fernandez, and Emilio Vargas-Castrillón. Discovery of anticoagulant drugs: a historical perspective. *Current drug discovery technologies*, 9(2):83–104, 2012.

[9] Michael Diodato and Edgar G Chedrawy. Coronary artery bypass graft surgery: the past, present, and future of myocardial revascularisation. *Surgery research and practice*, 2014, 2014.

[10] Charles T Dotter and Melvin P Judkins. Transluminal treatment of arteriosclerotic obstruction description of a new technic and a preliminary report of its application. *Circulation*, 30(5):654–670, 1964.

[11] Andreas R Grüntzig, Åke Senning, and Walter E Siegenthaler. Nonoperative dilatation of coronary-artery stenosis: percutaneous transluminal coronary angioplasty. *New England Journal of Medicine*, 301(2):61–68, 1979.

[12] Dasdo A Sinaga, Alyssa S Sim, Hee Hwa Ho, Fahim Haider Jafary, Jason Loh, Yau Wei Ooi, Julian Tan, and Paul Ong. Tct-408 de novo small vessel coronary disease: To stent or not to stent? can drug coated balloon be a safe and effective alternative to modern drug eluting stent? *Journal of the American College of Cardiology*, 66(15_S), 2015.

[13] Lloyd W Klein, Donald L Miller, Stephen Balter, Warren Laskey, David Haines, Alexander Norbash, Matthew A Mauro, and James A Goldstein. Occupational health hazards in the interventional laboratory: time for a safer environment. *Catheterization and Cardiovascular Interventions*, 73(3):432–438, 2009.

[14] Lloyd W Klein, Yolande Tra, Kirk N Garratt, Wayne Powell, Georgina Lopez-Cruz, Charles

Chambers, and James A Goldstein. Occupational health hazards of interventional cardiologists in the current decade: Results of the 2014 scai membership survey. *Catheterization and Cardiovascular Interventions*, 86(5):913–924, 2015.

[15] Piera Capranzano, Vijay Kunadian, Josepa Mauri, Anna Sonia Petronio, Neus Salvatella, Yolande Appelman, Martine Gilard, Ghada W Mikhail, Stefanie Schüpke, Maria D Radu, et al. Motivations for and barriers to choosing an interventional cardiology career path: results from the eapci women committee worldwide survey. *EuroIntervention*, 12:53–59, 2016.

[16] Alaide Chieffo, Angela Hoye, Fina Mauri, Ghada Mikhail, Michelle Ammerer, Cindy Grines, Liliana Grinfeld, Mina Madan, Patrizia Presbitero, Kimberly A Skelding, et al. Gender-based issues in interventional cardiology: a consensus statement from the women in innovations (win) initiative1. *Revista Española de Cardiología (English Edition)*, 63(2):200–208, 2010.

[17] Faisal Hasan and Johannes Bonatti. Robotically assisted percutaneous coronary intervention: benefits to the patient and the cardiologist. *Expert Review of Cardiovascular Therapy*, 13(11):1165–1168, 2015.

[18] RV Leena and NK Shyamkumar. Glove perforations during interventional radiological procedures. *Cardiovascular and interventional radiology*, 33(2):375–378, 2010.

[19] Marco A Costa, Dominick J Angiolillo, Mark Tannenbaum, Mitchell Driesman, Alan Chu, John Patterson, William Kuehl, Joseph Battaglia, Samir Dabbons, Fayez Shamoon, et al. Impact of stent deployment procedural factors on long-term effectiveness and safety of sirolimus-eluting stents (final results of the multicenter prospective stllr trial). *The American journal of cardiology*, 101(12):1704–1711, 2008.

[20] George Dangas, Ioannis Iakovou, Eugenia Nikolsky, Eve D Aymong, Gary S Mintz, Nicholas N Kipshidze, Alexandra J Lansky, Issam Moussa, Gregg W Stone, Jeffrey W Moses, et al. Contrast-induced nephropathy after percutaneous coronary interventions in relation to chronic kidney disease and hemodynamic variables. *The American journal of cardiology*, 95(1):13–19, 2005.

[21] Sabine Ernst, Feifan Ouyang, Christian Linder, Klaus Hertting, Fabian Stahl, Julian Chun, Hitoshi Hachiya, Dietmar Bänsch, Matthias Antz, and Karl-Heinz Kuck. Initial experience with remote catheter ablation using a novel magnetic navigation system magnetic remote catheter ablation. *Circulation*, 109(12):1472–1475, 2004.

[22] Rafael Beyar, Luis Gruberg, Dan Deleanu, Ariel Roguin, Yaron Almagor, Silviu Cohen, Ganesh Kumar, and Tal Wenderow. Remote-control percutaneous coronary interventions: concept, validation, and first-in-humans pilot clinical trial. *Journal of the American College of Cardiology*, 47(2):296–300, 2006.

[23] David B Camarillo, Christopher F Milne, Christopher R Carlson, Michael R Zinn, and J Kenneth Salisbury. Mechanics modeling of tendon-driven continuum manipulators. *IEEE Transactions on Robotics*, 24(6):1262–1273, 2008.

[24] Juan F Granada, Juan A Delgado, Maria Paola Uribe, Andres Fernandez, Guillermo Blanco, Martin B Leon, and Giora Weisz. First-in-human evaluation of a novel robotic-assisted coronary angioplasty system. *JACC: Cardiovascular Interventions*, 4(4):460–465, 2011.

[25] Giora Weisz, D Christopher Metzger, Ronald P Caputo, Juan A Delgado, J Jeffrey Marshall, George W Vetrovec, Mark Reisman, Ron Waksman, Juan F Granada, Victor Novack, et al. Safety and feasibility of robotic percutaneous coronary intervention: Precise (percutaneous robotically-enhanced coronary intervention) study. *Journal of the American College of Cardiology*, 61(15):1596–1600, 2013.

[26] Hiram G Bezerra, Emile Mehanna, George W Vetrovec, Marco A Costa, and Giora Weisz. Longitudinal geographic miss (lgm) in robotic assisted versus manual percutaneous coronary interventions. *Journal of interventional cardiology*, 28(5):449–455, 2015.

[27] Paul T Campbell, Kevin R Kruse, Christopher R Kroll, Janet Y Patterson, and Michele J Esposito. The impact of precise robotic lesion length measurement on stent length selection: Ramifications for stent savings. *Cardiovascular Revascularization Medicine*, 16(6):348–350, 2015.

[28] Nathaniel R Smilowitz, Jeffrey W Moses, Fernando A Sosa, Benjamin Lerman, Yasir Qureshi, Kate E Dalton, Lauren T Privitera, Diane Canone-Weber, Varinder Singh, Martin B Leon, et al. Robotic-enhanced pci compared to the traditional manual approach. *The Journal of invasive cardiology*, 26(7):318–321, 2014.

[29] Michail M Pankratov. Robotically assisted pci with corpath 200 system: early evidence of potential benefits for patient and physician. *Cardiovascular Revascularization Medicine*, 3(12):e40, 2011.

[30] Nathaniel R Smilowitz and Giora Weisz. Evaluating the use of robotically assisted percutaneous coronary intervention: a matter of being precise. *Interventional Cardiology*, 4(5):501–503, 2012.

[31] Tsuyoshi Kaneko and Walter Randolph Chitwood. Current readings: status of robotic cardiac surgery. *Seminars in thoracic and cardiovascular surgery*, 25(2):165–170, 2013.

[32] Arnold H Seto and Morton J Kern. Robotic-assist pci: Precision guided pci or a rube goldberg solution? *Catheterization and Cardiovascular Interventions*, 83(6):922–923, 2014.

[33] Ryan Madder, Paul Campbell, Ehtisham Mahmud, David Wohns, Tomasz Stys, Ronald Caputo, Mark Leimbach, Manish Parikh, Vijaykumar Kasi, and Giora Weisz. Multi-center post-market registry for the evaluation of robotic assisted pci. *Journal of the American College of Cardiology*, 67(13_S):224–224, 2016.

[34] Ryan D Madder, Stacie M VanOosterhout, Mark E Jacoby, J Stewart Collins, Andrew S Borgman, Abbey N Mulder, Matthew A Elmore, Jessica L Campbell, Richard F McNamara, and David H Wohns. Percutaneous coronary intervention using a combination of robotics and telecommunications by an operator in a separate physical location from the patient: an early exploration into the feasibility of telestenting (the remote-pci study). *EuroIntervention*, 12(13):1569–1576, 2017.

[35] Mark E Jacoby, Manivannan Veerasamy, and Ryan D Madder. Robotic percutaneous coronary intervention. In *Textbook of Catheter-Based Cardiovascular Interventions*, pages 133–143. Springer, 2018.

[36] Prapa Kanagaratnam, Michael Koa-Wing, Daniel T Wallace, Alex S Goldenberg, Nicholas S Peters, and D Wyn Davies. Experience of robotic catheter ablation in humans using a novel remotely steerable catheter sheath. *Journal of Interventional Cardiac Electrophysiology*, 21(1):19–26, 2008.

[37] Carlos Tercero, Seiichi Ikeda, Tomomi Uchiyama, Toshio Fukuda, Fumihito Arai, Yuta Okada, Yoshinari Ono, Ryohei Hattori, Tokunori Yamamoto, Makoto Negoro, et al. Autonomous catheter insertion system using magnetic motion capture sensor for endovascular surgery. *The International Journal of Medical Robotics and Computer Assisted Surgery*, 3(1):52–58, 2007.

[38] Steve Ramcharitar, Mark S Patterson, Robert Jan Van Geuns, Carlos Van Meighem, and Patrick W Serruys. Technology insight: magnetic navigation in coronary interventions. *Nature Clinical Practice Cardiovascular Medicine*, 5(3):148–156, 2008.

[39] Chad M Dugas and Jeffrey M Schussler. Advanced technology in interventional cardiology: A roadmap for the future of precision coronary interventions. *Trends in cardiovascular medicine*, 26:466–473, 2016.

[40] Kamran Ahmed, Aoife N Keeling, Morkos Fakhry, Hutan Ashrafian, Rajesh Aggarwal, Peter A Naughton, Ara Darzi, Nicholas Cheshire, Thanos Athanasiou, and Mohammed Hamady. Role of virtual reality simulation in teaching and assessing technical skills in endovascular intervention. *Journal of Vascular and Interventional Radiology*, 21(1):55–66, 2010.

[41] Hedyeh Rafii-Tari, Christopher J Payne, and Guang-Zhong Yang. Current and emerging robot-assisted endovascular catheterization technologies: a review. *Annals of biomedical engineering*, 42(4):697–715, 2014.

[42] Hedyeh Rafii-Tari, Christopher J Payne, Colin Bicknell, Ka-Wai Kwok, Nicholas JW Cheshire, Celia Riga, and Guang-Zhong Yang. Objective assessment of endovascular navigation skills with force sensing. *Annals of Biomedical Engineering*, 45(5):1315–1327, 2017.

[43] Hedyeh Rafii-Tari, Celia V Riga, Christopher J Payne, Mohamad S Hamady, Nicholas JW Cheshire, Colin D Bicknell, and Guang-Zhong Yang. Reducing contact forces in the arch and supra-aortic vessels using the magellan robot. *Journal of Vascular Surgery*, 64(5):1422–1432, 2016.

[44] Yu Song, Shuxiang Guo, Xuanchun Yin, Linshuai Zhang, Hideyuki Hirata, Hidenori Ishihara, and Takashi Tamiya. Performance evaluation of a robot-assisted catheter operating system with haptic feedback. *Biomedical microdevices*, 20(2):50, 2018.

[45] Klaus A Hausegger, Peter Schedlbauer, Hannes A Deutschmann, and Kurt Tiesenhausen. Complications in endoluminal repair of abdominal aortic aneurysms. *European journal of radiology*, 39(1):22–33, 2001.

[46] Shuxiang Guo, Mingyang Qin, Nan Xiao, Yuan Wang, Weili Peng, and Xianqiang Bao. High precise haptic device for the robotic catheter navigation system. In *Mechatronics and Automation (ICMA), 2016 IEEE International Conference on*, pages 2524–2529. IEEE, 2016.

[47] Christopher J Payne, Hedyeh Rafii-Tari, and Guang-Zhong Yang. A force feedback system for endovascular catheterisation. In *2012 IEEE/RSJ International Conference on Intelligent Robots and Systems*, pages 1298–1304. IEEE, 2012.

[48] Yasuo Okumura, Susan B Johnson, T Jared Bunch, Benhur D Henz, Christine J O'brien, and Douglas L Packer. A systematical analysis of in vivo contact forces on virtual catheter tip/tissue surface contact during cardiac mapping and intervention. *Journal of cardiovascular electrophysiology*, 19(6):632–640, 2008.

[49] Luigi Di Biase, Andrea Natale, Conor Barrett, Carmela Tan, Claude S Elayi, Chi Keong Ching, Paul Wang, AMIN AL-AHMAD, Mauricio Arruda, J David Burkhardt, et al. Relationship between catheter forces, lesion characteristics,"popping," and char formation: experience with robotic navigation system. *Journal of cardiovascular electrophysiology*, 20(4):436–440, 2009.

[50] Stuart Schecter, Wei Lin, Aasha Gopal, Roger Fan, and Eric Rashba. Haptics and the heart:

Force and tactile feedback system for cardiovascular interventions. *Cardiovascular Revascularization Medicine*, 19(6):36–40, 2018.

[51] Yusof Ganji, Farrokh Janabi-Sharifi, et al. Catheter kinematics for intracardiac navigation. *IEEE Transactions on Biomedical Engineering*, 56(3):621–632, 2009.

[52] Awaz Ali, Dick H Plettenburg, and Paul Breedveld. Steerable catheters in cardiology: Classifying steerability and assessing future challenges. *IEEE Transactions on Biomedical Engineering*, 63(4):679–693, 2016.

[53] Javad Dargahi, Saeed Sokhanvar, Siamak Najarian, and Siamak Arbatani. *Tactile Sensing and Display: Haptic Feedback For Minimally Invasive Surgery And Robotics*. John Wiley & Sons, 2012.

[54] G Dagnino, J Liu, MEMK Abdelaziz, W Chi, C Riga, and G-Z Yang. Haptic feedback and dynamic active constraints for robot-assisted endovascular catheterization. In *2018 IEEE/RSJ International Conference on Intelligent Robots and Systems (IROS)*, pages 1770–1775. IEEE, 2018.

[55] Amir Hooshiar, Mohammad Jolaei, and Javad Dargahi. Sensor-free force and position control of tendon-driven catheters through interaction modeling, January 11 2021. US Patent application no. 63/136100.

[56] Amir Hooshiar, Mohammad Jolaei, and Javad Dargahi. Sensor-free force control of tendon-driven ablation catheters through position control and contact modeling, January 17 2020. US Patent application no. 62/962522.

[57] Amir Hooshiar, Ali Alkhalaf, and Javad Dargahi. Tactile interface system with magnetorheological elastomer and method for stiffness adaptation, October 4 2019. US Patent application no. 62/910916.

[58] Amir Hooshiar, Javad Dargahi, and Siamak Najarian. Real-time image-based force estimation along endovascular devices using inverse cosserat rod model (icord) for robot-assisted

cardiovascular interventional surgery. *IEEE Transactions on Robotics*, Revision requested, 2021.

[59] Amir Hooshiar, Amir Sayadi, Javad Dargahi, and Siamak Najarian. An integral-free rotation measurement method via stereo-accelerometery with application in robot-assisted catheter intervention. *IEEE/ASME Transactions on Mechatronics*, In-press, 2021.

[60] Amir Hooshiar, Alireza Payami, Javad Dargahi, and Siamak Najarian. Magnetostriction-based force feedback for robot-assisted cardiovascular surgery using smart magnetorheological elastomers. *Mechanical Systems and Signal Processing*, In-press, 2021.

[61] Ali Alkhalaf, Amir Hooshiar, and Javad Dargahi. Composite magnetorheological elastomers for tactile displays: Enhanced mreffect through bi-layer composition. *Composites Part B: Engineering*, page 107888, 2020.

[62] A. Hooshiar, S. Najarian, and J. Dargahi. Haptic telerobotic cardiovascular intervention: A review of approaches, methods, and future perspectives. *IEEE Reviews in Biomedical Engineering*, 13:32–50, 2020.

[63] Amir Hooshiar, Ali Alkhalaf, and Javad Dargahi. Development and assessment of a stiffness display system for minimally invasive surgery based on smart magneto-rheological elastomers. *Materials Science and Engineering: C*, 108:110409, 2020.

[64] Mohammad Jolaei, Amir Hooshiar, Javad Dargahi, and Muthukumaran Packirisamy. Toward task autonomy in robotic cardiac ablation: Learning-based kinematic control of soft tendon-driven catheters. *Soft Robotics*, Accepted(2020.0006), 2020.

[65] Amir Hooshiar, Amir Sayadi, Javad Dargahi, and Siamak Najarian. Analytical tip force estimation on tendon-driven catheters through inverse solution of cosserat rod model. In *International Conference on Intelligent Robots and Systems (IROS) 2021 (Under review)*. IEEE, 2021.

[66] Amir Hooshiar, Amir Sayadi, Mohammad Jolaei, and Javad Dargahi. Accurate estimation of

tip force on tendon-driven catheters using inverse cosserat rod model. In *2020 International Conference on Biomedical Innovations and Applications (BIA)*, pages 37–40. IEEE, 2020.

[67] Amir Sayadi, Amir Hooshiar, and Javad Dargahi. Impedance matching approach for robust force feedback rendering with application in robot-assisted interventions. In *2008 IEEE International Conference on Control, Mechatronics, and Automation*, pages 18–22. IEEE, 2020.

[68] Alireza Payami, Amir Hooshiar, Ali Alkhalaf, and Javad Dargahi. Modeling of rate-dependent force-displacement behavior of mres using neural networks for torque feedback applications. In *2008 IEEE International Conference on Control, Mechatronics, and Automation*, pages 58–62. IEEE, 2020.

[69] Pegah Yaftian, Naghmeh Bandari, Amir Hooshiar, and Javad Dargahi. Image-based contact detection and static force estimation on steerable rfa catheters. In *2020 International Conference on Biomedical Innovations and Applications (BIA)*, pages 57–60. IEEE, 2020.

[70] Mohammad Jolaei, Amir Hooshiar, Amir Sayadi, Javad Dargahi, and Muthukumaran Packirisamy. Sensor-free force control of tendon-driven ablation catheters through position control and contact modeling. In *2020 42nd Annual International Conference of the IEEE Engineering in Medicine & Biology Society (EMBC)*, pages 5248–5251. IEEE, 2020.

[71] Mohammad Jolaei, Amir Hooshiar, and Javad Dargahi. Displacement-based model for estimation of contact force between rfa catheter and atrial tissue with ex-vivo validation. In *2019 IEEE International Symposium on Robotic and Sensors Environments (ROSE)*, pages 1–7. IEEE, 2019.

[72] Ali Alkhalaf, Amir Hooshiar, and Javad Dargahi. Enhancement of mr-effect in magnetorheological elastomers through bi-layer composition: Theory and validation. In *Proceeding of 30th International Conference on Adaptive Structures and Technologies*, volume 1, pages 1–2. Concordia University, 2019.

[73] Mohammad Jolaei, Amir Hooshiar, and Dargahi. Kinematic analysis and position control of

flexible tendon-driven catheter for minimally invasive cardiac surgery. In *30th International Conference on Adaptive Structures and Technologies*, pages 1–2. Concordia University, 2019.

[74] Amir Hooshiar, Naghmeh M Bandari, and Javad Dargahi. Image-based estimation of contact forces on catheters for robot-assisted cardiovascular intervention. In *Proc. Hamlyn Symp. Med. Robot.*, pages 119–120, 2018.

[75] A. Molaei, A. H. Ahmadi, V. Karamzadeh, E. Abedloo, and J. Dargahi. Pretensioned structures as multi axis force sensors. In *2017 5th RSI International Conference on Robotics and Mechatronics (ICRoM)*, pages 416–420, 2017.

[76] Amir Hooshiar, Masoud Razban, Naghmeh M Bandari, and Javad Dargahi. Sensing principle for real-time characterization of viscoelasticity in the beating myocardial tissue. In *Computational Intelligence and Virtual Environments for Measurement Systems and Applications (CIVEMSA), 2017 IEEE International Conference on*, pages 72–77. IEEE, 2017.

[77] Naghmeh M Bandari, Amir Hooshair, Muthukumaran Packirisamy, and Javad Dargahi. Optical fiber array sensor for lateral and circumferential force measurement suitable for minimally invasive surgery: Design, modeling and analysis. In *Specialty Optical Fibers*, pages JTu4A–44. Optical Society of America, 2016.

[78] OAJ Van der Meijden and MP Schijven. The value of haptic feedback in conventional and robot-assisted minimal invasive surgery and virtual reality training: a current review. *Surgical endoscopy*, 23(6):1180–1190, 2009.

[79] Thorsten Mei, Christoph Budelmann, Thorsten A Kern, Stephanie Sindlinger, Carlos Minamisava, and Roland Werthschutzky. Intravascular palpation and haptic feedback during angioplasty. In *EuroHaptics Conference, 2009 and Symposium on Haptic Interfaces for Virtual Environment and Teleoperator Systems. World Haptics 2009. Third Joint*, pages 380–381. IEEE, 2009.

[80] Shuxiang Guo, Nan Xiao, and Baofeng Gao. A novel robot-assisted catheter surgery system with force feedback. In *Selected Topics in Micro/Nano-robotics for Biomedical Applications*, pages 175–190. Springer, 2013.

[81] Youngjin Moon and Jaesoon Choi. A tele-operated robotic platform for cardiovascular catheter intervention with haptic guidance. In *Control, Automation and Systems (ICCAS), 2014 14th International Conference on*, pages 299–303. IEEE, 2014.

[82] Haoyu Wang, Jianhuang Wu, Mingqiang Wei, and Xin Ma. A robust and fast approach to simulating the behavior of guidewire in vascular interventional radiology. *Computerized Medical Imaging and Graphics*, 40:160–169, 2015.

[83] Shahir Hasanzadeh and Farrokh Janabi-Sharifi. Model-based force estimation for intracardiac catheters. *IEEE/ASME Transactions on Mechatronics*, 21(1):154–162, 2016.

[84] Xianqiang Bao, Shuxiang Guo, Nan Xiao, Yuan Wang, Mingyang Qin, Yan Zhao, Changqi Xu, and Weili Peng. Design and evaluation of a novel guidewire navigation robot. In *Mechatronics and Automation (ICMA), 2016 IEEE International Conference on*, pages 431–436. IEEE, 2016.

[85] Guan-Chun Chen, Chia-Hung Lin, Chien-Ming Li, Kai-Sheng Hsieh, Yi-Chun Du, and Tainsong Chen. Virtual-reality simulator system for double interventional cardiac catheterization using haptic force producer with visual feedback. *Computers & Electrical Engineering*, 2015.

[86] Xuanchun Yin, Shuxiang Guo, Hideyuki Hirata, and Hidenori Ishihara. Design and experimental evaluation of a teleoperated haptic robot–assisted catheter operating system. *Journal of Intelligent Material Systems and Structures*, 27(1):3–16, 2016.

[87] Mohammad Ali Tavallaei, Daniel Gelman, Michael Konstantine Lavdas, Allan C Skanes, Douglas L Jones, Jeffrey S Bax, and Maria Drangova. Design, development and evaluation of a compact telerobotic catheter navigation system. *The International Journal of Medical Robotics and Computer Assisted Surgery*, 12(3):442–452, 2016.

[88] Linshuai Zhang, Shuxiang Guo, Huadong Yu, and Yu Song. Performance evaluation of a strain-gauge force sensor for a haptic robot-assisted catheter operating system. *Microsystem Technologies*, pages 1–10, 2017.

[89] Shuxiang Guo, Yuan Wang, Nan Xiao, Youxiang Li, and Yuhua Jiang. Study on real-time force feedback for a master–slave interventional surgical robotic system. *Biomedical microdevices*, 20(2):37, 2018.

[90] Yuan Wang, Shuxiang Guo, Nan Xiao, Youxiang Li, and Yuhua Jiang. Online measuring and evaluation of guidewire inserting resistance for robotic interventional surgery systems. *Microsystem Technologies*, pages 1–11, 2018.

[91] Mitsutaka Tanimoto, Fumihito Arai, Toshio Fukuda, Kouichi Itoigawa, Masashi Hashimoto, Ikuo Takahashi, and Makoto Negoro. Telesurgery system for intravascular neurosurgery. In *International Conference on Medical Image Computing and Computer-Assisted Intervention*, pages 29–39. Springer, 2000.

[92] T Meiß, TA Kern, S Klages, and R Werthschützky. Hapcath: Miniaturized force sensors for catheterization. *Biomedizinische Technik. Proceedings*, 6(09.09), 2006.

[93] T Meiß, TA Kern, S Sindlinger, and R Werthschützky. Hapcath: highly miniaturized piezoresistive force sensors for interior palpation of vessels during angioplasty. In *World Congress on Medical Physics and Biomedical Engineering, September 7-12, 2009, Munich, Germany*, pages 228–231. Springer, 2009.

[94] Jun Woo Park, Jaesoon Choi, Hui-Nam Pak, Seung Joon Song, Jung Chan Lee, Yongdoo Park, Seung Min Shin, and Kyung Sun. Development of a force-reflecting robotic platform for cardiac catheter navigation. *Artificial organs*, 34(11):1034–1039, 2010.

[95] R Ahmadi, J Dargahi, M Packirisamy, and R Cecere. A new hybrid catheter-tip tactile sensor with relative hardness measuring capability for use in catheter-based heart surgery. In *Sensors, 2010 IEEE*, pages 1592–1595. IEEE, 2010.

[96] Tianmiao Wang, Dapeng Zhang, and Liu Da. Remote-controlled vascular interventional surgery robot. *The International Journal of Medical Robotics and Computer Assisted Surgery*, 6(2):194–201, 2010.

[97] Yili Fu, Anzhu Gao, Hao Liu, and Shuxiang Guo. The master-slave catheterisation system for positioning the steerable catheter. *International Journal of Mechatronics and Automation*, 1(3-4):143–152, 2011.

[98] Naghmeh M Bandari, Roozbeh Ahmadi, Amir Hooshiar, Javad Dargahi, and Muthukumaran Packirisamy. Hybrid piezoresistive-optical tactile sensor for simultaneous measurement of tissue stiffness and detection of tissue discontinuity in robot-assisted minimally invasive surgery. *Journal of biomedical optics*, 22(7):077002, 2017.

[99] Naghmeh M. Bandari, Amir Hooshair, Muthukumaran Packirisamy, and Javad Dargahi. Bending-based formulation of light intensity modulation for miniaturization of optical tactile sensors. In *Advanced Photonics 2018 (BGPP, IPR, NP, NOMA, Sensors, Networks, SPPCom, SOF)*, page SeM2E.3. Optical Society of America, 2018.

[100] Panagiotis Polygerinos, Pinyo Puangmali, Tobias Schaeffter, Reza Razavi, Lakmal D Seneviratne, and Kaspar Althoefer. Novel miniature mri-compatible fiber-optic force sensor for cardiac catheterization procedures. In *Robotics and Automation (ICRA), 2010 IEEE International Conference on*, pages 2598–2603. IEEE, 2010.

[101] Panagiotis Polygerinos, Asghar Ataollahi, Tobias Schaeffter, Reza Razavi, Lakmal D Seneviratne, and Kaspar Althoefer. Mri-compatible intensity-modulated force sensor for cardiac catheterization procedures. *IEEE Transactions on biomedical engineering*, 58(3):721–726, 2011.

[102] Pinyo Puangmali, Hongbin Liu, Lakmal D Seneviratne, Prokar Dasgupta, and Kaspar Althoefer. Miniature 3-axis distal force sensor for minimally invasive surgical palpation. *Ieee/Asme Transactions On Mechatronics*, 17(4):646–656, 2012.

[103] Yohan Noh, Sina Sareh, Jungwhan Back, Helge A Würdemann, Tommaso Ranzani, Emanuele Lindo Secco, Angela Faragasso, Hongbin Liu, and Kaspar Althoefer. A three-axial body force sensor for flexible manipulators. In *Robotics and Automation (ICRA), 2014 IEEE International Conference on*, pages 6388–6393. IEEE, 2014.

[104] Daniele Tosi, Edoardo Gino Macchi, Giovanni Braschi, Alfredo Cigada, Mario Gallati, Sandro Rossi, Sven Poeggel, Gabriel Leen, and Elfed Lewis. Fiber-optic combined fpi/fbg sensors for monitoring of radiofrequency thermal ablation of liver tumors: ex vivo experiments. *Applied optics*, 53(10):2136–2144, 2014.

[105] Zhenda Yang, Hao Liu, Yuanyuan Zhou, Anzhu Gao, and Hongyi Li. A miniature force sensor for catheter based on optical micro deformation detection. In *Cyber Technology in Automation, Control, and Intelligent Systems (CYBER), 2015 IEEE International Conference on*, pages 441–445. IEEE, 2015.

[106] Yohan Noh, Hongbin Liu, Sina Sareh, Damith Suresh Chathuranga, Helge Würdemann, Kawal Rhode, and Kaspar Althoefer. Image-based optical miniaturized three-axis force sensor for cardiac catheterization. *IEEE Sensors Journal*, 16(22):7924–7932, 2016.

[107] Hao Su, Iulian I Iordachita, Junichi Tokuda, Nobuhiko Hata, Xuan Liu, Reza Seifabadi, Sheng Xu, Bradford Wood, and Gregory S Fischer. Fiber-optic force sensors for mri-guided interventions and rehabilitation: A review. *IEEE Sensors Journal*, 17(7):1952–1963, 2017.

[108] Daniele Tosi, Emiliano Schena, Carlo Molardi, and Sanzhar Korganbayev. Fiber optic sensors for sub-centimeter spatially resolved measurements: Review and biomedical applications. *Optical Fiber Technology*, 43:6–19, 2018.

[109] Israel Gannot. Optical fibers and sensors for medical applications. In *Optical Fibers and Sensors for Medical Applications*, volume 4253, 2001.

[110] Naghmeh M Bandari, Amir Hooshair, Muthukumaran Packirisamy, and Javad Dargahi. Bending-based formulation of light intensity modulation for miniaturization of optical tactile sensors. In *Optical Sensors*, pages SeM2E–3. Optical Society of America, 2018.

[111] Michael C Yip, Shelten G Yuen, and Robert D Howe. A robust uniaxial force sensor for minimally invasive surgery. *IEEE transactions on biomedical engineering*, 57(5):1008–1011, 2010.

[112] Thomas George Thuruthel, Benjamin Shih, Cecilia Laschi, and Michael Thomas Tolley. Soft robot perception using embedded soft sensors and recurrent neural networks. *Science Robotics*, 4(26):eaav1488, 2019.

[113] Aizhan Issatayeva, Aidana Beisenova, Carlo Molardi, and Daniele Tosi. Distributed strain sensing medical catheter for epidural anesthesia. In *Optics in Health Care and Biomedical Optics VIII*, volume 10820, page 108203P. International Society for Optics and Photonics, 2018.

[114] Yogesh Thakur, Jeffrey S Bax, David W Holdsworth, and Maria Drangova. Design and performance evaluation of a remote catheter navigation system. *IEEE Transactions on biomedical engineering*, 56(7):1901–1908, 2009.

[115] Takeo Yamada, Yuhei Hayamizu, Yuki Yamamoto, Yoshiki Yomogida, Ali Izadi-Najafabadi, Don N Futaba, and Kenji Hata. A stretchable carbon nanotube strain sensor for human-motion detection. *Nature nanotechnology*, 6(5):296, 2011.

[116] Joseph T Muth, Daniel M Vogt, Ryan L Truby, Yiğit Mengüç, David B Kolesky, Robert J Wood, and Jennifer A Lewis. Embedded 3d printing of strain sensors within highly stretchable elastomers. *Advanced Materials*, 26(36):6307–6312, 2014.

[117] Feng Ju, Yaming Wang, Zhao Zhang, Yaoyao Wang, Yahui Yun, Hao Guo, and Bai Chen. A miniature piezoelectric spiral tactile sensor for tissue hardness palpation with catheter robot in minimally invasive surgery. *Smart Materials and Structures*, 28(2):025033, jan 2019.

[118] Katsuaki Yokoyama, Hiroshi Nakagawa, Dipen C Shah, Hendrik Lambert, Giovanni Leo, Nicolas Aeby, Atsushi Ikeda, Jan V Pitha, Tushar Sharma, Ralph Lazzara, et al. Novel contact force sensor incorporated in irrigated radiofrequency ablation catheter predicts lesion size and incidence of steam pop and thrombus. *Circulation: Arrhythmia and Electrophysiology*, pages CIRCEP–108, 2008.

[119] Jagadeesan Jayender, Rajnikant V Patel, and Suwas Nikumb. Robot-assisted active catheter insertion: algorithms and experiments. *The International Journal of Robotics Research*, 28(9):1101–1117, 2009.

[120] Mahta Khoshnam and Rajni V Patel. Estimating contact force for steerable ablation catheters based on shape analysis. In *2014 IEEE/RSJ International Conference on Intelligent Robots and Systems*, pages 3509–3514. IEEE, 2014.

[121] Meysam T Chorsi, Eli J Curry, Hamid T Chorsi, Ritopa Das, Jeffrey Baroody, Prashant K Purohit, Horea Ilies, and Thanh D Nguyen. Piezoelectric biomaterials for sensors and actuators. *Advanced Materials*, 31(1):1802084, 2019.

[122] Tushar Sharma, Sahil Naik, Jewel Langevine, Brijesh Gill, and John XJ Zhang. Aligned pvdf-trfe nanofibers with high-density pvdf nanofibers and pvdf core–shell structures for endovascular pressure sensing. *IEEE Transactions on Biomedical Engineering*, 62(1):188–195, 2015.

[123] Mahta Khoshnam, Aaron Yurkewich, and Rajni V Patel. Model-based force control of a steerable ablation catheter with a custom-designed strain sensor. In *Robotics and Automation (ICRA), 2013 IEEE International Conference on*, pages 4479–4484. IEEE, 2013.

[124] Siamak Najarian, Javad Dargahi, and Ali Abouei Mehrizi. *Artificial tactile sensing in biomedical engineering*. McGraw Hill Professional, 2009.

[125] Brenda Martínez-González, María del Carmen Theriot-Girón, Norberto López-Serna, Rodolfo Morales-Avalos, Alejandro Quiroga-Garza, Cynthia G Reyes-Hernández, Arnulfo Villanueva-Olivo, Jorge I Leyva-Villegas, Adolfo Soto-Domínguez, David de la Fuente-Villarreal, et al. Morphological analysis of major segments of coronary artery occlusion. importance in myocardial revascularization surgery. *Int. J. Morphol*, 33(4):1205–1212, 2015.

[126] Thomas Allsop, Ranjeet Bhamber, Glynn Lloyd, Martin R Miller, Andrew Dixon, David Webb, Juan Diego Ania Castañón, and Ian Bennion. Respiratory function monitoring using a real-time three-dimensional fiber-optic shaping sensing scheme based upon fiber bragg gratings. *Journal of biomedical optics*, 17(11):117001–117001, 2012.

[127] International Organization for Standardization. Sterile single-use intravascular introducers, dilators and guidewires. Standard, International Organization for Standardization, Geneva, CH, October 2014.

[128] Yan Bailly and Yacine Amirat. Modeling and control of a hybrid continuum active catheter for aortic aneurysm treatment. In *Proceedings of the 2005 IEEE International Conference on Robotics and Automation*, pages 924–929. IEEE, 2005.

[129] Robert J Webster and Bryan A Jones. Design and kinematic modeling of constant curvature continuum robots: A review. *The International Journal of Robotics Research*, 2010.

[130] Mahta Khoshnam, Mahdi Azizian, and Rajni V Patel. Modeling of a steerable catheter based on beam theory. In *Robotics and Automation (ICRA), 2012 IEEE International Conference on*, pages 4681–4686. IEEE, 2012.

[131] Larry L Howell. Compliant mechanisms. In *Compliant mechanisms*, chapter 2, pages 45–55. John Wiley & Sons, 2001.

[132] Baofeng Gao, Shuxiang Guo, Nan Xiao, and Jin Guo. Design of the virtual reality based robotic catheter system for minimally invasive surgery training. In *2012 IEEE International Conference on Automation and Logistics*, pages 611–616. IEEE, 2012.

[133] Klaus-Jürgen Bathe and Said Bolourchi. Large displacement analysis of three-dimensional beam structures. *International Journal for Numerical Methods in Engineering*, 14(7):961–986, 1979.

[134] Michael A Crisfield. A consistent co-rotational formulation for non-linear, three-dimensional, beam-elements. *Computer methods in applied mechanics and engineering*, 81(2):131–150, 1990.

[135] Siamak Arbatani, Alfonso Callejo, József Kövecses, Masoud Kalantari, Nick R Marchand, and Javad Dargahi. An approach to directional drilling simulation: finite element and finite segment methods with contact. *Computational Mechanics*, 57(6):1001–1015, 2016.

[136] E Kerrien, A Yureidini, J Dequidt, C Duriez, R Anxionnat, and S Cotin. Blood vessel modeling for interactive simulation of interventional neuroradiology procedures. *Medical Image Analysis*, 2016.

[137] Yun Teng, Mark Meyer, Tony DeRose, and Theodore Kim. Subspace condensation: full space adaptivity for subspace deformations. *ACM Transactions on Graphics (TOG)*, 34(4):76, 2015.

[138] Olgierd Cecil Zienkiewicz and Robert Leroy Taylor. Generalization of finite element concept. galerkin-weighted residual and variational approaches. In *The finite element method: solid mechanics*, volume 2, chapter 3, pages 45–55. Butterworth-heinemann, 2000.

[139] Yaoping Wang, Cheekong Chui, Honglip Lim, Yiyu Cai, and Koonhou Mak. Real-time interactive simulator for percutaneous coronary revascularization procedures. *Computer Aided Surgery*, 3(5):211–227, 1998.

[140] Christian Duriez, Stéphane Cotin, Julien Lenoir, and Paul Neumann. New approaches to catheter navigation for interventional radiology simulation. *Computer Aided Surgery*, 11(6):300–308, 2006.

[141] Stéphane Cotin, Christian Duriez, Julien Lenoir, Paul Neumann, and Steven Dawson. New approaches to catheter navigation for interventional radiology simulation. In *International Conference on Medical Image Computing and Computer-Assisted Intervention*, pages 534–542. Springer, 2005.

[142] MK Konings, EB Van de Kraats, T Alderliesten, and WJ Niessen. Analytical guide wire motion algorithm for simulation of endovascular interventions. *Medical and Biological Engineering and Computing*, 41(6):689–700, 2003.

[143] Ahmed A Shabana. Flexible multibody dynamics: review of past and recent developments. *Multibody system dynamics*, 1(2):189–222, 1997.

[144] Venkatasubramanian Kalpathy Venkiteswaran and Hai-Jun Su. A parameter optimization framework for determining the pseudo-rigid-body model of cantilever-beams. *Precision Engineering*, 40:46–54, 2015.

[145] Tanja Alderliesten, Maurits K Konings, and Wiro J Niessen. Simulation of minimally invasive vascular interventions for training purposes. *Computer Aided Surgery*, 9(1-2):3–15, 2004.

[146] Jin Guo, Shuxiang Guo, Nan Xiao, and Baofeng Gao. Virtual reality simulators based on a novel robotic catheter operating system for training in minimally invasive surgery. *Journal of Robotics and Mechatronics*, 24(4):649, 2012.

[147] Pramod Chembrammel, Habib Mohd Younus, and Thenkurussi Kesavadas. Modelling and simulation of guide-wire interaction with vasculature using constrained multibody dynamics. In *ASME 2013 International Mechanical Engineering Congress and Exposition*, pages V04AT04A083–V04AT04A083. American Society of Mechanical Engineers, 2013.

[148] Jia-Jung Wang, Shing-Hong Liu, Hung-Mao Su, Steven Chang, and Wei-Kung Tseng. A vibration-based approach to quantifying the dynamic elastance of the superficial arterial wall. *Biomedical engineering online*, 15(1):1, 2016.

[149] Dongjin Huang, Yin Wang, Pengbin Tang, Zhifeng Xie, Wen Tang, and Youdong Ding. Modeling and simulation of multi-frictional interaction between guidewire and vasculature. In *International Conference on Image and Graphics*, pages 524–537. Springer, 2015.

[150] Paulo Flores and Hamid M Lankarani. *Contact Force Models for Multibody Dynamics*. Springer, 2016.

[151] Jianhuang Wu, Haoyu Wang, Peng Zhang, Xin Ma, and Qingmao Hu. A preliminary real-time and realistic simulation environment for percutaneous coronary intervention. *BioMed research international*, 2015, 2015.

[152] Pier Paolo Valentini and Ettore Pennestrì. Modeling elastic beams using dynamic splines. *Multibody system dynamics*, 25(3):271–284, 2011.

[153] Jonas Spillmann and Matthias Teschner. C o r d e: Cosserat rod elements for the dynamic simulation of one-dimensional elastic objects. In *Proceedings of the 2007 ACM SIGGRAPH/Eurographics symposium on Computer animation*, pages 63–72. Eurographics Association, 2007.

[154] Matthew F Dixon. *Geometric integrators for continuum dynamics*. PhD dissertation, Imperial College London (University of London), 2007. *ch. 3: Moser-Veselov Integrators for Elastic Body and Rod Motions*.

[155] Jack B Kuipers et al. *Quaternions and rotation sequences*, volume 66. Princeton university press Princeton, 1999.

[156] Wen Tang, Tao Ruan Wan, Derek A Gould, Thien How, and Nigel W John. A stable and real-time nonlinear elastic approach to simulating guidewire and catheter insertions based on cosserat rod. *IEEE Transactions on Biomedical Engineering*, 59(8):2211–2218, 2012.

[157] Maisheng Luo, Hongzhi Xie, Le Xie, Ping Cai, and Lixu Gu. A robust and real-time vascular intervention simulation based on kirchhoff elastic rod. *Computerized medical imaging and graphics*, 38(8):735–743, 2014.

[158] Fernando M Cardoso and Sergio S Furuie. Guidewire path determination for intravascular applications. *Computer methods in biomechanics and biomedical engineering*, 19(6):628–638, 2016.

[159] Mafalda Camara, Erik Mayer, Ara Darzi, and Philip Pratt. Soft tissue deformation for surgical simulation: a position-based dynamics approach. *International journal of computer assisted radiology and surgery*, pages 1–10, 2016.

[160] Shuai Li, Qing Xia, Aimin Hao, Hong Qin, and Qinping Zhao. Haptics-equiped interactive pci simulation for patient-specific surgery training and rehearsing. *Science China Information Sciences*, 59(10):103101, 2016.

[161] Jinwoo Jung, Ryan S Penning, and Michael R Zinn. A modeling approach for robotic

catheters: effects of nonlinear internal device friction. *Advanced Robotics*, 28(8):557–572, 2014.

[162] Julien Lenoir, Stephane Cotin, Christian Duriez, and Paul Neumann. Interactive physically-based simulation of catheter and guidewire. *Computers & Graphics*, 30(3):416–422, 2006.

[163] Franck Jourdan, Pierre Alart, and Michel Jean. A gauss-seidel like algorithm to solve frictional contact problems. *Computer methods in applied mechanics and engineering*, 155(1):31–47, 1998.

[164] Wenpeng Gao, Lili Chu, Yili Fu, and Shuguo Wang. A non-linear, anisotropic mass spring model based simulation for soft tissue deformation. In *Ubiquitous Robots and Ambient Intelligence (URAI), 2014 11th International Conference on*, pages 7–10. IEEE, 2014.

[165] Paolo Patete, Maria Ida Iacono, Maria Francesca Spadea, Giovanna Trecate, Daniele Vergnaghi, Luca Tommaso Mainardi, and Guido Baroni. A multi-tissue mass-spring model for computer assisted breast surgery. *Medical engineering & physics*, 35(1):47–53, 2013.

[166] Ehsan Basafa and Farzam Farahmand. Real-time simulation of the nonlinear visco-elastic deformations of soft tissues. *International journal of computer assisted radiology and surgery*, 6(3):297–307, 2011.

[167] Jean-Claude Samin and Paul Fisette. Multibody systems with flexible beams. In *Symbolic modeling of multibody systems*, pages 301–344. Springer Science & Business Media, 2013.

[168] RE Valembois, Paul Fisette, and Jean-Claude Samin. Comparison of various techniques for modelling flexible beams in multibody dynamics. *Nonlinear Dynamics*, 12(4):367–397, 1997.

[169] Gregory S Chirikjian. Hyper-redundant manipulator dynamics: a continuum approximation. *Advanced Robotics*, 9(3):217–243, 1994.

[170] G Robinson and J Bruce C Davies. Continuum robots-a state of the art. In *Robotics and Automation, 1999. Proceedings. 1999 IEEE International Conference on*, volume 4, pages 2849–2854. IEEE, 1999.

[171] Ian A Gravagne, Christopher D Rahn, and Ian D Walker. Large deflection dynamics and control for planar continuum robots. *IEEE/ASME transactions on mechatronics*, 8(2):299–307, 2003.

[172] Alperen Degirmenci, Paul M Loschak, Cory M Tschabrunn, Elad Anter, and Robert D Howe. Compensation for unconstrained catheter shaft motion in cardiac catheters. In *2016 IEEE International Conference on Robotics and Automation (ICRA)*, pages 4436–4442. IEEE, 2016.

[173] Caleb Rucker and Robert J Webster. Mechanics of bending, torsion, and variable precurvature in multi-tube active cannulas. In *Robotics and Automation, 2009. ICRA'09. IEEE International Conference on*, pages 2533–2537. IEEE, 2009.

[174] Caleb Rucker, Robert J Webster III, Gregory S Chirikjian, and Noah J Cowan. Equilibrium conformations of concentric-tube continuum robots. *The International journal of robotics research*, 29(10):1263–1280, 2010.

[175] Matthias Hoffmann, Alexander Brost, Carolin Jakob, Martin Koch, Felix Bourier, Klaus Kurzidim, Joachim Hornegger, and Norbert Strobel. Reconstruction method for curvilinear structures from two views. *SPIE medical imaging. International Society for Optics and Photonics*, pages 86712F–86712F, 2013.

[176] Matthias Hoffmann, Alexander Brost, Martin Koch, Felix Bourier, Andreas Maier, Klaus Kurzidim, Norbert Strobel, and Joachim Hornegger. Electrophysiology catheter detection and reconstruction from two views in fluoroscopic images. *IEEE transactions on medical imaging*, 35(2):567–579, 2016.

[177] Edgar J Lobaton, Jinghua Fu, Luis G Torres, and Ron Alterovitz. Continuous shape estimation of continuum robots using x-ray images. In *Robotics and Automation (ICRA), 2013 IEEE International Conference on*, pages 725–732. IEEE, 2013.

[178] Xia Zhong, Matthias Hoffmann, Norbert Strobel, and Andreas Maier. Improved semi-automatic basket catheter reconstruction from two x-ray views. In *Bildverarbeitung für die Medizin 2016*, pages 26–31. Springer, 2016.

[179] Bor-Jeng Chen, Ziyan Wu, Shanhui Sun, Dong Zhang, and Terrence Chen. Guidewire tracking using a novel sequential segment optimization method in interventional x-ray videos. In *Biomedical Imaging (ISBI), 2016 IEEE 13th International Symposium on*, pages 103–106. IEEE, 2016.

[180] Kenneth R Hoffmann, Anindya Sen, Li Lan, Kok-Gee Chua, Jacqueline Esthappan, and Marco Mazzucco. A system for determination of 3d vessel tree centerlines from biplane images. *The International Journal of Cardiac Imaging*, 16(5):315–330, 2000.

[181] Michael Hannan and Ian Walker. Vision based shape estimation for continuum robots. In *Robotics and Automation, 2003. Proceedings. ICRA'03. IEEE International Conference on*, volume 3, pages 3449–3454. IEEE, 2003.

[182] Michael W Hannan and Ian D Walker. Real-time shape estimation for continuum robots using vision. *Robotica*, 23(5):645–651, 2005.

[183] Jordan M Croom, Caleb Rucker, Joseph M Romano, and Robert J Webster. Visual sensing of continuum robot shape using self-organizing maps. In *Robotics and Automation (ICRA), 2010 IEEE International Conference on*, pages 4591–4596. IEEE, 2010.

[184] Hunter B Gilbert, Caleb Rucker, and Robert J Webster III. Concentric tube robots: The state of the art and future directions. In *Robotics Research*, pages 253–269. Springer, 2016.

[185] Mohsen Moradi Dalvand, Saeid Nahavandi, and Robert D Howe. Fast vision-based catheter 3d reconstruction. *Physics in Medicine & Biology*, 61(14):5128, 2016.

[186] Shuxiang Guo, Miao Yu, Yu Song, and Linshuai Zhang. The virtual reality simulator-based catheter training system with haptic feedback. In *Mechatronics and Automation (ICMA), 2017 IEEE International Conference on*, pages 922–926. IEEE, 2017.

[187] Jiayin Cai, Hongzhi Xie, Shuyang Zhang, and Lixu Gu. Blood flow-induced physically based guidewire simulation for vascular intervention training. *International Journal of Computer Assisted Radiology and Surgery*, pages 1–13, 2017.

[188] Junghwan Back, Lukas Lindenroth, Kawal Rhode, and Hongbin Liu. Three dimensional force estimation for steerable catheters through bi-point tracking. *Sensors and Actuators A: Physical*, 279:404–415, 2018.

[189] Ping-Lin Chang, Alexander Rolls, Herbert De Praetere, Emmanuel Vander Poorten, Celia V Riga, Colin D Bicknell, and Danail Stoyanov. Robust catheter and guidewire tracking using b-spline tube model and pixel-wise posteriors. *IEEE Robotics and Automation Letters*, 1(1):303–308, 2016.

[190] David B Dooner. Introducing radius of torsure and cylindroid of torsure. *Journal of Field Robotics*, 20(8):429–436, 2003.

[191] Jagadeesan Jayender, Mahdi Azizian, and Rajni V Patel. Autonomous robot-assisted active catheter insertion using image guidance. In *Intelligent Robots and Systems, 2007. IROS 2007. IEEE/RSJ International Conference on*, pages 889–894. IEEE, 2007.

[192] Jagadeesan Jayender and Rajnikant V Patel. Master-slave control of an active catheter instrumented with shape memory alloy actuators. In *Intelligent Robots and Systems, 2007. IROS 2007. IEEE/RSJ International Conference on*, pages 759–764. IEEE, 2007.

[193] Dongwen Zhang, Qingsong Zhu, Jing Xiong, and Lei Wang. Dynamic virtual fixture on the euclidean group for admittance-type manipulator in deforming environments. *Biomedical engineering online*, 13(1):51, 2014.

[194] Yan Zhao, Shuxiang Guo, Nan Xiao, Yuxin Wang, Youxiang Li, and Yuhua Jiang. Operating force information on-line acquisition of a novel slave manipulator for vascular interventional surgery. *Biomedical microdevices*, 20(2):33, 2018.

[195] Xianqiang Bao, Shuxiang Guo, Nan Xiao, Youxiang Li, and Liwei Shi. Compensatory force measurement and multimodal force feedback for remote-controlled vascular interventional robot. *Biomedical Microdevices*, 20(3):74, 2018.

[196] YingLiang Ma, Graeme P Penney, Dennis Bos, Peter Frissen, George de Fockert, Andy King, Gang Gao, Cheng Yao, John Totman, Matthew Ginks, et al. Evaluation of a robotic arm

for echocardiography to x-ray image registration during cardiac catheterization procedures. In *Engineering in Medicine and Biology Society, 2009. EMBC 2009. Annual International Conference of the IEEE*, pages 5829–5832. IEEE, 2009.

[197] YingLiang Ma, Graeme P Penney, Dennis Bos, Peter Frissen, C Aldo Rinaldi, Reza Razavi, and Kawal S Rhode. Hybrid echo and x-ray image guidance for cardiac catheterization procedures by using a robotic arm: a feasibility study. *Physics in Medicine & Biology*, 55(13):N371, 2010.

[198] Nan Xiao, Shuxiang Guo, Jian Guo, Xufeng Xiao, and Takashi Tamiya. Development of a kind of robotic catheter manipulation system. In *Robotics and Biomimetics (ROBIO), 2011 IEEE International Conference on*, pages 32–37. IEEE, 2011.

[199] Xianqiang Bao, Shuxiang Guo, Nan Xiao, Youxiang Li, Cheng Yang, Rui Shen, Jinxin Cui, Yuhua Jiang, Xinke Liu, and Keyun Liu. Operation evaluation in-human of a novel remote-controlled vascular interventional robot. *Biomedical microdevices*, 20(2):34, 2018.

[200] Kundong Wang, Qingsheng Lu, Bin Chen, Yu Shen, Hongbing Li, Manhua Liu, and Zhuoyan Xu. Endovascular intervention robot with multi-manipulators for surgical procedures: Dexterity, adaptability, and practicability. *Robotics and Computer-Integrated Manufacturing*, 56:75–84, 2019.

[201] Hao Shen, Cheng Wang, Le Xie, Shoujun Zhou, and Xionghui Zhou. Research for a master-slave cerebrovascular interventional robotic system. In *2018 IEEE International Conference on Real-time Computing and Robotics (RCAR)*, pages 395–398. IEEE, 2018.

[202] Hao Shen, Cheng Wang, Le Xie, Shoujun Zhou, Lixu Gu, and Hongzhi Xie. A novel remote-controlled robotic system for cerebrovascular intervention. *The International Journal of Medical Robotics and Computer Assisted Surgery*, 14(6):e1943, 2018.

[203] Fulong Chen, Hao Shen, Cheng Wang, Le Xie, Shoujun Zhou, and Hesheng Wang. The model experimental evaluation of the cardiovascular interventional surgery robot system. In *2018 IEEE 16th Intl Conf on Dependable, Autonomic and Secure Computing, 16th Intl Conf on Pervasive Intelligence and Computing, 4th Intl Conf on*

Big Data Intelligence and Computing and Cyber Science and Technology Congress (DASC/PiCom/DataCom/CyberSciTech), pages 114–120. IEEE, 2018.

[204] Olatunji Mumini OMISORE, HAN ShiPeng, REN LingXue, and WANG Lei. A teleoperated robotic catheter system with motion and force feedback for vascular surgery. In *2018 18th International Conference on Control, Automation and Systems (ICCAS)*, pages 172–177. IEEE, 2018.

[205] Xuanchun Yin, Shuxiang Guo, Nan Xiao, Takashi Tamiya, Hideyuki Hirata, and Hidenori Ishihara. Safety operation consciousness realization of a mr fluids-based novel haptic interface for teleoperated catheter minimally invasive neurosurgery. *IEEE/ASME Transactions on Mechatronics*, 21(2):1043–1054, 2016.

[206] Linshuai Zhang, Shuxiang Guo, Huadong Yu, Shuoxin Gu, Yu Song, and Miao Yu. Electromagnetic braking-based collision protection of a novel catheter manipulator. In *2017 IEEE International Conference on Mechatronics and Automation (ICMA)*, pages 1726–1731. IEEE, 2017.

[207] Xuanchun Yin, Shuxiang Guo, and Yu Song. Magnetorheological fluids actuated haptic-based teleoperated catheter operating system. *Micromachines*, 9(9):465, 2018.

[208] Zhengyou Zhang. Flexible camera calibration by viewing a plane from unknown orientations. In *Proceedings of the Seventh IEEE International Conference on Computer Vision*, volume 1, pages 666–673. Ieee, 1999.

[209] Mohsen Moradi Dalvand, Saeid Nahavandi, and Robert D Howe. High speed vision-based 3d reconstruction of continuum robots. In *2016 IEEE International Conference on Systems, Man, and Cybernetics (SMC)*, pages 000618–000623. IEEE, 2016.

[210] Rida T Farouki. *Pythagorean—hodograph Curves*. Springer, 2008.

[211] J. Spillmann and M. Teschner. CORDE: Cosserat Rod Elements for the Dynamic Simulation

of One-Dimensional Elastic Objects. In Dimitris Metaxas and Jovan Popovic, editors, *Eurographics/SIGGRAPH Symposium on Computer Animation*, pages 1–10. The Eurographics Association, 2007.

[212] Zhihao Zuo, Weixin Yinling Qian, Xiangyun Liao, and Pheng-Ann Heng. Position based catheterization and angiography simulation. In *2018 IEEE 6th International Conference on Serious Games and Applications for Health (SeGAH)*, pages 1–7. IEEE, 2018.

[213] John Till, Vincent Aloi, and Caleb Rucker. Real-time dynamics of soft and continuum robots based on cosserat rod models. *The International Journal of Robotics Research*, 38(6):723–746, 2019.

[214] ASTM-F2063:18. Standard specification for wrought nickel-titanium shape memory alloys for medical devices and surgical implants. Standard, ASTM International, West Conshohocken, PA, USA, 2018.

[215] GR Zadno and TW Duerig. Linear and non-linear superelasticity in niti. In *Proceedings of the MRS International Meeting on Advanced Materials.*, volume 9, pages 201–206, 1988.

[216] Kazuto Takashima, Rei Shimomura, Takayuki Kitou, Hiroki Terada, Kiyoshi Yoshinaka, and Ken Ikeuchi. Contact and friction between catheter and blood vessel. *Tribology International*, 40(2):319–328, 2007.

[217] Sergei Igorevich Kabanikhin. Definitions and examples of inverse and ill-posed problems. *Journal of Inverse and Ill-Posed Problems*, 16(4):317–357, 2008.

[218] Vincent Aloi and Caleb Rucker. Estimating loads along elastic rods. In *2019 International Conference on Robotics and Automation (ICRA)*, pages 2867–2873, May 2019.

[219] Seyedali Mirjalili and Jin Song Dong. Multi-objective particle swarm optimization. In *Multi-Objective Optimization using Artificial Intelligence Techniques*, pages 21–36. Springer, 2020.

[220] ISO-14125. Fibre-reinforced plastic composites — determination of flexural properties — amendment 1. Standard, International Organization for Standardization, 02 2011. Edition 1.

[221] Tejas M Patel, Sanjay C Shah, and Samir B Pancholy. Long distance tele-robotic-assisted percutaneous coronary intervention: a report of first-in-human experience. *EClinicalMedicine*, 14:53–58, 2019.

[222] Gavin W Britz, Johnny Tomas, and Alan Lumsden. Feasibility of robotic-assisted neurovascular interventions: initial experience in flow model and porcine model. *Neurosurgery*, 86(2):309–314, 2020.

[223] Vitor Mendes Pereira, Nicole Mariantonia Cancelliere, Patrick Nicholson, Ivan Radovanovic, Kaitlyn E Drake, John-Michael Sungur, Timo Krings, and Aquilla Turk. First-in-human, robotic-assisted neuroendovascular intervention. *Journal of NeuroInterventional Surgery*, 12(4):338–340, 2020.

[224] Sandip S Panesar, John J Volpi, Alan Lumsden, Virendra Desai, Neal S Kleiman, Trevis L Sample, Eric Elkins, and Gavin W Britz. Telerobotic stroke intervention: a novel solution to the care dissemination dilemma. *Journal of Neurosurgery*, 1(aop):1–8, 2019.

[225] P Stefan, J Traub, C Hennersperger, M Esposito, and N Navab. Challenges in computer assisted interventions: Challenges in design, development, evaluation, and clinical deployment of computer assisted intervention solutions. In *Handbook of Medical Image Computing and Computer Assisted Intervention*, pages 979–1012. Elsevier, 2020.

[226] Anzhu Gao, Ning Liu, Mali Shen, Mohamed EMK Abdelaziz, Burak Temelkuran, and Guang-Zhong Yang. Laser-profiled continuum robot with integrated tension sensing for simultaneous shape and tip force estimation. *Soft Robotics*, 2020.

[227] Ran Xu, Aaron Yurkewich, and Rajni V Patel. Curvature, torsion, and force sensing in continuum robots using helically wrapped fbg sensors. *IEEE Robotics and Automation Letters*, 1(2):1052–1059, 2016.

[228] N. Bandari, J. Dargahi, and M. Packirisamy. Miniaturized optical force sensor for minimally invasive surgery with learning-based nonlinear calibration. *IEEE Sensors Journal*, pages 1–1, 2019.

[229] N. Bandari, J. Dargahi, and M. Packirisamy. Tactile sensors for minimally invasive surgery: A review of the state-of-the-art, applications, and perspectives. *IEEE Access*, 8:7682–7708, 2020.

[230] Mahta Khoshnam, Allan C Skanes, and Rajni V Patel. Modeling and estimation of tip contact force for steerable ablation catheters. *IEEE Transactions on Biomedical Engineering*, 62(5):1404–1415, 2015.

[231] Shahir Hasanzadeh and Farrokh Janabi. Model-based force estimation for intracardiac catheters. *IEEE/ASME Transactions on Mechatronics*, 21(1):154–162, 2015.

[232] Shuxiang Guo, Jinxin Cui, Nan Xiao, and Xianqiang Bao. Simulation analysis of catheter bending in vascular intervention robot based on ansys. In *2018 IEEE International Conference on Mechatronics and Automation (ICMA)*, pages 585–590. IEEE, 2018.

[233] Hidefumi Wakamatsu and Shinichi Hirai. Static modeling of linear object deformation based on differential geometry. *The International Journal of Robotics Research*, 23(3):293–311, 2004.

[234] Caleb Rucker, Bryan A Jones, and Robert J Webster III. A geometrically exact model for externally loaded concentric-tube continuum robots. *IEEE Transactions on Robotics*, 26(5):769–780, 2010.

[235] Thomas Waite. *Cosserat Model for Robotic Catheter Systems*. PhD thesis, Harvard University, 2017.

[236] Caleb Rucker and Robert Webster III. Statics and dynamics of continuum robots with general tendon routing and external loading. *IEEE Transactions on Robotics*, 27(6):1033–1044, 2011.

[237] Kaitlin Oliver-Butler, John Till, and Caleb Rucker. Continuum robot stiffness under external loads and prescribed tendon displacements. *IEEE Transactions on Robotics*, 35(2):403–419, 2019.

[238] M. Mahvash and P. E. Dupont. Stiffness control of surgical continuum manipulators. *IEEE Transactions on Robotics*, 27(2):334–345, 2011.

[239] Hwan-Taek Ryu, Jaehong Woo, Byung-Rok So, and Byung-Ju Yi. Shape and contact force estimation of inserted flexible medical device. *International Journal of Control, Automation and Systems*, 18(1):163–174, 2020.

[240] Janis Edelmann, Andrew J Petruska, and Bradley J Nelson. Magnetic control of continuum devices. *The International Journal of Robotics Research*, 36(1):68–85, 2017.

[241] Haoyu Wang, Jianhuang Wu, and Yiyu Cai. An adaptive deviation-feedback approach for simulating multiple devices interaction in virtual interventional radiology. *Computer-Aided Design*, 117:102738, 2019.

[242] Josef Stoer and Roland Bulirsch. *Introduction to numerical analysis*, volume 12. Springer Science & Business Media, 2013.

[243] SP Venkateshan and P Swaminathan. Chapter 9 - numerical integration. In S.P. Venkateshan and Prasanna Swaminathan, editors, *Computational Methods in Engineering*, pages 317 – 373. Academic Press, Boston, 2014.

[244] Richard M Murray. *A mathematical introduction to robotic manipulation*. CRC press, 2017.

[245] Yogesh Thakur, David W Holdsworth, and Maria Drangova. Characterization of catheter dynamics during percutaneous transluminal catheter procedures. *IEEE Transactions on Biomedical Engineering*, 56(8):2140–2143, 2009.

[246] A. Salimi, J. Mohammadpour, K. Grigoriadis, and N. V. Tsekos. Dynamic Simulation of Blood Flow Effects on Flexible Manipulators During Intra-Cardiac Procedures on the Beating Heart. In *Dynamic Systems and Control Conference*, volume ASME 2011 Dynamic Systems and Control Conference and Bath/ASME Symposium on Fluid Power and Motion Control, Volume 2, pages 487–494, 10 2011.

[247] Raffaella Trivisonne, Erwan Kerrien, and Stéphane Cotin. Constrained stochastic state estimation of deformable 1d objects: Application to single-view 3d reconstruction of catheters

with radio-opaque markers. *Computerized Medical Imaging and Graphics*, page 101702, 2020.

[248] G. Bradski. The OpenCV Library. *Dr. Dobb's Journal of Software Tools*, 2000.

[249] Conrad Sanderson and Ryan Curtin. Armadillo: a template-based c++ library for linear algebra. *Journal of Open Source Software*, 1(2):26, 2016.

[250] M Wood, J Miller, H Chen, and B Petrellis. Catheter ablation of accessory atrioventricular connections. *Catheter ablation of cardiac arrhythmias. Philadelphia: Elsevier*, pages 364–5, 2010.

[251] Mark Runciman, Ara Darzi, and George P Mylonas. Soft robotics in minimally invasive surgery. *Soft robotics*, 2019.

[252] Filip Jelínek, Ewout A Arkenbout, Paul WJ Henselmans, Rob Pessers, and Paul Breedveld. Classification of joints used in steerable instruments for minimally invasive surgery-a review of the state of the art. *Journal of Medical Devices*, 9(1):010801, 2015.

[253] N. Bandari, J. Dargahi, and M. Packirisamy. Tactile sensors for minimally invasive surgery: A review of the state-of-the-art, applications, and perspectives. *IEEE Access*, 8:7682–7708, 2020.

[254] Dipen C Shah, Hendrik Lambert, Hiroshi Nakagawa, Arne Langenkamp, Nicolas Aeby, and Giovanni Leo. Area under the real-time contact force curve (force–time integral) predicts radiofrequency lesion size in an in vitro contractile model. *Journal of cardiovascular electrophysiology*, 21(9):1038–1043, 2010.

[255] Mohsen Moradi Dalvand, Saeid Nahavandi, and Robert D Howe. An analytical loading model for n-tendon continuum robots. *IEEE Transactions on Robotics*, 34(5):1215–1225, 2018.

[256] Mahta Khoshnam and Rajni V Patel. A pseudo-rigid-body 3r model for a steerable ablation catheter. In *Robotics and Automation (ICRA), 2013 IEEE International Conference on*, pages 4427–4432. IEEE, 2013.

[257] Robert K Katzschmann, Cosimo Della Santina, Yasunori Toshimitsu, Antonio Bicchi, and Daniela Rus. Dynamic motion control of multi-segment soft robots using piecewise constant curvature matched with an augmented rigid body model. In *2019 2nd IEEE International Conference on Soft Robotics (RoboSoft)*, pages 454–461. IEEE, 2019.

[258] Byungjeon Kang, Risto Kojcev, and Edoardo Sinibaldi. The first interlaced continuum robot, devised to intrinsically follow the leader. *PloS one*, 11(2):e0150278, 2016.

[259] Minou Kouh Soltani, Sohrab Khanmohammadi, Farzan Ghalichi, and Farrokh Janabi-Sharifi. A soft robotics nonlinear hybrid position/force control for tendon driven catheters. *International Journal of Control, Automation and Systems*, 15(1):54–63, 2017.

[260] Junghwan Back, Thomas Manwell, Rashed Karim, Kawal Rhode, Kaspar Althoefer, and Hongbin Liu. Catheter contact force estimation from shape detection using a real-time cosserat rod model. In *Intelligent Robots and Systems (IROS), 2015 IEEE/RSJ International Conference on*, pages 2037–2042. IEEE, 2015.

[261] Hedyeh Rafii-Tari, Jindong Liu, Su-Lin Lee, Colin Bicknell, and Guang-Zhong Yang. Learning-based modeling of endovascular navigation for collaborative robotic catheterization. In *International conference on medical image computing and computer-assisted intervention*, pages 369–377. Springer, 2013.

[262] Wenqiang Chi, Jindong Liu, Hedyeh Rafii-Tari, Celia Riga, Colin Bicknell, and Guang-Zhong Yang. Learning-based endovascular navigation through the use of non-rigid registration for collaborative robotic catheterization. *International journal of computer assisted radiology and surgery*, 13(6):855–864, 2018.

[263] Piotr R Slawinski, Nabil Simaan, Keith L Obstein, and Pietro Valdastri. Sensorless estimation of the planar distal shape of a tip-actuated endoscope. *IEEE robotics and automation letters*, 4(4):3371–3377, 2019.

[264] Malini Govindan, Anatoli Kiotsekoglou, Samir K Saha, and A John Camm. Right atrial myocardial deformation by two-dimensional speckle tracking echocardiography predicts recurrence in paroxysmal atrial fibrillation. *Journal of echocardiography*, 15(4):166–175, 2017.

[265] Stephen Timoshenko, S Timoshenko, and JN Goodier. *Theory of Elasticity*. McGraw-Hill book Company, 1951.

[266] Ali Pourdjabbar, Lawrence Ang, Omid Behnamfar, Mitul P Patel, Ryan R Reeves, Paul T Campbell, Ryan D Madder, and Ehtisham Mahmud. Robotics in percutaneous cardiovascular interventions. *Expert review of cardiovascular therapy*, 15(11):825–833, 2017.

[267] Su-Lin Lee, Mihaela Constantinescu, Wenqiang Bobby Chi, and Guang-Zhong Yang. Devices for endovascular interventions: technical advances and translational challenges. Technical report, National Institute for Health Research, 2017.

[268] Wenqiang Chi, Hedyeh Rafii-Tari, Christopher J Payne, Jindong Liu, Celia Riga, Colin Bicknell, and Guang-Zhong Yang. A learning based training and skill assessment platform with haptic guidance for endovascular catheterization. In *2017 IEEE International Conference on Robotics and Automation (ICRA)*, pages 2357–2363. IEEE, 2017.

[269] Wenqiang Chi, Jindong Liu, Mohamed EMK Abdelaziz, Giulio Dagnino, Celia Riga, Colin Bicknell, and Guang-Zhong Yang. Trajectory optimization of robot-assisted endovascular catheterization with reinforcement learning. In *2018 IEEE/RSJ International Conference on Intelligent Robots and Systems (IROS)*, pages 3875–3881. IEEE, 2018.

[270] Vahid Farrahi, Maisa Niemelä, Maarit Kangas, Raija Korpelainen, and Timo Jämsä. Calibration and validation of accelerometer-based activity monitors: A systematic review of machine-learning approaches. *Gait Posture*, 68:285–299, 2019.

[271] Juho Vihonen, Janne Honkakorpi, Janne Tuominen, Jouni Mattila, and Ari Visa. Linear accelerometers and rate gyros for rotary joint angle estimation of heavy-duty mobile manipulators using forward kinematic modeling. *IEEE/ASME Transactions on Mechatronics*, 21(3):1765–1774, 2016.

[272] Glen Cooper, Ian Sheret, Louise McMillian, Konstantinos Siliverdis, Ning Sha, Diana Hodgins, Laurence Kenney, and David Howard. Inertial sensor-based knee flexion/extension angle estimation. *Journal of biomechanics*, 42(16):2678–2685, 2009.

[273] Shaghayegh Zihajehzadeh and Edward J Park. A novel biomechanical model-aided imu/uwb fusion for magnetometer-free lower body motion capture. *IEEE Transactions on Systems, Man, and Cybernetics: Systems*, 47(6):927–938, 2016.

[274] Sebastian OH Madgwick, Andrew JL Harrison, and Ravi Vaidyanathan. Estimation of and marg orientation using a gradient descent algorithm. In *2011 IEEE international conference on rehabilitation robotics*, pages 1–7. IEEE, 2011.

[275] Daquan Feng, Chunqi Wang, Chunlong He, Yuan Zhuang, and Xiang-Gen Xia. Kalman-filter-based integration of imu and uwb for high-accuracy indoor positioning and navigation. *IEEE Internet of Things Journal*, 7(4):3133–3146, 2020.

[276] Jin Wu, Zebo Zhou, Hassen Fourati, Rui Li, and Ming Liu. Generalized linear quaternion complementary filter for attitude estimation from multisensor observations: An optimization approach. *IEEE Transactions on Automation Science and Engineering*, 16(3):1330–1343, 2019.

[277] Luciano Cantelli, Giovanni Muscato, Marco Nunnari, and Davide Spina. A joint-angle estimation method for industrial manipulators using inertial sensors. *IEEE/ASME Transactions On Mechatronics*, 20(5):2486–2495, 2015.

[278] Leonardo Zacchini, Vincenzo Calabro, Mauro Candeloro, Francesco Fanelli, Alessandro Ridolfi, and Fredrik Dukan. Novel non-continuous carouseling approaches for mems-based north seeking using kalman filter: theory, simulations and preliminary experimental evaluation. *IEEE/ASME Transactions on Mechatronics*, 2020.

[279] João Luís Marins, Xiaoping Yun, Eric R Bachmann, Robert B McGhee, and Michael J Zyda. An extended kalman filter for quaternion-based orientation estimation using marg sensors. In *Proceedings 2001 IEEE/RSJ International Conference on Intelligent Robots and Systems. Expanding the Societal Role of Robotics in the the Next Millennium (Cat. No. 01CH37180)*, volume 4, pages 2003–2011. IEEE, 2001.

[280] Xiaoping Yun and Eric R Bachmann. Design, implementation, and experimental results of

a quaternion-based kalman filter for human body motion tracking. *IEEE transactions on Robotics*, 22(6):1216–1227, 2006.

[281] Malcolm David Shuster and S D_ Oh. Three-axis attitude determination from vector observations. *Journal of guidance and Control*, 4(1):70–77, 1981.

[282] Ya Tian, Hongxing Wei, and Jindong Tan. An adaptive-gain complementary filter for real-time human motion tracking with marg sensors in free-living environments. *IEEE Transactions on Neural Systems and Rehabilitation Engineering*, 21(2):254–264, 2012.

[283] Alexander David Young. Use of body model constraints to improve accuracy of inertial motion capture. In *2010 International Conference on Body Sensor Networks*, pages 180–186. IEEE, 2010.

[284] Riccardo Costanzi, Francesco Fanelli, Niccolo Monni, Alessandro Ridolfi, and Benedetto Allotta. An attitude estimation algorithm for mobile robots under unknown magnetic disturbances. *IEEE/ASME Transactions on Mechatronics*, 21(4):1900–1911, 2016.

[285] Giancarlo Troni and Louis L Whitcomb. Field sensor bias calibration with angular-rate sensors: Theory and experimental evaluation with application to magnetometer calibration. *IEEE/ASME Transactions on Mechatronics*, 24(4):1698–1710, 2019.

[286] Sebastian OH Madgwick, Samuel Wilson, Ruth Turk, Jane Burridge, Christos Kapatos, and Ravi Vaidyanathan. An extended complementary filter (ecf) for full-body marg orientation estimation. *IEEE/ASME Transactions on Mechatronics*, 2020.

[287] S. Majumder and M. J. Deen. A robust orientation filter for wearable sensing applications. *IEEE Sensors Journal*, 20(23):14228–14236, 2020.

[288] Diego A Aligia, Bruno A Roccia, Cristian H De Angelo, Guillermo A Magallán, and Guillermo N González. An orientation estimation strategy for low cost imu using a non-linear luenberger observer. *Measurement*, page 108664, 2020.

[289] Antônio CB Chiella, Bruno OS Teixeira, and Guilherme AS Pereira. Quaternion-based robust attitude estimation using an adaptive unscented kalman filter. *Sensors*, 19(10):2372, 2019.

[290] Donghoon Kang, Cheongjae Jang, and Frank C Park. Unscented kalman filtering for simultaneous estimation of attitude and gyroscope bias. *IEEE/ASME Transactions on Mechatronics*, 24(1):350–360, 2019.

[291] Amanda Fransson and Oscar Lundström. Learning a better attitude: A recurrent neural filter for orientation estimation. Master's thesis, Chalmers University of Technology, 2020.

[292] Huseyin Coskun, Felix Achilles, Robert DiPietro, Nassir Navab, and Federico Tombari. Long short-term memory kalman filters: Recurrent neural estimators for pose regularization. In *Proceedings of the IEEE International Conference on Computer Vision*, pages 5524–5532, 2017.

[293] Tobias Zimmermann, Bertram Taetz, and Gabriele Bleser. Imu-to-segment assignment and orientation alignment for the lower body using deep learning. *Sensors*, 18(1):302, 2018.

[294] Milad Nazarahari and Hossein Rouhani. 40 years of sensor fusion for orientation tracking via magnetic and inertial measurement units: Methods, lessons learned, and future challenges. *Information Fusion*, 2020.

[295] Carmen MN Brigante, Nunzio Abbate, Adriano Basile, Alessandro Carmelo Faulisi, and Salvatore Sessa. Towards miniaturization of a mems-based wearable motion capture system. *IEEE Transactions on industrial electronics*, 58(8):3234–3241, 2011.

[296] Mahmoud El-Gohary and James McNames. Human joint angle estimation with inertial sensors and validation with a robot arm. *IEEE Transactions on Biomedical Engineering*, 62(7):1759–1767, 2015.

[297] Markus Miezal, Bertram Taetz, and Gabriele Bleser. On inertial body tracking in the presence of model calibration errors. *Sensors*, 16(7):1132, 2016.

[298] Xavier Robert-Lachaine, Hakim Mecheri, Christian Larue, and André Plamondon. Validation of inertial measurement units with an optoelectronic system for whole-body motion analysis. *Medical & biological engineering & computing*, 55(4):609–619, 2017.

[299] Klaus Schittkowski. Nlpql: A fortran subroutine solving constrained nonlinear programming problems. *Annals of operations research*, 5(2):485–500, 1986.

[300] N. Wang, M. J. Er, and M. Han. Generalized single-hidden layer feedforward networks for regression problems. *IEEE Transactions on Neural Networks and Learning Systems*, 26(6):1161–1176, 2015.

[301] Tae Seob Kim, David Dae Hwan Park, Young Bae Lee, Dong Gil Han, Jeong su Shim, Young Jig Lee, Peter Chan Woo Kim, et al. A study on the measurement of wrist motion range using the iphone 4 gyroscope application. *Annals of plastic surgery*, 73(2):215–218, 2014.

[302] F Landis Markley, Yang Cheng, John L Crassidis, and Yaakov Oshman. Averaging quaternions. *Journal of Guidance, Control, and Dynamics*, 30(4):1193–1197, 2007.

[303] S. Sarabandi, A. Shabani, J. M. Porta, and F. Thomas. On closed-form formulas for the 3-d nearest rotation matrix problem. *IEEE Transactions on Robotics*, 36(4):1333–1339, 2020.

[304] J. Wu, Y. Jiang, C. Li, R. Sun, C. Zhang, Y. Yu, Y. Zhu, and M. Liu. Circuit synthesis of 3-d rotation orthonormalization. *IEEE Transactions on Circuits and Systems II: Express Briefs*, pages 1–1, 2020.

[305] Marco Caruso, Angelo Maria Sabatini, Marco Knaflitz, Marco Gazzoni, Ugo Della Croce, and Andrea Cereatti. Orientation estimation through magneto-inertial sensor fusion: A heuristic approach for suboptimal parameters tuning. *IEEE Sensors Journal*, 2020.

[306] World Health Organization (WHO). *Cardiovascular diseases (CVDs) factsheets,*, 4 2017. Accessed: 15-12-2020.

[307] Masato Nakamura. Angiography is the gold standard and objective evidence of myocardial ischemia is mandatory if lesion severity is questionable. *Circulation Journal*, pages 1012101024–1012101024, 2011.

[308] Faisal Hasan and Johannes Bonatti. Robotically assisted percutaneous coronary intervention: benefits to the patient and the cardiologist. *Expert Review of Cardiovascular Therapy*, 13(11):1165–1168, 2015. PMID: 26377605.

[309] Hiram G. Bezerra, Emile Mehanna, George W. Vetrovec, Marco A. Costa, and Giora Weisz. Longitudinal geographic miss (lgm) in robotic assisted versus manual percutaneous coronary interventions. *Journal of interventional cardiology*, 28(5):449–455, 2015.

[310] Chad M Dugas and Jeffrey M Schussler. Advanced technology in interventional cardiology: a roadmap for the future of precision coronary interventions. *Trends in cardiovascular medicine*, 26(5):466–473, 2016.

[311] Karlin Bark, Jason W Wheeler, Sunthar Premakumar, and Mark R Cutkosky. Comparison of skin stretch and vibrotactile stimulation for feedback of proprioceptive information. In *2008 Symposium on Haptic Interfaces for Virtual Environment and Teleoperator Systems*, pages 71–78. IEEE, 2008.

[312] Shuxiang Guo, Yu Song, Xuanchun Yin, Linshuai Zhang, Takashi Tamiya, Hideyuki Hirata, and Hidenori Ishihara. A novel robot-assisted endovascular catheterization system with haptic force feedback. *IEEE Transactions on Robotics*, 35(3):685–696, 2019.

[313] Baoliang Zhao and Carl A Nelson. A sensorless force-feedback system for robot-assisted laparoscopic surgery. *Computer Assisted Surgery*, pages 1–8, 2019.

[314] Xuanchun Yin, Shuxiang Guo, Nan Xiao, Takashi Tamiya, Hideyuki Hirata, and Hidenori Ishihara. Safety operation consciousness realization of a mr fluids-based novel haptic interface for teleoperated catheter minimally invasive neurosurgery. *IEEE/ASME Transactions on Mechatronics*, 21(2):1043–1054, 2015.

[315] Anil K Bastola and Mokarram Hossain. A review on magneto-mechanical characterizations of magnetorheological elastomers. *Composites Part B: Engineering*, page 108348, 2020.

[316] Victor Birman and George A Kardomateas. Review of current trends in research and applications of sandwich structures. *Composites Part B: Engineering*, 142:221–240, 2018.

[317] Alex Mazursky, Jeong-Hoi Koo, and Tae-Heon Yang. Design, modeling, and evaluation of a slim haptic actuator based on electrorheological fluid. *Journal of Intelligent Material Systems and Structures*, page 1045389X19836172, 2019.

[318] Smita Kanjanapas, Cara M Nunez, Sophia R Williams, Allison M Okamura, and Ming Luo. Design and analysis of pneumatic 2-dof soft haptic devices for shear display. *IEEE Robotics and Automation Letters*, 4(2):1365–1371, 2019.

[319] Pyunghwa Kim, Soomin Kim, Young-Dai Park, and Seung-Bok Choi. Force modeling for incisions into various tissues with mrf haptic master. *Smart Materials and Structures*, 25(3):035008, 2016.

[320] Okan Topcu, Yiğit Taşcıoğlu, and Erhan Ilhan Konukseven. Design and multi-physics optimization of rotary mrf brakes. *Results in physics*, 8:805–818, 2018.

[321] Nicola Sgambelluri, Enzo P Scilingo, Rocco Rizzo, and Antonio Bicchi. A free-hand haptic interface based on magnetorheological fluids. In *The Sense of Touch and its Rendering*, pages 155–178. Springer, 2008.

[322] Ali Alkhalaf, Amir Hooshiar, and Javad Dargahi. Composite magnetorheological elastomers for tactile displays: Enhanced mr-effect through bi-layer composition. *Composites Part B: Engineering*, 190:107888, 2020.

[323] Xin Yuan, Xuefeng Zhou, Yudai Liang, Lijuan Wang, Riming Chen, Mengying Zhang, Huayan Pu, Shouhu Xuan, Jinbo Wu, and Weijia Wen. A stable high-performance isotropic electrorheological elastomer towards controllable and reversible circular motion. *Composites Part B: Engineering*, page 107988, 2020.

[324] Martin Culjat, Chih-Hung King, Miguel Franco, James Bisley, Warren Grundfest, and Erik Dutson. Pneumatic balloon actuators for tactile feedback in robotic surgery. *Industrial Robot: An International Journal*, 35(5):449–455, 2008.

[325] Jong Seok Oh, Young Min Han, and Seung Bok Choi. Design and performance evaluation of

mr tactile device for medical application. In *Applied Mechanics and Materials*, volume 433, pages 869–872. Trans Tech Publ, 2013.

[326] Jong-Seok Oh, Jin-Kyu Kim, and Seung-Bok Choi. Experimental test of mr fluid based tactile device for minimally invasive surgery. In *Active and Passive Smart Structures and Integrated Systems 2013*, volume 8688, page 86882C. International Society for Optics and Photonics, 2013.

[327] Amy Kyungwon Han, Jung Hwa Bae, Katerina C Gregoriou, Christopher J Ploch, Roger E Goldman, Gary H Glover, Bruce L Daniel, and Mark R Cutkosky. Mr-compatible haptic display of membrane puncture in robot-assisted needle procedures. *IEEE transactions on haptics*, 11(3):443–454, 2018.

[328] Hiroshi Yanatori, Kazuki Tsuji, Konomu Abe, Kenji Iwasaki, and Takashi Mineta. Fabrication and characterization of an arrayed shape memory alloy thick film actuator device for planar tactile displays. *IEEJ Transactions on Sensors and Micromachines*, 139(1):15–20, 2019.

[329] Ashkan Dargahi, Ramin Sedaghati, and Subhash Rakheja. On the properties of magnetorheological elastomers in shear mode: Design, fabrication and characterization. *Composites Part B: Engineering*, 159:269–283, 2019.

[330] Hossein Vatandoost, Masoud Hemmatian, Ramin Sedaghati, and Subhash Rakheja. Dynamic characterization of isotropic and anisotropic magnetorheological elastomers in the oscillatory squeeze mode superimposed on large static pre-strain. *Composites Part B: Engineering*, 182:107648, 2020.

[331] Anna Boczkowska, Stefan F Awietjan, Stanisław Pietrzko, and Krzysztof J Kurzydłowski. Mechanical properties of magnetorheological elastomers under shear deformation. *Composites Part B: Engineering*, 43(2):636–640, 2012.

[332] A Dorfmann and RW Ogden. Some problems in nonlinear magnetoelasticity. *Zeitschrift für angewandte Mathematik und Physik ZAMP*, 56(4):718–745, 2005.

[333] JL Ericksen. Electromagnetism in steadily rotating matter. *Continuum Mechanics and Thermodynamics*, 17(5):361–371, 2006.

[334] Mostafa Asadi Khanouki, Ramin Sedaghati, and Masoud Hemmatian. Experimental characterization and microscale modeling of isotropic and anisotropic magnetorheological elastomers. *Composites Part B: Engineering*, 176:107311, 2019.

[335] Anil K Bastola, Milan Paudel, and Lin Li. Magnetic circuit analysis to obtain the magnetic permeability of magnetorheological elastomers. *Journal of Intelligent Material Systems and Structures*, 29(14):2946–2953, 2018.

[336] Darius Diogo Barreto, Ajeet Kumar, and Sushma Santapuri. Extension-torsion-inflation coupling in compressible magnetoelastomeric thin tubes with helical magnetic anisotropy. *Journal of Elasticity*, pages 1–30, 2020.

[337] Luis Dorfmann and Ray W Ogden. *Nonlinear theory of electroelastic and magnetoelastic interactions*, volume 1. Springer, 2014.

[338] Xavier Oliver and C Agelet de Saracibar. Continuum mechanics for engineers. *Theory and problems*, 2017.

[339] Takehito Kikuchi, Yusuke Kobayashi, Mika Kawai, and Tetsu Mitsumata. Elastic properties of magnetorheological elastomers in a heterogeneous uniaxial magnetic field. *International journal of molecular sciences*, 19(10):3045, 2018.

[340] Stephan Rudykh and Katia Bertoldi. Stability of anisotropic magnetorheological elastomers in finite deformations: a micromechanical approach. *Journal of the Mechanics and Physics of Solids*, 61(4):949–967, 2013.

[341] A Bagheri, D Taghizadeh, and H Darijani. On the behavior of rotating thick-walled cylinders made of hyperelastic materials. *Meccanica*, 51(3):673–692, 2016.

[342] Ashkan Dargahi, Subhash Rakheja, and Ramin Sedaghati. Development of a field dependent prandtl-ishlinskii model for magnetorheological elastomers. *Materials & Design*, 166:107608, 2019.

[343] Christoph Hartmann, Jue Wang, Daniel Opristescu, and Wolfram Volk. Implementation and evaluation of optical flow methods for two-dimensional deformation measurement in comparison to digital image correlation. *Optics and Lasers in Engineering*, 107:127–141, 2018.

[344] Mackram F Eleid, Park P Zheng, Rajiv Gulati, Per Bergman, Nicholas Kottenstette, Yao Li, Amir Lerman, and Gurpreet S Sandhu. Remote robotic percutaneous coronary intervention: An animal feasibility study. *Catheterization and Cardiovascular Interventions*, 2020.

[345] Zhengyang Chen, Shuxiang Guo, and Wei Zhou. A novel clamping mechanism for circumferential force feedback device of the vascular interventional surgical robot. In *2020 IEEE International Conference on Mechatronics and Automation (ICMA)*, pages 1625–1630. IEEE, 2020.

Appendix A

(1) Definition of Frenet-Serret frame, $\boldsymbol{\lambda}_{1-3}$:

$$\boldsymbol{\lambda}_1(s) = \frac{\mathbf{c}'(s)}{||\mathbf{c}'(s)||},$$

$$\boldsymbol{\lambda}_2(s) = -\boldsymbol{\lambda}_1(s) \times \frac{\mathbf{c}'(s) \times \mathbf{c}''(s)}{||\mathbf{c}'(s) \times \mathbf{c}''(s)||},$$

$$\boldsymbol{\lambda}_3(s) = \boldsymbol{\lambda}_1(s) \times \boldsymbol{\lambda}_2(s),$$

(2) Definition of the total twist angle τ:

$$\tau(s) = \mathbf{c}'''(s) \cdot \frac{\mathbf{c}'(s) \times \mathbf{c}''(s)}{||\mathbf{c}' \times \mathbf{c}''(s)||^2},$$

$$\alpha(s) = -\int_0^s \tau(\psi) d\psi,$$

(3) Rotation matrix about $\boldsymbol{\lambda}_1$ with α angle (Rodrigues' rotation formula):

$$\mathbf{R}_\alpha(s) = \mathbf{I}_3 + \sin\alpha(s)\boldsymbol{\lambda}_1^\wedge(s) + (1 - \cos\alpha(s))\boldsymbol{\lambda}_1^{\wedge 2}(s)$$

(4) Definition of the Darboux frame, $\mathbf{d}_{1-3}$:

$$\begin{pmatrix} \mathbf{d}_1(s) \\ \mathbf{d}_2(s) \\ \mathbf{d}_3(s) \end{pmatrix}^T = \mathbf{R}_\alpha(s) \begin{pmatrix} \boldsymbol{\lambda}_1(s) \\ \boldsymbol{\lambda}_2(s) \\ \boldsymbol{\lambda}_3(s) \end{pmatrix}^T,$$

(5) Definition of the curvature in Frenet-Serret frame, $\kappa(s)$:

$$\kappa(s) = \frac{||\mathbf{c}'(s) \times \mathbf{c}''(s)||}{||\mathbf{c}'(s)||^3},$$

(6) Definition of geodesic curvature, $\kappa_g(s)$, geodesic torsion, $\tau_g(s)$, and normal curvature $\kappa_n(s)$ in Darboux frame based on Frenet-Serret frame:

$$\begin{pmatrix} \kappa_g(s) \\ \kappa_n(s) \\ \tau_g(s) \end{pmatrix} = \begin{pmatrix} \cos\alpha(s) & 0 & 0 \\ 0 & \sin\alpha(s) & 0 \\ 0 & 0 & 2 \end{pmatrix} \begin{pmatrix} \kappa(s) \\ \kappa(s) \\ \tau(s) \end{pmatrix}.$$

(7) Definition of the first, second, and third derivative of $\mathbf{c}(s)$ using de Casteljau's algorithm:

$$\mathbf{c}'(s) = \sum_{i=0}^{n-1} n \begin{pmatrix} n-1 \\ i \end{pmatrix} (1-s)^{n-i-1}\, s^i (P_{i+1} - P_i),$$

$$\mathbf{c}''(s) = \sum_{i=0}^{n-2} n(n-1) \begin{pmatrix} n-2 \\ i \end{pmatrix} (1-s)^{n-i-2}\, s^i (P_{i+2} - 2P_{i+1} + P_i),$$

$$\mathbf{c}'''(s) = \sum_{i=0}^{n-3} n(n-1)(n-2) \begin{pmatrix} n-3 \\ i \end{pmatrix} (1-s)^{n-i-3}\, s^i (P_{i+4} - 3P_{i+2} + 3P_{i+1} - P_i).$$

(8) Definition of the hat operator, a mapping from $\mathbb{R}^3$ to $\mathfrak{so}(3)$:

$$\begin{pmatrix} u_1 \\ u_2 \\ u_3 \end{pmatrix}^{\wedge} \triangleq \begin{pmatrix} 0 & -u_3 & u_2 \\ u_3 & 0 & -u_1 \\ -u_2 & u_1 & 0 \end{pmatrix}.$$